Study the composition, processing and microstructural relationship of light alloys

ABDULRAHMAN IDRIS SUMAYLI

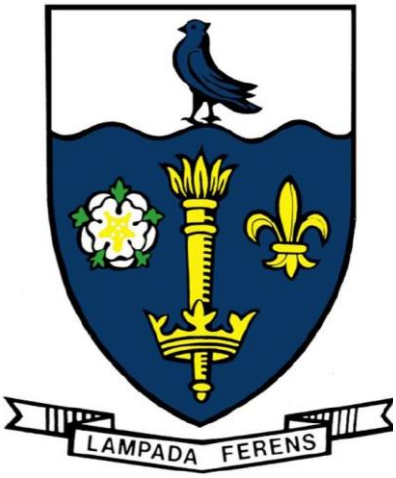

University of Hull

March 2022

Study of the composition, processing and microstructure relationship of light alloys

ABDULRAHMAN IDRIS SUMAYLI

A thesis submitted for the degree of

Doctor of Philosophy at the

University of Hull

March 2022

Abstract

This research consists of two main parts. The first part concerns the study of the effect of pulse electromagnetic fields on the microstructural evolution and the hardness of an Al-20%Si alloy. A pulse magnetic field apparatus is used to produce different magnetic field fluxes during the solidification of an Al-20%Si alloy. The size of the primary Si particles of the alloy is reduced to ~6 times (from 14078.7 μm^2 to 2427.3 μm^2) when the peak pulse magnetic field flux was increased from 0 to 1.4 T. In addition, the magnetic field resulted in the formation of lamellar Al + Si eutectic colonies, and more uniformed eutectic Si in the matrix. Such structure refinement increased the hardness of the alloy from 65 to 75 (Vickers hardness).

The second part of the research is to study the composition-microstructure relationship and corrosion properties of three Mg-Gd based alloys. The alloys used are (1) Mg-10%Gd, (2) Mg-10%Gd-0.4%Zr and (3) Mg-5%Gd-5%Nd-0.4%Zr (weight percentage). The focus of the research is to investigate the effects of adding Nd and Zr on the changes of phases and structures. Very effective grain refinement effect for the alloys were found when adding Nd and Zr, decreasing the size of Gd cuboids, and resulting in higher hardiness for the Mg-5%Gd-5%Nd-0.4%Zr. The mechanism is mainly due to the precipitation hardening and grain boundary strengthening. In addition, the corrosion behaviour is also tested in the Hank's solution. Noticeably, corrosion rate of the master alloy increased when alloyed with Nd and Zr.

Acknowledgment

I would like to express my wholehearted appreciation to University of Najran and Royal Embassy of Saudi Arabia Cultural Bureau for awarding me an International PhD Studentship to study a PhD degree at the University of Hull.

I am extremely grateful for the academic guidance and personal encouragement given by my supervisors, Professor Jiawei Mi and Dr Louise France, during my PhD study. At first, I am not very familiar with the research topic and lack of the background knowledge in this particular field of research. Prof. Mi has patiently educated and guided me through this difficult period of time and provided me with the strongest possible intellectual and hands-on experimental skills development support for me to climb up a steep learning path and overcome the difficult issues and challenges in the first two years, reaching the level that allow me to move onto a standard PhD research programme.

Additionally, I appreciate the technical and administrative help provided by the following members of staff at the University of Hull's School of Engineering:

Garry Robinson for assistance with sample preparation and SEM training, Professor Michael Fagan and Miss Sue Taft for performing X-ray imaging and nano-indentation testing, as well as, Mr Simon Cowell, Mr Stuart Butterick, and Mr Mike Jost for technical assistance throughout the workshop. Mr David Wright, Ms Sara Ord for providing administrative support.

Finally, I would like to express my gratitude to my father, Mr Idris Abdo, who passed away when I just began my PhD study, my mother, Ms. Zinab Mohammed, my brothers and sisters for their unwavering love and support throughout my life, without those, I wouldn't have gone this far. I want to thank my wife, Mrs. Aeshah for all the affection she has given me throughout my PhD research. She was always there to share, help, and accompany me

during one of the most stressful periods of my studies. I will not forget to express my gratitude to my children for demonstrating the beauty and positive side of life and allowing my soul to relax throughout the difficult moments of my thesis, they have been providing me with an endless supply of joy, love and happiness.

Table of Contents

Chapter 1 Introduction

1.1 The background

Metal alloys have widely been used in many industrial applications, for example in aerospace, transportation, energy, biomedical industry, etc. Among all metal-based alloys, aluminium-based and magnesium-based alloys are the most widely used light alloys in the world. To tailor and control the mechanical properties of Al and Mg based alloys for different industry applications, the microstructure of the alloys, i.e. the grain size of the alloy matrix, the size, morphologies, volume fraction and distribution of the intermetallic phases in those alloys need to be controlled to meet the designed requirement.

Most essential of all the cast alloys is the aluminum silicon (Al-Si) alloy. Al-Si foundry alloys, with weight percentages ranging from 5 to 25, are the most preferred and the most studied alloys. 80% to 90% of the world's aluminum castings are made from aluminum silicon compositions. Because it creates brittle crystals, Fe is the most problematic contaminant in Al-Si alloys (intermetallic). Because of the damaging Fe intermetallic, Manganese (Mn) is added to change them into the less dangerous Chinese script phase [1]. The mechanical properties, wear resistance, and physical characteristics of aluminum silicon alloys, such as fluidity, density thermal expansion coefficient, and so on, make them an excellent replacement for cast iron and other high-density alloys. Aluminum silicon hypereutectic alloys, for example, are an excellent choice to replace cast iron cylinder liners in engines.The cylinder liners used in aluminium silicon engine blocks are cast iron and are subjected to extreme wear, dynamic loading, and high temperatures at the present time. Aluminum silicon hypereutectic alloys are primarily utilised in die casting for purposes such as pistons, cylinder liners, and a limited number of engine blocks. They are also employed in a variety of other applications. It is still debatable whether or not the Al-Si hypereutectic engine blocks have been effective so far, but they have been employed in a limited number of automobiles [2]–[4]. The existence of coarse and brittle primary Si particles

in aluminum silicon hypereutectic alloys, which split and break quickly in the presence of high and repeated cycle loading, is thought to be the cause of their inability to succeed. As soon as a main Si particle splits, the soft aluminum matrix is subjected to extremely harsh wear conditions. It is suggested by several authors that the solution is to refine the primary Si particles before they can be used successfully in dynamic loading applications. Al-Si hypereutectic alloys have been extensively studied by Alpas' team at the University of Windsor. These alloys are suggested for use in applications where ultra-low wear is required [5], [6].

There are number of techniques for the grain refinement of Al based alloys. Compared to the numerous conventional methods, pulse magnetic field is one of the most efficient low energy methods [7]. It is a non-contact method that is applicable to all metal alloys, especially for high melting temperature alloys. The first main task of this research is to control and optimize the microstructures of Al-20%Si using pulse magnetic field method during the solidification, studying the effect of different magnetic field flux intensities on the solidification microstructures.

Regarding Magnesium, it is the lightest of the metals used in engineering application of the alloys, and it is also the most abundant. Low density and good mechanical capabilities distinguish these alloys from their competitors. When exposed to high temperatures, they, on the other hand, demonstrated unsatisfactory characteristics. Magnesium based alloys are promising materials for bio-medical implant applications due to their bio-degradability and biocompatibility [8].

The diverse alloying elements used in typical magnesium alloys have been introduced for a variety of specialised purposes. Due to the widespread usage of magnesium alloys as construction materials, mechanical qualities are frequently the most important concern. Using aluminium as an alloying element, for example, can be utilised for both solid-solution strengthening and precipitation hardening, both of which are desirable when the yield stress needs to be increased [9], [10]. In contrast, practically any strengthening has a negative impact on the ductility of the material being strengthened.

Additionally, it is clear from the Mg–Al phase diagram that Al lowers the melting and casting temperatures of magnesium alloys. So, the use of Al has an impact on the processing approach as well. As a result, the microstructure, which is essential for the qualities relevant to an application, is influenced by both the alloying elements and the processing conditions. Similarly, other alloying elements can be examined in the same way.

For a design engineer, strength is a crucial quality to have. Although it is important, it is not the only factor to take into account. This property profile includes ductility, elastic moduli, corrosionbehavior under service conditions, degradation rate (if applicable), and toxicology, among others. The alloy composition and various processing steps applied before a component is ready, such as an implant, are largely responsible for the properties of the alloy. Implants have a wide range of qualities that need to be determined in a variety of ways. An interdisciplinary approach is required, as is collaboration between experts from many fields of study [11].

Rare earth-containing magnesium alloys are recognised to have outstanding mechanical qualities as well as excellent creep resistance when compared to other magnesium alloys. Magnesium alloys are widely used in a variety of industries, including the aircraft industry and biomedical applications, mostly because of their advantages. Cast magnesium alloys with gadolinium and additional rare earth elements have lately been studied [12], [13]. Due to its high solubility at eutectic temperatures (23.49 wt%) and the development of intermetallic phases like Mg5Gd, these studies have shown that Gd can be employed to modify mechanical properties in a wide variety of alloy compositions and heat treatments. Gd is a single alloying element present in the solid solution and can contribute to precipitation strengthening in a concentration-dependent manner. Despite the fact that many publications claim gadolinium is extremely hazardous, the acute toxicity is merely modest. Acute toxicity from intraperitoneal $GdCl_3$ was 550 mg kg1 in mice, while acute toxicity from intraperitoneal $GdNO_3$ was 300 mg kg1 in mice and 230 mg kg1 in rats, respectively [14].

Magnesium alloys containing neodymium and gadolinium are particularly fascinating since they are light alloys with excellent mechanical characteristics even at elevated temperatures in the laboratory. Magnesium alloys containing Mg-Nd-Gd-Zr have high strength and good creep resistance, making them suitable for a wide range of applications, including automotive and aerospace applications. The rare earth elements have favourable effects on the mechanical properties of magnesium alloys, as well as on a variety of other qualities.

The second main task of the research is to design and optimise the microstructures of Gd-containing Mg alloys, studying the effect of different alloying elements on the resulting microstructures and their corrosion behaviour.

1.2 The structure of the thesis

The thesis consists of six chapters as described below,

Chapter 1 is the introduction of the research and describes the structure of the thesis.

Chapter 2 is the literature review, evaluating and critically reviewing the relevant literatures for this research.

Chapter 3 describes the experiment and analyses of the Al-20%Si alloy.

Chapter 4 describe the experiment and analyses of the Mg based alloys.

Chapter 5 is the discussion for the results described in Chapter 3.

Chapter 6 is the discussion for the results described in Chapter 4.

Chapter 7 is conclusion and comments on future work.

Chapter 2 Literature Review

In this chapter, the relevant literature and scientific papers published in the field of biocompatible and biodegradable materials are critically reviewed and analysed. In addition, the techniques that are used to melt and cast magnesium Mg based alloys, and the microstructure characterisation techniques, for example X-ray diffraction, X-ray imaging, and tomography as well as electron microscopy, are examined and discussed in this study.

2.1 A brief description of the pulse magnetic field solidification device

Among various techniques available for the environment friendly grain refinement, pulsed magneto oscillation method is efficient in terms of energy consumption and achieving the desired mechanical properties by refining the grain size of alloys [7]. In this work, a pulse electromagnetic device available in Prof Mi's group was used in solidification experiment of an Al-20% Si alloy. Figure 2. 1 shows a 3D of the conceptual design of the electromagnetic pulse device.

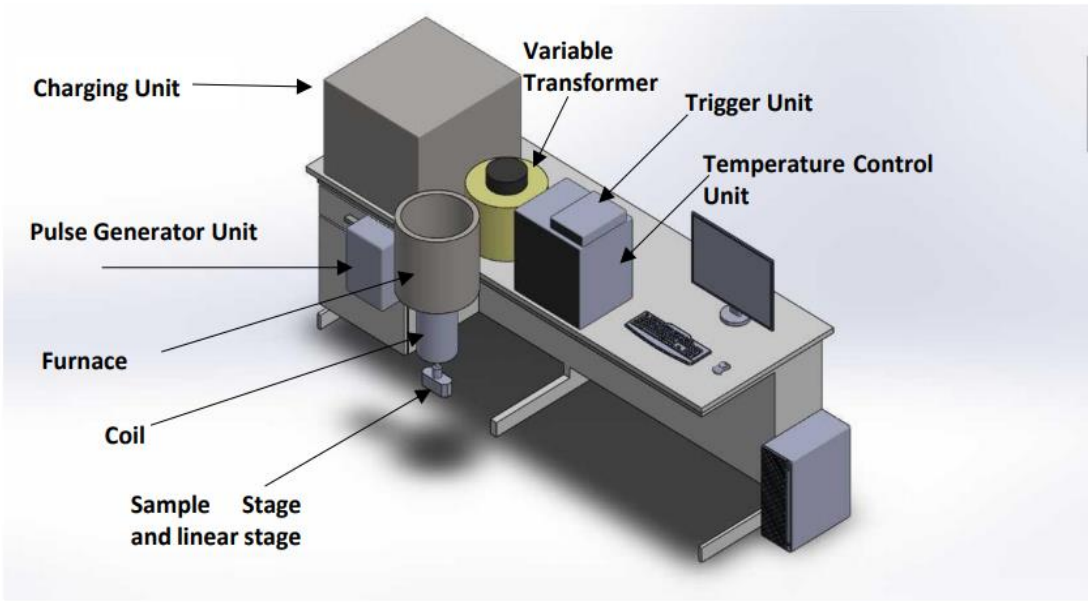

Figure 2. 1: Novel design of the electromagnetic pulse device consisting electromagnetic energy charging unit and pulse generating unit based on developed concept.

The energy charging unit consists of a variable transformer (Carroll & Meynell, 6.72 kVA Variac, 240 V AC, 28 A) performing the following functions; firstly it transforms the standard 240 V AC current obtained from the electrical source point into currents of variable voltages ranging from 10 to 270 V. Secondly, it charges the capacitor bank (2050 µF, 800 V). This is executed by connecting two series capacitor banks in parallel mode. Each series capacitor bank consists of five capacitors and each of them characterized by 820 µF and 400V. From the following expression the potential difference generated into the capacitor as well as the energy stored in terms capacitance and voltage can be obtained [15], [16].

$$V_C = V\left[1 - e^{\left(\frac{-t}{R_1 C}\right)}\right] \qquad \text{Equation 2. 1}$$

Where $t = R_1 \mathrm{C} \ln\left(1 - \frac{V_C}{V}\right)$

And $E = 0.5\mathrm{C}\mathrm{V}_C^2$

where V is the charging voltage received from the transformer, V_C is the voltage charged (potential difference generated) into the capacitor bank, t is the charging time, R_1 is the resistor that was utilized in the charging unit to regulate the current through the charging circuit in order to control the charging time, and C is a capacitance of capacitor bank. E is the energy stored inside the capacitor bank. The profile of the voltage charged into the capacitor bank using a 120 V current from the transformer with respect to time is shown in Figure 2. 1. It was observed that the capacitor bank was fully charged in a time period nearly equivalent to 226ms.

The second unit of the experimental set up is concerned to the electromagnetic pulse generation where the energy stored in the capacitor bank is discharged into the working unit. The helix metallic coil in this set up generates the short magnetic flux pulse with high peak current [17]. The following expressions can be utilized to calculate the voltage discharged and the time needed to fully discharge the energy.

$$V_d = V_c \left[e^{\left(\frac{-t}{zC}\right)} \right] \qquad \text{Equation 2. 2}$$

$$t = -z\,\mathrm{C} \ln\left(\frac{V_d}{V_c}\right) \qquad \text{Equation 2. 3}$$

Where V_d is the voltage discharged from the capacitor bank, and Z = 0.049, and Ω is the total impedance of the LC circuit.

The unique feature of the device is that a thyristor trigger switch is designed and associated with the discharging circuit to control and optimise the release of the energy stored inside the capacitor bank in terms of time, duration, and repetition. This procedure is followed in the experimental setup to generate programmable high magnetic flux pulses with tuneable amplitudes, frequencies, and duration to be applicable to different alloys systems in the process of solidification treatments.

2.2 Solidification structures of Al-Si alloy

The phase diagram shown in Figure 2. 2 furnishes the existence of various phases like α -Al, Liquid + α, Liquid + Si, and eutectic Al + Si with respect to variation in Silicon (Si) percentage and temperature. The eutectic transformation of the liquid transforming into solid Al and solid Si during the solidification happens to be at 557 ^{0}C for Si concentration of 12.6 weight percentage [18]. In cast alloys of Al, Si is important alloying elements since it does enhance the castability of the alloy to a greater extent. In addition, it gives the advantages like smooth filling of the die and not promoting hot cracking during casting processes. Being the hard phase Silicon happens to increase the strength of the alloy to a greater extent upon alloying with Al [18]–[20]. Further, the solidification path of the Al-Si alloy is influential in deciding the mechanical properties of cast products.

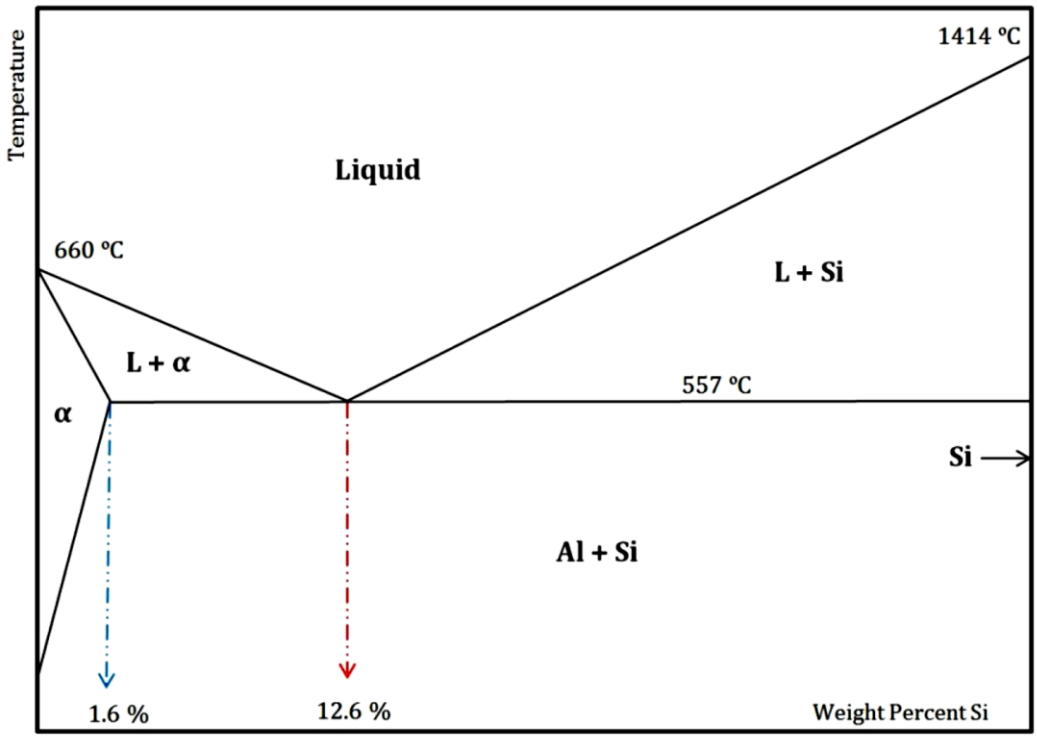

Figure 2. 2: Al-Si Binary Phase Diagram [18].

The majority of aluminium casting alloys contain Si as a key alloying element. Si is used as a major alloying element in aluminium casting alloys. Si is used as a eutectic former to regulate the shrinkage that happens during the casting process. Silicon is an excellent alloying element in metallic alloys. This is due to the fact that it increases the fluidity of the melt, lowers the melting temperature, reduces shrinkage during solidification, and is a relatively inexpensive raw material to begin with. A further advantage of silicon is that it has a low density, which may be beneficial in lowering overall weight of the cast component. Silicon has a very low solubility in aluminium; as a result, it precipitates as virtually pure silicon, which is hard and improves abrasion resistance [1–7]. Silicon has a very low solubility in aluminium; as a result, it precipitates as virtually pure silicon, which is hard and improves abrasion resistance. During the initial stage of solidification formation, primary precipitation of dendrites takes place. The following microstructure (Figure 2. 3) shows the presence of primary aluminium dendrite (α-Al) structure along with the Al- Si eutectic phase in (Al-11.6 wt% Si) alloys [21].

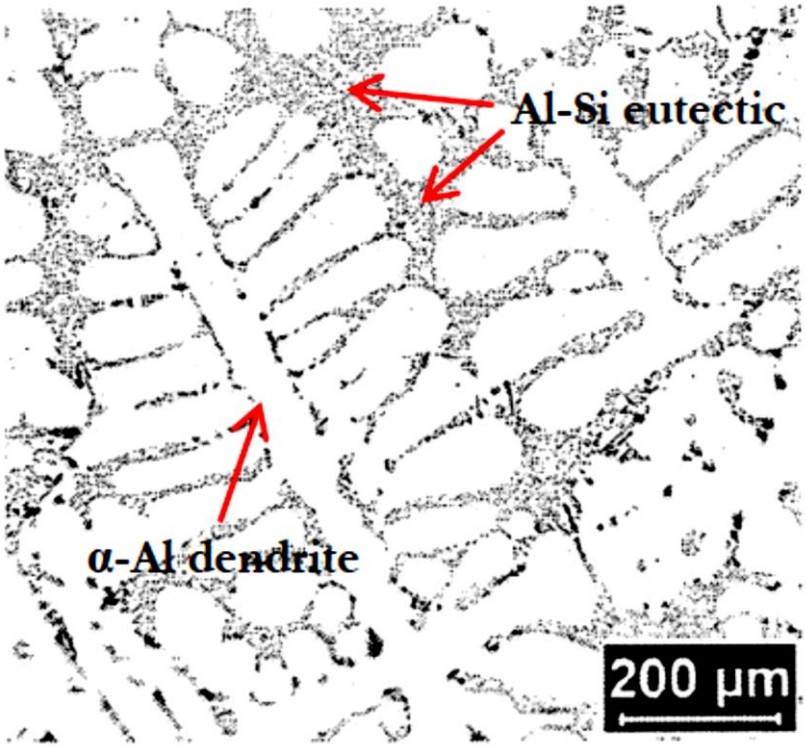

Figure 2. 3**:** Microstructure of an Al-Si alloy [21].

In general, the hypoeutectic alloy contains Silicon up to 12.6 %. If the Silicon percentage happens to be more than 12 then the Al- Si alloy is known as *hyper eutectic alloy*. Precipitation of Silicon phase as well as the Aluminium phase occurs simultaneously during solidification. In hypoeutectic alloys the primary dendrites of Aluminium and eutectic Al -Si phases can be identified clearly. The hypereutectic alloy solidification give rise to complex microstructural features with higher percentage of eutectic Al - Si phase and coarser silicon particles [18]–[20], [22]. Careful observation of the microstructures of the solidified eutectic or near eutectic Al – Si alloy reveals the presence of acicular or lamellar eutectic silicon dispersed in the Aluminium matrix. When additional alloying elements other than Si, are added to Al, the silicon precipitates into fibrous shape in matrix of Aluminium [23]. Most of the alloying elements added to Aluminium are less soluble in solid phase when compared to that of liquid phase. Due to this reason, during

the solidification the solute dendrite formation is inevitable. This is also known as “micro segregation” in Al-Si alloy. Actually, the size and distribution of solute phase depends on solute concentration, the arm spacing of dendritic structure and the grain size. This in turn influences the mechanical properties of the alloy.

One of the major issues with the cast Al-Si alloy products is the defect formations during casting. There are two different types of defects; Firstly, the macro porosity occurs when the evolving gas is entrapped inside the cast structure during solidification. Secondly, micro shrinkage occurs when the molten liquid could not reach the inter dendritic regions during solidification [23]. The present study involves the application of pulse magnetic field to the molten alloy during solidifications and the precipitating particle of the liquid experience vibrations during solidification due to the traversing pulsed magnetic field. This in turn agitates the solidifying liquid and increases the possibility of minimising the defect formations in the cast structure. This is one of the intriguing facts of the present domain of research carried out.

2.3 Properties of Aluminium Silicon Alloys

The processes that happened all across the manufacturing process have an impact on the mechanical characteristics of metal products. Metal may be affected by defects created during each stage of manufacturing, and these defects could remain or change the behaviour of the metal throughout later processing stages. It has thus always been an important goal in the study of metal manufacturing to ensure that an acceptable microstructure is generated at each step with the least amount of flaws possible. The final microstructure of aluminium alloy form castings is directly dependent on the microstructure of the as-cast aluminium alloy since the only post-casting processing that is typically performed is a heat treatment. Microporosity is a microstructural feature of aluminium alloy shape castings that can have an impact on the final properties of the castings. Microporosity is formed as a result of the combined effects of volumetric shrinkage during solidification and the precipitation of dissolved hydrogen during the casting process.

In order to aid casting designers in achieving the greatest mechanical qualities in the final product, it is necessary to develop a model that can predict the production of microporosity in solidifying metal castings. Porosity in castings is a defect that occurs as a consequence of the combination of many processes, including volumechange, nucleation and development of the solid phase, diffusion of dissolved components, and the interactions of interphase surfaces. Cast technology and heat treatment processing can be used to improve the mechanical properties of cast aluminium-silicon alloys by increasing the strength of the soft matrix, decreasing the brittle fracture risk in the polyphase regions, and increasing the degree of dispersion of the dendritic structure. The hardening of α-aluminium solid solution's soft matrix with point defects such as substituted atoms and vacancies, or the precipitation hardening of dispersion particles in the second phase, may both improve the strength of the solution's soft matrix.

2.3.1 Evaluation of mechanical properties and strength

Testing for both static (tensile, compression/shearing) and fatigue mechanical properties is required for the first validation of a cast aluminium casting process or as part of an auditing programme. Other testing procedures include corrosion testing, cryogenic, permanent growth dimensional testing, machined surface strain gauge testing and casting dimensional (layout) testing.

Before delving into mechanical testing techniques for aluminium castings, it is necessary to first understand the entire strategy to how mechanical testing is addressed and investigated. Wrought materials have a texture created by shaping or rolling. Recrystallization of wrought aluminium components owing to heat processing after rolling, or during the tensile test bar removed. The defined tensile test bar form implies that failure will occur in the decreased gauge portion, reflecting the material's inherent mechanical condition. This is not the case with many current cast aluminium components, and this issue will discuss some of the factors to consider when determining the desired mechanical qualities [1]. Mechanical strength is influenced by alloy chemistry, solidification rate, phase size, homogeneity, and heat treatment

protocol, these are basic metallurgical factors. Supplementary variables that impact mechanical strength make assessing the underlying metallurgy of an aluminium casting more challenging. Pores and oxide damage are two frequent additional concerns. Both variables have caused stress concentration. Porous and oxide type and amount might impact the amount of specimen necessary to achieve a competent metallurgical result. Statistical approaches may assist determine information composition. Porous and oxides are noninherent metallurgical variables. The fracture surface of a tensile test sample retrieved from a sand casting is depicted in Figure 2. 4a:

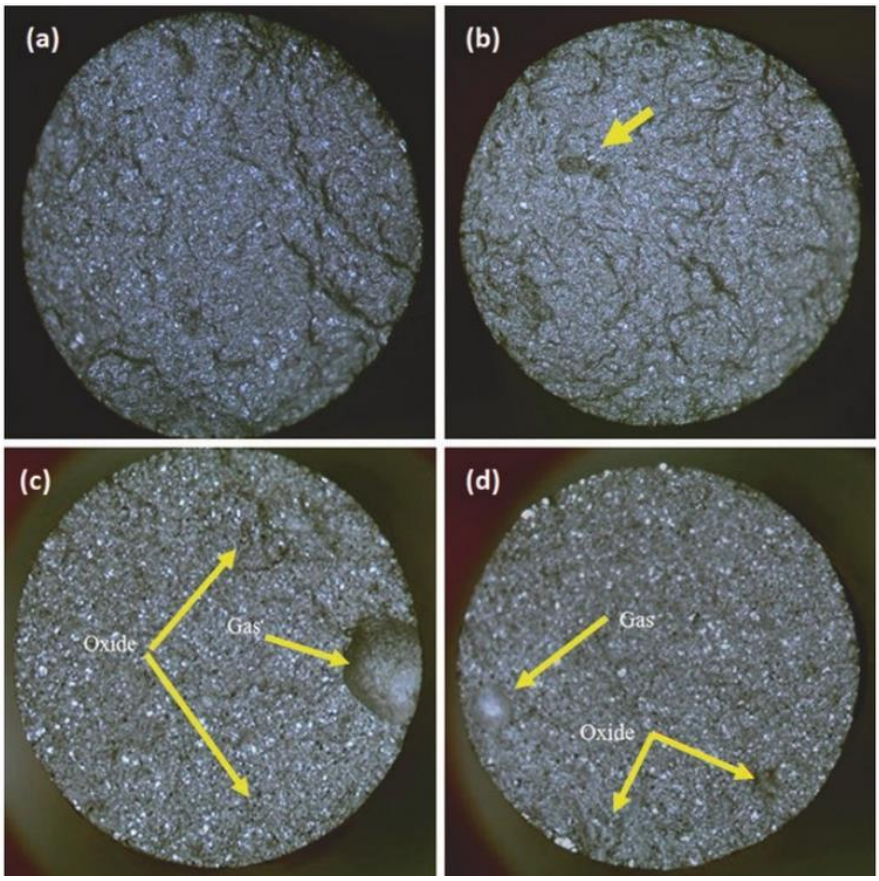

Figure 2. 4: a) casting in sand with no side effects. b) A sand-casting process that includes oxide effects. c) Gas gaps and oxides HPDC and d) Gas lower gaps and oxides HPDC [2].

There is an oxide present in this test sample, which is seen in Figure 2. 4b of the same cast sample. The oxide may have helped to reduce the final tensile stress and/or elongation. Images of fracture surfaces taken from High Pressure Die Casting (HPDC) tensile test bars reveal both gas gaps and oxides. The reduced elongation and final tensile stress were caused by both secondary artefacts. The crucial issue in this example is that if the dispersion of test results is considerable, the tensile fracture surfaces may need to be examined to establish an alloy composition and/or heat treatment programme. For unfavourable tensile test findings, the casting process (metal filling turbulence tendencies) or metal treatment methods may need to be investigated further.

2.3.2 Al-Si semi solid metal processing and heat treatment

Semi-solid metal (SSM) processing, which was developed more than 30 years ago at the Massachusetts Institute of Technology (MIT) (Spencer, 1971), is a metal casting process in which a mould is filled with partially solidified metal with globular structure, rather than liquid metal, to produce a finished product. Conventionally cast aluminium alloys are well understood in terms of heat treatment fundamentals; however, the differences in microstructure and solidification history of SSM components indicate that heat treatment conditions that have been optimised for normally cast materials are not pertinent to SSM modules [2,3] [3]. Precipitation hardening, annealing, and homogenization are the three most common heat treatment techniques used (T6 heat treatment). The T6 heat treatment consists of a solution heat treatment, soaking, and ageing, with the parameters typically used in industry being those proposed by the ASTM B917 and ASTM B91 standards: solution heat treatment at a temperature of 5401C, with residence times that may vary between 6 h and 12 h, and then artificial ageing at 1551C, with residence times that may vary between 3 h and 5 h, respectively. The casting industry often specifies that a cast component should be solution treated for 6 hat 5401C before being used in a final product. Several writers, on the other hand, contend that the recommended temperature cycles are far from ideal for components manufactured in the semisolid state [4]. In

order to get a solid solution that is almost uniform in composition, the solution treatment conditions are dependent on the casting procedure. Only a solution heat treatment of 50 minutes at 5401C was necessary to provide a homogenous distribution of silicon and magnesium in the -aluminium dendrites of A356 alloy, according to Sivakumar [5].

Employing A356 formed by low pressure die casting, Zhang [6] investigated the potential of using 30 minutes of solution treatment at 5401C with A356.The alloy in the SSM procedures stays at semi solid temperature for a much longer amount of time than in traditional casting techniques, and the cooling rate is quicker than in high pressure die casting (HPDC). This results in a more uniform structure for these components, as well as a reduced size for the inter-metallic compounds that are positioned next to the eutectic microconstituent and surrounding-phase globules. When applied to components made in a semisolid state, these conditions may drastically minimise the solution time for the T6 heat treatment. It should be observed that the overall time required for the T6 heat treatment cycle has a significant impact on the productivity and manufacturing cost of a cast component, and as a result, there is a great deal of interest in determining whether it is possible to reduce the time required for the solution heat treatment cycle.

2.4 Wear Characteristics of Aluminium Silicon Alloys

Over time, friction between moving parts causes wear on their surfaces [7]. Since the world's need for material and energy is steadily decreasing, research on wear is becoming more prevalent across the globe. Knowledge the mechanism of wear is expected to lead to a better understanding and specification of the chemistry and surface treatment of the materials. The following are the main principles for the various types of wear: Delamination and oxidation are the most common signs of mild wear. Strong: adhesive and diffusive. This method is both adherent and diffuse. Abrasive is the grade assigned. Pitting: Exhaustion and an outside threat. It is useful to distinguish between the following forms of wear, which are categorised according to the nature of movement, or the media involved in a contact between joining surfaces under an external stress. In Figure 2. 5, you can see the worn

surfaces that are created as a consequence of various forms of wear. Adhesive wear: When two smooth bodies move over one other, this kind of wear develops [24]. Unidirectional or reciprocating motion may be used to describe the relative movement. As a result, pieces of one surface are pulled off and cling to the other, and these pieces may subsequently come off the surface on which they were produced and be transferred back to the original surface, or they may become loose wear particles (Figure 2. 5a). Because of cyclic forces that operate on surfaces of interfacing objects, it has been reported that adhesives used in reciprocating sliding situations wear out faster than unidirectional ones. In addition, abrasive wear and high loads usually cause this kind of wear, that happens when hard or soft surfaces containing hard particles move on one other and plough a series of grooves (Figure 2. 5b).

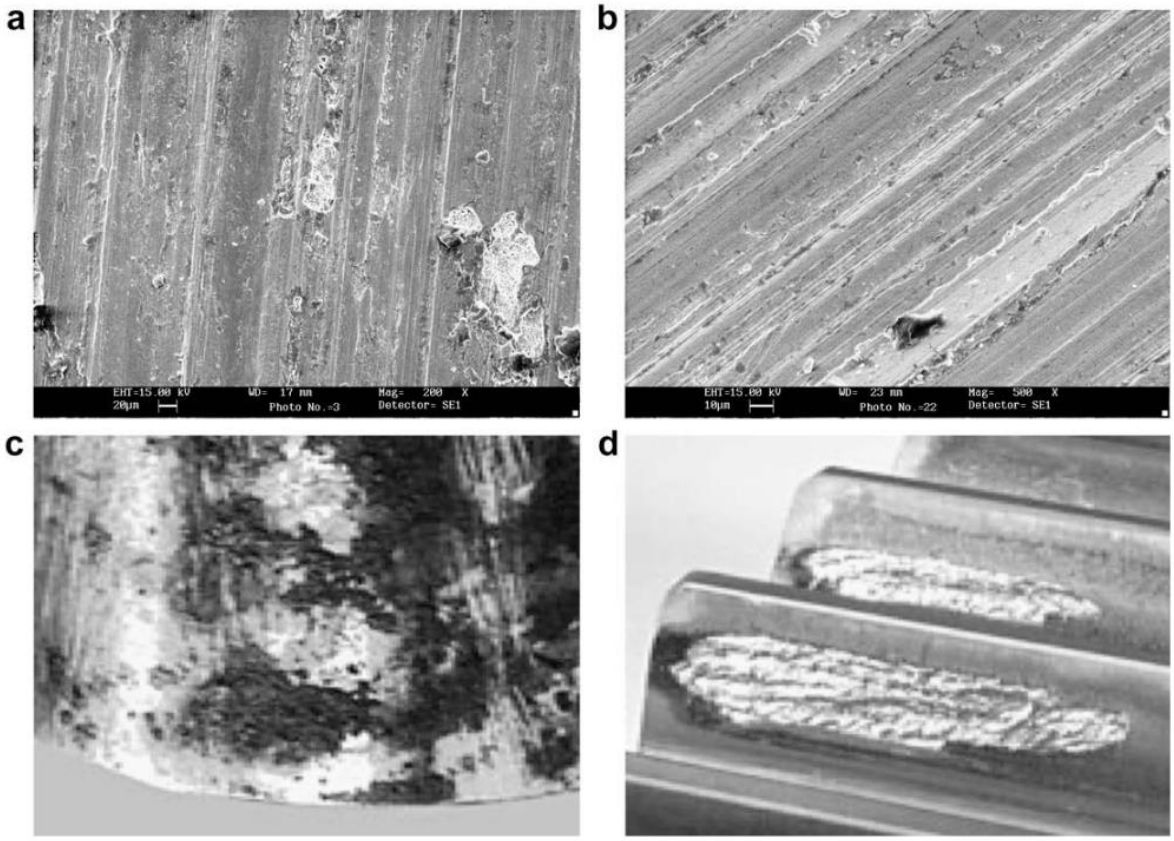

Figure 2. 5: Micrographs showing typical morphologies of different types of wear: (a) adhesive wear, (b) abrasive wear, (c) corrosive wear and (d) surface fatigue wear [24].

Wear due to corrosion ,corrosive environments cause this kind of wear, when sliding occurs. Corrosions by products create a layer on the surface in the absence of sliding, slowing or even stopping the corrosion (Figure 2. 5c). Surface oxides like alumina (Al2O3) and chromium oxide (Cr2O3), which are non-porous and adherent, may minimise corrosive wear on aluminium and stainless steel. Wear and tear on the surface, repeated sliding or rolling on a track causes surface fatigue. Surface or sub-surface fractures may emerge as a consequence of repeated loading and unloading cycles on the material, which may lead to its breakup and subsequent pitting of the surface (Figure 2. 5d).

2.4.1 Wear properties of cast Aluminium Silicon alloys

Some generally categorised processes such as moderate wear, severe wear, and seizure wear cause material loss from sliding surfaces when these alloys are moved dry (on the basis of wear rate) [9]. It has been possible to classify the forms of wear debris created during the sliding process for these alloys as either oxidative or metallic wear. It's unclear, though, just how the body's natural ageing process works. As a result of the sliding conditions (load, relative speed and the counter surface), the nature of the contact (pin on disc/ring/bush), the metallic properties of the sliding surfaces, oxidation and thermal softening behaviour of these alloys are generally held responsible for the wear of these alloys.

2.4.2 Effect of Silicon on the wear of Aluminium based alloys

When silicon is incorporated with aluminium, it increases the metal's resistance to wear. Adding silicon up to eutectic composition (12 percent silicon) boosts wear resistance up to a point, but beyond that, it degrades, according to several studies. However, there is no agreement on this point. The transition point (a combination of contact load and sliding speed) may be increased by as much as 20% when silicon content is increased. At low loads, it was found that the wear rate for hypoeutectic and hypereutectic alloys was same [8]. Alloy metallic characteristics are determined by their structure. As a result, silicon morphology has an effect on wear behaviour.

According to our previous findings, silicon crystal size, shape, and distribution in the alloy are more important to the mechanical characteristics of these alloys than their overall content. High ductility and reasonably high strength are achieved by using small, rounded particles of eutectic or primary silicon uniformly dispersed throughout the material. Due to differences in mechanical characteristics, fracture begins at silicon particles after the matrix has been distorted, resulting in reduced ductility, impact resistance, and fatigue resistance when using faceted, acicular silicon crystals [7], [10].

Mechanical characteristics, including as ductility, impact strength, and fatigue life, may be affected by changes in the morphology of eutectic silicon. It has previously been said that silicon's morphology may be altered either by the addition of a modifier such as sodium or antimony, or by increasing the cooling rate during solidification. The improvement in ductility and fracture toughness due to modification is significant, particularly at low solidification rates. The shape of eutectic silicon changes significantly from plate-like to practically spherical when alloys are heated. In addition to spheroidizing silicon particles, heat treatment promotes dispersion and refinement even more. Only at the grain boundaries can you find spheroidal silicon crystals. Increased tensile strength may result from this heat-treated eutectic silicon shape. Heat treatment of grain refined modified eutectic alloy seems to significantly improve mechanical characteristics by altering the structure of silicon crystals. Because to spheroidization, the likelihood of crack nucleation or fracture of a silicon particle at the silicon-aluminium matrix contact is reduced. Heat treatment has been shown to improve wear resistance [11], although the impact of change on wear behaviour is insignificant [12]. According to the author, primary silicon crystals in eutectic matrix improve thermal softening resistance and thus the transition point (load/speed) and results of the same are given in Figure 2. 6 [13].

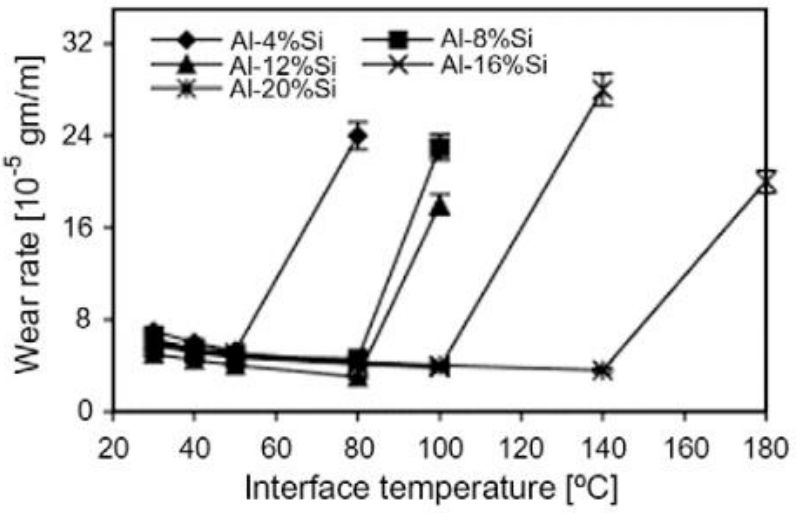

Figure 2. 6: Micrographs showing typical morphologies of different types of wear: (a) adhesive wear, (b) abrasive wear, (c) corrosive wear and (d) surface fatigue wear [25].

2.5 Relationship between hardness and mechanical properties of aluminium-silicon alloys

Various notable casting alloys are derived from the A1-Si eutectic. In situ composites are ductile and brittle, but their behaviour is complicated by the fact that the eutectic silicon morphology changes from rod-like angular silicon to flaky silicon to fibrous silicon and a complex regular morphology forms in areas with a high concentration of silicon, which is the case in this case.

The widespread use of Al-Si alloys may be due to their outstanding castability, fracture resistance, and superior technical characteristics that have been established [1–5]. We studied the mechanical characteristics of Al-Si alloys that were hypoeutectic, eutectic, and hypereutectic in composition and structure. The addition of Si has been shown to cause a considerable change in the tensile and hardness characteristics of materials [6–10]. Alloys with varied silicon eutectic phase morphologies exhibit distinct but distinct hardness-growth velocity and hardness-silicon interparticle

spacing correlations, as determined by hardness and tensile property tests performed on directionally solidified Al-Si eutectic alloys. Tensile property studies reveal that hardness and 0.2 percent proof stress are both governed by silicon interparticle spacing relationships of the same shape and form. It is proposed that hardness can only be utilised to evaluate proof stress when the eutectic structure exhibits a single silicon eutectic phase morphology in its eutectic phase morphology in its proof stress [12].

According to Figure 2. 7, the hardness values of the substrate and W-modified samples were compared to determine the hardness value.

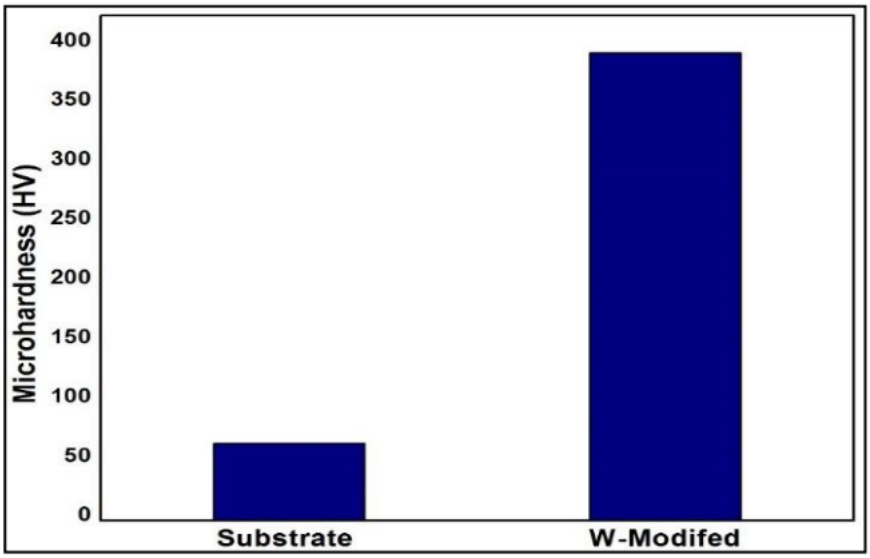

Figure 2. 7: Hardness chart for the substrate and W-modified samples [26].

It was discovered that the hardness of the Al-Si substrate rose from 65 HV to 394 HV for the W treated specimens, with the hardness of the W modified specimens being the highest. The creation of tiny granules on the top surface of the changed specimen is responsible for the increase in hardness observed. Along with grain refinement, which is found in changed specimens, the addition of tungsten to the surface of the modified area may be responsible for the significant increase in hardness (a rise of 606 percent with respect to the substrate) observed in modified specimens. As shown in Figure 2. 8, the surface hardness of the changed layer is higher initially and

then progressively declines along the depth direction, confirming the existence of a gradient in the pattern owing to the variation in cooling rate. The findings of prior investigations [13] have likewise verified this.

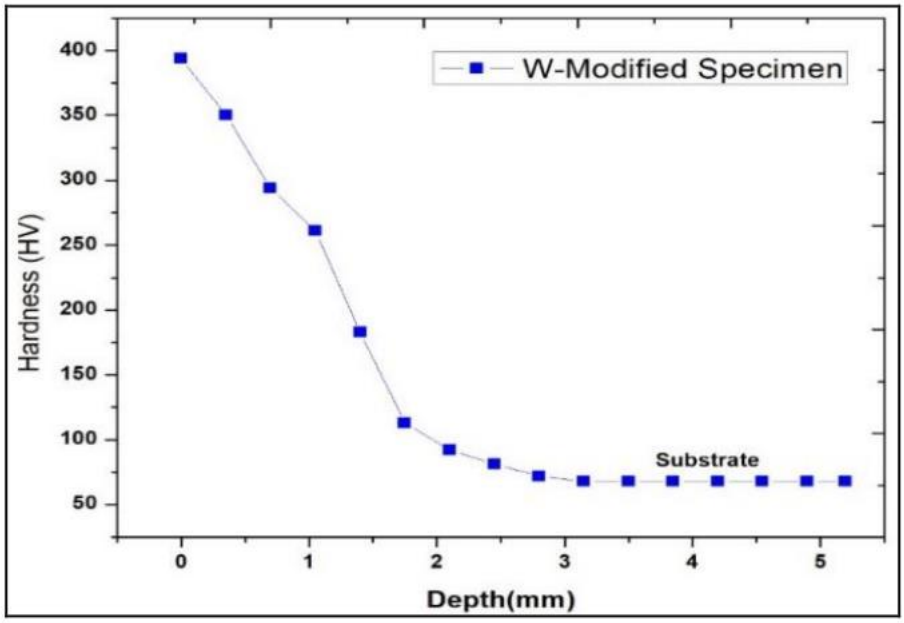

Figure 2. 8: Hardness profile along the depth direction [26].

As a consequence, the foregoing findings demonstrate that the Gas Tungsten Arc (GTA) might be regarded as a potential alternative heat source for the surface modification procedure (SMP).

2.6 Influence of Alloying elements on Al-based and Al-Si alloys

By employing a laser heat source to alloy Al-6.1Zn-2.9Mg-2.0Cu-0.15-Si alloy with Cr, Almeida et al. [1] examined the microstructure and corrosion behaviour of the alloy. They discovered that the corrosion resistance enhanced significantly after surface alloying with Cr. The results of another study conducted by Man et al. [2] on an aluminium alloy pasted with a layer of SiC and Si3N4 powders and also modified the surface using a laser as a heat source found that the formation of a metal matrix composite on the surface results in an improvement in the cavitation wear resistance for samples alloyed with Si3N4.

2.6.1 Addition of elements to Al-based alloys

Almeida et al. [3] and Garcia et al. [4] reported that the addition of alloying elements such as niobium, chromium, titanium, and silicon to aluminium alloys resulted in an improvement in the surface properties of the alloys. An experiment carried out by Liu et al. [5] and Mucklich et al. [6] on the surface of an aluminium alloy substrate after coating with Ni revealed the development of intermetallic compounds such as Al3Ni2, Al3Ni3, and AlNi on the surface of the aluminium alloy substrate. According to Gordani et al. [7], Razavi and Hasehmi [8], and Vaziri et al. [9], the development of intermetallic phases by Laser surface alloying has been observed. Senthil Selvan et al. [10] conducted TA research on the laser surface alloying of aluminium alloy with nickel and reported that the aluminium nickel intermetallic phase, precipitates are formed from the exothermic reaction between aluminium alloy and nickel inside the molten pool, and that the formation of intermetallic phase results in the improvement of hardness and wear resistance of the alloy. In their research on Al-11Si alloy, Biwas et al. [11] discovered that after surface altering with a laser, the wear resistance rose dramatically, and the microhardness increased from 55HV to 87HV. E-beams and lasers are two types of heat sources that are often employed for alloying elements. Using a laser as a heat source, the degree of crystallisation of the NiP coating on Al alloy, as well as the degree of dilution with the substrate, were used to determine the behaviour of NiP on Al alloy. Wong and Liang [12] and Watkins et al. [13] have shown that the interaction time of the laser beam with the specimen is a function of the laser travelling speed, and that both of these parameters are dictated by the laser interaction time with the specimen. Susnik et al. [14] investigated the wear behaviour of Al-Si alloys and discovered that the wear resistance was greatly increased when laser surface melting was performed. The results of a recent research done by Arul and Sellamuthu [15] on the GTA heat source reveal that the arc efficiency may be increased by up to 75 percent. Saravanan and Sellamuthu [16] investigated the viability of using GTA as a heat source for Surface Refining Process (SRP) coverage on Al-Si alloy in order to get more coverage.

2.6.2 Addition of elements to Al-Si alloys

The dendritic structure of the as-cast Al – Si alloy substrate is shown in Figure 1, demonstrating the elongated shape of the eutectic – Si, as previously described by Saravanan and Sellamuthu [16]. The microstructure of the Al – Si alloy treated with W by the surface modification technique is shown in Figure 2. 9.

When compared to the as-cast microstructure, the changed structure is substantially refined because tungsten particles are evenly distributed throughout the modified area as a consequence of rapid cooling and also owing to the dispersion strengthening process that occurs during solidification in the SMP.

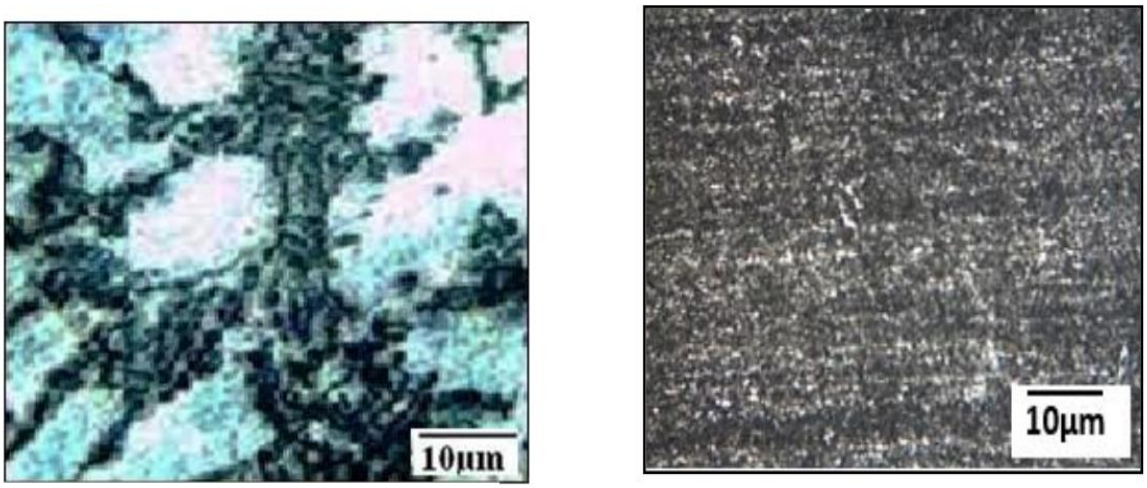

Figure 2. 9: a) Microstructure of as cast Al-Si Alloy. b) Microstructure of Al-Si Alloy modified with W [26].

Boyuk [17] used the directional solidification process to add 4.2 percent Ni to the Al -11Si alloy and discovered that the hardness of the base alloy rose from 82HV to 130HV for the Ni-added alloy, as well as an increase in tensile strength. Farkoosh et al. [18] evaluated the impact of 1% Ni addition on the surface of Al 7Si – 0.5Cu – 0.35Mg and discovered that an intermediate phase (Al5FeSi) formed during solidification. The scientists indicate, however, that the alloy's hardness will not drop in the 3000C temperature

range owing to the thermodynamic stability of the Al5FeSi phase. Venkateswara Rao [19] discovered that adding transition elements improves the mechanical characteristics of an Al - 5.6Zn - 2.5Mg - 1.5Cu alloy. Balasubramaniam et al. [20] studied the influence of 5% TiO2 particulates on the hardness of an Al - 4.15Zn - 2.12Mg alloy manufactured utilising liquid metallurgy and rheocasting processes and concluded that solid extrusions with TiO2 had a greater hardness than semi-solid and semi-liquid extrusions. Bharath et al. [21] investigated the effect of 12 percent Al203 addition on the hardness and wear rate of an Al - 0.43Si - 0.80Mg - 0.7Fe alloy using the stir casting technique and found that when reinforced with 12 percent Al2O3, the hardness increased from 95HV to 180HV and the wear rate decreased from 14.7x10-4 mm3/Nm to 11.4x10-4 mm3/Nm. Sajjadi et al. [22] reported that when Al metal matrix was cast utilising the compo-casting process, the hardness rose from 63BHN to 79BHN.

Gopalakrishnan and Murugan [23] evaluated the wear behaviour of an Al - 1.2 percent Mg - 0.8 percent Si - 0.7 percent Fe alloy reinforced with TiC particles using the stir casting process. They demonstrated that increasing the TiC percentage results in a reduction in the composite's wear rate. Himanshu Kala et al. [24] discovered that when the size of Al2O3 particles decreased, the hardness values rose. Additionally, they noticed that when the B4C level grew, the hardness values increased. Suresh and Moorthi [25] observed that when TiB2 was added to an Al-1.08Mg-0.63Si-0.52Mn alloy used to cast an Al metal matrix composite, the hardness rose from 65.53HV to 72.46HV. Additionally, they noticed that the inclusion of TiB2 particles enhanced the wear resistance. Huang et al. [26] investigated the effect of SiC reinforcement on the hardness of an Al-Si - 18Cu - Mg - Ni alloy used to fabricate pistons using the centrifugal casting technique. They found that the hardness increased from 73HRB at the piston skirt to 97HRB at the piston head and that the wear resistance was greatest at the piston head. Radhika et al. [27] reported that adding SiC and Al2O3 to an Al-7.5Si-0.6Mg-0.5Fe-0.1Cu alloy considerably enhanced the wear resistance and hardness. Additionally, it was discovered that just adding Al2O3 particles to the alloy increases the wear rate since it weakens the fracture toughness and destroys

the lubrication layer. Saravanan and Sellamuthu [28] investigated the hardness and wear rate of as-cast Al-Si alloys by varying the Si content from 4 to 16 wt. percent and using a Gas Tungsten Arc (GTA) as a heat source. They discovered that the hardness and wear resistance of the modified surface increase as the Si content increases.

2.7 Mechanical Testing of Magnesium Alloys Used in Implant Applications

The following mechanical properties of the magnesium-based alloys: strength, ductility, toughness, shear yield strength and damping ability are tested before the design process in finalising the parameters of the alloys in medical applications [27]. The capability of the material to resist the external load during the deformation process is known as strength. To determine the strength and other related mechanical properties, the material is subjected to incremental external loading and the strain in the material are observed. The registered data is utilized to plot a curve between stress and strain. This is also known as SS (Stress Strain) curve as shown in Figure 2. 10.

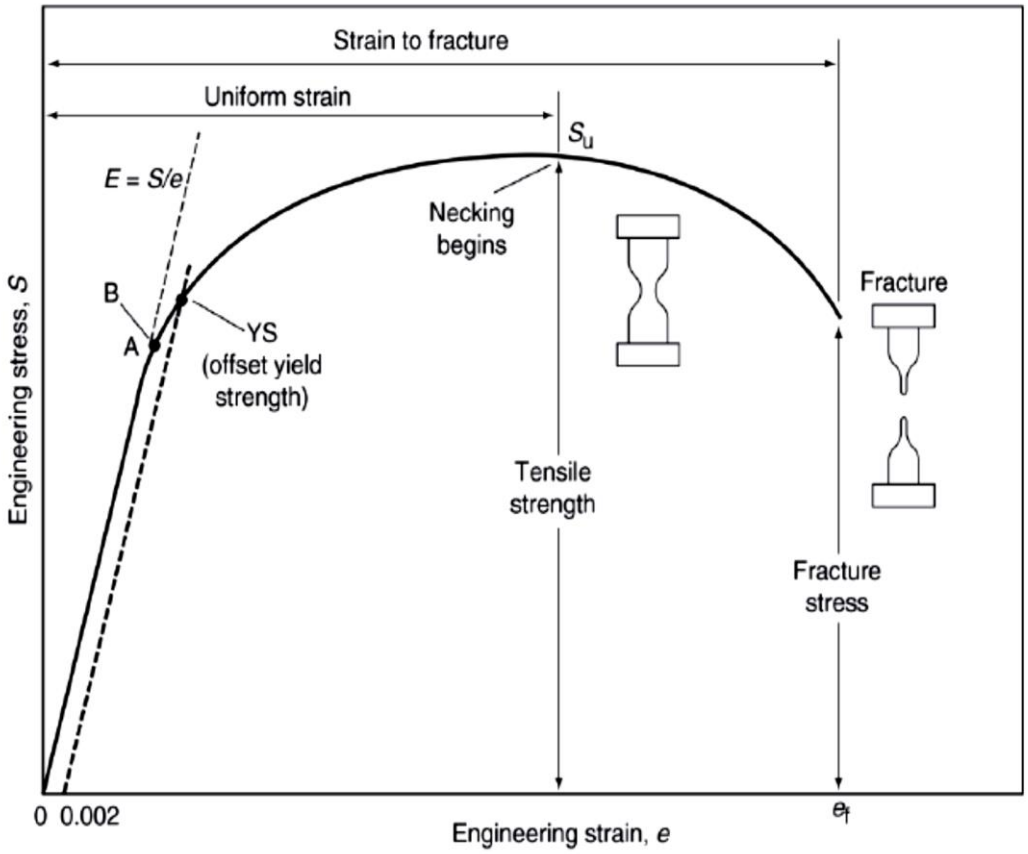

Figure 2. 10: Engineering stress-strain curve. Intersection of the dashed line with the curve determines the offset yield strength [28], [29].

The stress (S) of the material is obtained by the following expression: -

$$S = \frac{P}{A_0} \qquad \text{Equation 2. 4}$$

Where P represents load and A_0 represents the original area of cross section of the materials.

The strain (e) is given by the following expression,

$$e = \frac{\delta}{L_0} = \frac{\Delta L}{L_0} = \frac{L - L_0}{L_0} \qquad \text{Equation 2. 5}$$

Where δ and ∆L represent the elongation in gauge length, and the L represents the length of the specimen after the deformation due to specific load. L_0 represents the original length [28]. The nature of the drawn SS curve

depends on the following parameters of the tested material: composition of the alloy, heat treatment and conditioning, prior history of plastic deformation, the strain rate of the test, temperature at testing environment, and orientation of applied stress relative to the test specimens' structure, size and shape of the specimen utilized in the test. The SS curve can be successfully explored to calculate the mechanical properties of the test material such as resilience, elastic limit, ultimate tensile strength, yield strength, offset yield strength, toughness, and modulus of elasticity etc. [28], [30].

2.7.1 Mechanical properties of Mg alloys with various alloying

According to the medical point of view, the selection of appropriate alloying elements for Magnesium alloy design mainly focus on the biocompatible nature of the alloy with human tissues in real time applications. Metallurgy of alloy systems considers the improvement of mechanical properties by addition of alloying elements in minimum quantities without much affecting the corrosion behaviour of the alloy in bodily fluids. It is reported that the corrosion products can influence the healing process of human body after implant surgery [31]. Calcium is one of the prominent alloying elements for Magnesium based alloy system since it can promote bone healing in human body when released as corrosion debris [32], [33]. Another research reported that the excess calcium addition to Magnesium alloy results in deterioration of the mechanical properties and the prescribed maximum amount of Ca in Mg alloy is 1 % [34]. Strontium (Sr) is another promising candidate in biodegradable Magnesium alloys used in medical applications, to improve the growth of osteoblasts [35] and increase the mineral density of human body [36]. The improved mechanical properties of the Mg alloy with Sr is attributed to the formation of $Mg_{17}Sr_2$ precipitated along the grain boundaries (Figure 2. 11).

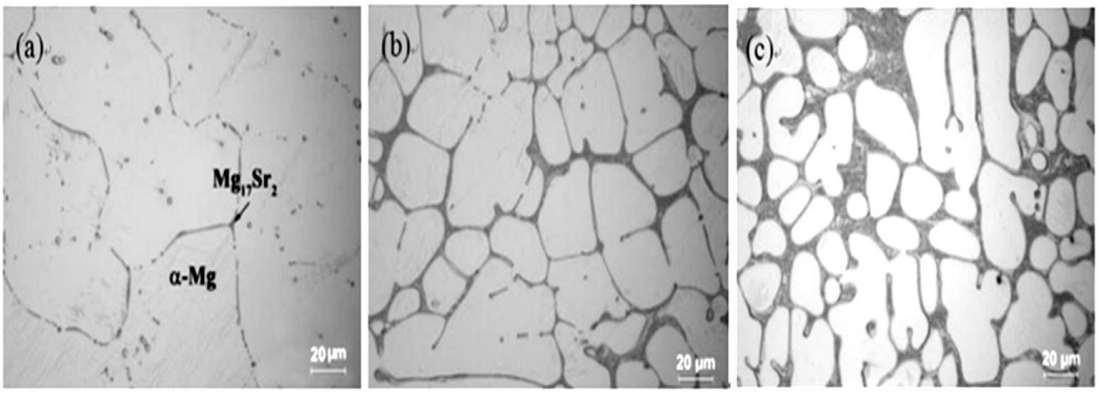

Figure 2. 11: Cross-sectional microstructures of as-cast samples; (a) Mg-0.5 Sr, (b) Mg-2.5 Sr (c) Sr and Mg-6 Sr [37].

Silicon (Si) is another alloying element, which can improve the mechanical properties of Mg alloy. A study registers that the addition of Si leads to formation of Mg_2Si as precipitates in the matrix, promoting the galvanic corrosion in bodily fluids acting as electrolyte. Aluminium is considered as one of the alloying elements options in Mg alloy systems used in medical application since it provides good corrosion resistance to the alloy when added and improves the mechanical properties to a desired level [38], [39]. Figure 2. 12 shows that the strength of Mg alloy improves as the percentile of Aluminium increases from 5 % to 7%.

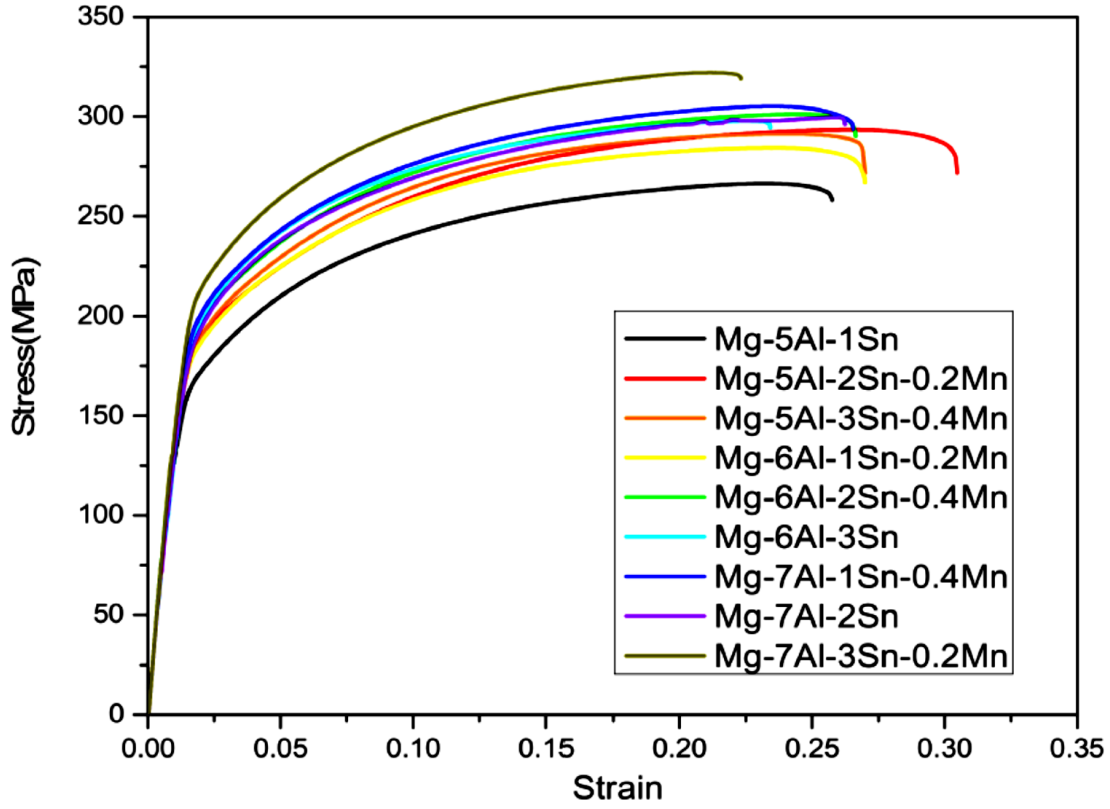

Figure 2. 12: The stress-strain curves of the extruded Mg-Al-Sn-Mn alloy [39].

Zinc improves the biocompatible nature of the Mg based alloy system with human tissue by being one of the trace elements of human body [40]. In addition, Zn improves the mechanical properties of the Mg alloy when added in specific amount, by promoting the solid solution and precipitation strengthening [41]. Therefore, I have concluded that zinc will be used as an alloying element in my experiments. I will not use aluminium although it was used by different researchers as well as, it can be melting in Advanced Materials Lab at the University of Hull, because of its drawbacks in the field of biomedical applications. A study describes that the presence of Aluminium in Human body as a strange or an alien element can affect the nerves system and may lead to a disease called Alzheimer when added excessively to the alloy system [42]. Rare earth elements can be added in a future study since some researchers have reported that the rare earth elements can effectively

improve the mechanical properties of the Mg based alloys when added in minimal quantities [43], [44].

2.7.2 Heat treatment effects on Mechanical properties of Mg Alloys

Several heat treatment techniques are followed in improving the mechanical properties of the Magnesium based alloys depending on the nature of the various Mg alloy systems. Some of the methods are solid solution treatment (T4), Aging treatment (T5) and the solution treatment combined with artificial aging (T6) [45].

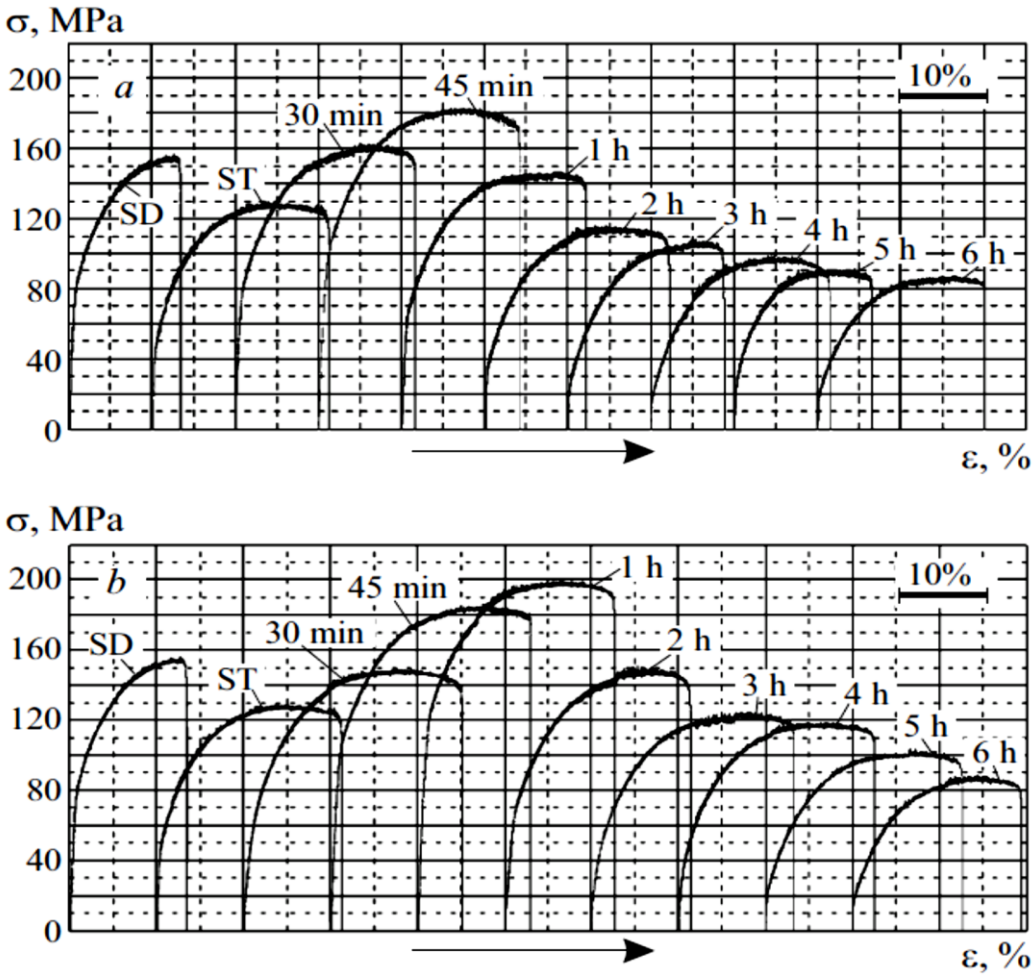

Figure 2. 13: Stress – strain curves for magnesium alloy AZ31 after aging at 180°C for different times (given at the curves): a) without preliminary deformation; b) before aging with 0.5% deformation; SD) state as delivered; ST) after solution treatment [46].

A study related to optimizing the mechanical properties of AZ31 magnesium alloy in terms of heat treatments, reveal that the optimum mechanical property is obtained when artificial aging carried out at 180 ˚C for 1 hour after solution treatment at 400 ˚C for three hours and water quenched. Moreover, this study employed the deformation of specimen before aging treatment [46]. Figure 2. 14 shows the stress versus strain curves of magnesium alloy specimens with and without deformation history. In both cases, the maximum strength is achieved after 45 minutes to 60 minutes of artificial aging treatment. The strength of the alloy depends on the size and shape of the precipitates formed during the aging treatment. Actually, the thermodynamics of aging treatment with respect to aging temperature and time decides the precipitates formation kinetics. Under aging and over aging are not resulting in improved mechanical properties since they cause non uniformity in distribution and coalescence of precipitates, respectively. The peak aging leads to improved mechanical properties by achieving the uniformity in precipitate distribution in matrix and desired shape and size, depending on the time and temperature of aging [47].

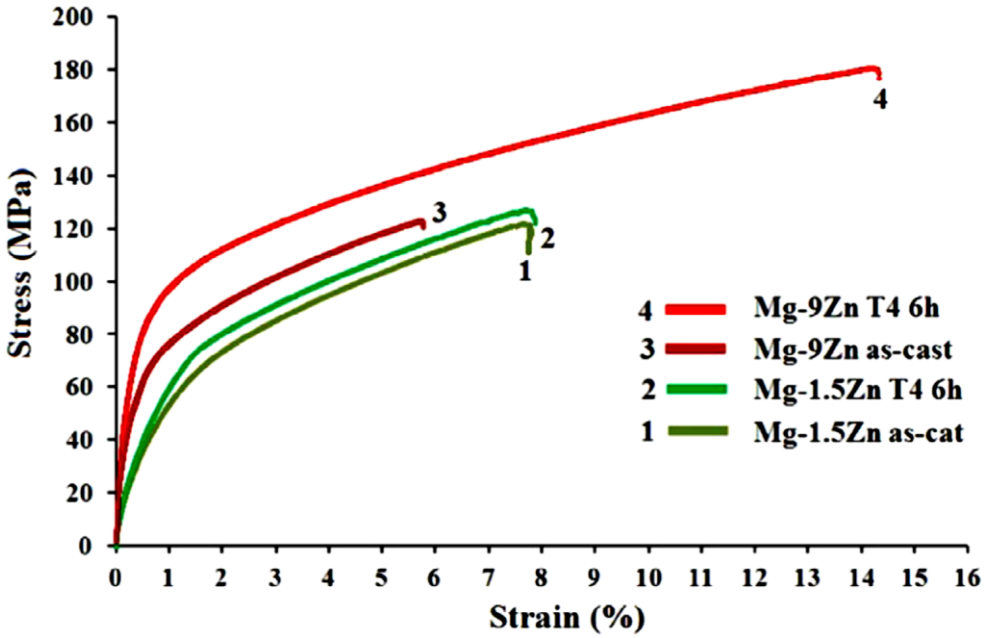

Figure 2. 14: Effect of 6 h of solid solution treatment on the yield and tensile strength of Mg-1.5Zn and Mg-9Zn alloys [48].

When Zi nc is added to Magnesium alloy system it improves the mechanical properties since it exhibits higher solubility in the alloy [49]. Higher solubility leads to possibility of significant addition of the alloying element in the system and hence the higher precipitation formability in quantitative nature. A research work concentrated on the aging studies of Magnesium – Zinc system, involving solid solution strengthening (T4 treatment) at 340 ˚C for 6 hours, observed that the strength and the elongation of the alloy are improving significantly. In addition, the study reported that the improvement in mechanical properties can be attributed to the presence of residual precipitates namely $Mg_{51}Zn_{20}$ and $Mg_{12}Zn_{13}$. Interestingly these two types of precipitates were identified to exist more along the grain boundary regions. Being higher energy regions, the grain boundary regions promotes hindering effects to the dislocation movements and hence the strength of the materials improves. The presence of aforementioned precipitates promotes the action of the grain boundaries in improving the strength by providing a synergic effect [48].

When rare earth elements are employed as alloying additions then the magnesium alloy is usually subjected to heat treatments at temperature range 500 - 530 ˚C to achieve over saturated solid solution. Further artificial aging is carried at temperature ranging from 150 ˚C to 250 ˚C resulting in much improved mechanical properties. A similar study reports that the Mg-Nd-Zn-Zr alloy after artificial aging at 200 ˚C for 10 hours of time period exhibits improved mechanical behaviour due to the observed precipitation strengthening effect [50]. In another study, solid solution strengthening as well as artificial aging of Mg-Y-Nd alloy was carried out and the mechanical testing registers a yield strength of 133 MPa, ultimate tensile strength of 235 MPa and increased elongation of 15.4 %. The significant increase in mechanical properties are attributed to the precipitation strengthening effect [51]. A group of researchers were interested in finding the effect of solution treatment combined with the equal channel angular press (ECAP) and low temperature rolling. In this study AZ 91 alloy was solution heat treated (SHT) at 430 ˚C for 20 hours and quenched in water. Further the alloy was subjected to ECAP for eight passes at 300 ˚C followed by low temperature rolling at

room temperature, 100 ˚C and 150 ˚C in hot rolling machine. The mechanical characteristics of the aforementioned alloy after the solution treatment, ECAP and hot rolling can be observed from Figure 2. 15. Figure 2. 15a shows the hardness value of the alloy specimen increases with low temperature rolling at room temperature. In addition, the same behaviour is observed with increase in rolling temperature [51].

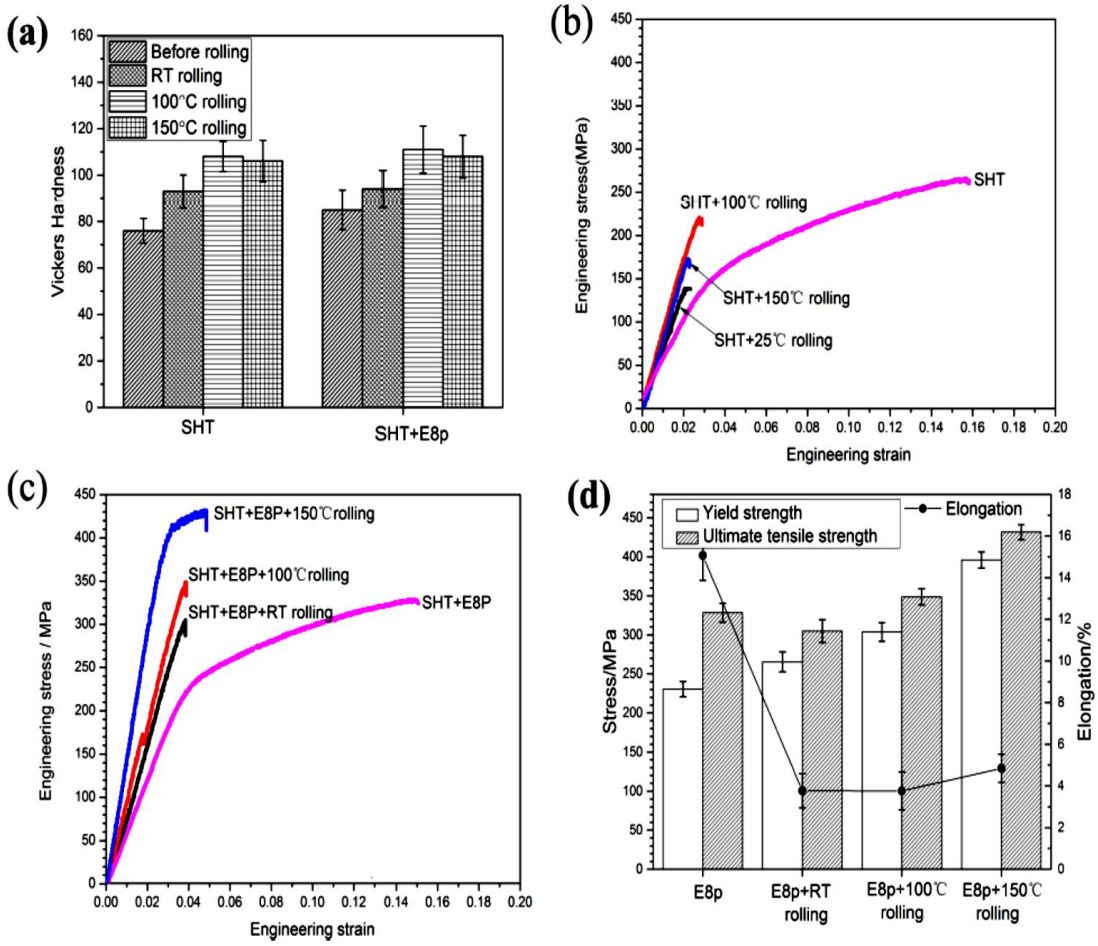

Figure 2. 15: (a) The hardness comparison of the AZ91 alloy at different processing state, and typical engineering stress-strain curves of AZ91 alloys processed by (b) solution heat treatment (SHT), SHT + rolling at different temperature; (c) SHT + ECAP 8p, SHT + ECAP 8p + rolling at different temperature; and (d) tensile properties comparison of samples in (c) [51].

Figure 2. 15b shows the increase in strength of the alloy as the rolling temperature increases, c and d, clearly reveal that the strength increases

significantly, when alloy is subjected to solution treatment, ECAP and low temperature rolling. The improved mechanical properties are attributed to precipitation strengthening after solution treatment, increased dislocation density and grain refinement after ECAP and low temperature rolling [51]. The literature of mechanical testing of magnesium-based alloys in medical applications clearly describes the necessity and types of mechanical characterisations to be carried out to test the implant materials in terms of various parameters and applications.

2.8 Biocompatible Alloying Elements

In biomedical applications, metal-based materials that are used as implants in the human body should be biocompatible, have high corrosion resistance or be inert, and have mechanical properties that are very similar to the body part that is being replaced. Biocompatible materials are defined as materials that collaborate with parts of the human body, or body tissues, and which totally or partially facilitate its function. As biocompatible materials have just been defined, another important term in the field of biocompatible materials needs to be explained, which is *incompatibility*. Incompatibility is defined as when the mechanical properties of a metal are not compatible with the mechanical properties of the human body member that it is going to replace.

Fe, Zn, and Mg are considered basic biodegradable materials for biomedical application. Fe was recorded as the first element that was used in the human body as bone replacement and then afterward in dental treatments [52]–[53]. Various biocompatible materials have been used over the last decade, but the most common applications are heart valve prostheses and artificial hip joints [54]. With regard to aluminium, Mg–Al alloys have to be avoided in the field of biomedical applications, except in the analyses and examination of refinement processing and surface modification technologies such as coatings [55]. Rare earth elements such as yttrium, lanthanum, cerium, and neodymium can improve the structure and properties of cast Mg alloys. A new study shows intermetallic C36 leaves type phase forms during solidification process when aluminium (Al) and calcium (Ca) added to magnesium. Armco iron (Fe > 99.8%) was implanted as a biodegradable material for the first time in the descending aorta of New Zealand white rabbits in 2001 [56]. The results from the implantation of the first Fe stent showed no significant evidence of either an inflammatory response or neointimal proliferation, and organ examination did not reveal any systemic toxicity. However, the slow degradation rate (0.16 mm year $^{-1}$) and the ferromagnetic nature of pure Fe led to problems when this material was used as an implantable device [5]. The addition of manganese (Mn) increased the degradation rate up to 0.44 mm year−1, but it still does not have wide

application. At present, Mg alloys have attracted great attention as biocompatible materials and as orthopaedic biodegradable implant materials due to their perfect biocompatibility and similar mechanical properties to natural bone [31]. One of the best alloying element compositions is Zn with Mg, as it has been concluded that amorphous Mg–Zn alloys have excellent strength, high corrosion resistance, a low hydrogen evolution rate, and good biocompatibility in animals [57]. As the advantages of magnesium based with aluminium outweigh other elements, I decide to use Mg alloys with Zn element in my study.

At the initial stages of utilisation of Magnesium based alloys in clinical field, some issues were raised regarding the nonuniform degradation of the secondary phases and primary α Magnesium phase in bodily fluids as electrolytic medium. Then the corrosion problem was minimised by proper design of Magnesium alloys with appropriate alloying elements such as Zn and Ca with desired quantitative measures [58] [59]. Some of the research works concentrated on the development of Magnesium alloys with elements either Zn or Ca, where as many works opted for the alloy design with inclusion of both elements along with others to develop a perfect combination to improve the alloys properties to expected level. One such work carried out by Xi et al. has proved that the Magnesium alloy with composition (Mg-2.0%Zn-0.5%Y-0.5%Nd) is user friendly in vascular stent applications. The aforementioned alloy is prepared by cyclic extrusion compression technique to achieve homogeneous nano-particle distribution with improved mechanical properties as well as degradation resistance [60]. Another study, came up with statements of supporting Magnesium Zinc alloy system, prepared by clean melting process and utilizing high purity elements, capable to be used as bio implant material with mechanical properties such as the tensile strength of 279.5 MPa and elongation achieved equivalent to 18.8%.Also the grain refinement of the alloy has led to the improved mechanical properties as mentioned [61]. As the search for new materials in implant applications continued, some research work concentrated on developing Magnesium alloys with Aluminium and Rare earth elements. It is reported that, Aluminium in human body causes disturbances to neurons,

Alzheimer's disease, [62] osteoblasts, [63] and hence the Aluminium added Magnesium alloys are inappropriate for the bio implant applications. Another report furnishes that the rare earth elements added to Magnesium alloys could cause hepatotoxicity in human body [64]. Yttrium ions (Y^{3+}) lead to the adverse effect in rat research showing DNA transcription [65] . Hence it is well-understood that the Magnesium alloys developed with additions of Aluminium induce harmful effects to the human body and are not suitable for the implant applications. This necessitates the find for appropriate Magnesium alloy to be used in implant applications with biodegradation in bodily fluid to an acceptable level. Song et al. [66] carried out a research to analyse the corrosion rates of Magnesium based alloys and reiterated that Magnesium alloy with Ca, Mn and Zn additions are suitable for the implant applications. In the similar domain of work, few research works stated that Mg-Ca [6] and Mg-Mn-Zn [67] alloys exhibit a degradation pattern in bodily fluids which are biocompatible according to medical standards.

2.8.1 Zn Alloys for Biomedical Applications

Zn is one of the most abundant nutritional elements in the human body, and it is one of the essential elements for metabolism. Zn metal and its alloys are considered to be promising candidates for biomedical applications, particularly in orthopaedic implants and some cardiovascular treatments, however, Zn has low strength and low plasticity, which results in disadvantages when using Zn or its alloys for biodegradable applications [68], [69]. Zn is also an important alloying element with a relatively high solubility in Mg. Zn contributes to the mechanical properties of the alloy. One of the most important research findings is that the improvement in mechanical performance of Mg–Zn alloys with Zn content up to 5% of weight is because of the fine grain size strengthening, the solid solution strengthening, and the second phase strengthening [70]. In one study, X-ray photon spectroscopy (XPS) illustrated that ion implantation formed a thin Zn layer in rich metallic state. A thin, Zn-rich surface layer exists in the metallic state, which may happen as a result of galvanic corrosion. Moreover, the

mechanical properties were not affected by the formation of Zn ion implantation [71].

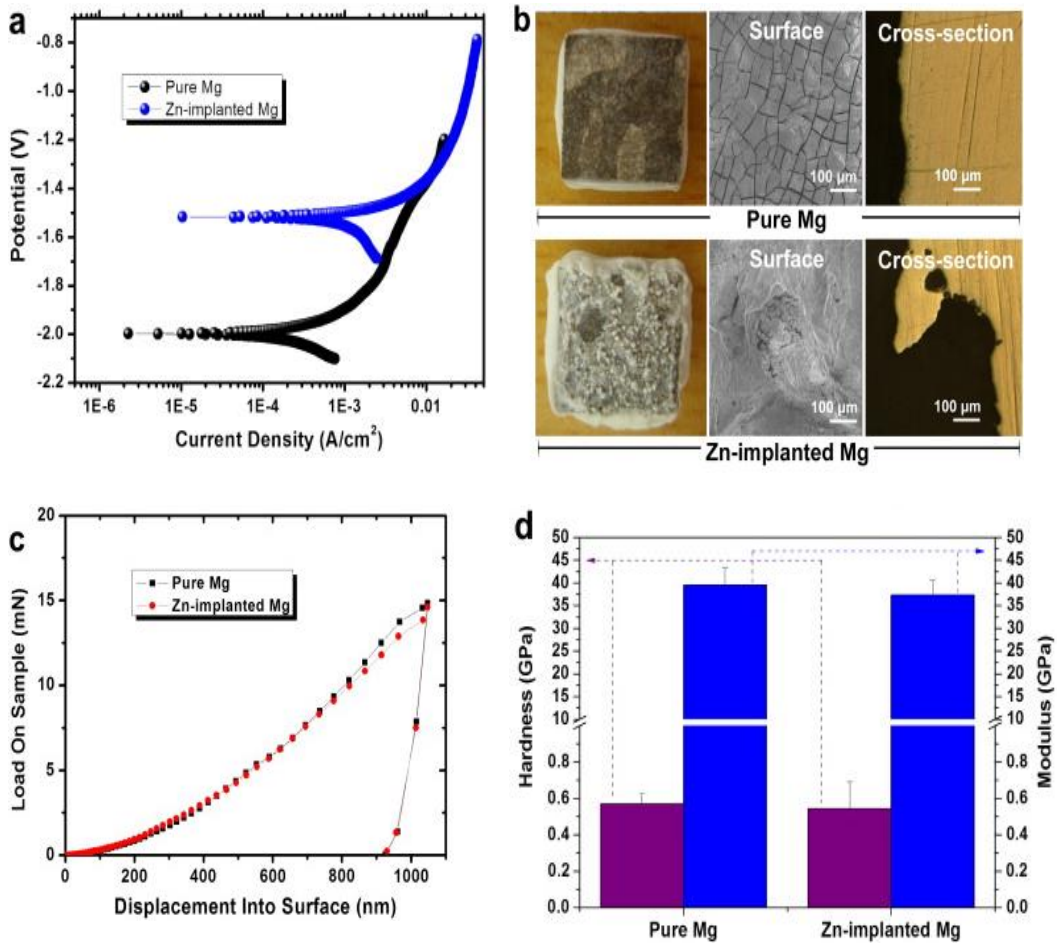

Figure 2. 16: (a) Polarisation curves of pure magnesium and Zn implanted magnesium in Simulated Body Fluid (SBF). (b) Surface and cross-section pictures of the samples after immersion in SBF for 18 h. (c) Load on sample as a function of displacement into surface for (Hardness measurements test). (d) Hardness and elastic modulus of pure magnesium and Zn implanted magnesium [71].

In terms of mechanical properties, Zn has insufficient strength, with a tensile strength of 20 MPa, 0.3% elongation, and low hardness with approximately 25 Hv, which constrains its use as a clinical biodegradable material [72]. With regards to degradation rate, the degradation rate of Zn-based alloys is about quarter lower than that of pure Mg when immersed in simulated body fluid (pH = 7.4), and its excellent biocompatibility could provide a new alternative for overcoming the challenges of Mg alloy systems [61].

2.8.2 Other Metals for Biomedical Applications

There are metal-based elements other than Mg and Zn that could be discussed in this chapter, although they will not be used in the experimental work of this thesis.

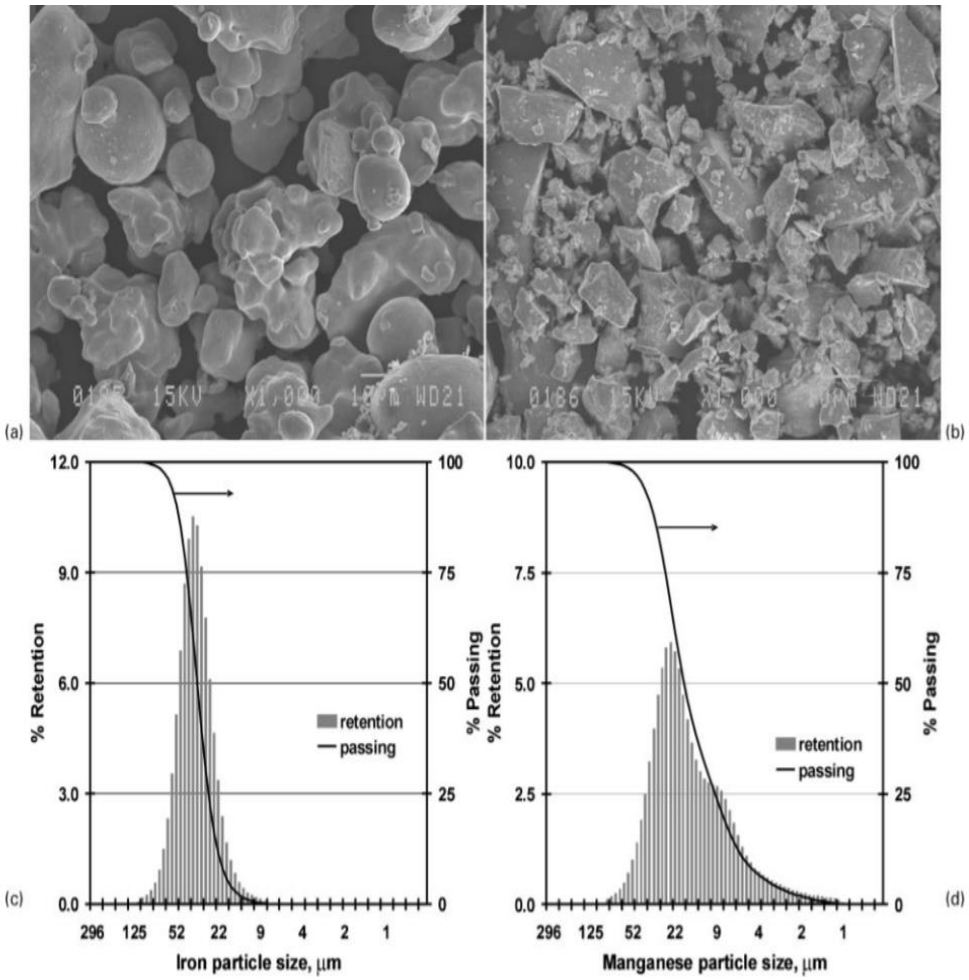

Figure 2. 17: Morphological particle analysis of powders as shown by SEM: (a) iron and (b) manganese; particle size distributions are also given for (c) iron and (d) manganese particles [73].

There are other materials that could be used for biocompatible application, such as titanium (Ti), stainless steel and/or Fe, zirconium (Zr), chromium (Cr), tungsten (W), and molybdenum (Mo) [74]. Fe-based alloys are the most popular in the field of biomaterials and are a preferable material for body parts that sustain a load, as they have high strength with a medium corrosion rate. Pure Fe exhibited a low corrosion rate when it was firstly implanted *in*

vivo, but after 35% manganese was added to Fe, the corrosion rate increased, (Figure 2. 17) [73], [75].

Therefore, low corrosion rates are considered to be one of the worst problems associated with pure Fe and Fe alloys as biocompatible and biodegradable materials. Ti and its alloys have been widely used as biocompatible and biodegradable materials in the field of biomaterials (Figure 2. 18) [76].

Figure 2. 18: Different biomaterials made from titanium and its alloys [76].

It has been concluded that Ti experiences a high corrosion rate, and it has been shown that Ti containing palladium (Pd) demonstrates a high corrosion resistance in the *in vitro* state. Moreover, Ti alloys, particularly α-phase, have excellent properties such as high strength, good resistance to corrosion, and low density, which make them promise biocompatible materials. I have not decided to make titanium alloys since the facilities in Advanced Materials Lab at the department cannot melt to high temperature like titanium melting point.

2.8.3 The Effect of Alloying Elements on Physical and Mechanical Properties

The basic design consideration of alloy systems to accommodate the tailormade properties of the metal by addition of appropriate alloying elements depends on critical change in corrosion properties of the metal when alloyed with other elements. By proper design of the alloy system, the metallurgical and mechanical engineers can ensure the oxidation and corrosion resistance of the metal is retained to a greater level with specific alloying elements selection. This concept is applicable to Magnesium based alloys also.

In general, there are three major categories of Magnesium based materials; First the pure Magnesium itself, secondly Magnesium alloyed with Aluminium (AZ91, AZ31 and AE21 GROUPS) and thirdly the Aluminium free alloys of Magnesium containing Calcium, Lithium, Manganese, Yttrium, Zinc, Zirconium etc,. As mentioned in earlier statement some of the alloying elements are added to improve mechanical properties by grain refinement, formation of intermetallic leading to improved strength, few of them are included to enhance the corrosion behaviour of the alloy as a whole and some are added to improve formability of the alloy and hence the manufacturing processes. Especially in implant applications, the alloying elements that are bio compatible with human tissues, preferred to make an alloy of improved and desired level of properties. Calcium, Manganese, Zinc and Rare earth elements are coming under this category.

A researcher stated that a small addition of Rare earth element along with Manganese and Zinc increases the corrosion resistance of Magnesium with tolerable biocompatibility [77]. In general, Manganese in minor quantity is added to many alloy systems to improve their corrosion resistance. When the Rare earth elements are added to magnesium alloy systems, the flow rate of the Mg_2^+ in corrosion reaction is decreased and hence the corrosion rate of the alloy tends to decrease [78]. Actually, the Rare earth elements are mostly inert in nature and do not contribute to the corrosion process. Another research revealed that the Rare earth elements associate with Calcium and

Phosphorous to form a complex oxide layer which tend to resist further corrosion during exposure to corroding atmosphere [31] , [77]. While selecting metals and their alloys in the field of biomedical applications, the following properties need to be accounted for such as: corrosion resistance, biocompatible properties, mechanical properties, and wear resistance. In some applications, thermal and electrical conductivity are also important. Chemical and physical properties of biocompatible materials should be examined at clinics and medical centres. Furthermore, the *in vivo* relationship with the host organs of the human body should be also analysed [80].

2.8.4 Magnesium (Mg) and Mg Alloys for Biomedical Applications

There are a lot of types of metallic elements that are widely available in engineering applications, but magnesium is considered one of the most complex elements in terms of mechanical, chemical and physical properties, as a result, the usage of magnesium has been limited [81][82]. Magnesium are much more suitable than other metals or even than polymers or ceramics in terms of biomaterials applications because of their mechanical properties are similar to mechanical properties of human body particularly to bone [83], [84]. Although some polymers such as polylactide acid polyglycolic acid have widely been used as biocompatible materials, but they are not suitable for load bearing applications, in addition, ceramics such as (hydroxyapatite) are also not preferable materials for load bearing applications. In contrast, the currently used metallic implant materials such as titanium, cobalt-chromium-based alloys and stainless steels, have higher modulus of elasticity than bone. Mg is a chemical element with atomic number 12. It is the ninth most abundant element in the earth and the eleventh most abundant element by mass in the human body. It is essential to approximately all cells and about 300 enzymes and magnesium is naturally occurring in bone tissues [85].

Mg is considered to be one of the lightest metallic elements, with a density of 1.738 g/cm^3, and an alloy density between 1.75 g/cm^3 and 1.85 g/cm^3 [86]. Mg and its alloys have been extensively explored as possible biodegradable

implant materials for orthopaedic application, such as fracture fixation. However, the rapid corrosion of Mg-based alloys in physiological conditions is a barrier to be overcome in therapeutic application. Mg metal and its alloys are promising biocompatible materials with appropriate biocompatible and mechanical properties that biodegrade inside a biological system [52]. Mg was first examined as a metal-based material for diverse orthopaedic application in 1900, yet the study did not completely succeed because Mg, at that time, had inadequate mechanical strength (pure Mg). In addition, there was insufficient production of hydrogen gas during the *in vivo* degradation process [87]. Mg alloys, especially those containing rare earth elements, seem to be suitable for use in biomedical applications, and for use as implant materials in bone surgery.

There are many factors that need to be considered when choosing Mg as a base alloying element for a biocompatible material, the most important factor is biocompatibility. Other factors are wear and corrosion resistance, which are needed in long-term implantation in the body, especially toxic metals ions such as Cr, Ni, and Co, which lead to reduced biocompatibility of the material. One of the best advantages of Mg metal as an implant material is its degradation under physiological conditions, which makes it unnecessary to do another operation to remove the implant after recovery, moreover, excess Mg might result from the corrosion process can be excreted via the urine [88]. Mg has a hexagonal structure with only two easily organised independent modes of deformation. Therefore, failure is more likely to occur before activation of other required deformation modes such as dislocation glide, twinning, or grain boundary sliding. One of the major characterizations of Mg alloys that makes it good promising material as an orthopaedic biodegradable implant is their perfect biocompatibility and good mechanical properties that are very close to those of natural bone, no other element has a closer properties to bone than magnesium [89]. One of the major disadvantages of magnesium is the low corrosion resistance it has [90], [91].

2.8.4.1 Magnesium Based Alloys for Implant Applications

In pure state, the Magnesium in elemental form is thermodynamically unstable due to its existence in meta stable state. When exposed to atmospheric conditions, Magnesium surface tend to oxidize to form thick greyish and amorphous Magnesium oxide layer. It is determined that the oxidation rate of the pure Magnesium in atmospheric condition happens to be nearly equal to 0.01 milli meter per year. Also the corrosion rate of the aforementioned element in salt water resembling the sea water is nearly 0.30 milli meter per year [92].

2.9 Microstructures of Mg-Gd Based Alloys

Figure 2. 19 is the binary equilibrium phase diagram of the Mg–Gd alloy.

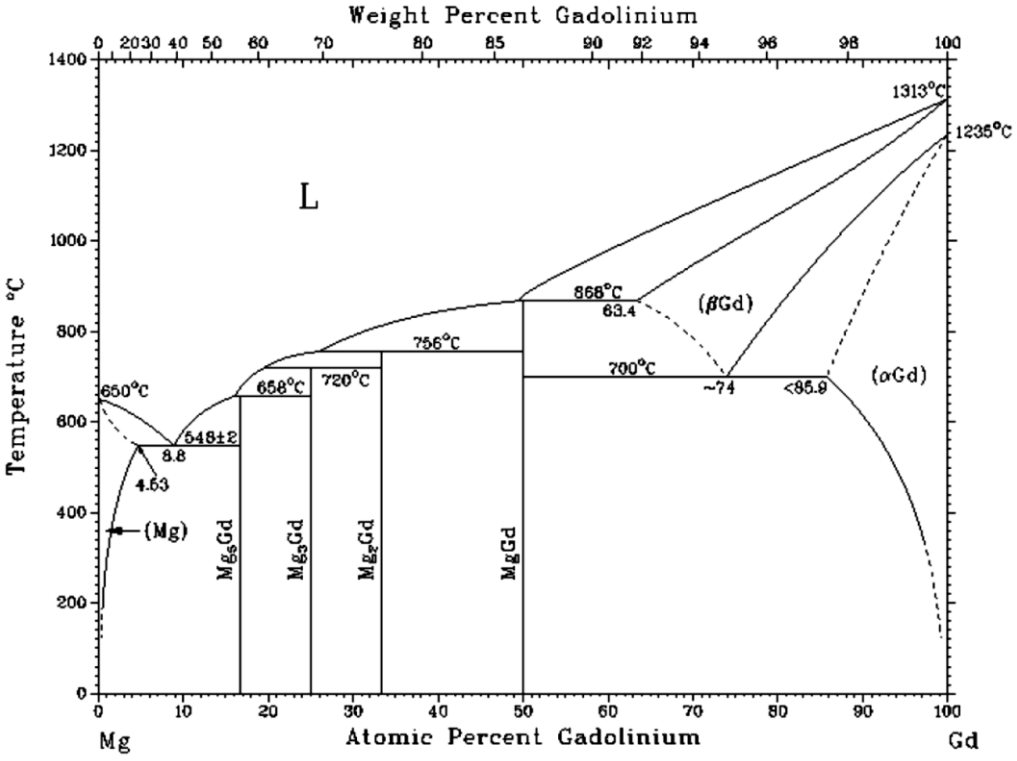

Figure 2. 19: Magnesium- Gadolinium phase diagram [93].

Intermetallic phases Mg_5Gd, Mg_3Gd, Mg_2Gd, MgGd, α-Gd, β-Gd and solid solution of Mg are present in the equilibrium state. Almost all the intermetallic phases between Mg and Gd are formed by peritectic reactions.

In addition, the eutectic equilibrium and the eutectoid equilibrium are associated with the allotropic transformations of Gd as described below:

$$\beta\text{-Gd} \longrightarrow \alpha\text{-Gd} + MgGd$$

The eutectic temperature of the Mg-Gd alloy is ~540 ^{0}C. The composition of the alloy at this temperature consists of 40%wt Gd. The maximum solid solubility of Gd in Mg is ~24% at eutectic temperature. According to the phase diagram, at room temperature, the Mg_5Gd intermetallic phase contain ~50%Gd [93].

2.9.1 Microstructures of Mg-Gd-Nd Alloy

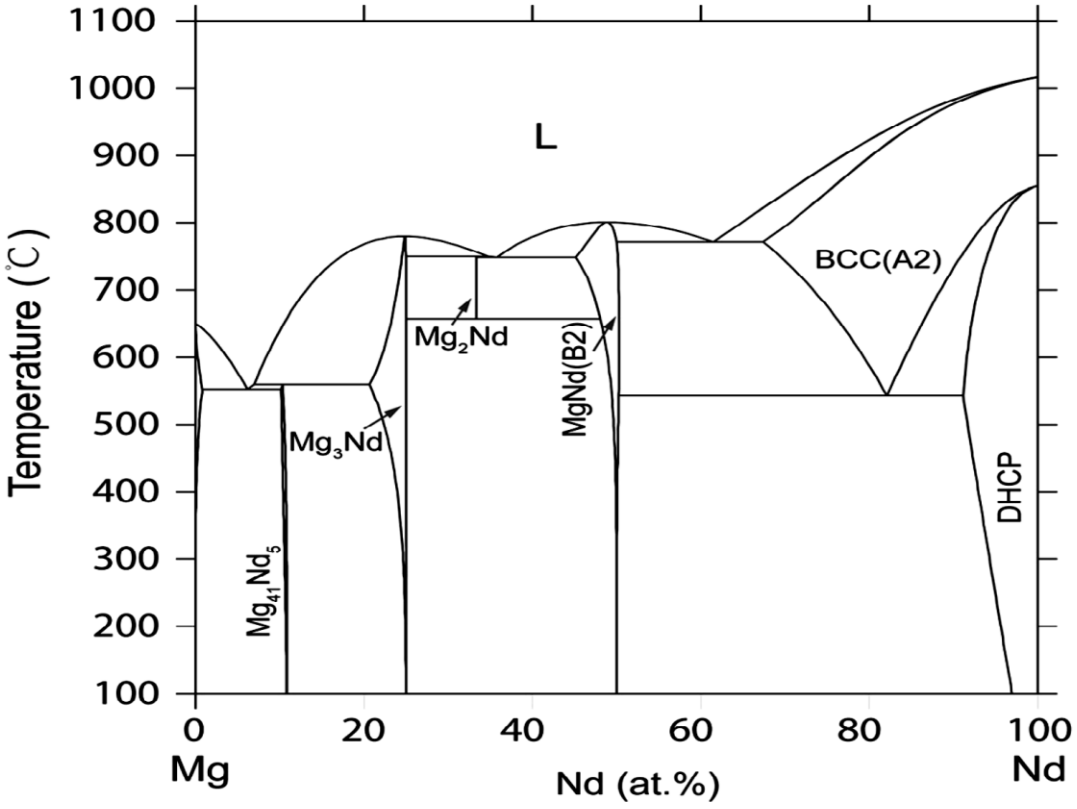

Figure 2. 20 Binary phase diagram of Magnesium- Neodymium system [94]

Figure 2. 20 shows the binary phase relationship between Magnesium and Neodymium. It exhibits the various phases of Mg-Nd system with parameters like temperature and Gd atomic percentage. It can be noticed that at lower

Gd percentage (Less than 20 atomic percentage) the predominant phase observed is $Mg_{41}Nd_5$. As the Gd percentage increases, the possibility of other intermetallic phase existence like Mg_3Nd, Mg_2Nd, MgNd are noticed [94]. Figure 2. 21 shows the Iso thermal section at 300 ^{0}C of Magnesium-Gadolinium- Neodymium system. It is reported that the formation of Mg_5Gd phase with ternary extension leads to an important solid solution phase. In the ternary system, the intermetallic phase $Mg_{41}Nd_5$ has a very narrow solid solubility value around 2.5 atomic percentage of Gd. But the Mg_5Gd intermetallic phase with ternary extension has higher solid solubility in the ternary system when compared to that of the former mentioned phase [95].

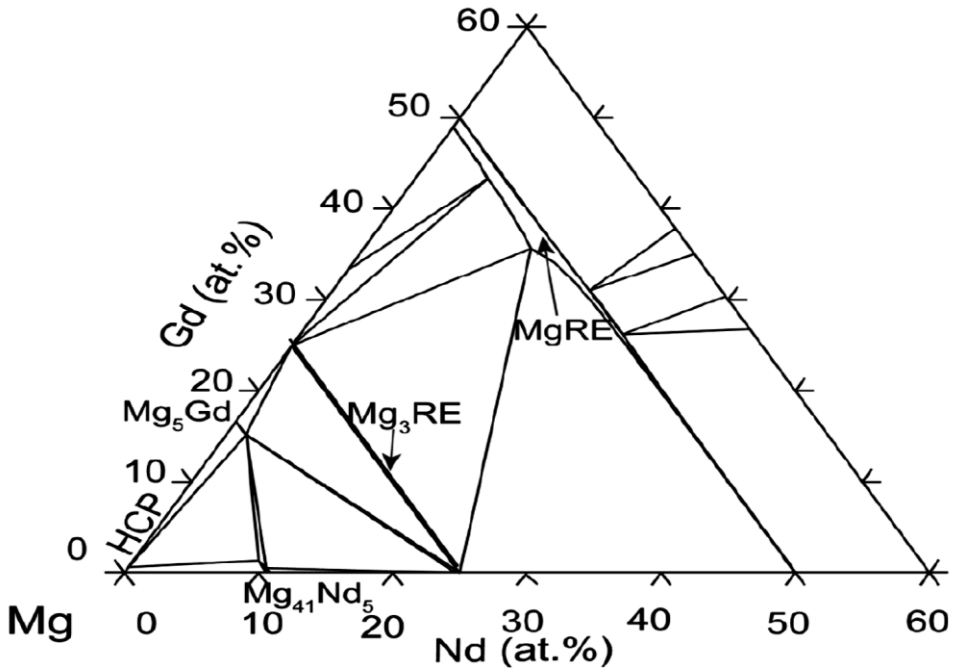

Figure 2. 21:Ternary phase diagram of Magnesium- Gadolinium- Neodymium system (Iso thermal section at 300^0 C) phase [95]

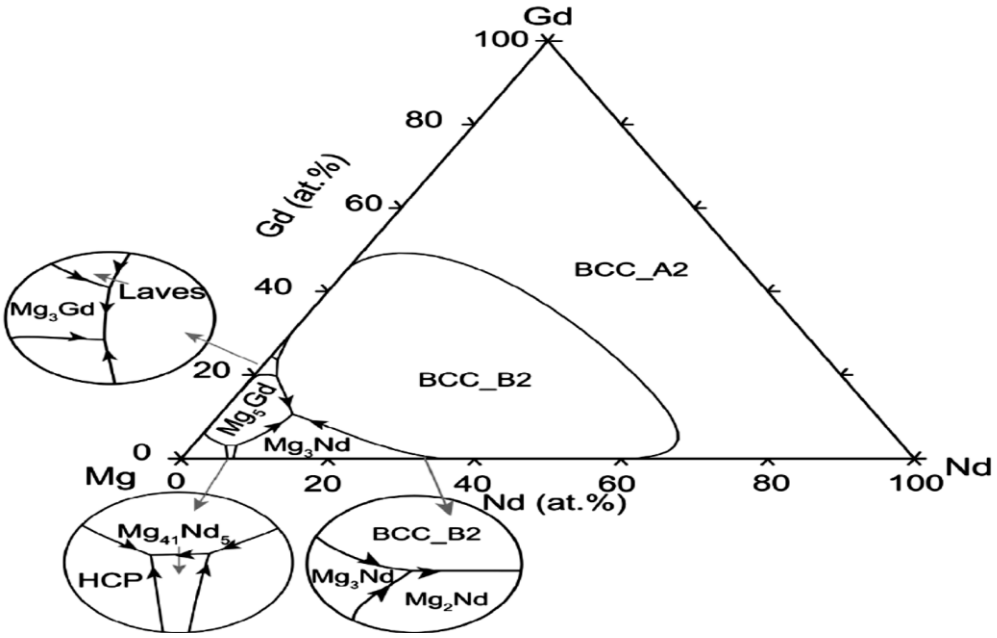

Figure 2. 22: Ternary phase diagram of Magnesium- Gadolinium- Neodymium system (Liquidus Projection) phase [95]

The liquidus projection of the Magnesium- Gadolinium- Neodymium system (Figure 2. 22) reveals that at lower percentages of Gd and Nd in the ternary system, the following phases are observable; primary Mg, Mg_5Gd, $Mg_{41}Nd_5$ and Mg_3Nd.

2.10 Corrosion Behaviour of Biomaterials

Wear that results from an oxidation process, or chemical substances from the surrounding atmosphere can occur in materials and alloys. The resultant wear can cause damage to the surface or to the structure of material; the ability to cope and withstand oxidation and chemical damage is called *corrosion resistance* [96], [97].

2.10.1 Biocompatibility of Magnesium alloys with human tissues

Magnesium is the first option category element among many in the material selection for the base element of biocompatible and bio degradable materials design, since:

a) it is one among the most abundantly available elements on earth crust as quantitative value nearly equal to1.3 Mt/km^3 [98].

b) interestingly it has a distinct advantage of having specific gravity value of 1.7 g/cm^3, which is nearly equivalent to that of human bone specific gravity namely 1.75 g/cm^3. The specific gravity value of Magnesium is approximately two third of the specific gravity of Aluminium and one third of specific gravity an alloy Ti6Al4V used in bio implantation applications.

c) it possesses a very important mechanical strength property as specific strength of numerical value nearly equivalent to 475 GPa.cm^3/g when the alloy is casted through fast solidification technique which is higher than that of Ti6Al4V by two-fold.

d) It has a low elastic modulus value equivalent to 45 GPa which is almost near value to that of human bone of elastic modulus 50 GPa. This elastic modulus value of Magnesium is only half of the value of modulus of Ti6Al4V alloy, compelling the research community to proceed with a material replacement in the form of Magnesium alloys in bio implant research recently, since the common problem identified with the developed bio implant materials arose due to the greater difference in elastic modulus between the material and the hosting human tissues registering stress shielding effects in human bodies implanted with bio implantation parts. Hence, pure Magnesium and Magnesium based alloys are about to replace the existing bio implantation materials in near future.

e) It is an element finding the importance in the formation of biological apatite's and it might become a major replacement for the bio implants used for bone replacement since the bone matrix requirements in implant research data automatically falls nearly to the properties of Magnesium [99].

In another bio implant research, It is revealed that the magnesium coated on Aluminium improves the attachment and spreading of human cells where the same is not observed when the tests are carried out with Aluminium only [100]. Very importantly, Magnesium does not lead to intoxication in human body when it is used as implants, because the human body accepts the

meagre amount of magnesium ions released into the human system over a prolonged time period since it is biocompatible with human body. Therefore, biodegradable Magnesium implants research is under way and will reveal very interesting out comes sooner or later [101]. Biocompatibility is one of the important factors among many in bio implant research and material design. The existing literature insists that the importance of carrying out the biocompatibility related research of Magnesium and Magnesium based alloys to the fullest potential in order to realize the applications of Magnesium and Magnesium based alloys in implant manufacturing industry in near future. It also opens another big investigation domain concerned to the corrosion behaviour of the Magnesium and Magnesium based alloys in biological and cytotoxicity environments. Some of the registered research information's about corrosion behaviour of the Magnesium and its alloys state that the metal or alloy containing Magnesium has a topographical transformation to magnesium hydroxide further changing to soluble Magnesium chloride upon exposure to aggressive chloride ion containing environments[101].

2.10.2 Corrosion Behaviour of Magnesium and other Alloys

Corrosion, another electrochemical process, can be controlled in a manner such that Mg based implants with controlled rates of biodegradation are feasible. Amorphous alloys have diverse beneficial properties, as they are likely stronger than crystalline alloys of similar chemical composition and can withstand higher deformation than crystalline alloys. Fe-based amorphous alloys have been extensively studied based on their low cost and likelihood of obtaining high corrosion resistance. Moreover, amorphous structures are free from many faults that affect the properties of the produced alloys, such as Taylor's dislocation and the most popular 2D defects, grain boundaries [102]. Fe-Cr based amorphous alloys have been widely studied and analysed using two methods of production: BMGs, and coating and ribbon design. It has been proven that Fe-Cr based materials have great corrosion resistance and excellent wear resistance in comparison with other amorphous materials. Heat treatment, or annealing can adjust the properties of Fe-Cr based

amorphous alloys, in particular the corrosion resistance. It has been concluded that the influence of structural relaxation on corrosion resistance depends on the composition as well as the corrosive environment [103]. For example, the inclusion of alloys can significantly advance the corrosion resistance of the metal alloy [104].

Chromium (Cr) is considered to be a vital element when corrosion resistance is desirable in Fe-based amorphous alloys and has obtained better results in Fe-based amorphous alloys than in stainless steel. Therefore, Fe-based amorphous alloys may supersede stainless steel alloys in various applications, as Fe based alloys have a lower cost than stainless steel (Figure 2. 23).

Many studies have been done for other magnesium-based alloys to study both corrosion resistance and wear resistance. Magnesium materials tend to degrade too fast for Orthopaedic application under the condition of physiological stress [105], [106]. To overcome this problem Mg alloys with improving alloying elements are produced. There are several alloying elements available which are known to enhance the corrosion resistance of Mg (aluminum, manganese, zinc, rare earth elements and yttrium), which are used to tailor the mechanical properties of the implant and the corrosion rate of magnesium. Moreover, protective coatings can be added to the produced materials with no toxicity and with biocompatible and biodegradable properties. Great attempts are done to find non-cytotoxic alloying elements which can improve mechanical properties and corrosion resistance.

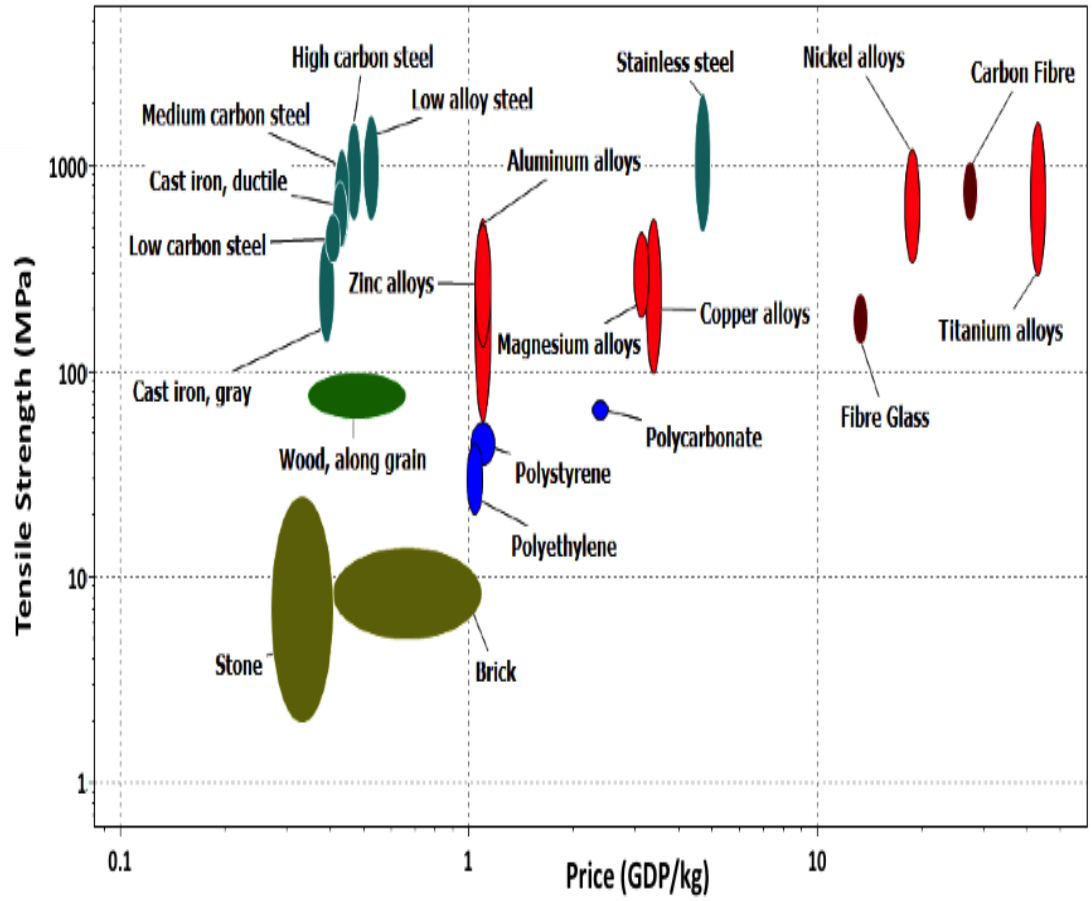

Figure 2. 23: Cost of different materials in relation to tensile strength [107].

Because materials with a thickness less than 6μm usually experience pitting corrosion, it can be concluded that deposition of a multilayer coting or the addendum of other elements leads to significant development of corrosion resistance.

2.10.3 Corrosion Behavior of Magnesium Alloys

In a research article, it is mentioned that the critical level of chloride ion concentration which will initiate the pitting of Magnesium due to galvanic corrosion is 0.002 to 0.02 M NaCl. Also, it is mentioned that the critical ion concentration increases with increase in pH value of the electrolyte. Hence these researches are raising the concerns over the utilization of Magnesium and Magnesium based alloy in bio implant applications [108]. Further the

literature survey is extended to the research domain of corrosion behaviour of Magnesium and Magnesium based alloys [109]. Like Aluminium, Magnesium is also an element which depends on forming an inherent oxide layer over its surface upon exposure to ambient conditions so that the further surface degradation is hindered. The inherent oxide layer of Aluminium is studied in detail and have been reported in literature for several decades. But the passive layer behaviour of Magnesium with various atmospheric conditions are yet to be understood fully. The passive layer is one which prevents the outward diffusion of cations and inward diffusion of damaging anions in red- ox reactions. Moreover, if the inherent oxide layer is stable then it adjusts itself with self-repairing ability when localised corrosion is experienced at the topography [110]. In reality, the corrosion rate of Magnesium in electrolytes of physiological environments falls into higher side and revealing its limitations to be utilized as replacement material in bio implant applications. Actually, during the exposure to aggressive atmosphere, the Magnesium surface transforms into Magnesium hydroxide having a grey colour and decreases the further possibility of corrosion to some extent.

The Magnesium hydroxide films are water soluble and maximum corrosion can occur when the chloride ion concentration in the electrolyte is reaching a numerical value around 150 milli mols per litter. Further, the reaction leads to the formation of Magnesium chloride which is highly water soluble and the release of hydrogen gas. Pitting corrosion is observed in Magnesium based alloys when the chloride ion concentration exceeds the aforementioned value of 30 milli mole per litter [111]. It is very important to understand the steps involved in corrosion behaviour of Magnesium so that the corrosion kinetics can be described in a better way. Following equations are the corrosion reactions of Magnesium in chloride containing electrolytes [109].

$$\mathbf{Mg(s) + 2H_2O \longrightarrow Mg(OH)_2(S) + H_2(g)} \qquad \text{Equation 2. 6}$$

$$\mathbf{Mg(s) + 4Cl^-(aq) \longrightarrow 2Cl(aq) + MgCl_2} \qquad \text{Equation 2. 7}$$

$$\mathbf{Mg(OH)_2(s) + 2Cl^- \longrightarrow MgCl_2 + 2(OH)^-} \qquad \text{Equation 2. 8}$$

In Magnesium based alloys, few of them have been developed by addition of 2-10 weight percentage of Aluminium being major alloying element to Magnesium and minor alloying elements like Zinc and Manganese. These alloys show an improvement in corrosion behaviour with better mechanical properties. In another group of Magnesium based alloys rare earth elements like zinc, yttrium, or silver, and a small amount of zirconium are added in order to achieve grain refinement which in turn improves the mechanical properties of the alloy to a greater level [112].

2.11 Corrosion Characterisation of Magnesium Based Alloys

A group of researchers investigated the corrosion behaviour of the magnesium with and without chloride containing environments and the cytocompatibility of magnesium was determined. Addition of Manganese to ternary alloy system namely Mg-Al-Zn leads to improvement in corrosion resistance in an indirect manner.

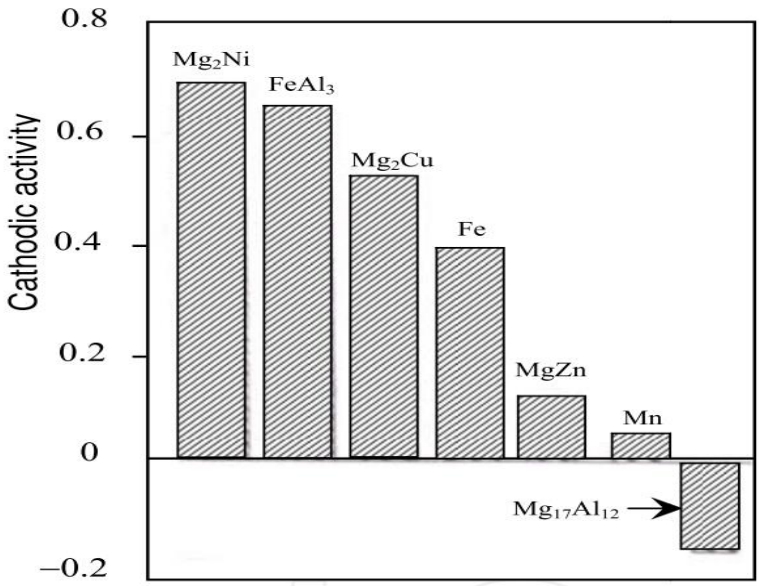

Figure 2. 24: Cathodic activity of precipitated phases in Mg alloys in saltwater relative to their alloy matrix [113].

Even though the Manganese has higher potential (Figure 2. 24) [113], addition of the same to the alloy system decreases the detrimental effects of

most of the impurities of the system and enhance the Ni tolerance level [110] of the alloy system.

The ratio of Iron to Manganese atoms in the system controls the corrosion effect since Iron and the Manganese tolerance limit of the alloy is 3.2% to the system which is independent of casting technique (Figure 2. 25).

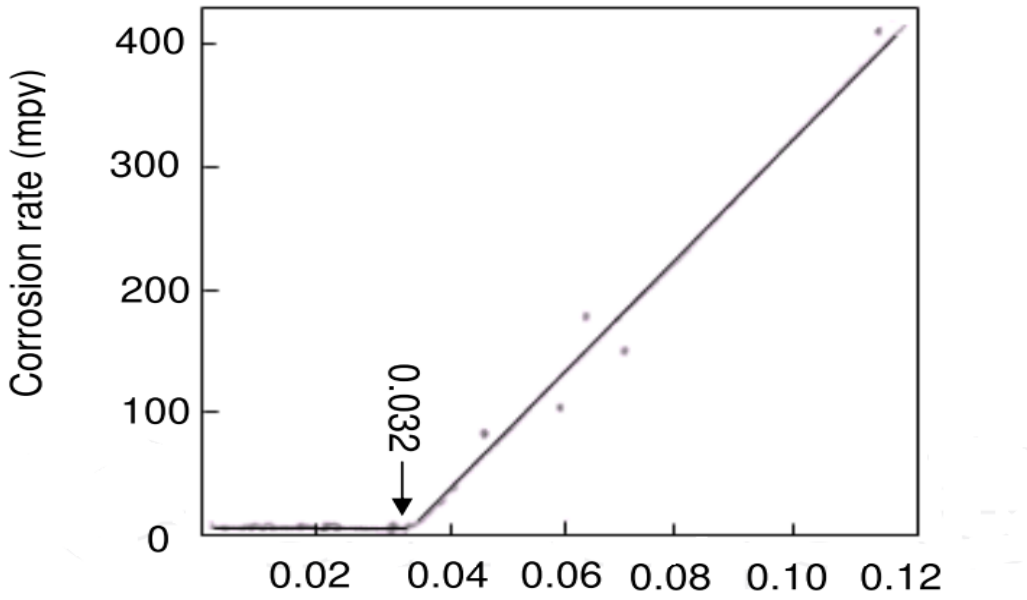

Figure 2. 25: Effect of Fe/Mn ratio on corrosion rate of magnesium, 1 mpy ≈ 40μm/year [114].

That means Manganese indirectly improve the corrosion resistance of the alloy and could be used with magnesium to improve corrosion resistance. The mechanism by which the improvement in corrosion resistance of the alloy due to the addition of Manganese is detailed as follows [98]. The galvanic activity of Mg and Fe is more since the galvanic potential difference is more between these two elements. However, when Manganese is added to the system the galvanic activity between Mn and Mg found to be at lower side when compared to that of Mg and Fe. In reality the Manganese atoms prefer to form precipitates with Iron atoms and hence leads to the decrease in galvanic activity of Fe and Mg. In the alloy system, the manganese atoms and aluminium [115] atoms have greater tendency to form Al-Mn-Fe

intermetallic precipitates by combining with available Fe atoms rather than forming $FeAl_3$ precipitates.

To the matter of fact, the $FeAl_3$ precipitates are active cathodic sites for Magnesium matrix. It reveals that if $FeAl_3$ is allowed to form then more of Magnesium matrix will corrode due to its anodic nature [115], [116]. Also, another intriguing factor to be considered is the optimum level of Manganese addition to the alloy system. Excess Manganese addition leads to formation of Al_8Mn_5 particles with higher observed cathodic current density leading to more corrosion. If the Manganese addition is optimum, then the low Mn binary precipitates like Al-Mn, Al_4Mn and Al_6Mn form with lower current density values. Strictly, the excess addition of Mn to the alloy should be avoided to prevent formation of Al_8Mn_5 particles which are detrimental with higher current density to the alloy system. Hence the corrosion related problems of Magnesium and Magnesium based alloys can be minimized by means of proper alloy design. Another very important property of Magnesium which has to be discussed from here onwards is the porosity since it has several advantages when the Magnesium and Magnesium based alloys are considered for bio implant replacement materials. The presence of interconnected pores in the matrix of the alloy effectively alters its density as well as the deformation behaviour during the application at extreme loading conditions. In particular, the integration of implant material with the human tissues is enhanced by the presence of appropriate sized pores in the matrix of implant materials [117]. Figure 2. 26 depicts the microstructure consisting the pores of compatible sizes with human tissues reported in a research carried out by Wen et al. [118].

In comparison, the material with desired amount of porosity exhibit a shortened region of linear elasticity near to the loading condition of yield strength and a constant flow stress in responds to large experienced strains.

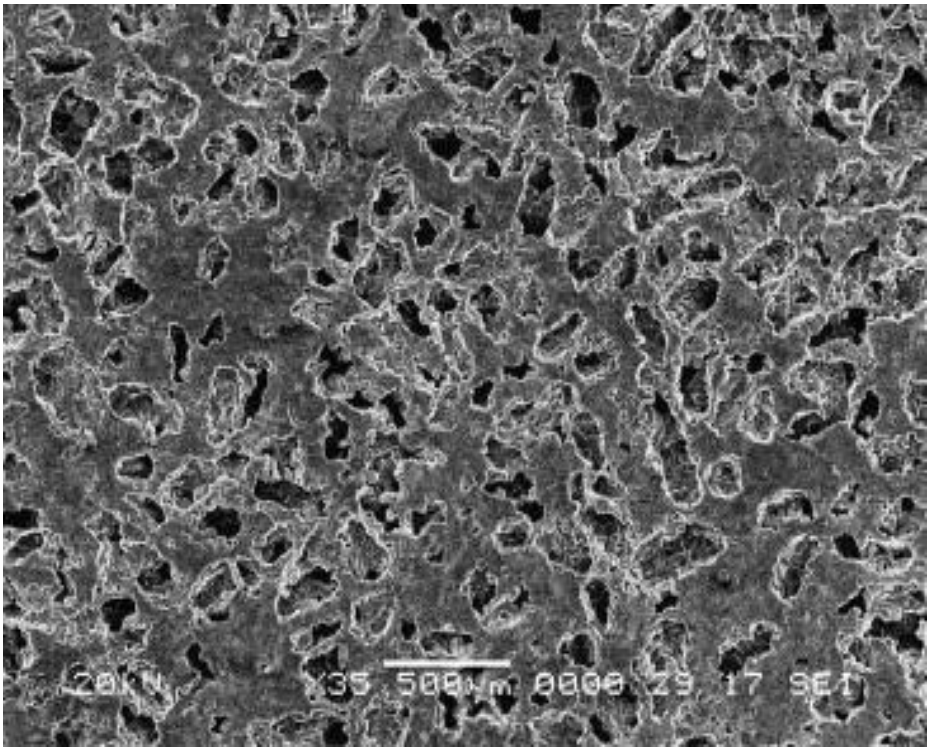

Figure 2. 26: SEM microstructure consisting the pores of compatible sizes with human tissues [118].

The young's modulus and the mechanical strength of the alloy having pores is influenced greatly by the quantitative nature of the pores, size, shape and the interconnection between them. In nature, the Cancellous bones are characterized by interconnected pores leading to an exhibition of typical deformation behaviour in comparison with other bones under various loading conditions [119]. In this type of bones the porosity variation is differing from approximately 35 % to 90 % resulting in appreciable variation in its yield stress reported as 3 to 20 MPa, young's modulus as 10GPa to 40GPa revealing the fact that the porosity play a crucial role in deciding the mechanical properties [119]. In summary, it can be inferred that the introduction of porosity in the bio implant grade alloy presents the possibility of adjusting the mechanical properties to a desired level and enhancing the compatibility of the interface between the alloy and the living tissues of human body. Conversely, the excess presents of the porosity in the bio implant grade alloy leads to destruction of the mechanical properties and

making the alloy unsuitable for many applications. In general, there are several techniques developed in order to introduce pores into metals and alloy systems [120]. But one must select an appropriate technique to execute the introduction of pores in bio implant research since the bio compatibility of the pores generated alloy with human tissue is the major factor which depends on the type of reagents and methods utilized for generation of pores in the alloy [121].

Magnesium with appropriate pore morphology for bio implant applications is fabricated by injection of argon gas to the molten metal during the casting process [121]. In another technique, polyurethane foam is used in plaster casting technique to introduce pores into Magnesium matrix [122], whereas the same is possible through powder metallurgy technique by utilizing space-holding particles [118], [123]. The powder metallurgy technique and plaster casting give rise to the fabrication of the alloy with controllable and uniform pore morphology. On the other hand, the foam injection method proved to be in-efficient in controlling the pore morphology during manufacturing [124]. Many research groups have stated that the volume of the pores present in the Magnesium alloy and the size of the pores can be directly correlated to the mechanical properties of the alloy [118], [123]. To summarize the mechanical property-porosity correlation, it can be said that the presence of porosity to a desired level results in reduction of yield strength and modulus of the bio implant grade Magnesium alloy falling near to the mechanical properties of natural bone systems. In appropriate mentioning, the introduction of predetermined level of the pores to the alloy, transforms it to a bio implant grade alloy with tailor made properties especially meant for the implant application. Also, the same is insisted in the design guidelines of the bio implant research to the level of compromise to be achieved in mechanical properties with pore introduction to the alloy matrix. In this regard, a research publication reported that the magnesium with introduction of pores by foam injection method resulted in 97% of porosity with pore radius of 2.25 mm. This kind of material will not be useful in bio implant applications with modified mechanical properties like yield strength equivalent to 0.1 MPa. Also the specimens with 50% porosity and pore sizes of range nearly equivalent to

200 or 300 mm are characterized with resulting compressive strength value equivalent to 0.35 MPa [125]. Wen et.al reported that the yield strength and young's modulus of the alloy of porous nature observed to decrease with decrease in pore volume and pore size. In the same research, it is stated that the quantitative value of the porosity in the alloy with predetermined and achieved pore size of 250 mm results in compressive strength value ranging from 12 to 17 MPa [126].

In conclusion, selecting the right magnesium alloy-by-alloy design should be summarized briefly. According to the literature review carried out, rare earth elements added to magnesium alloys proved to be quite successful in bio implant applications. But a systematic approach is needed to design the magnesium alloy with appropriate percentage of rare earth elements with respect to the needs of each type of applications. Also it is understood that the rare earth elements effectively increase the corrosion resistance of the alloy [127].

In recent decades many researchers have worked on Mg Al alloy for the bio implant applications. Even though there are many advantages of Mg Al systems, literature have not recommended the same due to its demerits. The following flow chart is constructed in furnishing the steps involved in the protocol of right selection of Magnesium alloy in bio implant applications (Fig 2.18).

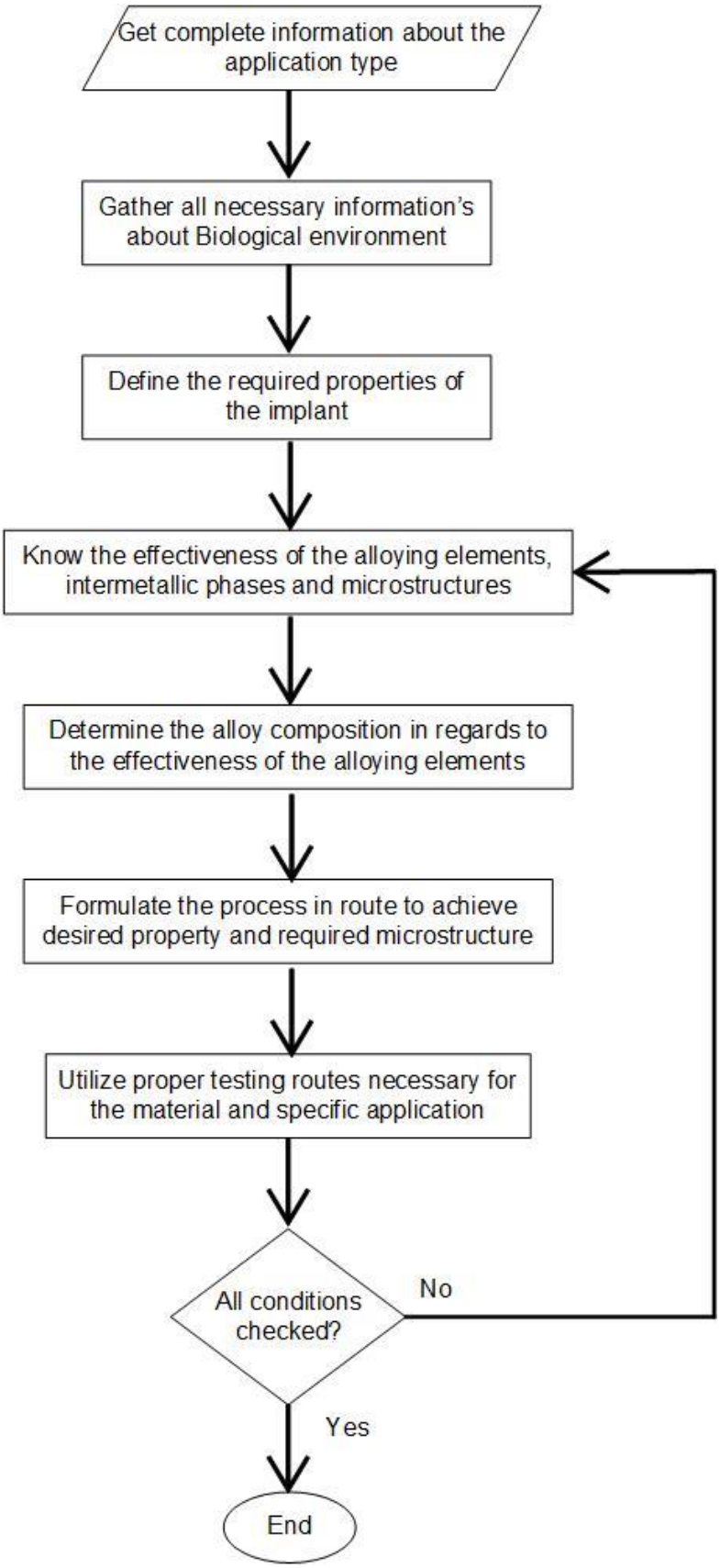

Figure 2. 27: Flow chart of Magnesium alloy selection protocol [55].

2.12 Surface Modifications and Treatment Processes Mg Alloys in Biomedical Applications

As the literature suggests clearly, the degradation behaviour of the Magnesium based alloys used in implant applications can be altered by means of proper design of alloy system with alloying elements. Also there is another possibility in terms of surface modifications to achieve reduced degradation behaviour of the Magnesium based alloys. The surface treatment gives rise a coating over the alloy to resist the aggressive body fluids as electrolyte in corrosion process. The design of the surface modification techniques for the implant materials require many considerations including the biocompatibility of the coating with the human tissues in terms of not affecting the natural process of healing and regeneration of tissues. This can be understood clearly by knowing the stages of healing and regenerative process of tissues in human body. The regenerative process begins with inflammation and proceeds with reparative and remodelling processes. The first phase called inflammation happens at the initial stages of recovery after the implantation and extends for few days depending on the immune systems of every individual person. The reparative process is second to inflammation and exists for three to four months with integration of implant with human tissue by regeneration mechanism. The final stage called remodelling may take several months of time and this varies with respect to different patience [128].

In the case of Magnesium alloy to be used as successful implant material, the basic requirement is the lower degradation rate so that the space for the human tissues exists in order to regenerate and proceed with an integrity along the contact of the alloy. This process requires a minimum period of three months [129]. But the fact is the Magnesium alloy surface gets corroded to a greater extend during this period and hence the mechanical properties of the alloy is affected adversely. Further the interaction of the released ions with the bodily fluids surroundings to the implant affect the regeneration process of the tissues vice versa. This implies the importance of surface modification technique to enhance the degradation resistance of the

Magnesium based alloys in implant applications. Physical vapour deposition methods, chemical vapour deposition techniques and chemical bath techniques etc., are available to fabricate a corrosion resistant coating on the implant components.

2.13 Biocompatibility and Biodegradability of Mg-based Alloys

2.13.1 Biodegradability of the Metal Based Alloys

The implant structures made of the biodegradable materials should not cause any unusual sensations or chronic inflammatory discomforts. The Mg-based alloys as implant materials does not cause toxic effects in human body. In general Mg has the tendency to undergo rapid corrosion in chloride containing environments, but in body fluids the corrosion occurs at a lower rate due to less aggressiveness of the bodily fluids. In addition, the release of magnesium ions has to be controlled within the acceptable limit even though it is one of the trace elements exist in human body [130]. Actually, investigations of Mg alloys for the medical applications started in the late of 19^{th} century and continued to the 20^{th} century [131]. At first, it was difficult in manufacturing pure magnesium which lead to higher corrosion rates of the implant structures [131]. Then the research works were focusing on exploring new techniques to manufacture pure and high-quality Mg alloys at the beginning of 20th century. Now, the industry is successful in design and manufacturing of suitable Mg implant structures, however, challenges remains in controlling the corrosion rate in the human body environment. This is attributed to the nature of human body and the amount of hydrogen gas released around the implant regions of human body. Many techniques have been suggested for controlling the Magnesium degradation by adding special coatings [132]–[135] and modified manufacturing techniques [136]–[139]. The design of biodegradable alloy should consider the control of dissolution rate or delayed corrosion behaviour in body fluids. Many decades of research indicates that adding suitable alloying elements can control the dissolution rate in body fluids [140]. In-vitro corrosion tests are not always accurate in predicting the in-vivo corrosion behaviour. There is a need for a more

accurate method of corrosion tests [141]. Hence, new in vitro methods are introduced, for example electrochemical methods and immersion techniques.

Different corrosion results cannot be easily compared because the different parameters used, for example different solutions, temperature, buffer selection and surface conditions etc. So extreme care is required when the results of in vitro experiments are compared with that of in vivo experiments. A research stated that the material was cut into small coupons of dimension of 2 cm^3 and further subjected corrosion tests. Before the test, the specimens were polished using emery papers of grade up to 1000 grit and then cleaned in distilled water. The specimens are weighed in body fluids and the pH value of the Hank solution used is also registered. After the removal from the solution, the specimens were cleaned and brushed immediately followed by the gravimetric analysis. In the case of AZ91D Magnesium research the alloy coupons as well as the anodized specimens were analysed and compared [67].

In another related work, ingots of pure Mg, Mg-0.8Ca, Mg-1Zn, Mg-1Mn, and Mg-1.34Ca-3Zn (wt %) and AZ31 alloys in rectangular shapes were used in experimentations. The rectangular specimens were prepared with dimensions 12 mm × 4 mm × 3mm and then subjected to polishing using polishing sheets of grade up to 1200 grit. After polishing the specimens were cleaned in ultrasonic bath containing ethanol of 100%, mild detergent and double distilled water. Further, the specimens were weighed separately before subjecting them to sterilizing treatment using Gamma irradiation (25 kGy, Schering-Plough Animal Health). Procedural modifications were employed by Yamamoto and Hiromoto [142] during in vitro testing of implant material. Earle's balanced salt solution (EBSS; Sigma-Aldrich), minimum essential media (MEM; Invitrogen), and MEM containing 40 g/L bovine serum albumin (MEMp; ICP Bio, New Zealand), (the constituents of the solutions are furnished in table 2.1) are used as solutions in immersion method of analysis. In this work, serum albumin of bovine system is prepared to match the concentration of human plasma albumin concentration [143].

The pH of all solutions used in this study were maintained to 7.1 and then subjected to filter sterilizations at 0.22lm. This led to the change of pH from the aforementioned value to 7.4. The solution of immersion volume is maintained to be 30 mL by compensating additions every day. This is adjusted in accordance with the urinary excretion system of human body [144]. In view of considering the implant structures of real time applications, the sample size and the solution volumes of the experiments were predetermined. Sterilized T25 cell-culture flasks, one end with filter caps were used in all experiments.

Table 2. 1: The constituents of the solutions of the in vitro immersion testing [145].

Elements	**Plasma**	**EBSS**	**MEM**	**MEMp**
Na^+	140	144	143	143
K^+	5	5.4	5.4	5.4
Mg^{2+}	1	0.4	0.4	0.4
Ca^{2+}	2.5	1.8	1.8	1.8
Cl^-	100	125	125	125
$H_2PO_4^-$	0.8	1.0	0.9	0.9
SO_4^{2-}	0.5	0.4	0.4	0.4
HCO_3^-	22 - 30	26	26	26
Glucose	5	5.6	5.6	5.6
Phenol red	-	0.03	0.03	0.03
Albumin	35 - 50	-	-	40
Amino acids	Variable	-	0.95	0.95
Vitamins	Variable	-	8.1	8.1

Following table depicts the composition of the test solutions (Table 2.2) containing either 26 mM sodium bicarbonate ($NaHCO_3$), 25 mM 4-(2-hydroxyethyl)-1-piperazineethanesulfonic acid (HEPES), or a combination of the two. The solutions prepared in the experiments containing bicarbonate were maintained at temperature namely 37˚C and 5 percentile CO_2. The solution which contains only 4-(2-hydroxyethyl)-1-piperazineethanesulfonic acid was maintained at temperature 37˚C under normal atmospheric conditions. Compensating additions of the solutions were made after every removal in 7 days, 14 days and 21 days. An orbital shaking platform was used to maintain the solutions at required concentration and temperature. In

order to maintain the pH value of the solution to match the physiological range, the pH of the solutions is adjusted periodically. In negative control of pH, three flasks of each solutions were employed. After the removal of the specimens from the immersion solutions as well as the subcutaneous tissue, they were transferred to a bath containing chromic acid solution (200 g/L CrO_3 and 10 g/L $AgNO_3$) for 15 min. This procedure is employed to remove the corrosion products formed on the specimen surfaces [88]. Further the specimens were subjected to gravimetric analysis after the cleaning process in distilled water and drying. The corrosion rate of the material is calculated from the weight loss measurements using the following expression,

$$Corrosion\ Rate\ (CR) = \frac{\mathrm{KW}}{\mathrm{ATD}} \qquad \text{Equation 2. 9}$$

Where CR is the corrosion rate (mm/year), K is the constant 8.76×10^4, W is the mass loss (g), A is the surface area (cm^2), T is the time of exposure (h), and D is the density of the materials (g/cm^3). ASTM-G31-72 standard[146] is followed in another immersion experiment to prepare the Hank's solution. The specimens for the degradation's tests were prepared in disc shape with diameter of 10 mm and a thickness of 2 mm. The specimens were further immersed in 50ml solutions kept in a temperature water bath of 37 ^{0}C. The immersed specimens were removed from the Hank's solution, washed in distilled water, and dried in air. Environmental Scanning Electron Microscope (ESEM; Quanta-200FEG) associated with an energy-dispersive spectrometer is employed in analysing the topographical information's of the degraded specimens. Actually, the amount of hydrogen released during these experiments were monitored and registered for further analysis [130].

Chapter 3 Pulse magnetic field processing of an Al-20%Si alloy and microstructure characterization

This chapter describes the experimental details of the electromagnetic pulse magnetic field processing of an Al-20% Si alloy and the microstructure characterization work. Specifically, the aim of this chapter is to investigate the effect of pulse electromagnetic fields on the microstructural evolution and hardness of an Al-20 percent Si alloy. The first part of the chapter describes pulse magnetic field parameters used in the solidification process. The second part describes the detailed microstructure analysis of the alloy using optical microscopy and scanning electron microscopy.

3.1 Al- 20%Si alloy making.

The Al-20%Si alloy samples were cast by melting together pure Al (purity of 99.97 pct), and pure Si (purity of 99.97 pct) with the appropriate weight ratio in an electrical resistance furnace. The metallic feedstock was dried in an oven at 110 ^{0}C for 8 hours to remove the residual moisture. Prior to placing of the sectioned metallic pieces of Al and Si into the crucible, the inner surface of the crucible was coated with boron nitride spray and dried in 150 ^{0}C for 30 minutes. It created a uniform boron nitride film on the inner surface of the crucible, protecting the crucible from being reacted with the molten alloy.

The feedstock was then added into the crucible and the furnace temperature was raised in steps of 150 ^{0}C until 750 ^{0}C. The temperature of the molten liquid was monitored using a thermocouple. One hour holding time was used to homogenise the melt. The oxide layer at the melt top surface was removed carefully by means of a ceramic or a stainless-steel stick. The molten alloy was sucked into a quartz tube by negative pressure (0.1 to 0.3 bar) via a counter gravity casting device.

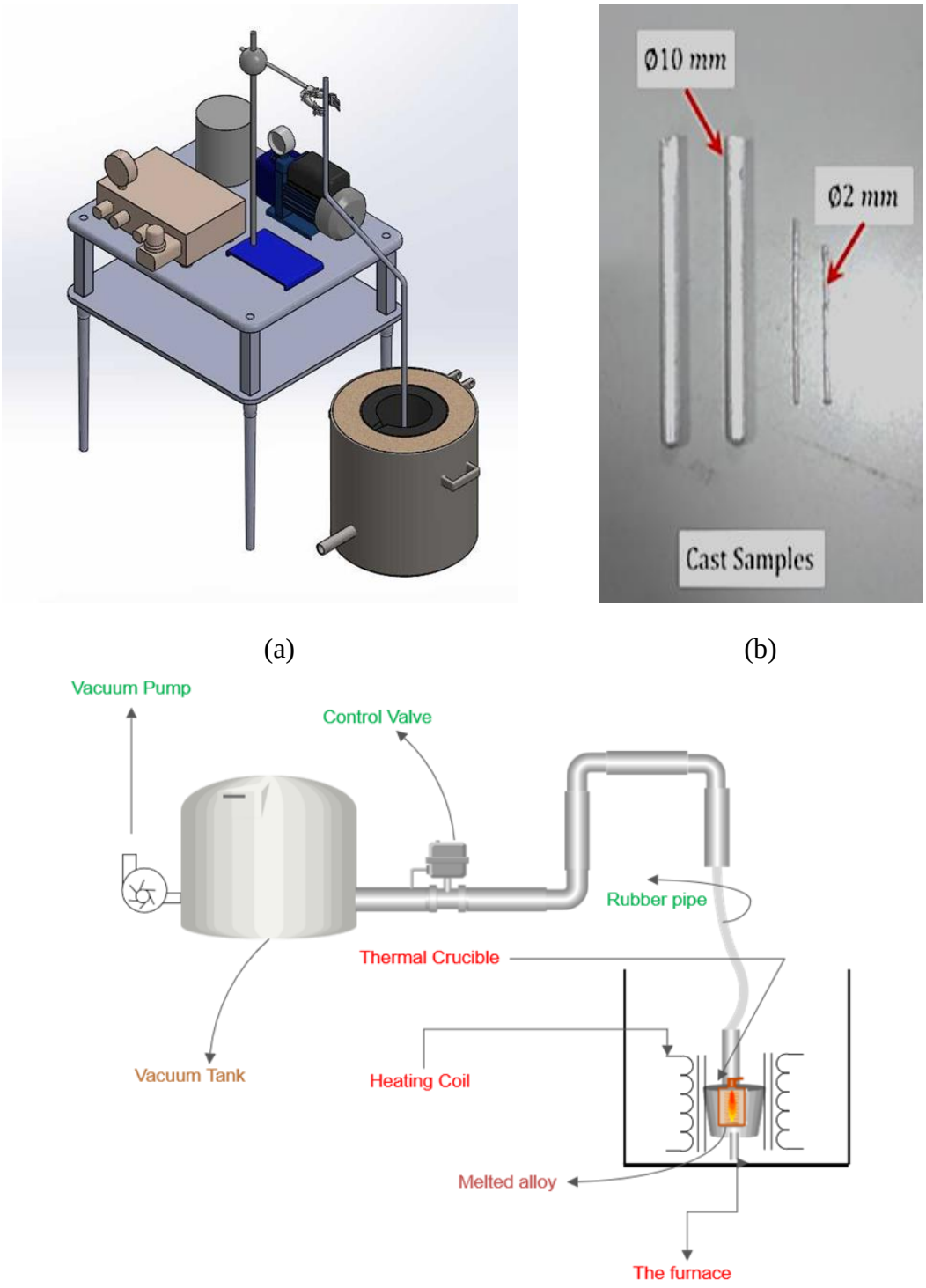

Figure 3. 1: A counter-gravity casting apparatus a) a 3D CAD drawing of the experiments set-up. b) Samples of the specimens can be produced in as cast condition based on the quartz tube diameter [147]. c) A schematic diagram of solidification process.

Figure 3.1 illustrates the counter gravity casting apparatus used for making the Al–20%Si alloy samples. The quartz tube is 130mm long and inner diameter of 9 mm. The controlled negative pressure maintained in the apparatus drew the liquid metal uphill (counter gravity direction), minimising turbulence and bubble entrainment.

3.2 Pulse magnetic field processing of the Al-20%Si alloy

The virgin quartz tube prior to the insertion of the specimen during melting process is subjected to the magnetic pulse generated by varying the voltages namely 40, 80, 120, and 160 V. The discharge summary from the capacitor bank are registered using a Gauss meter (Hirst Gauss Meter, model GM08) at the P1 point furnished in figure 3.2 (a) and the corresponding plot is shown in figure 3.2 (b). The registered magnetic flux density with respect to time as the varying parameter in milliseconds, show similar pattern and increasing tendency as the voltage increases. It infers that the peak magnetic pulse registered increases with respect to increase in discharging voltage. The full width at half maximum (FWHM) of the registered peaks are measured at 0.25, 0.45, 0.55, and 0.65 ms ((c)), respectively. The critical observation is that the generation of magnetic pulses happens to be well within one millisecond of all varying discharging voltages. Figure 3.2 (d) clearly suggest that the simulated results of magnetic flux densities at various discharging voltages are in good agreement with the experimentally obtained results. A small difference in the measured and simulated flux density peak values is observed when the experiment is carried out with C=1 mF. The C parameter specifies the capacitance of the capacitor bank in Farads (F), as explained in section 2.1 of chapter 2, equation 2.1. This is because of the fact that there is a possibility for energy loss in real time experiments due to heat generation and dissipation in discharging circuit.

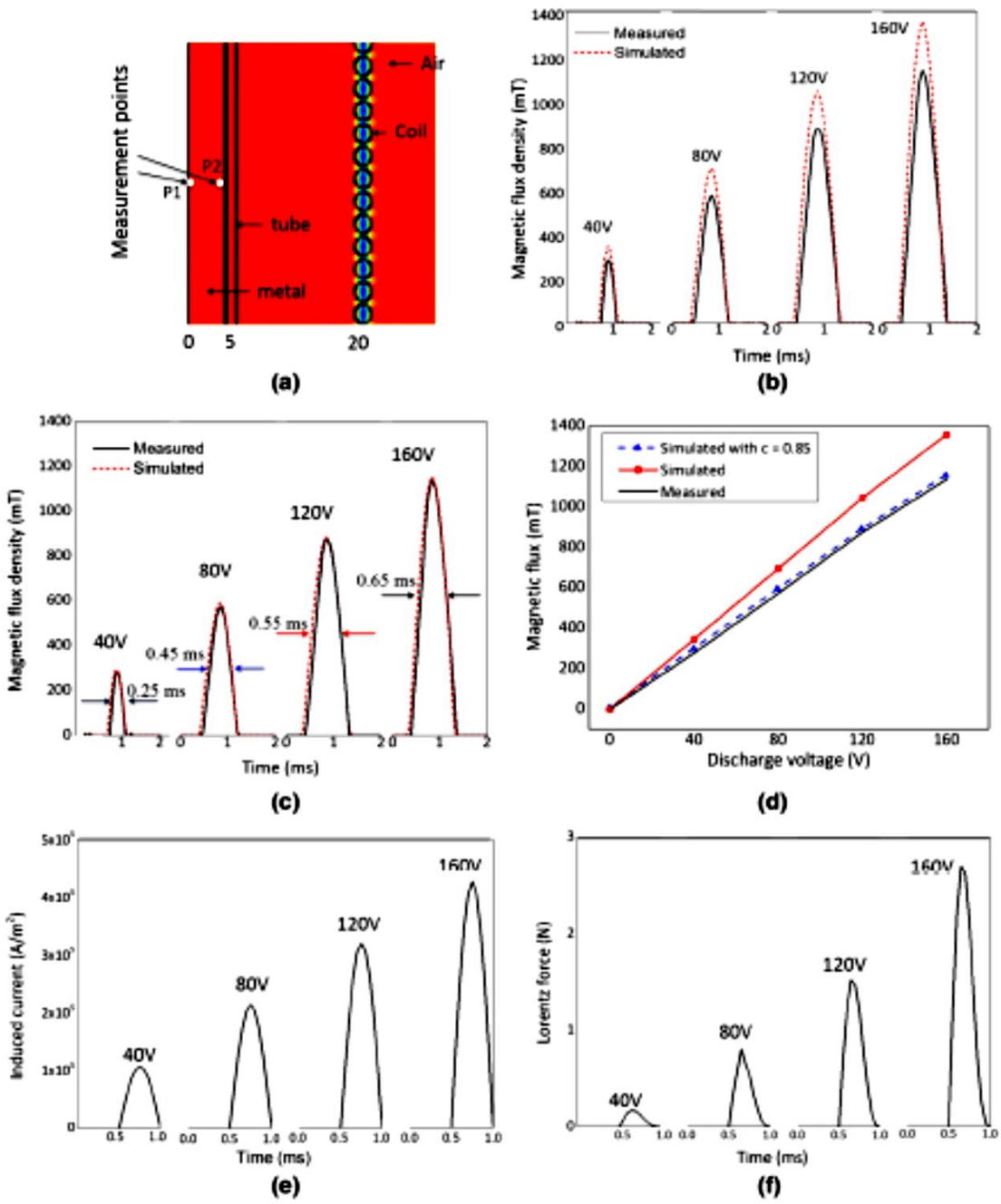

Figure 3. 2**:** Calibration of magnetic pulse generation setup (a) Schematic representation of the measurement points of the magnetic flux density (PI), induced current and Lorentz force (P2) within the quartz tube (b) Correlation profile of the measured and simulated (C = 1 mF) pulses of magnetic flux densities (c) Correlation profile of the measured and simulated (C = 0.85 mF) pulses of magnetic flux densities (d) Profile showing the variation of the peaks of the magnetic flux density with respect to discharging voltages, (e) the simulated induced current fluxes inside metal alloy, and (f) the simulated Lorentz forces.

In addition, Close agreement is observed and registered for C = 0.85 mF (figure 3.2 c and d). This indicates that the energy conversion is maximum in the case of the experiment carried out at condition C = 0.85 mF. Another intriguing observation is the exhibition of similar patterns of plots showing the variation of induced current with time and the Lorentz force with the time (figure 3.2 e and f). These results of calibration of electromagnetic pulse generation unit are effectively utilized in setting up the parameters in magnetic pulse generation during the solidification of the Al-% 20 Si alloy.

The bar specimen cast inside the quartz tubes were removed carefully by breaking the quartz tube. The surface of the bars was ground to allow them to fit into the new quartz tube of 130-mm long and inner diameter of 9 mm for pulse magnetic field solidification experiments. An adopter was used to seal one end of the quartz tube with ceramic paste. To measure temperature during the experiment a thermocouple was attached to the bar from the other open end. Such sample assembly was heated in an oven for 24 hours at 110 ^{o}C to dry up before set them up inside the furnace with a pulse magnetic coil surrounded. The thermal blanket was used to cover the furnace top to minimise thermal variation. The furnace was switched on by setting up the first target temperature to 200 ^{0}C, at this temperature, the pulsed electromagnetic set up is switched on (see figure 3.3). It was then raised in steps of 150 ^{0}C until 750 ^{0}C. A holding time of one hour at this temperature ensures the homogenisation of the alloy. As soon as the sample cooled down and reached a solidification temperature of 500C, the magnetic field was turned off. The voltage discharged from the capacitor controlled the flux intensity of the magnetic field acting onto the solidifying alloy melt. In this work, the discharge voltage used were 0V, 40 V, 80V, 100V, 120V, and 160V.

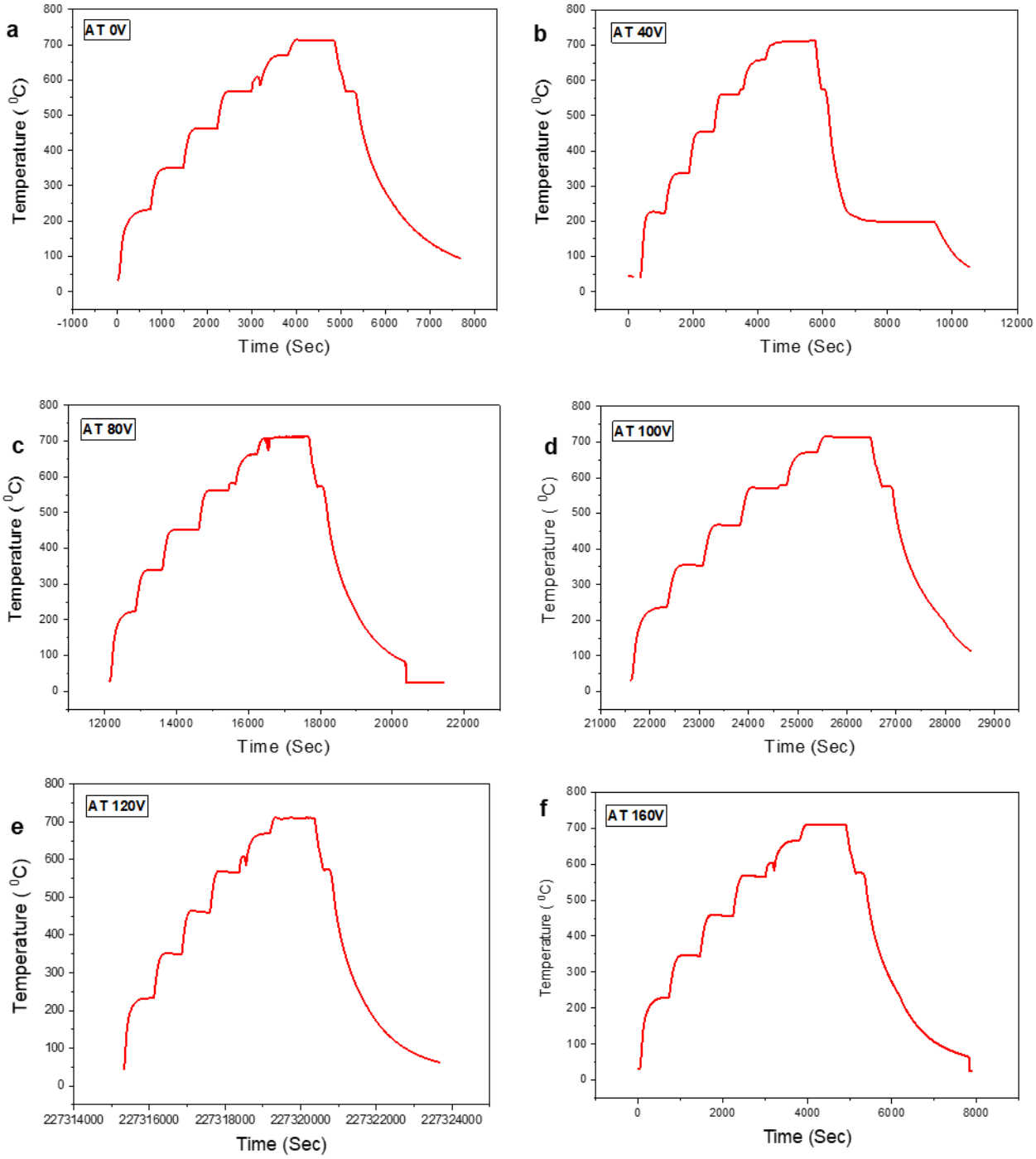

Figure 3. 3**:** The measured temperature profile recorded by a data logger (TC-08) during the pulse magnetic field experiment with the discharge voltage of a) 0V b) 40 v c) 80 V d) 100 V e) 120 V and f) 160 V.

3.3 Specimen preparation for metallographic analysis.

After casting, the specimens were removed from the quartz tube and cut in half along the longitudinal direction by hacksaw. The sectioned specimens were mounted on a rotating disk specimen holder which then was mounted onto a grinding and polishing machine for grinding and polishing. Different grit size papers, i.e. 80, 120 ,220. 320, 600, 800 and 1000 were used. The pressure was maintained at 15 lbf and the rotating speed was 200 rpm. Water was applied continuously during grinding and polishing to cool and lubricate the samples. The polishing was made by using diamond paste, 9 µm, 3 µm and 1 µm. During the fine polishing stage, the rotating speed was set at 150 with a pressure of 10 lbf. The *kemet* blue liquid was used as the lubricant. The last step of polishing was the use of colloidal silica suspension. Keller's reagent with concentration of 3% nitric acid, 1% hydrochloric acid and 1% Hydro fluoric acid was used for etching the specimen surface if necessary.

3.4 Microstructure analysis of the processed Al– 20%Si alloys.

To understand the effect of pulse magnetic field on the structure refinement of the alloy samples. Optical microscopy and SEM with Energy Dispersive X-Ray Analysis (EDAX) were used to characterise microstructures. (SEM) and (EDAX) tools (Carl Zeiss EVO-60) were used at the University of Hull to determine the actual composition of the cast alloys, and the results are listed in the following table (Table 3. 1: Chemical composition of three different Al-Si alloys and the details are shown in appendix B:

Table 3. 1: Chemical composition of three different Al-Si alloys

Sample	**Chemical Composition**		
	Si (Wt%)	**Si (At%)**	**Al**
1 (top)	19.35	16.84	Balance
2 (Mid)	20.01	17.19	Balance
3 (Bottom)	24.42	21.31	Balance

3.4.1 Microstructures

It is essential to fully characterise of the solidified microstructures at different regions of the sample length, and three regions were identified as “bottom part”, “middle part” and “top part”. Figure 3.4 illustrates the SEM back scattered electron images for the bottom part of the Al-20%Si alloy at 20x magnification made by using different discharge voltages. The Figure 3.4a is that for 0 V. It exhibits long and thick plate like primary Si phases, randomly distributed throughout the Al matrix. Figure 3.4b shows the microstructures for 40 V case. There are less number of the very long plate like primary Si, but more of the short primary Si phases. This indicates that there is a change in the primary silicon size and shapes in the matrix. Figure 3.4c illustrates the microstructure for the 80 V. Interesting observation is that the long, thick, and continuous primary Si phases started to disappear. More short primary Si plates are present and uniformly distributed in the matrix. The thickness of the primary Si decreases when compared to that of the 40 V case. When the discharge voltage was increased to 100V, the corresponding microstructure (Figure 3.4d) exhibits the presence of shorter and smaller (in thickness) primary Silicon plates. Increase in discharging voltage to 120 and 160 V, has greater influence on the microstructure of the solidified Al-20%Si alloy. Figure 3.4e and f show that some of the shorter primary silicon plates have transformed into small primary silicon islands. This in turn increases the uniformity of the distribution of secondary phase Silicon in the matrix of Aluminium and eutectic mixture. Figure 3.4 show the SEM graphs of the bottom part at 100 X magnification. Figure 3.4a is the case for 0V that clearly shows the presence of only thicker primary Si in all directions. There are no smaller Si plates or Si islands, just the big thicker primary Si plate like structures.

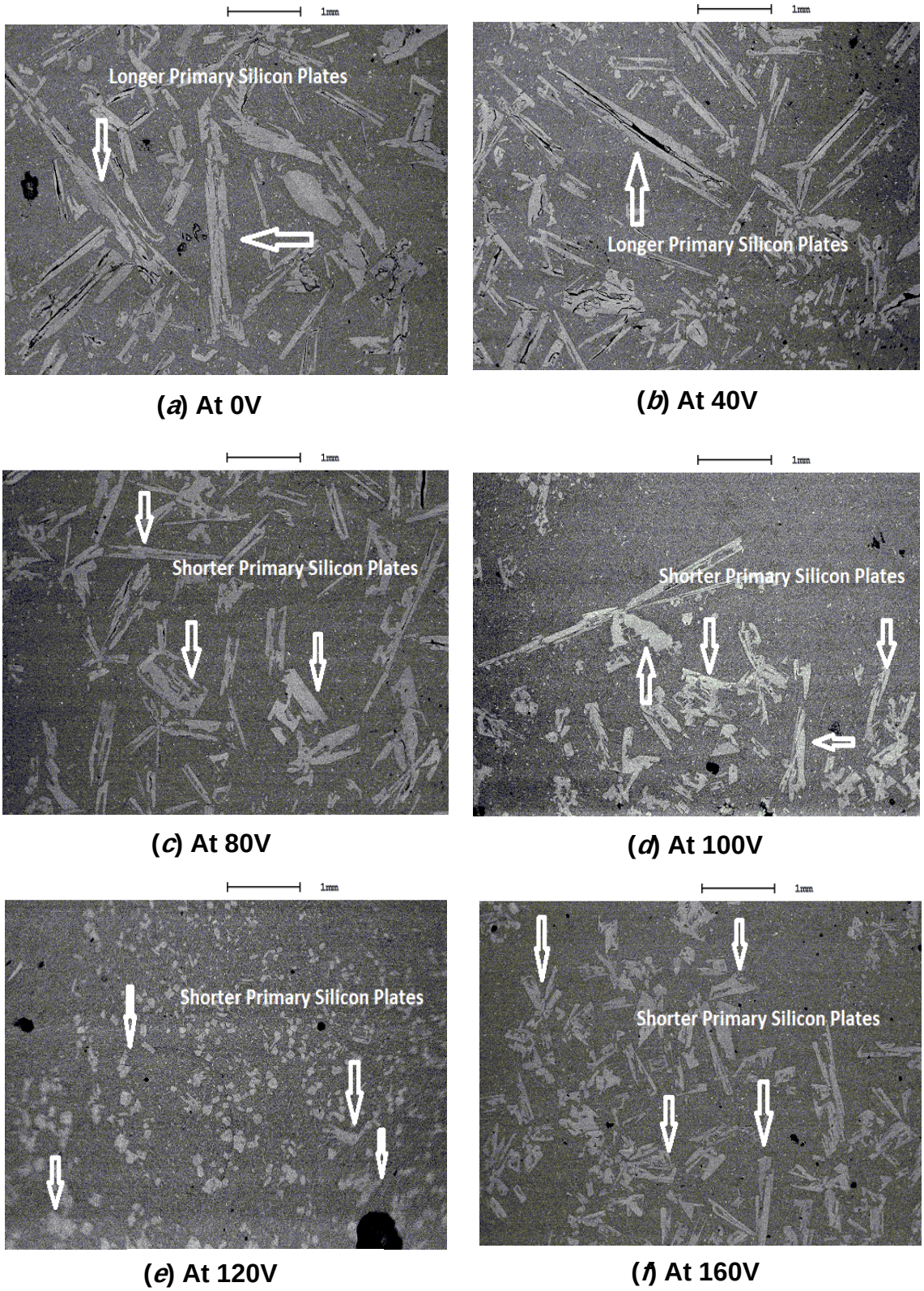

Figure 3.4: The SEM micrographs of the ***bottom part*** of the Al- 20%Si samples subjected to discharge voltages of a) 0V b) 40 V c) 80 V d) 100 V e) 120 V and f) 160 V at ***20 X*** magnification.

Figure 3.4 illustrates the back scattered electron beam scanning electron microscope images of bottom portion of electromagnetic pulse assisted solidified Al- 20% Si alloy at 20 X magnification with various discharge voltages. The Figure 3.4a is corresponding to zero discharge voltage and solidification of the alloy without the influence of magnetic field. It exhibits the presents of long and thick plate like primary Silicon structures. These plate like Silicon structures are present throughout the microstructure and they are oriented in almost all directions. It is noticeable that there is quantitatively minimum short primary silicon plate like structures observed. Figure 3.4b shows the microstructure corresponding to 40 discharging voltage. Hence, the solidification has taken place under the influence of magnetic field of smaller intensity. The interesting features are the presence of very few long plates like primary Silicon structures and increased amount of short primary silicon plates. This indicates that there is a change in the primary silicon size and shapes embedded in the eutectic matrix. Figure 3.4c illustrates the microstructure corresponding to 80 discharging voltage. Interesting observation is the absence of long thick and continuous primary Silicon plate like structures. Only short primary silicon plates are visible. In addition, the uniformity in the distribution of the short primary Silicon plates are improved. Thickness of the primary Silicon plate like structures has decreased when compared to that of the microstructure corresponding to 40 V. When the discharge voltage is increased to 100V, the corresponding microstructure (Figure 3.4d) exhibits the presence of shorter and smaller (in thickness) primary Silicon plates. Increase in discharging voltage to 120 and 160 V, has greater influence on the microstructure of the solidified Al-20%Si alloy. Figure 3.4e and f show that some of the shorter primary silicon plates have transformed into small primary silicon islands. This in turn increases the uniformity of the distribution of secondary phase Silicon in the matrix of Aluminium and eutectic mixture.

Figure 3. 5 represents the SEM microstructures of bottom portion of electromagnetic pulse assisted solidified Al- 20 % Si alloy at 100 X magnification. Figure 3.4a corresponds to solidified alloy specimen without the application magnetic field (Zero discharging voltage). It clearly shows the

presence of only thicker primary silicon plates ordinated in all directions. When Silicon precipitation happens to be thicker and region concentrated then depletion in Silicon atoms arises in other regions of matrix. Hence, there are no smaller Silicon plates or Silicon islands are observed other than massive thicker primary Silicon plate like structures.

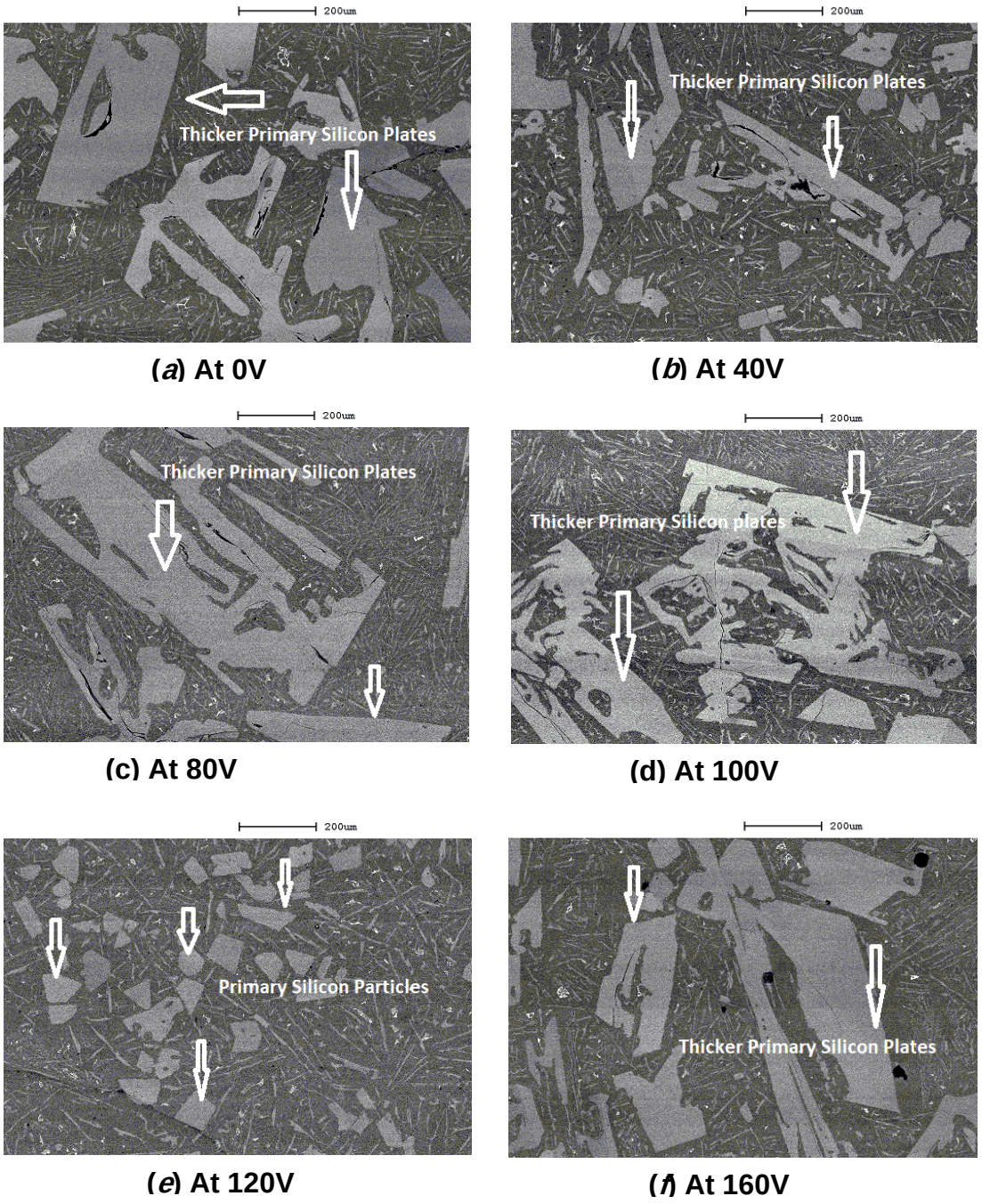

Figure 3. 5: The SEM micrographs of the ***bottom part*** of the Al- 20%Si samples subjected to discharge voltages of a) 0V b) 40 V c) 80 V d) 100 V e) 120 V and f) 160 V at ***100 X*** magnification.

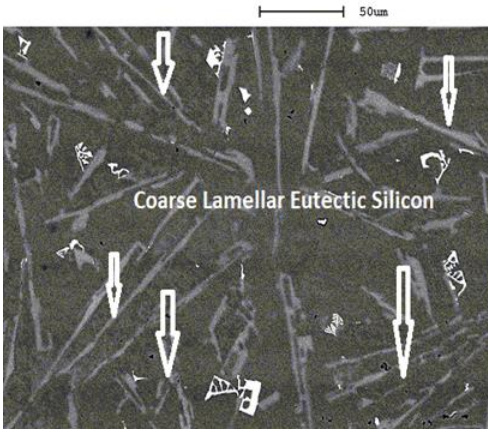

(a) At 0V

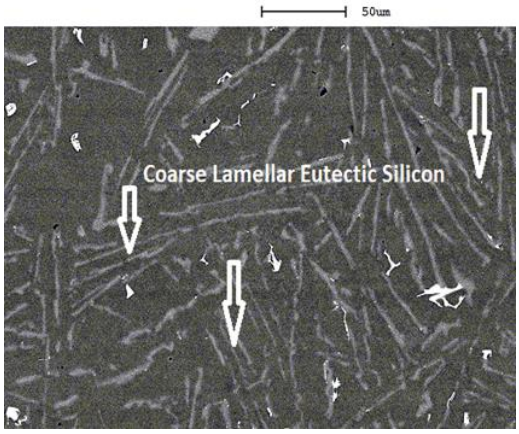

(b) At 40V

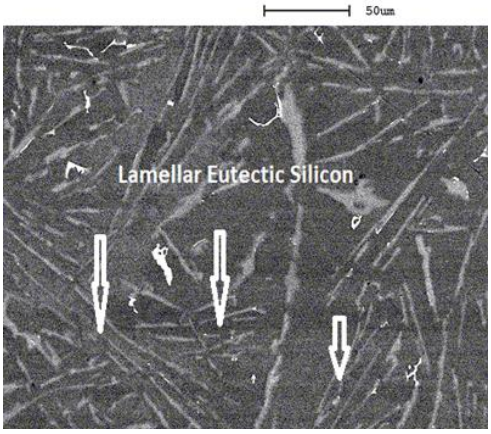

(c) At 80V

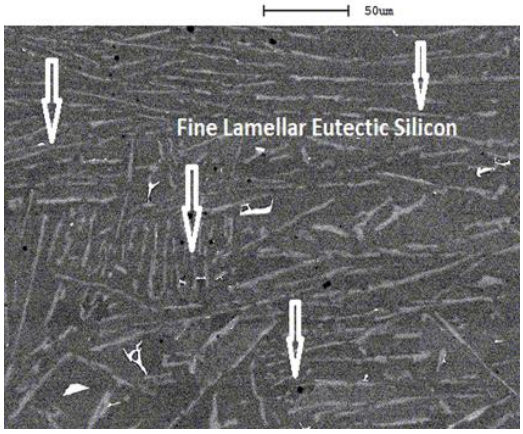

(e) At 100V

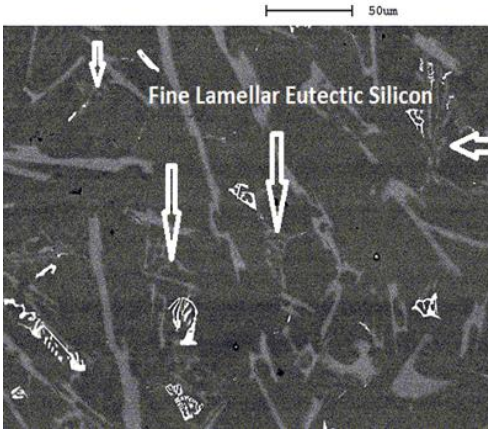

(e) At 120V

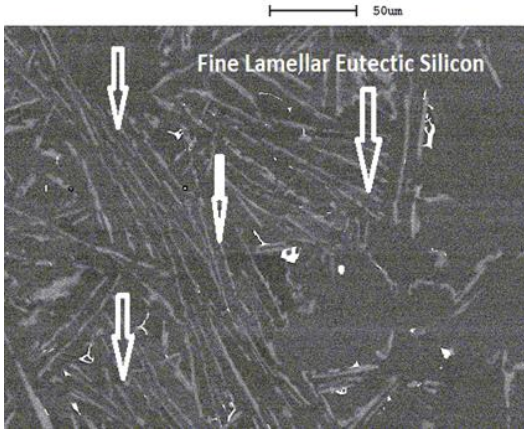

(f) At 160V

Figure 3. 6: The SEM micrographs of the ***bottom part*** of the Al- 20%Si samples subjected to discharge voltages of a) 0V b) 40 V c) 80 V d) 100 V e) 120 V and f) 160 V at ***400 X*** magnification

Figure 3. 5b represents the microstructure of the pulsed electromagnetic field assisted solidified alloy at discharging voltage as 40 V. It differs with the former microstructure by showing the presence of thinner primary Silicon plates and smaller Silicon islands along with the thicker primary Silicon plates. Moreover, the quantitative increase in eutectic lamellar or acicular structures of Al and Si embedded in α phase is clearly visible. As the micrographs of increased discharge voltages (Figure 3.4 c to f) are analysed, the inference is that the quantitative presence of thicker primary Silicon plates is decreasing and the formation of thinner Silicon plates as well as smaller Silicon islands are increasing. Another intriguing fact to be noted is that the increase in discharge voltage leads to quantitative increase in the formation and growth of lamellar Al + Si eutectic colonies. As the formation of massive primary Silicon plates are affected adversely by means of the presence of magnetic field, the uniformity of the secondary phase Silicon distribution in the matrix increases and it can be shown by the presence of many lamellar Al + Si eutectic colonies. The primary Silicon growth is restricted as the discharging voltage increases leading to minimisation of Silicon depletion in the matrix. This trend is re-observed when the micrographs of the bottom portion of solidified alloys at higher magnifications are examined (Figure 3. 6 a – f). The Figure 3. 6 a is the micrograph corresponding to zero influence magnetic field on the solidification of the Al-20% Si. It reveals the formation of coarse acicular or lamellar eutectic Silicon in the matrix. When the careful microstructural survey is carried out from Figure 3. 6 a to Figure 3. 6 f, it is apparent that the coarse lamellar eutectic silicon is gradually transforming into finer lamellar eutectic structures. The finer lamellar structure further observed to transfigure into finest acicular structures at some regions of the microstructures. As the fine nature of the acicular structure of the primary Silicon takes place with increase in magnetic field intensity, the uniformity in the distribution of the Silicon in the matrix improves markedly. Later portion of the Figure 3. 6 exhibit the presence of virgin eutectic Al+ Si colonies with very fine acicular nature. This could be correlated to the minimisation of the Silicon depletion of the matrix, by the application magnetic field. The concerning heat treatment history of the analysed specimen relates to the solidification pattern of the bottom portion of the aforementioned alloy. The

possibility of variable Silicon percentage due to gravity assisted diffusion of the Silicon embryos during solidification can be analysed by means of careful reading of the microstructures of middle and top portions of the solidified alloy.

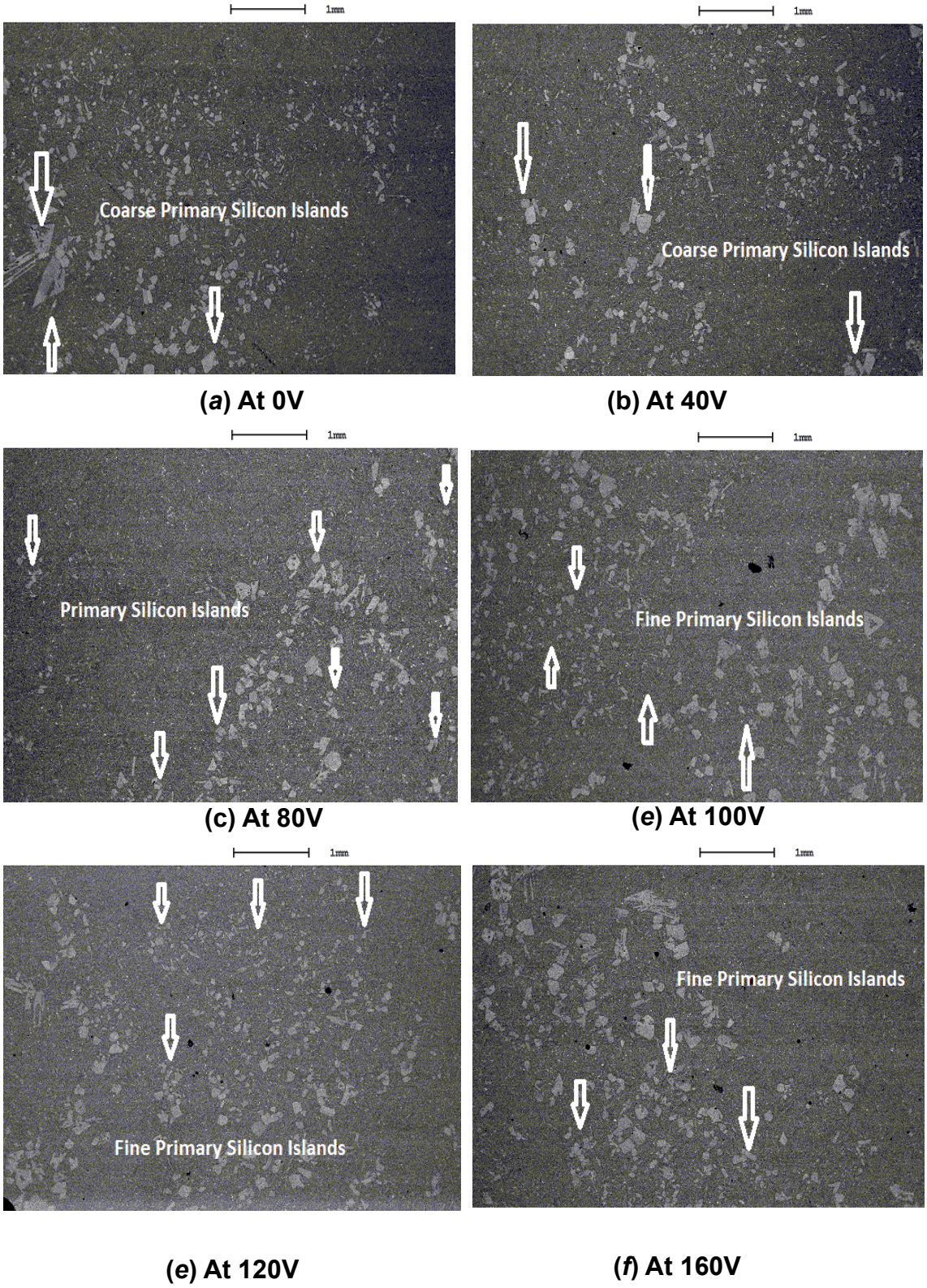

Figure 3. 7**:** The SEM micrographs of the ***middle part*** of the Al- 20%Si samples subjected to discharge voltages of a) 0V b) 40 V c) 80 V d) 100 V e) 120 V and f) 160 V at ***20 X*** magnification.

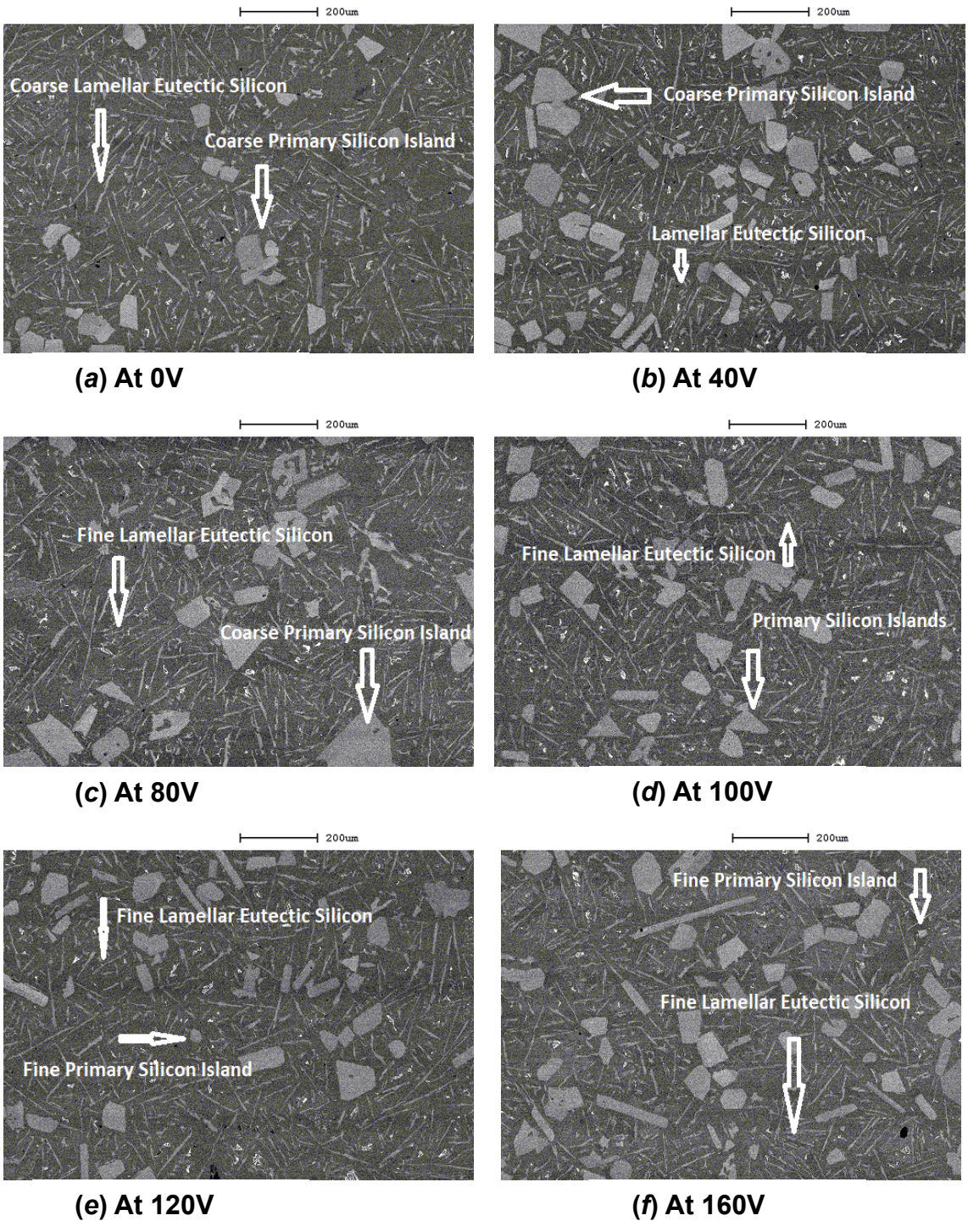

Figure 3. 8**:** The SEM micrographs of the ***middle part*** of the Al- 20%Si samples subjected to discharge voltages of a) 0V b) 40 V c) 80 V d) 100 V e) 120 V and f) 160 V at ***100 X*** magnification.

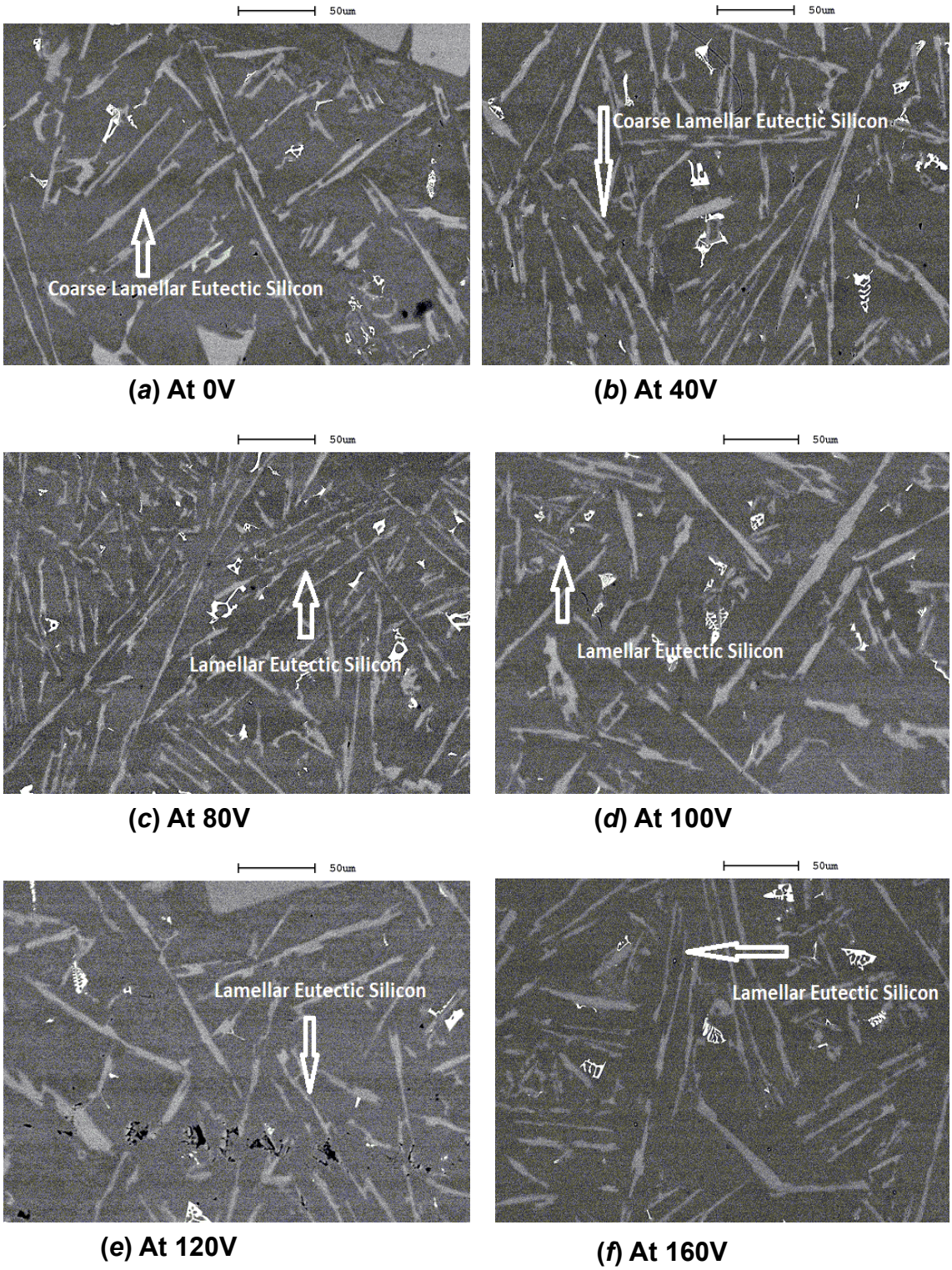

Figure 3. 9: The SEM micrographs of the ***middle part*** of the Al- 20%Si samples subjected to discharge voltages of a) 0V b) 40 V c) 80 V d) 100 V e) 120 V and f) 160 V at 40***0 X*** magnification.

Figure 3. 7 furnishes the SEM microstructures of middle portion of electromagnetic pulse assisted solidified Al- 20 Si alloy at 20 X magnification with aforementioned discharge voltage range. Figure 3. 6a shows the microstructure of the alloy corresponding to zero magnetic field influence on the solidification. It shows the presence of coarse primary silicon islands along with few short Silicon plate like structures. The proceeding microstructure Figure 3. 6b corresponding to the 40-discharging voltage, exhibits the presence of coarse primary Silicon islands as well as fine primary Silicon Island. Moreover, it does not contain the short primary Silicon plates indicating the transformation of plate like structures into small primary Silicon islands upon exposure to pulsed magnetic field during solidification. Further following micrographs (Figure 3. 6b-f) corresponding to increased discharging voltages (higher magnetic field intensity), reveal the gradual change in primary Silicon islands morphology into finer and finer leading to formation of refined primary Silicon islands as mini and micro islands. This clearly describes the refinement of primary Silicon islands into various structural morphologies like fine, finer, mini and micro islands. Again, this phenomenon of primary Silicon particles refinement can be attributed to the increase in the intensity of pulsed magnetic field.

Figure 3. 8 represents the SEM microstructures of middle portion of electromagnetic pulse assisted solidified Al- 20 Si alloy at 100 X magnification with various discharge voltages. Figure 3. 8 (a) is the microstructure of the alloy solidified without the influence of magnetic field, showing coarse primary Silicon islands as well as coarse lamellar eutectic Silicon. The following microstructures corresponding to increased discharging voltages show the presence of coarse primary Silicon islands and fine lamellar eutectic Silicon (Figure 3. 8 b, c and d). Further, the microstructures of higher discharging voltage reveal the presence of fine primary Silicon Island and fine lamellar eutectic Silicon (Figure 3. 8 e and f). This indicates one of the important inferences of this study, exhibiting the refinement in the case primary Silicon particles as well as the eutectic Al + Si acicular structures. In turn, the Silicon distribution in the matrix is greatly improved by the application of pulsed magnetic field. This observation is well

supported by Figure 3.8 illustrating the SEM microstructures of middle portion of electromagnetic pulse assisted solidified Al- 20 Si alloy at 400 X magnification. Careful observation (figure 3.8a-f) show that the interlamellar distance of eutectic Silicon decreases with increase in magnetic field intensity, stating that the magnetic field application led to the refinement of lamellar structure of eutectic Silicon.

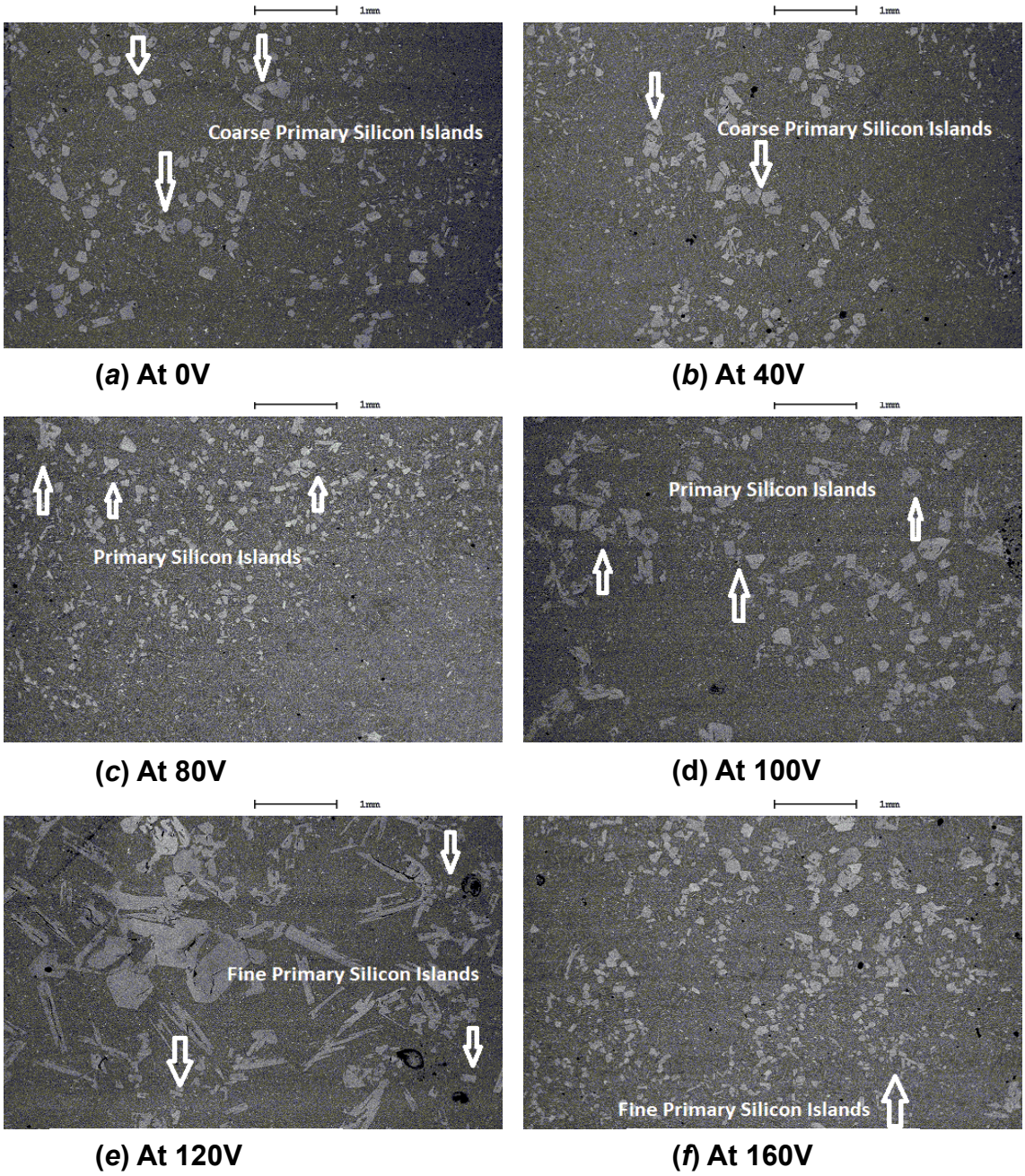

Figure 3. 10**:** The SEM micrographs of the ***top part*** of the Al- 20%Si samples subjected to discharge voltages of a) 0V b) 40 V c) 80 V d) 100 V e) 120 V and f) 160 V at ***20 X*** magnification.

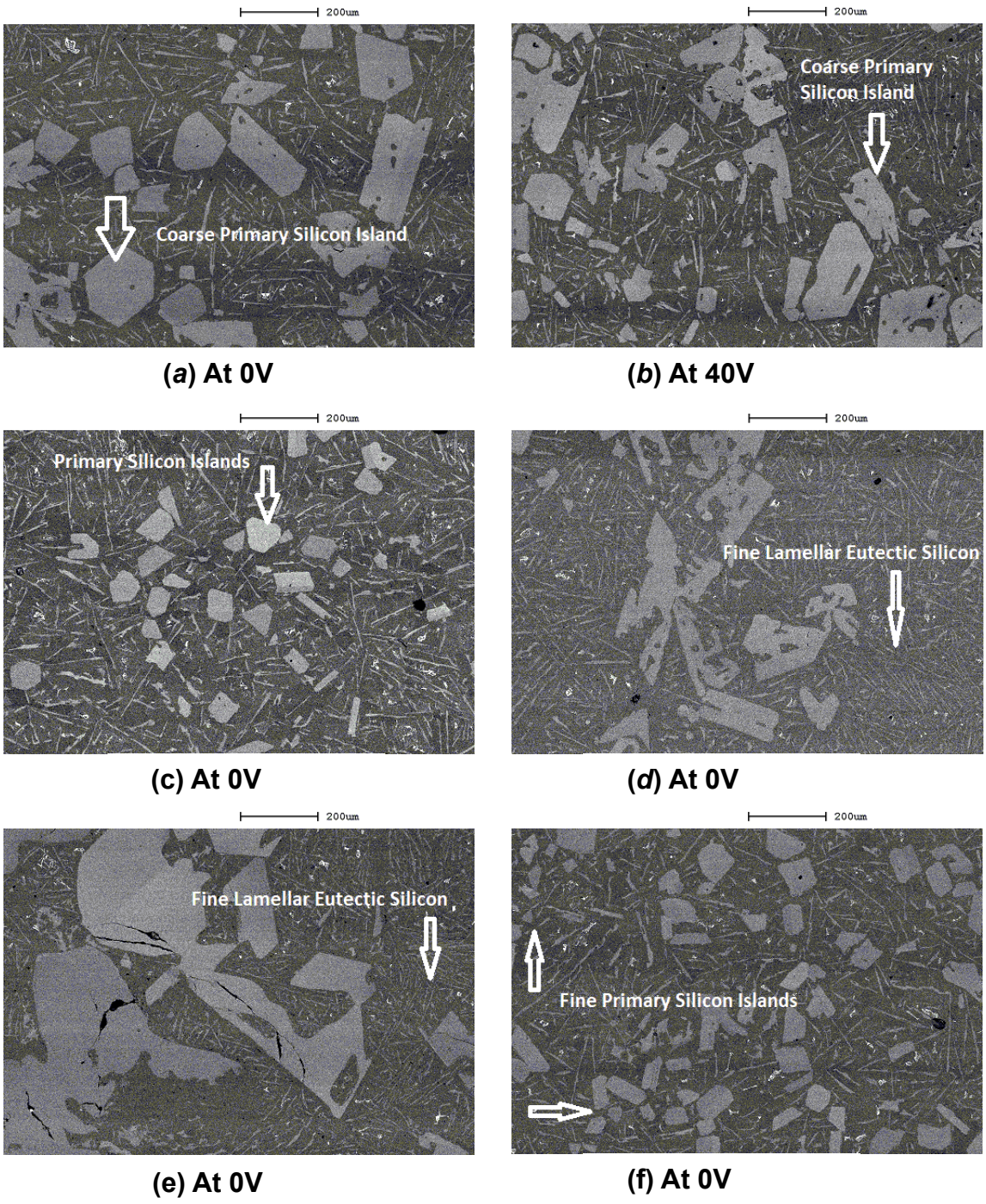

Figure 3. 11**:** The SEM micrographs of the ***top part*** of the Al- 20%Si samples subjected to discharge voltages of a) 0V b) 40 V c) 80 V d) 100 V e) 120 V and f) 160 V at ***100 X*** magnification.

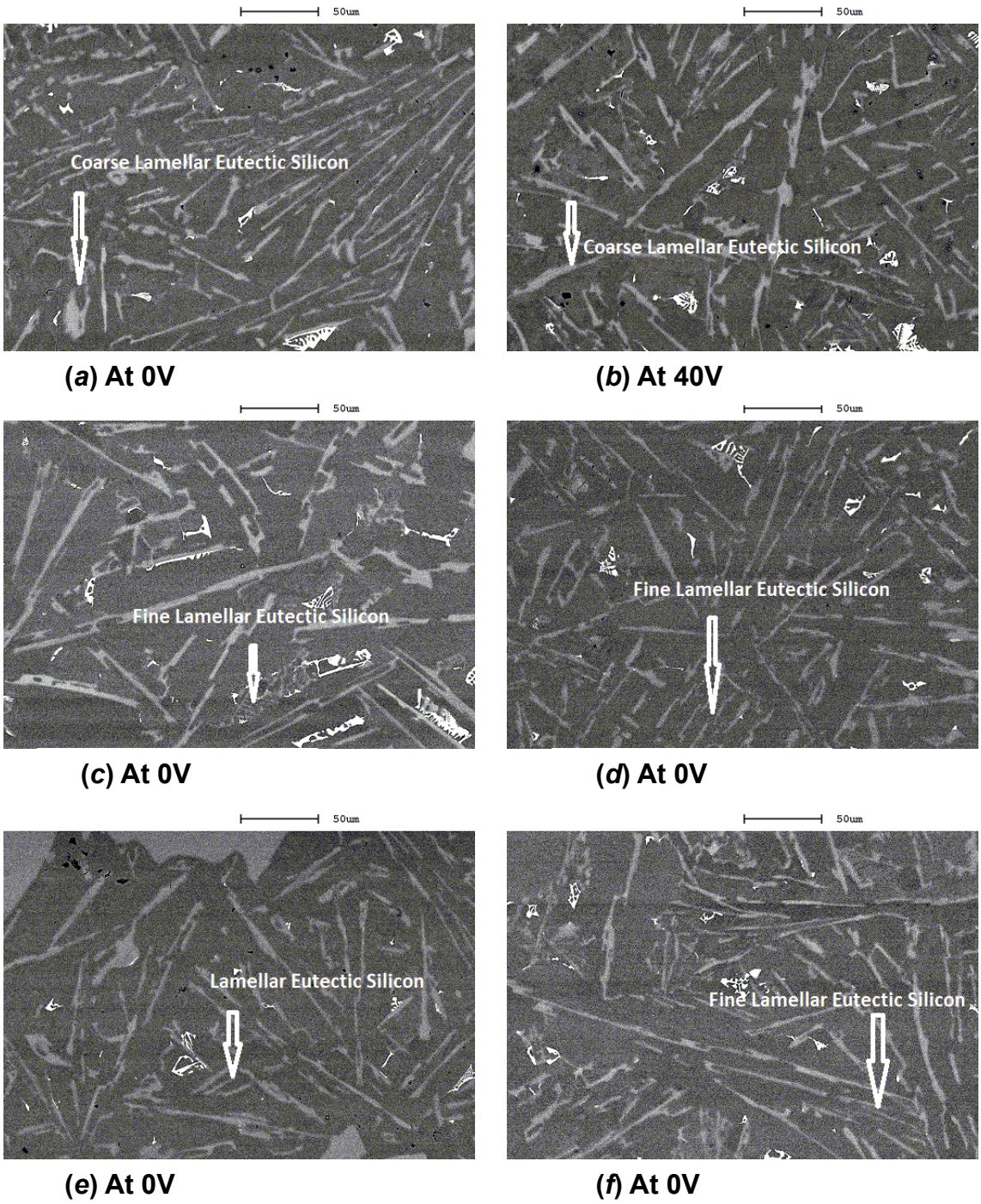

Figure 3. 12**:** The SEM micrographs of the ***top part*** of the Al- 20%Si samples subjected to discharge voltages of a) 0V b) 40 V c) 80 V d) 100 V e) 120 V and f) 160 V at ***400 X*** magnification.

Figure 3. 10, Figure 3. 11 and Figure 3. 12 demonstrate the SEM microstructures of top portion of electromagnetic pulse assisted solidified Al-20% Si alloy at various magnifications with variation in discharge voltages. The analysis of these microstructures show that there is a similarity of microstructural changes with respect to variation in pulsed magnetic field intensity between the middle portion and the top portion of the solidified alloy. The microstructural evaluations of top portion of the solidified alloy also reveal the refinement in the case of primary Silicon islands and lamellar eutectic Silicon structures. The coarse primary Silicon islands transform into fine, finer, mini and micro islands due to the increase in magnetic field intensity. Similarly, the decrease in interlamellar spacing of eutectic Silicon structures are observed as the discharging voltage increases. A study reported that the high magnetic field intensities can promote the reduction in the secondary dendrite arm spacing (SDAS) of the primary Al dendrites and the inter lamellar spacing (ILS) of the eutectic phase [148]. Moreover, the spotting of lamellar eutectic Silicon colonies of very fine nature give rise to following statements; The application of magnetic field directly influences the solidification pattern of the alloy by restricting the formation of massive primary Silicon plate like structures and coarser Primary Silicon islands. Hence the enrichment of Silicon atoms in the molten liquid further results in increase of quantitative nature of the eutectic Al+ Si acicular structures in the matrix. This in turn increase the uniform distribution of Silicon in the alloy matrix.

A similar research reported that the details of influence of magnetic field application on the microstructural features; the grain refinement takes place in primary α and in the eutectic Al + Si phase. In addition, it develops an adverse effect on the growth of eutectic α and its epitaxial growth, promoting the finer primary α phase formation. The segregation of Si in solid front is suppressed by the presence of magnetic field. The size of the eutectic phase colonies is attributed to the intensity of magnetic field. The inter-dendritic segregation is restricted and interlamellar Silicon segregation is promoted [149], [150]. In comparative study, the microstructures of the bottom portion of the alloy contains additional features as massive primary Silicon plate like

structures besides from the coarse primary Silicon islands and eutectic lamellar structures observed in the middle and top portions of the pulsed magnetic field assisted solidified alloy. The EDAX spectrum of the pulsed magnetic field aided solidified alloy at the aluminium matrix and bulk locations are depicted in Figure 3. 13. Figure 3.12a shows the only peak corresponding to Aluminium in primary α phase surrounded by the primary Silicon as well as the eutectic phase. Figure 3.12b shows the peaks of both Aluminium and Silicon with appropriate lengths according to the mass fractions of the designed alloy. The bulk analysis indicates the uniformity in the Silicon distribution well within the matrix.

Figure 3. 14 represents the EDAX spectrums of the pulsed magnetic field assisted solidified alloy at a) 40 V b) 160 V. The eutectic regions of the alloys solidified at different discharging voltages are chosen for the elemental analysis. The corresponding peaks observation reveal that the application of the magnetic field leads to the refinement in the eutectic lamellar or acicular Al + Si structure.

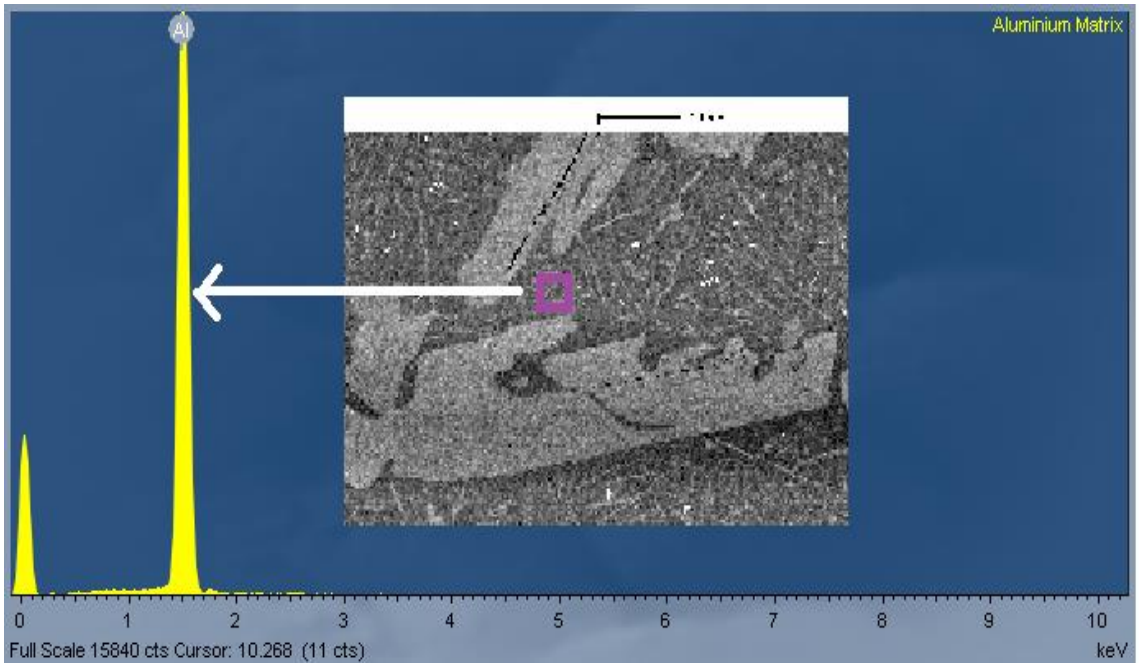

(*a*)

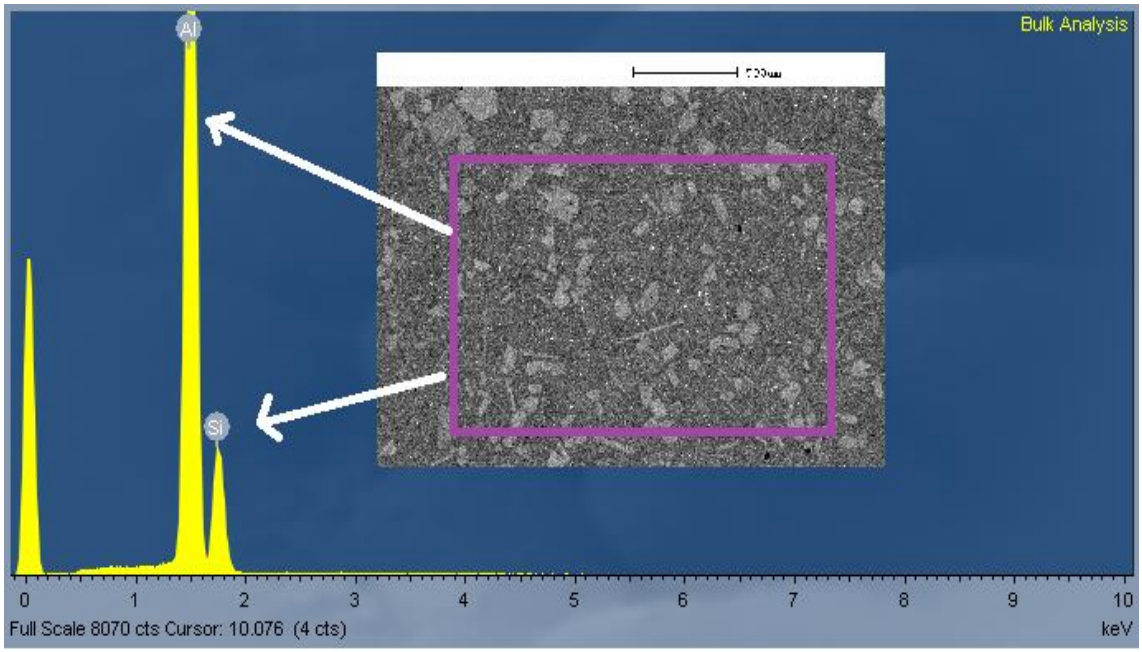

(*b*)

Figure 3. 13**:** represents the EDAX spectrums of the Pulsed magnetic field assisted solidified alloy analysed at regions namely a) Aluminium matrix b) Bulk region

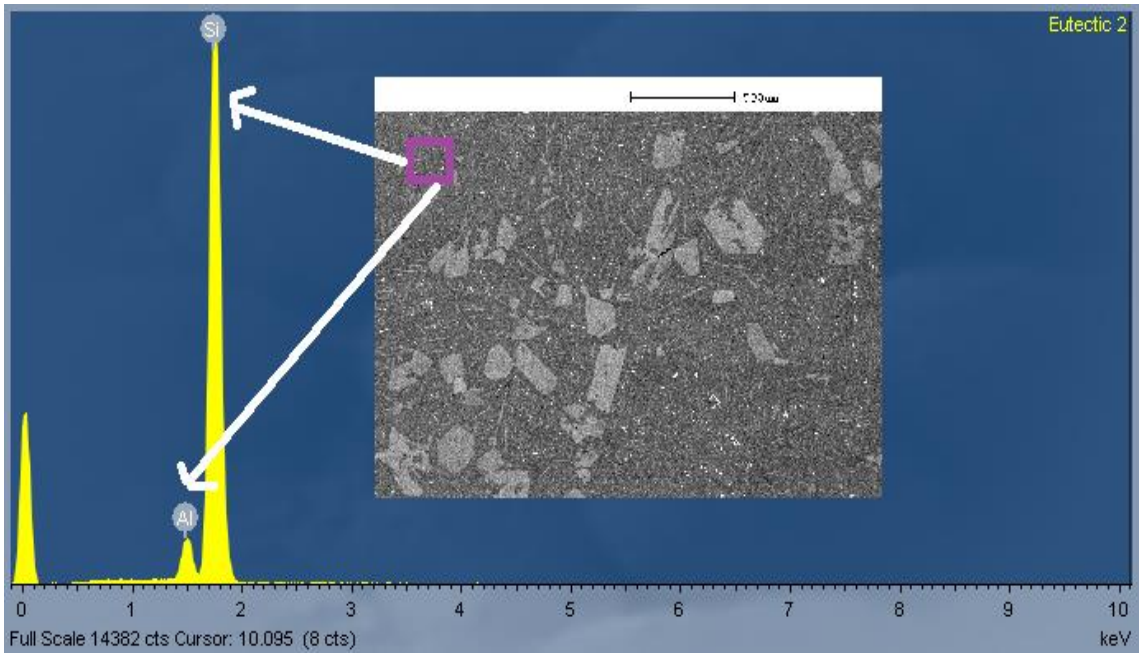

(***a***)

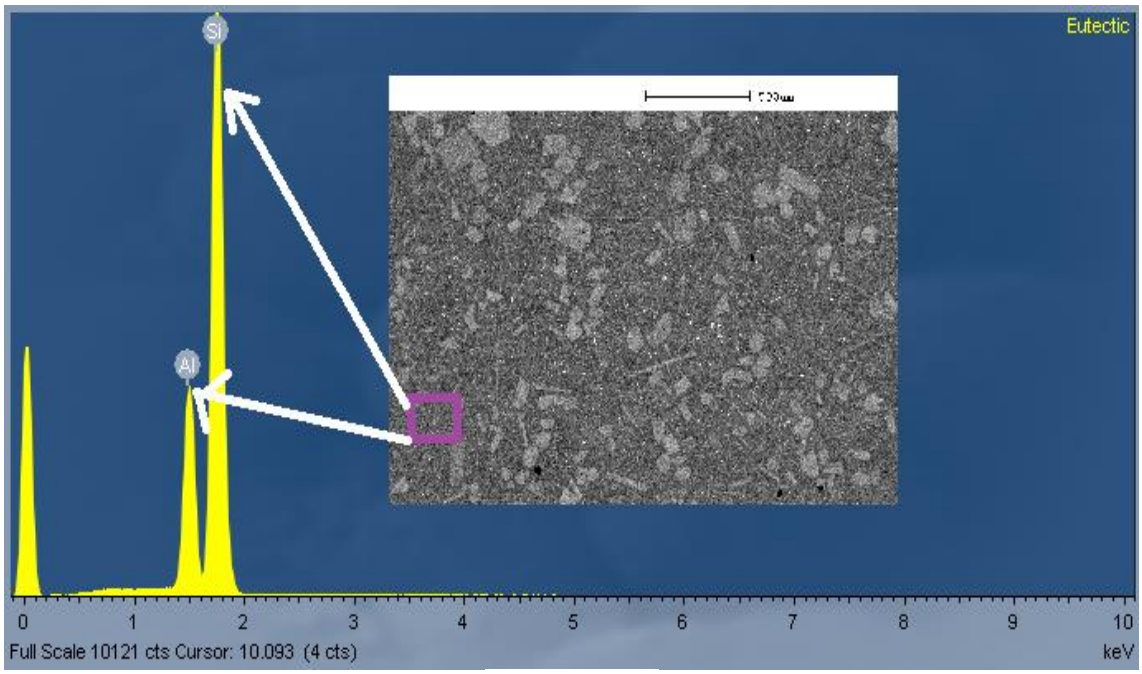

(***b***)

Figure 3. 14: represents the EDAX spectrums of the Pulsed magnetic field assisted solidified alloy analysed at a) 40 V b) 160 V.

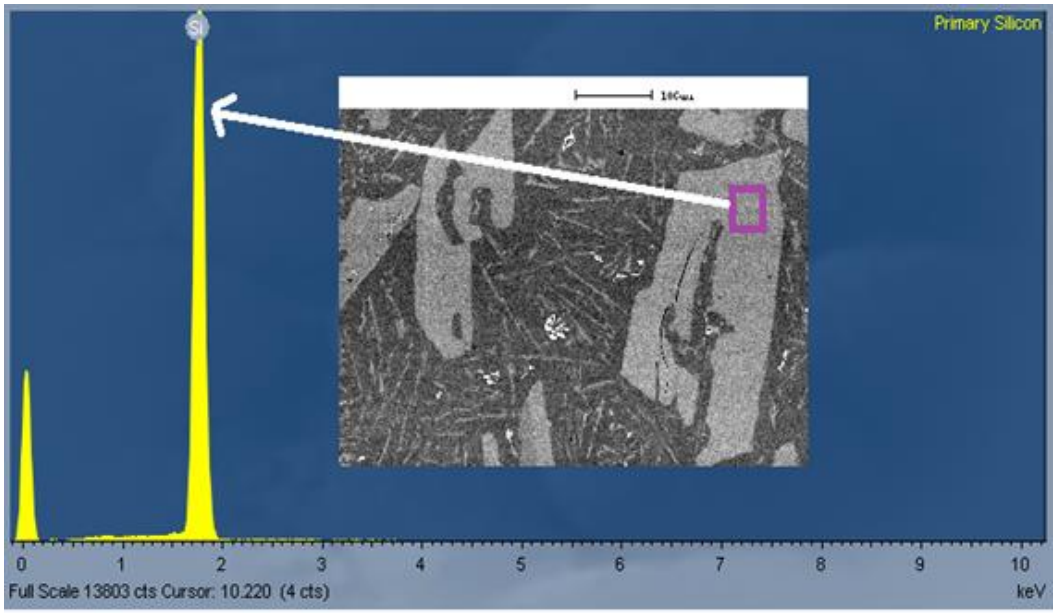

Figure 3. 15**:** represents the EDAX spectrums of the Pulsed magnetic field assisted solidified alloy analysed at primary Silicon region.

3.5 Particle size measurements

Average grain size by area [151] is one of the standard methods for grain size measurements. In this work, average grain size (i.e. area) from the SEM images is calculated. Along a straight region of the micrograph, 10 to 20 adjacent grains are isolated one by one and the area calculation is carried out. Extreme care is taken into consideration while isolation of each grain by boundary marking.

Figure 3.15 and figure 3.16 show the images for grain size measurement. At first, selected grains were isolated with a hand delineation tool. Then the isolated area was measured by the area counting function. Such measurement was applied to 10 to 20 adjacent grains of the selected.

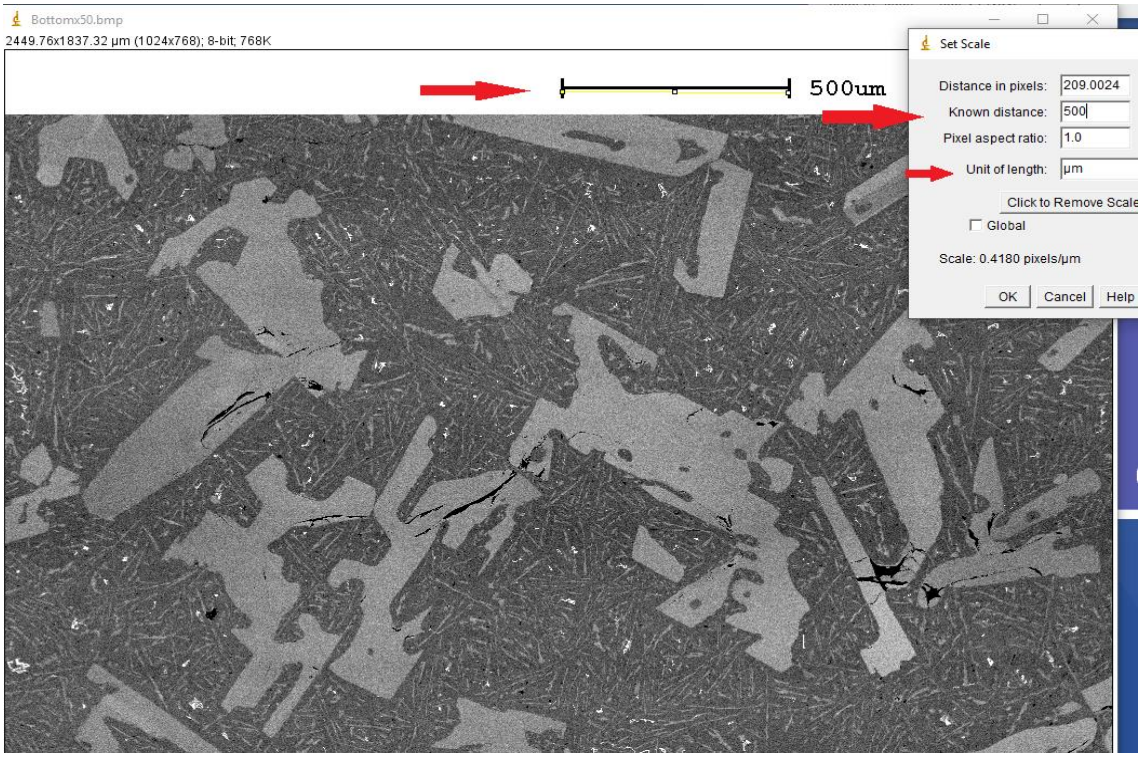

Figure 3. 16: The Calibration of the pixel size

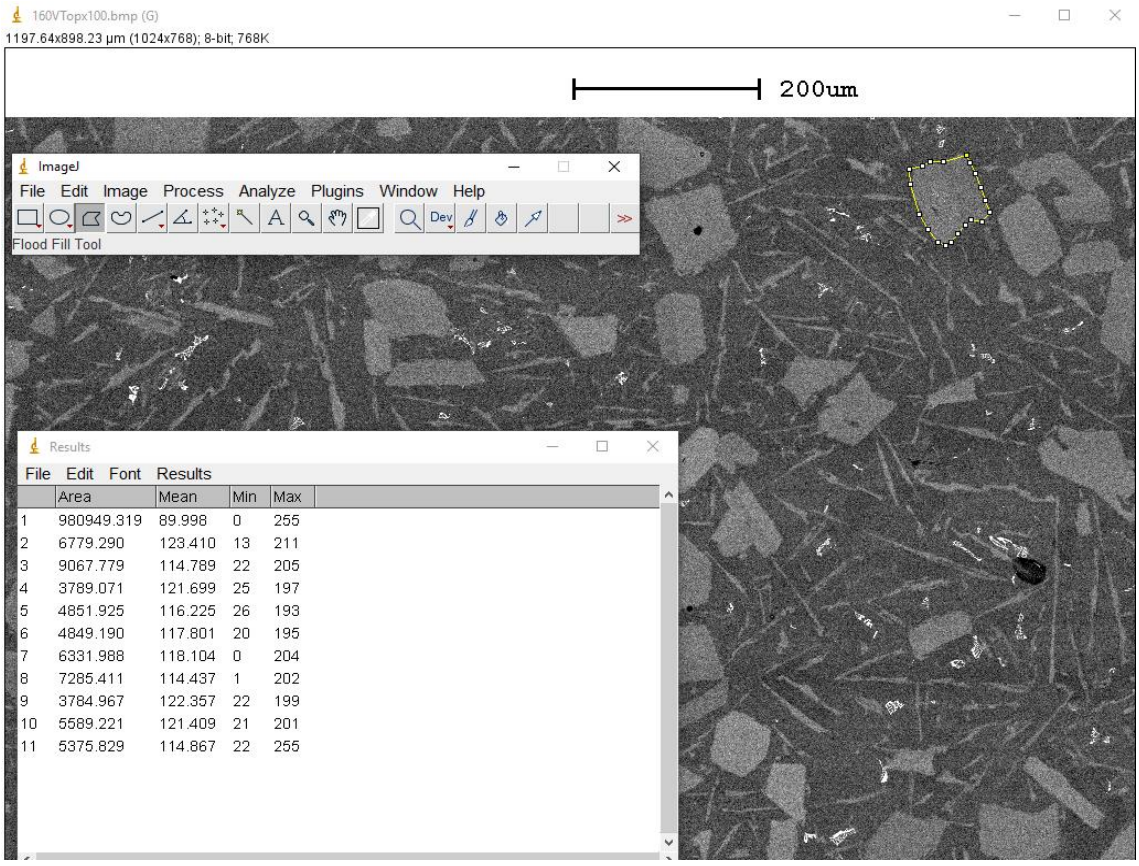

Figure 3. 17: The measurements of the primary Si particles areas

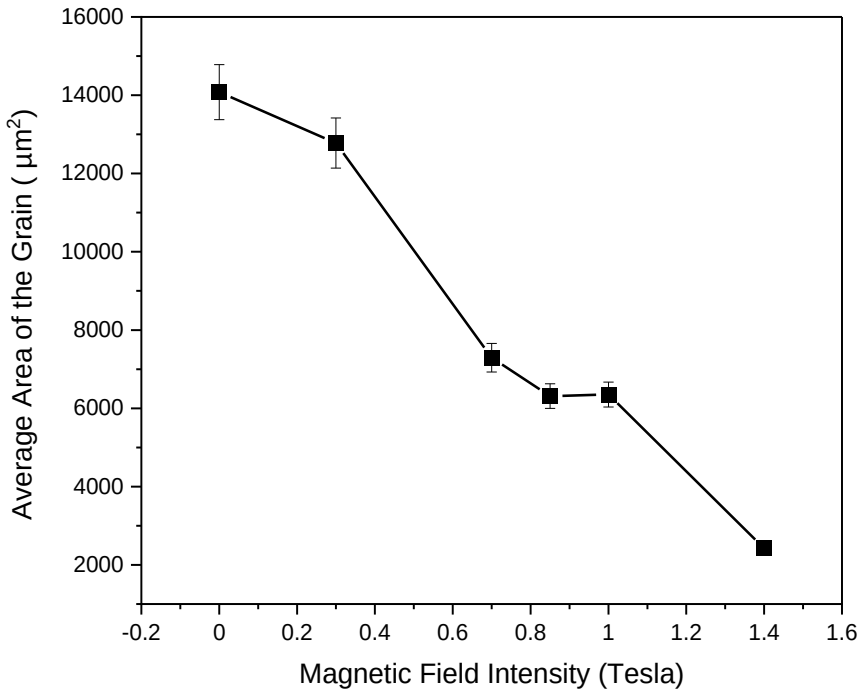

Figure 3. 18: The relationship between the primary Si particles size (Area) and the magnetic flux density

.

Figure 3. 18 show the variation of grain size with magnetic field intensity. The initial observation show that the average grain size measured of the alloy that was solidified without the influence of any magnetic field is relatively larger when compared to that of the average grain size of magnetic field induced solidified alloys. As the magnetic field is introduced during the solidification process, the grain size happens to be refined gradually with increase in magnetic field intensity. The approximate percentage reduction in grain size at 0.3 Tesla is 10%, at 0.7 Tesla, the same is increased to 48 %, at 0.85 Tesla and 1Tesla, the size reduction in Si grains are observed to be 55 % and maximum of 82 % reduction is noticed at 1.4 Tesla. Figure 3. 19 show the clear transformation of microstructural morphologies with respect to magnetic field intensity variation.

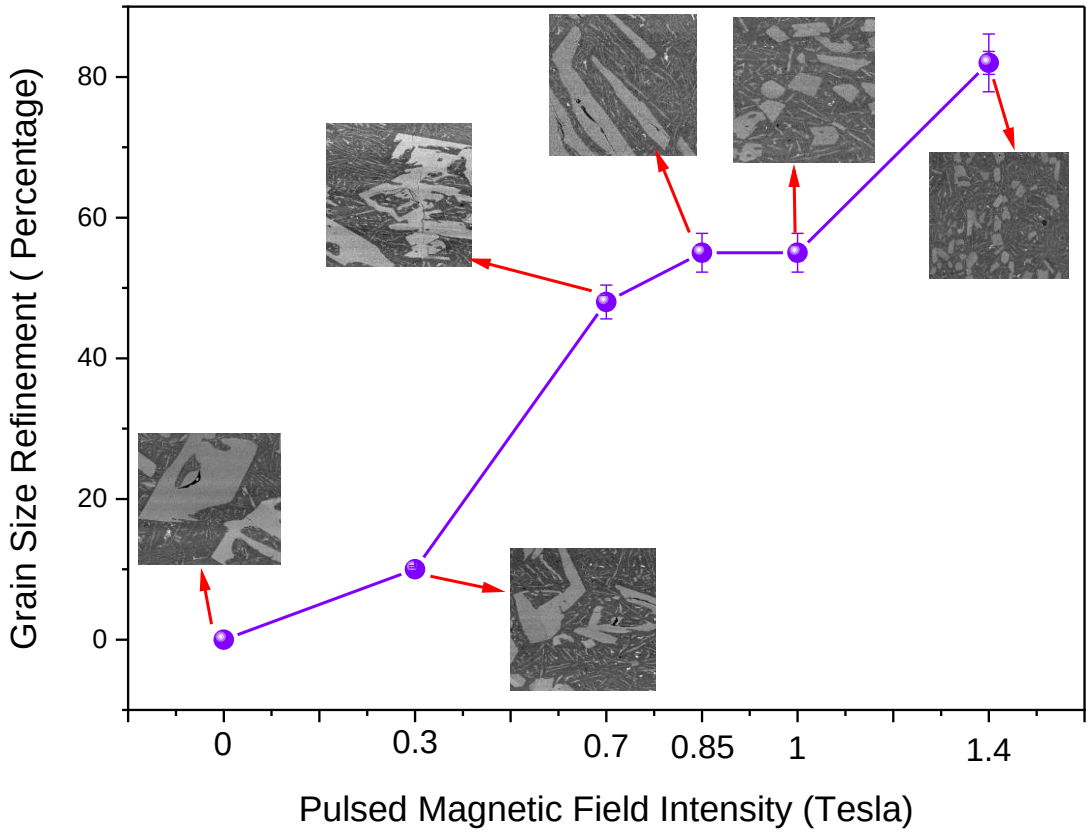

Figure 3. 19: The relative change of primary Si particle size as a function of magnetic flux density.

From figure 3.12 to figure 3.14, the EDAX spectrum of micrographs of pulsed magnetic field assisted solidified alloys revealed that the uniformity in the distribution of Silicon atoms in the morphology of Aluminium matrix is improved to a greater level as the intensity of the magnetic field is raised. The larger primary Silicon grains present in the solidified Al- Si alloy without the influence of magnetic field, gradually transform into macro, mini, micro primary Silicon Islands as the solidifying alloys are exposed to pulsed magnetic field. It is registered that at 1.4 Tesla, the pulsed magnetic field intensity is high and leads to maximum grain refinement in primary Silicon islands. In addition, figure 3.26 show the gradual transformations in microstructural features of the alloy during solidification with respect to varying pulsed magnetic field intensity.

3.6 Micro hardness measurements

Vickers micro hardness measurements were carried out using Vickers hardness testing machine (Leitz Wetzlar Germany, Model-8295). In general, the micro hardness measurement involves making an indentation mark on the alloy surface of examination by means of a diamond indenter or Knoop indenter resulting in an indentation having two diagonals x and y as shown in Figure 3. 20.

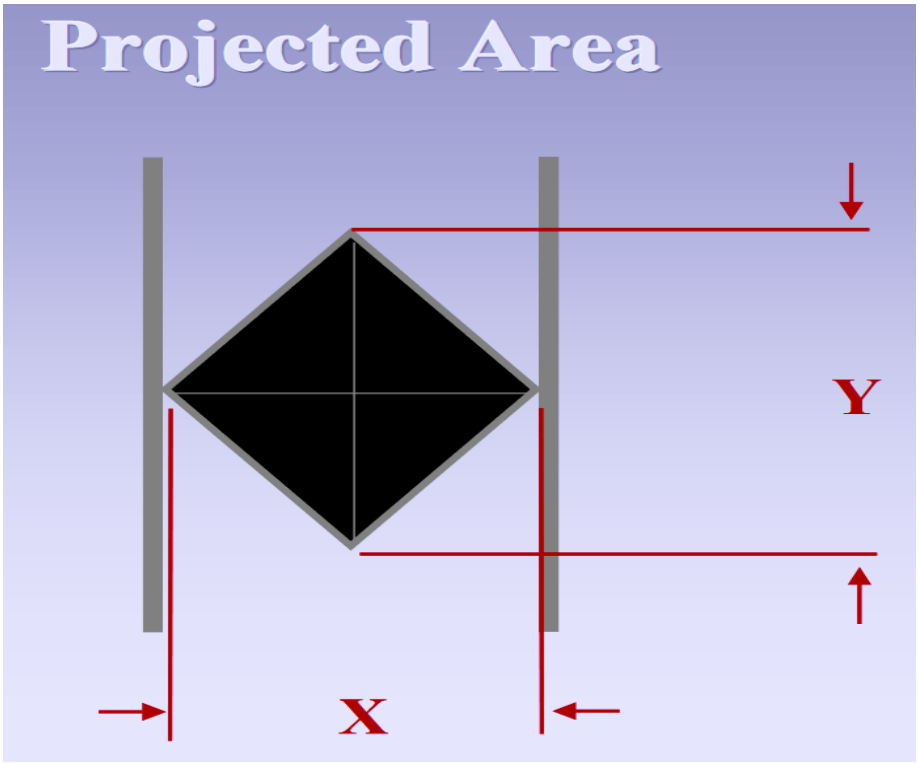

Figure 3. 20: The indentation mark with two diagonals x and y.

Figure 3.28 to figure 3.33 show the indentations performed and captured on the alloy specimens solidified with and without the influence of pulsed magnetic field. The corresponding Vickers hardness data are registered and furnished in Table 3. 2 to Table 3.13

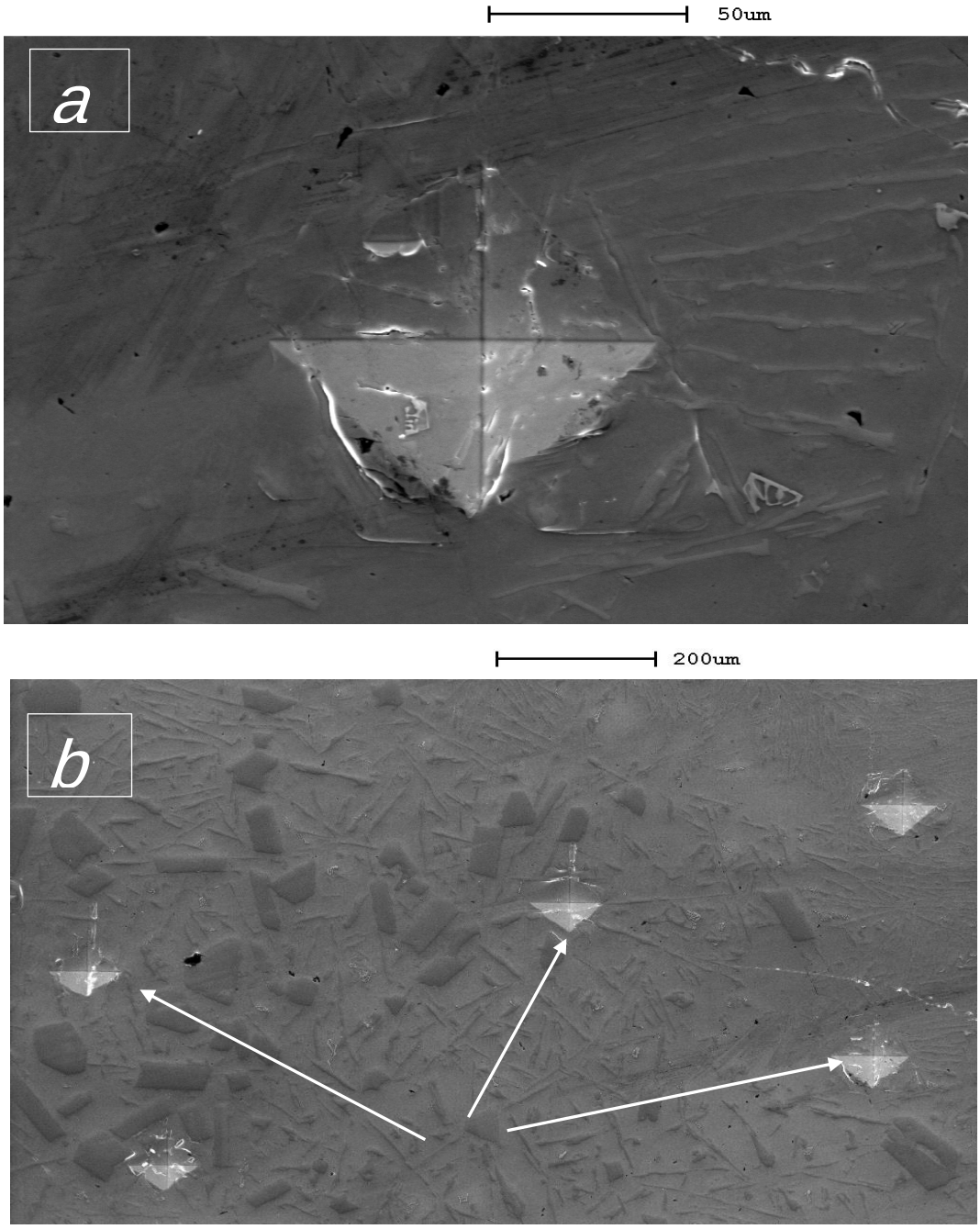

Figure 3. 21: The indentation picture on the Al-20% Si solidified without the exposure to pulsed magnetic field, a) at higher b) at lower magnifications.

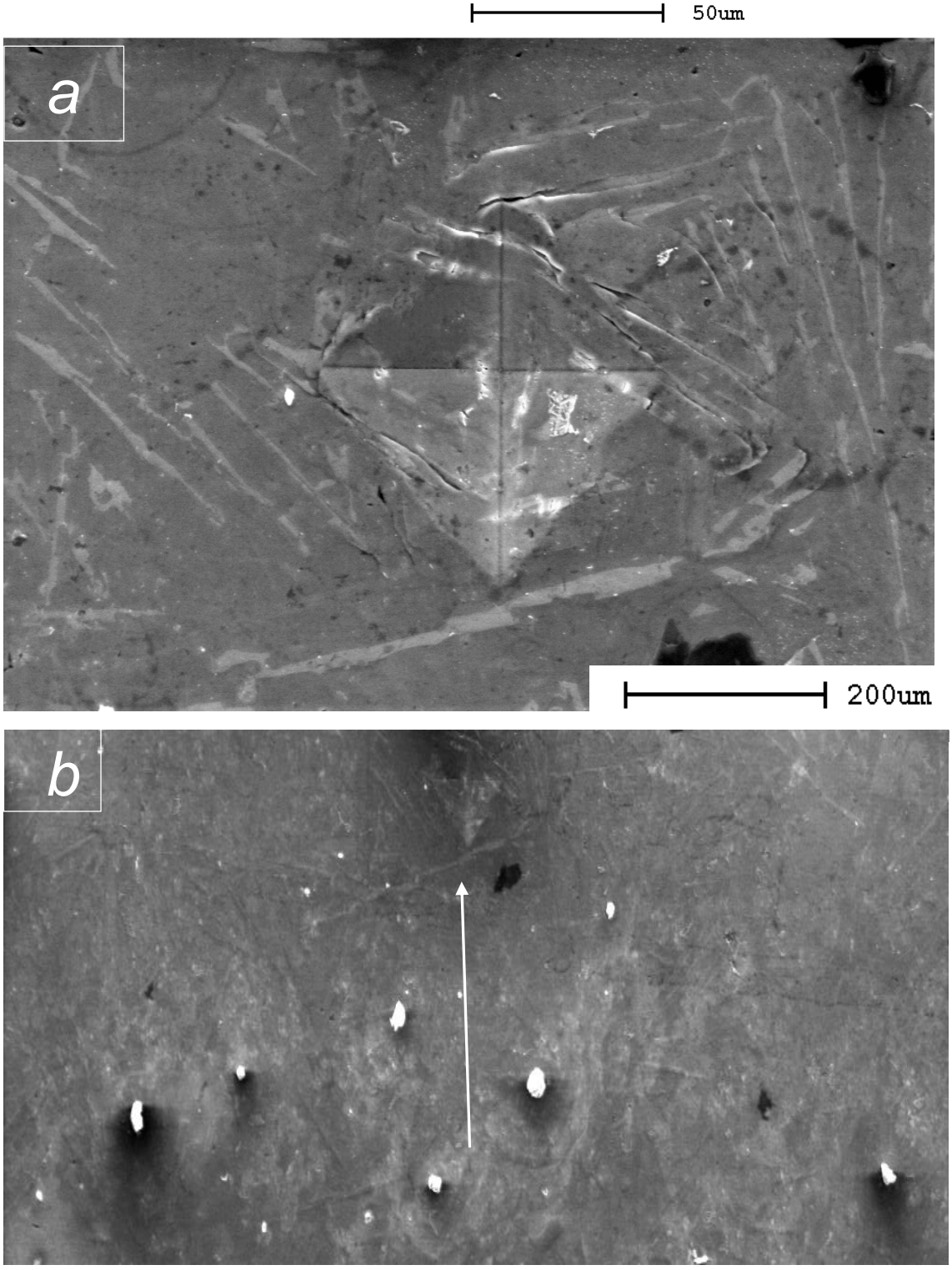

Figure 3. 22: The indentation picture on the Al-20% Si solidified with the exposure to pulsed magnetic field at 0.3 Tesla, a) at higher b) at lower magnifications.

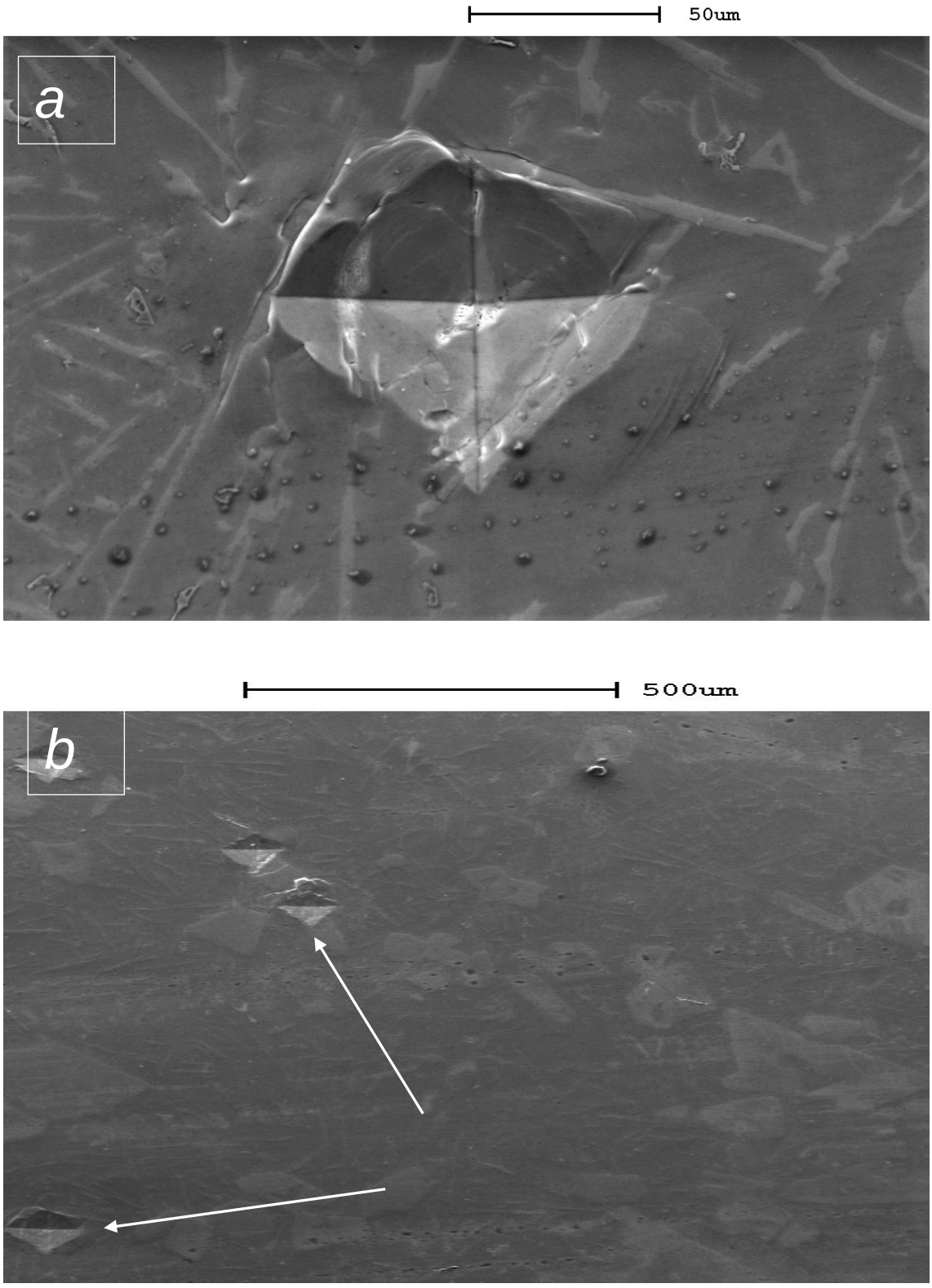

Figure 3. 23: The indentation picture on the Al-20% Si solidified with the exposure to pulsed magnetic field at 0.7 Tesla, a) at higher b) at lower magnifications

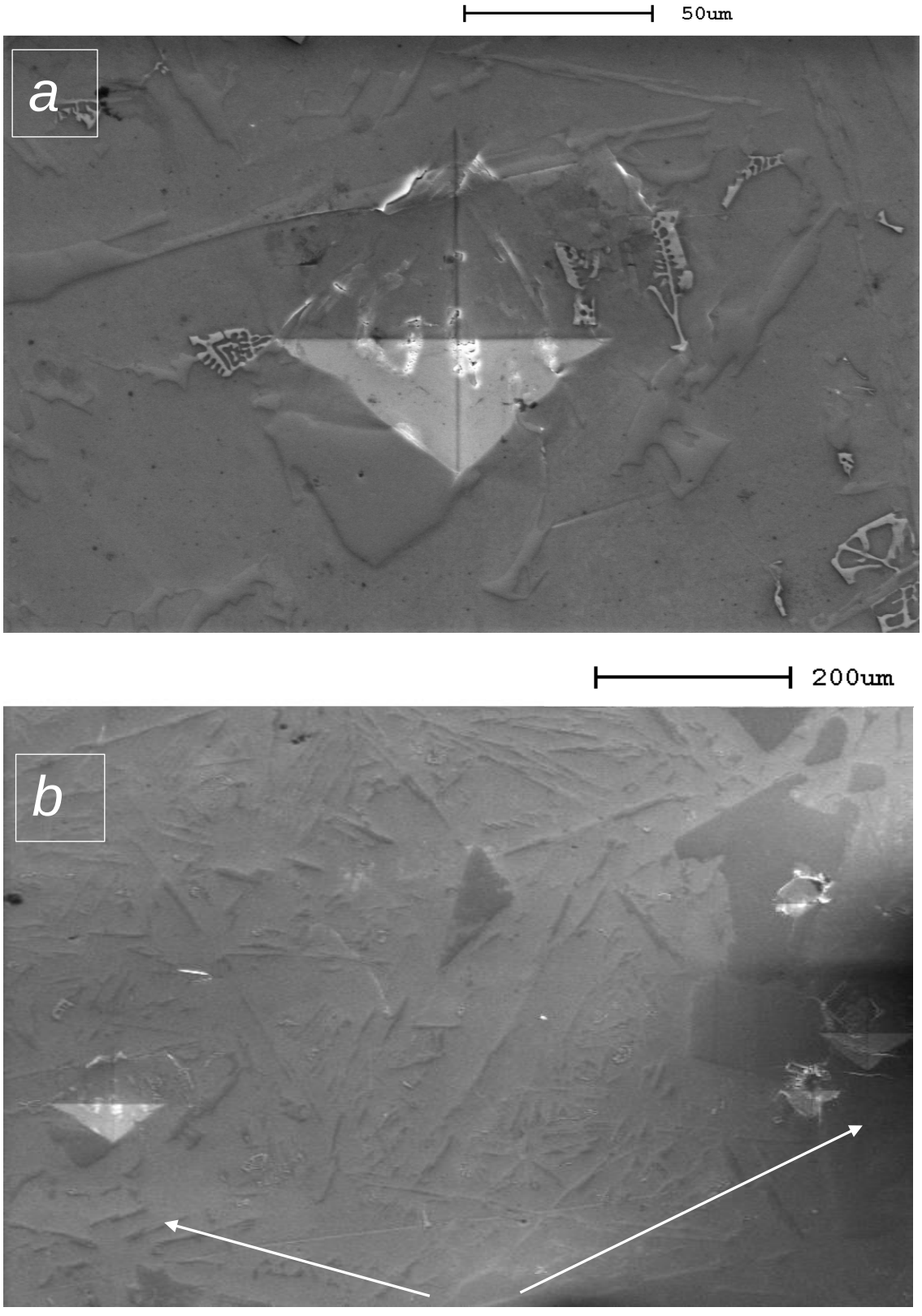

Figure 3. 24: The indentation picture on the Al-20% Si solidified with the exposure to pulsed magnetic field at 0.85 Tesla, a) at lower b) at higher magnifications.

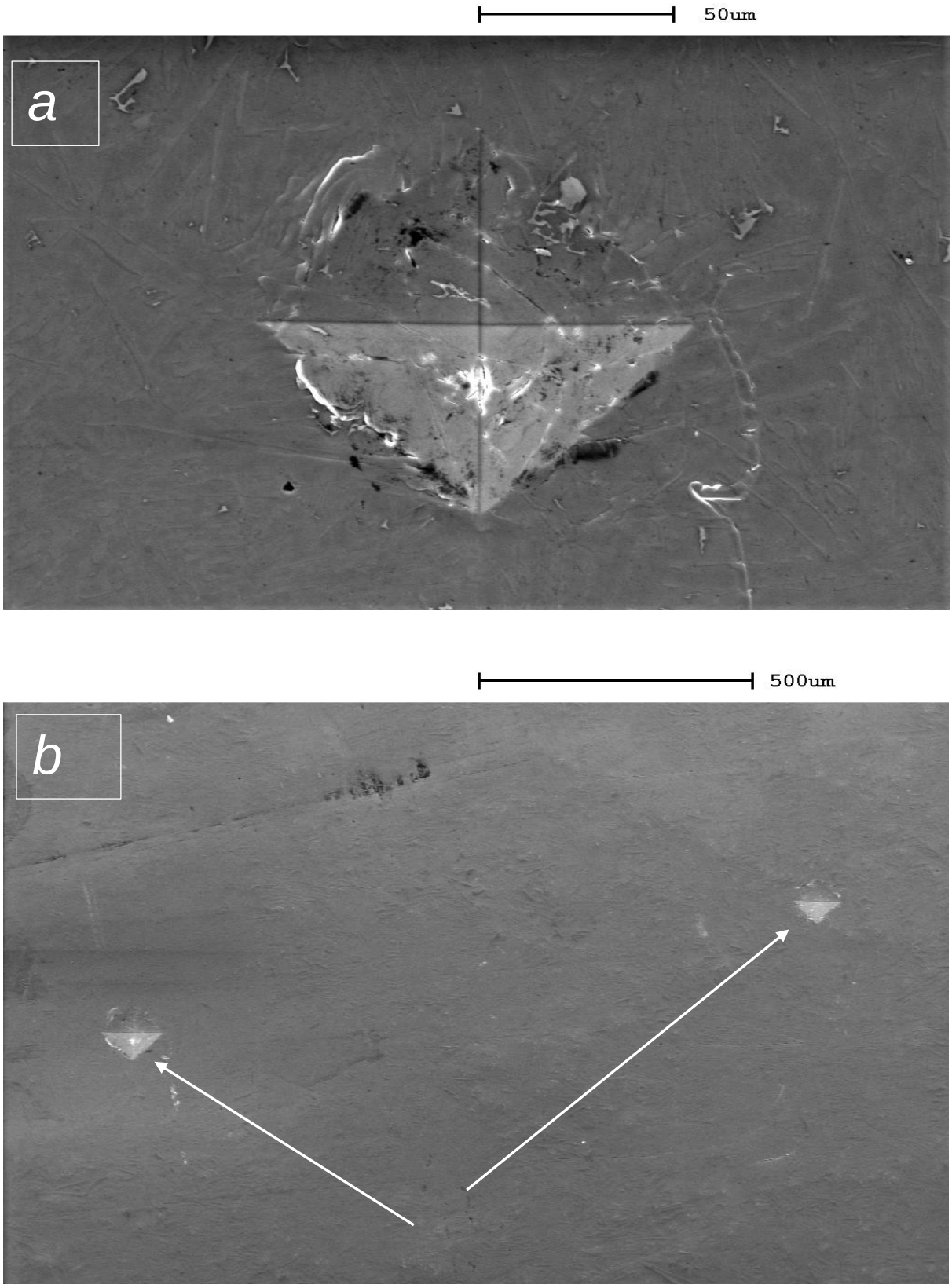

Figure 3. 25 : The indentation picture on the Al-20% Si solidified with the exposure to pulsed magnetic field at 1 Tesla, a) at higher b) at lower magnifications.

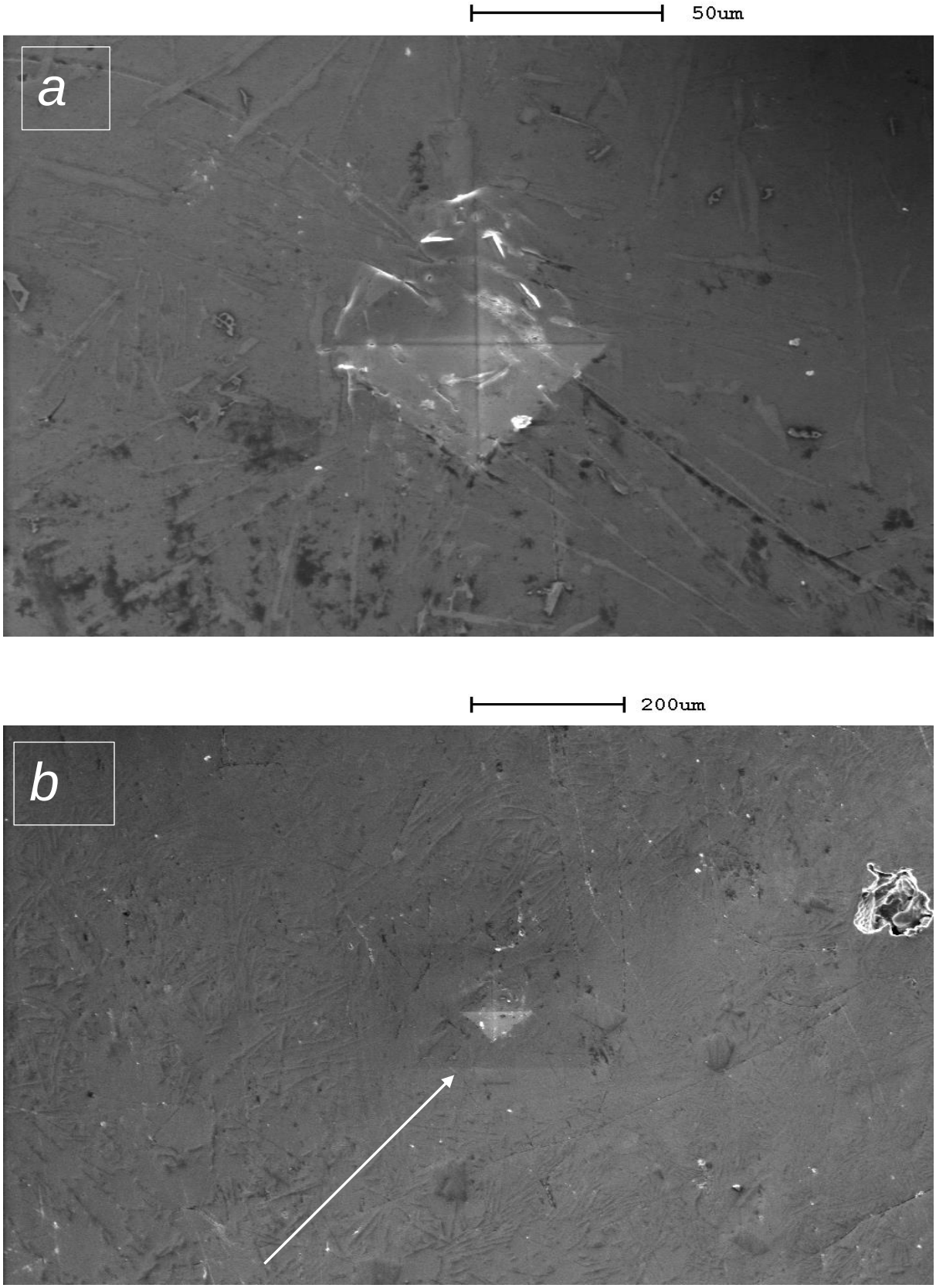

Figure 3. 26**:** The indentation picture on the Al-20% Si solidified with the exposure to pulsed magnetic field at 1.4 Tesla, a) at higher b) at lower magnifications.

Table 3. 2: The indentation data and hardness of Al-20 Si alloy solidified with 0 Tesla (Load = 0.3kgf and Dwell time of 15 seconds)

S.No	Diagonal Length X (µm)	Diagonal Length Y (µm)	Mean diagonal Length d (µm)	Hardness Vickers (VHN)
1	95	92	93.5	63.7
2	100	98	99	56.2
3	101	102	101.5	54
4	103	100	101.5	54
5	107	105	106	49.5
6	93	96	94.5	62.3
7	101.5	97.5	99.5	56.2
8	94	89	91.5	66.5
9	67	67	67	124
10	95	97	96	60.4
Average				**64.68**

Table 3. 3: The indentation data and hardness of Al-20 Si alloy solidified with the exposure of pulsed magnetic field at 0.3 Tesla (Load = 0.3kgf and Dwell time of 15 seconds)

S.No	Diagonal Length X (µm)	Diagonal Length Y (µm)	Mean diagonal Length d (µm)	Hardness Vickers (VHN)
1	120	100	110	46
2	100	98	99	56.8
3	96	100	98	57.9
4	95	103	99	56.8
5	93	95	94	63
6	104	101.5	102.75	52.9
7	76	69	72.5	106
8	64	72	68	120
9	99	93	96	60.4
10	98	99	97	57.1
Average				**67.69**

Table 3. 4: The indentation data and hardness of Al-20 Si alloy solidified with the exposure of pulsed magnetic field at 0.7 Tesla (Load = 0.3kgf and Dwell time of 15 seconds)

S.No	**Diagonal Length X** (µm)	**Diagonal Length Y** (µm)	**Mean diagonal Length d** (µm)	**Hardness Vickers (**VHN)
1	90	88	89	70.2
2	108	110	109	46.8
3	66	84	75	98.9
4	80	77	78.5	90.4
5	93	98	95.5	61.1
6	80	80	80	86.9
7	88	82	85	77
8	90	86	88	71.1
9	88	84	86	75.2
10	89	89	89	70.2
Average				**74.78**

Table 3. 5: The indentation data and hardness of Al-20 Si alloy solidified with the exposure of pulsed magnetic field at 0.85 Tesla (Load = 0.3kgf and Dwell time of 15 seconds)

S.No	**Diagonal Length X** (µm)	**Diagonal Length Y** (µm)	**Mean diagonal Length d** (µm)	**Hardness Vickers (**VHN)
1	94	95	64.5	62.3
2	86	71	69.5	115
3	89	95	92	65.7
4	93	100	96.5	59.8
5	75	79	77	93.8
6	78	75	76.5	63.4
7	80	70	75	65.9
8	72	76	74	67.7
9	76	68	72	71.5
10	94	95	64.5	62.3
Average				**73.9**

Table 3. 6: The indentation data and hardness of Al-20 Si alloy solidified with the exposure of pulsed magnetic field at 1 Tesla (Load = 0.3kgf and Dwell time of 15 seconds)

S.No	Diagonal Length X (µm)	Diagonal Length Y (µm)	Mean diagonal Length d (µm)	Hardness Vickers (VHN)
1	121.5	118	120	64
2	95	90.2	92.5	65.1
3	100.5	102.5	101.5	54
4	103	110	106	49.1
5	105	98.5	101.75	53.75
6	100.5	99.5	100	55.6
7	86	82	84	78.8
8	71	68	69.5	115
9	65.5	67.5	66.5	126
Average				**73.48333**

Table 3. 7: The indentation data and hardness of Al-20 Si alloy solidified with the exposure of pulsed magnetic field at 1.4 Tesla (Load = 0.3kgf and Dwell time of 15 seconds)

S.No	Diagonal Length X (µm)	Diagonal Length Y (µm)	Mean diagonal Length d (µm)	Hardness Vickers (VHN)
1	76	72	74	67.7
2	72	68	70	75.7
3	80	81	80.5	57.2
4	71	73	72	71.5
5	56	60	58	110
6	70	74	72	71.5
7	68	64	66	85.1
8	70	65	67.5	81.2
9	72	66	69	77.9
11	82	85	83.5	53.2
AVERAGE				**75.1**

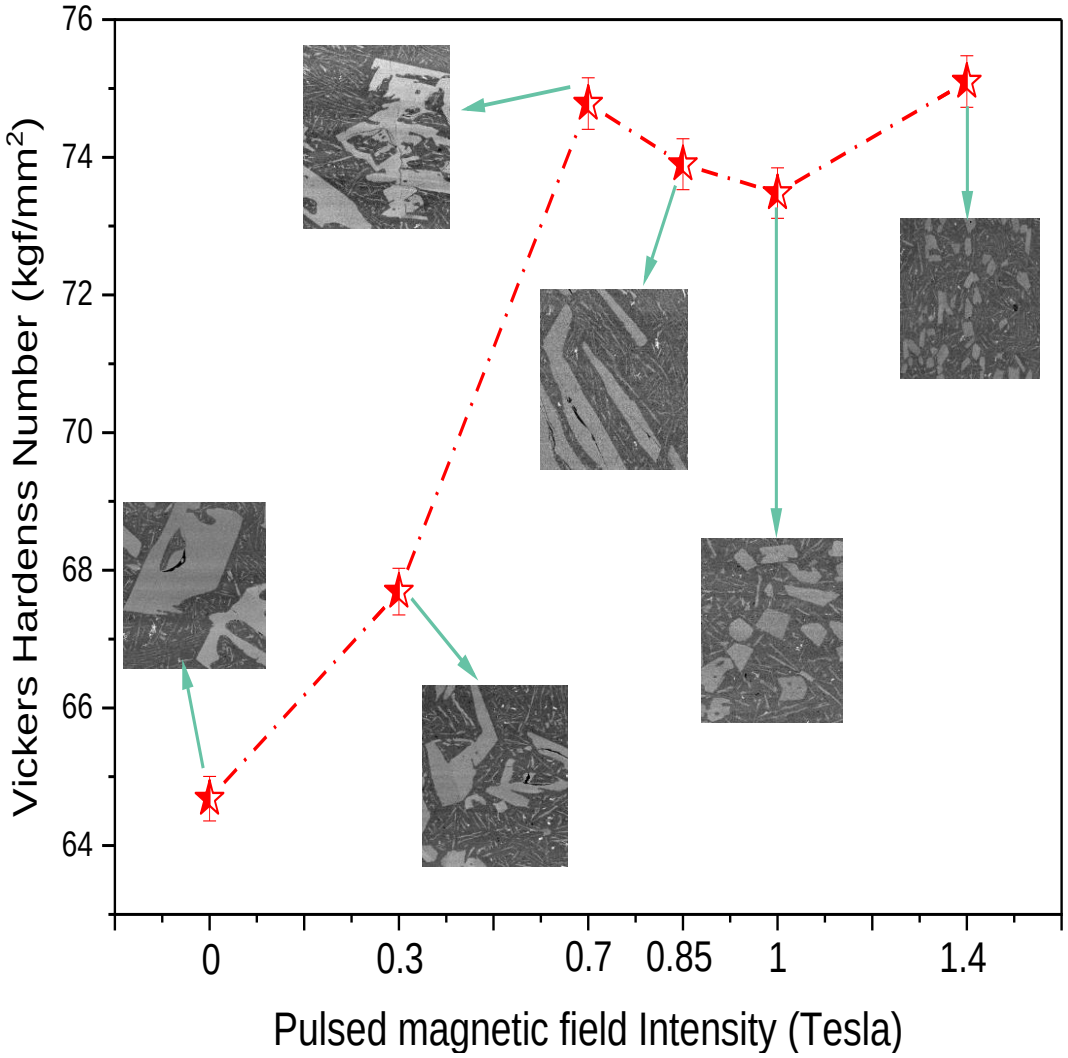

Figure 3. 27: The hardness values as a function of magnetic flux density.

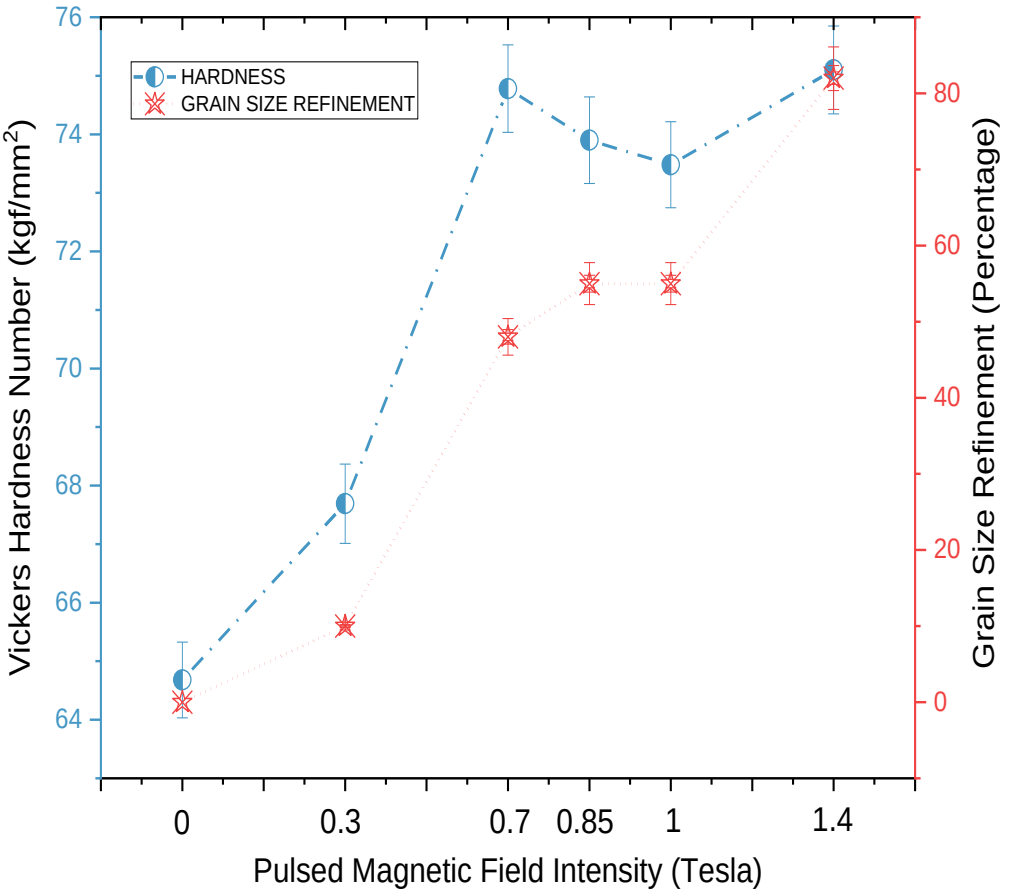

Figure 3. 28: The relationship between hardness/ particle size and the magnetic flux density.

In Figure 3. 28, the grain refinement versus hardness variation graph clearly show the two stage variation (Sharp and Gradual) of the hardness and the grain refinement with voltage of pulsed magnetic field. This can be inferred further as the restriction of larger primary Silicon phase happens predominantly in the first stage (0 – 0.7 Tesla) where as in the second stage (0.7 Tesla -1.4 Tesla), the genesis of finer eutectic Al-Si lamellar structure governs gradually.

3.7 Summary

Electromagnetic pulse assisted (Al-20% Si) alloy making is carried out and further subjected to microstructure and hardness characterizations. Al-20% Si alloys are casted by melting together pure Al (purity of 99.97%), and pure Si (purity of 99.97 %) with the appropriate weight ratio in a simple tube furnace. In this process, prior to electromagnetic pulse assisted solidification of aforementioned alloy, the billets of the alloy are made by controlled meting and casting. To understand the effect of the pulsed magnetic field on the grain refinement of the master alloys during solidification, metallographic study performed using optical and scanning electron microscopy. Microstructures results at lower magnifications can be summarised as the following:

Microstructures processed at 0V display lengthy and thick plate shaped primary Si structures, nearly oriented in all directions. Moreover, few short primary silicon plate-like formations are observed.

Microstructures processed at 40V reveals the presence of very few long plates like primary Silicon structures and increased amount of short primary silicon plates. This indicates that there is a change in the primary silicon size and shapes embedded in the eutectic matrix.

At 80 V, the morphologies are characterized by only short primary Si plate shaped, which became more homogenous and thinner than the microstructures related 40V. Increasing the discharge voltage to 100V utilize shorter and thinner primary Si plates.

Increased discharge voltage to 120 and to 160 volts has a greater effect on the microstructure of solidified Al-20% Si alloy. Importantly, the micrographs of the alloy solidified at 160 V demonstrate the transformation of several of the shorter primary Si plates into small primary Si islands. As a result, the distribution secondary phase Silicon in the matrix of Aluminium and eutectic mixture became much more uniform. At higher magnifications, the microstructures corresponding to 0 V reveals the presence of coarse lamellar eutectic Si in the matrix that gradually transform into finer lamellar eutectic

structures. Finer lamellar eutectic structures gradually evolve into finest acicular structures at some spots. The microstructures corresponding to 40 V has thicker primary Si plates and smaller Si islands around it. The quantitative increase in Al and Si eutectic lamellar or acicular structures imbedded in phase is also observed. Increased discharge voltage leads to decreasing in the quantitative of the thicker primary Si plates and increasing of the thinner Si plates and smaller Si islands. Furthermore, the number of lameller Al + Si eutectic colonies has increased, which suggests increasing the uniformity of the secondary phase Si distribution. The micrographs of the bottom part reveal restriction of primary silicon development leading to reducing silicon depletion in the matrix.

The systematic microstructural results interpret the following microstructural changes with respect to increase magnetic field intensity:

A magnetic field of 0.3 to 0.85 Tesla modified the enormous longer plate like primary Silicon structures and coarse Silicon islands into shorter plate like primary Silicon precipitates and Silicon islands. With increasing magnetic field intensity (1.0-1.4 Tesla), shorter plate-like silicon structures become primary silicon islands, and primary silicon islands become mini, micro, and fine silicon islands.

Because the large primary Silicon structures cannot develop, the solution becomes silicon-rich and new Si+ Al colonies form. When the amount of virgin eutectic Al+ Si colonies increases, it is clear that the lamellar structure is being refined by an increasing magnetic field.

Hardness measurements results show that the Vickers harness number increases abruptly up to 0.7 Tesla and then gradually increases up to 1.4 Tesla. The microstructural association with hardness demonstrates that the bigger sized primary Silicon plate-like structures found in the microstructures of zero magnetic field-solidified alloys exhibit a significant change into smaller longitudinal thin primary Silicon plates up to 0.7 Tesla.

Chapter 4 Correlations of three Mg-Gd based alloys

Mg based alloys are the materials of choices for bio-medical implant applications because they have similar mechanical strength to the human skeletal systems and the bio-degradable nature and biocompatibility with human body. To tailor their properties, some rare earth alloying elements with anti-carcinogenic properties are added to Mg alloys. Mg-Gd alloy system is one of those promising alloy systems, which have good combinations of mechanical strength and acceptable biocompatibility as well as reasonable degradation behaviour. Gd also has higher solid solubility in Mg. Other elements like Neodymium (Nd), Zirconium (Zr), Calcium (Ca), Silver (Ag) etc., are also added to these alloys to further tailor their properties for bio-medical applications [66], [86], [109], [152]–[154]. In this chapter, three alloys were studied and they are (1) Mg-10wt%Gd, (2) Mg-10wt%Gd-0.4wt%Zr, and (3) Mg-5wt%Gd-5wt%Nd-0.4wt%Zr.

4.1 Alloy making

The alloys were made by melting the Mg–20 wt.% Nd, Mg–21.6 wt.%Gd, Mg–33 wt.% Zr master alloy and pure Mg with the correct weight ratio. The feedstock ingots were melted in an electric resistance furnace protected with atmosphere of CO_2 and SF_6 (a ratio of 100:1). The Cl_6C_2 was used for degassing. The melt was held at 780 ^{0}C for 30 minutes before poured into pre heated steal die mould. The exact composition of the cast alloys was analysed by atomic emission spectrum (AES) instrument and listed in Table 4. 1. The microstructures of these alloys determine their mechanical and bio chemical properties (Degradation behaviour). This chapter describes the microstructural analysis and micro hardness testing of the alloys.

Table 4. 1 Chemical composition of the Mg alloys

ALLOY	Chemical Composition Percentage						
	Gd (Wt%)	Gd (At%)	Nd (Wt%)	Nd (At%)	Zr (Wt%)	Zr (At%)	Mg
1	10	1.69	0	0	0	0	Balance
2	9.65	1.61	0	0	0.44	0.13	Balance
3	4.69	0.79	4.39	0.79	0.38	0.11	Balance

4.2 Specimen preparation

The grinding and polishing procedure of the specimen are similar to that used in the Al-20%Si alloy. After polishing, specimens' surfaces were etched by immersing into 1 % NITOL (1% Nitric acid and 99 % Ethanol) for 15 seconds, removed and cleaned in running water by cotton wiper. Immediately after the etching and cleaning, the specimen surface was dried using air drier.

4.3 Optical microscopy analysis of the Mg alloys

The optical micrographs of the etched alloy specimens are shown in Figure 4. 1, Figure 4. 2, Figure 4. 3, and Figure 4. 4 (showing the grains, grain boundaries and intermetallic precipitates and agglomerations). Figure 4. 1 and Figure 4. 2 show the microstructures at 100x and 200x magnifications. In the Mg-10Gd alloy, the grains are bigger and the intermetallic phase Mg_5Gd are present uniformly throughout the Mg matrix. This means that the precipitation of the Mg_5Gd phase took place inside the grains as well as along the grain boundary regions. In the solution treated Mg–5Gd–5Nd–0.4Zr alloy, the XRD patterns and EDS analysis results indicated that the particles in the alloy were Mg5Gd phase containing Nd elements [155]. The Mg–Gd–Sm–Zr alloy system produced comparable outcomes. The solid solution-treated Mg–6Gd–6Sm–0.4Zr alloy contained a large amount of eutectic phases containing some Sm element, which exceeded the maximum solubility of Sm in solid Mg [156].

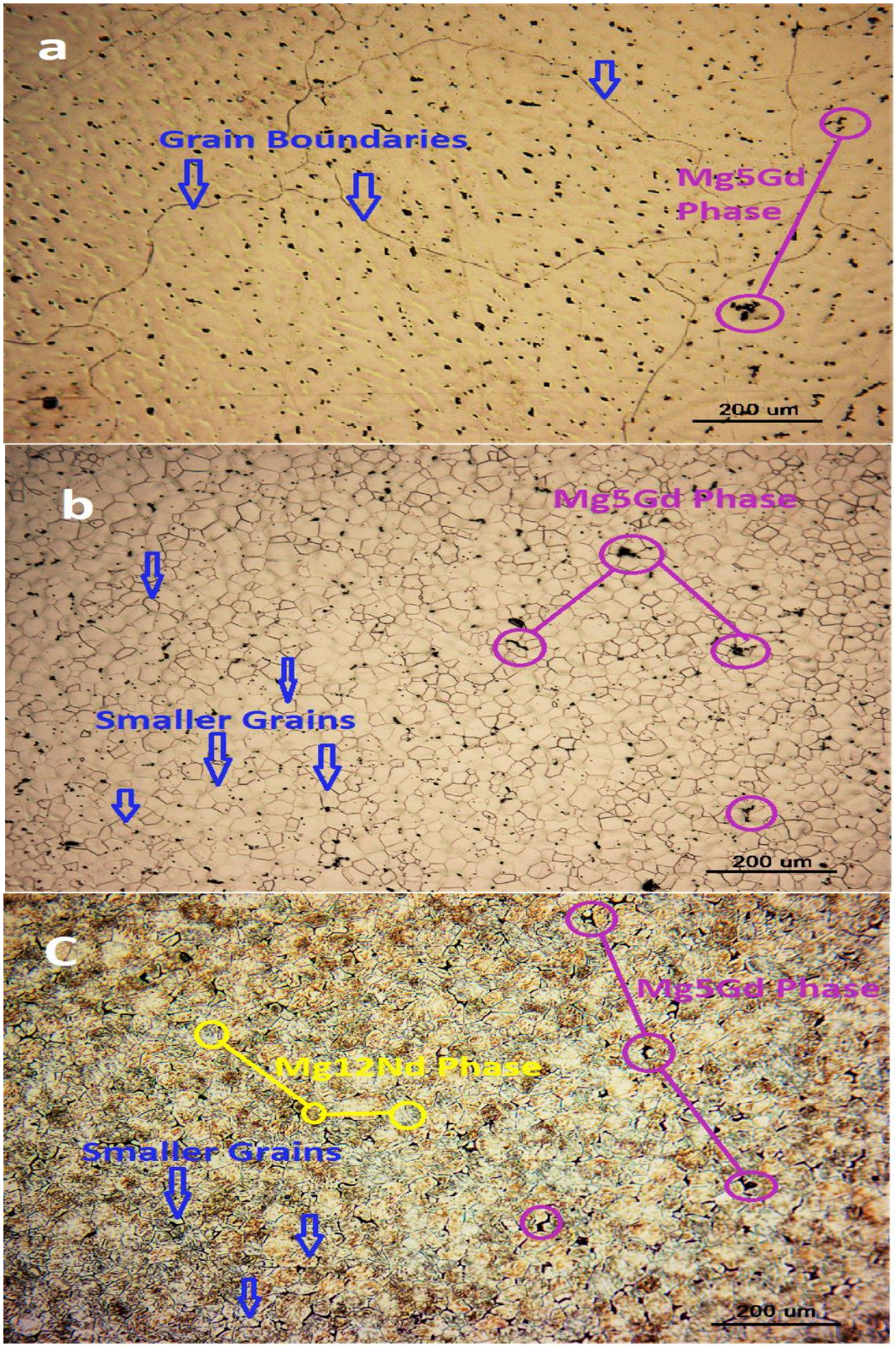

Figure 4. 1 Topographical features of alloy categories a) Mg-10wt%Gd b) Mg-10wt%Gd-0.4wt%Zr c) Mg-5wt%Gd-5wt%Nd-0.4wt%Zr obtained by optical microscope analysis at 100 X.

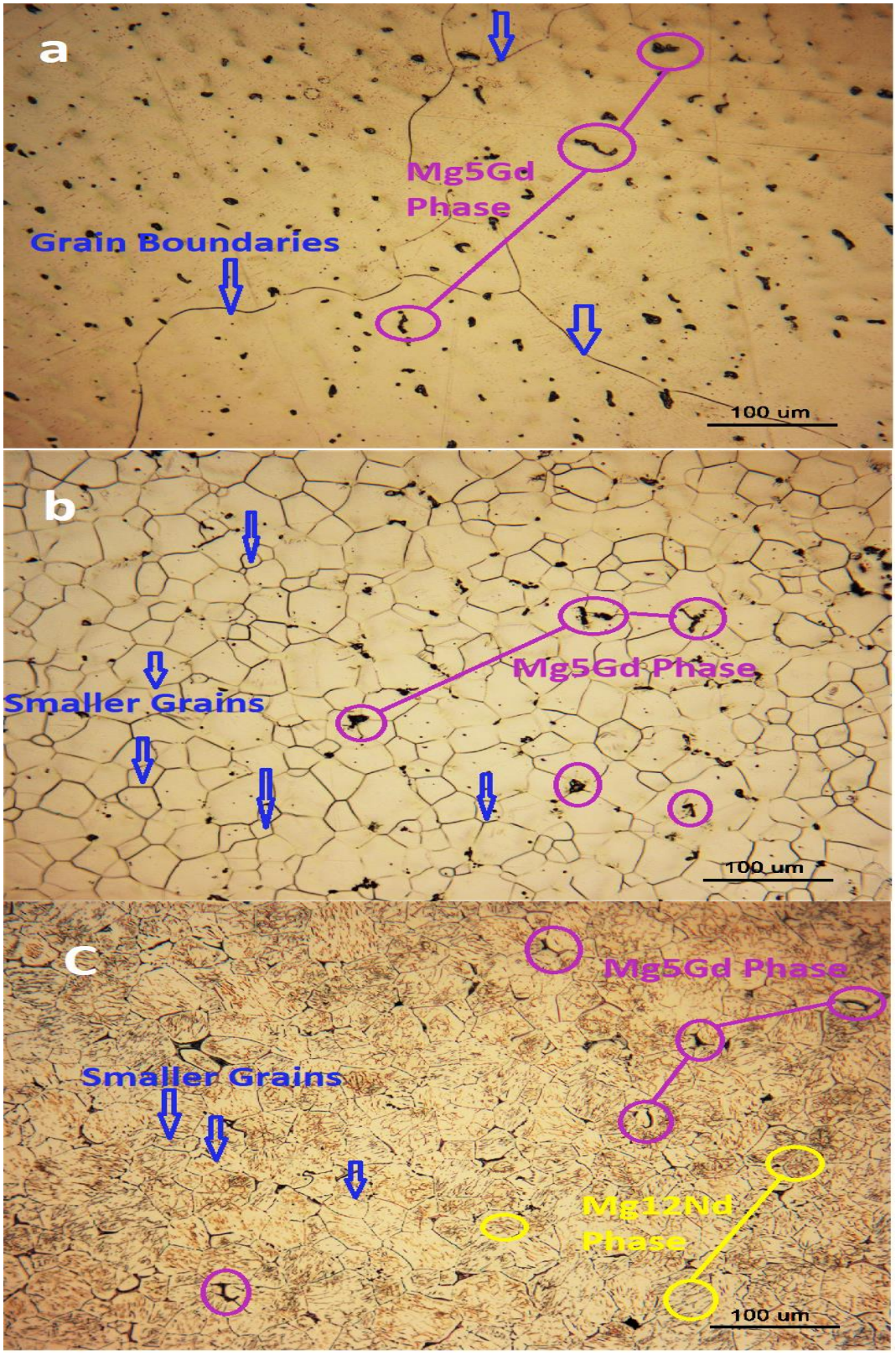

Figure 4. 2 Topographical features of alloy categories a) Mg-10wt%Gd b) Mg-10wt%Gd-0.4wt%Zr c) Mg-5wt%Gd-5wt%Nd-0.4wt%Zr obtained by optical microscope analysis at 200 X.

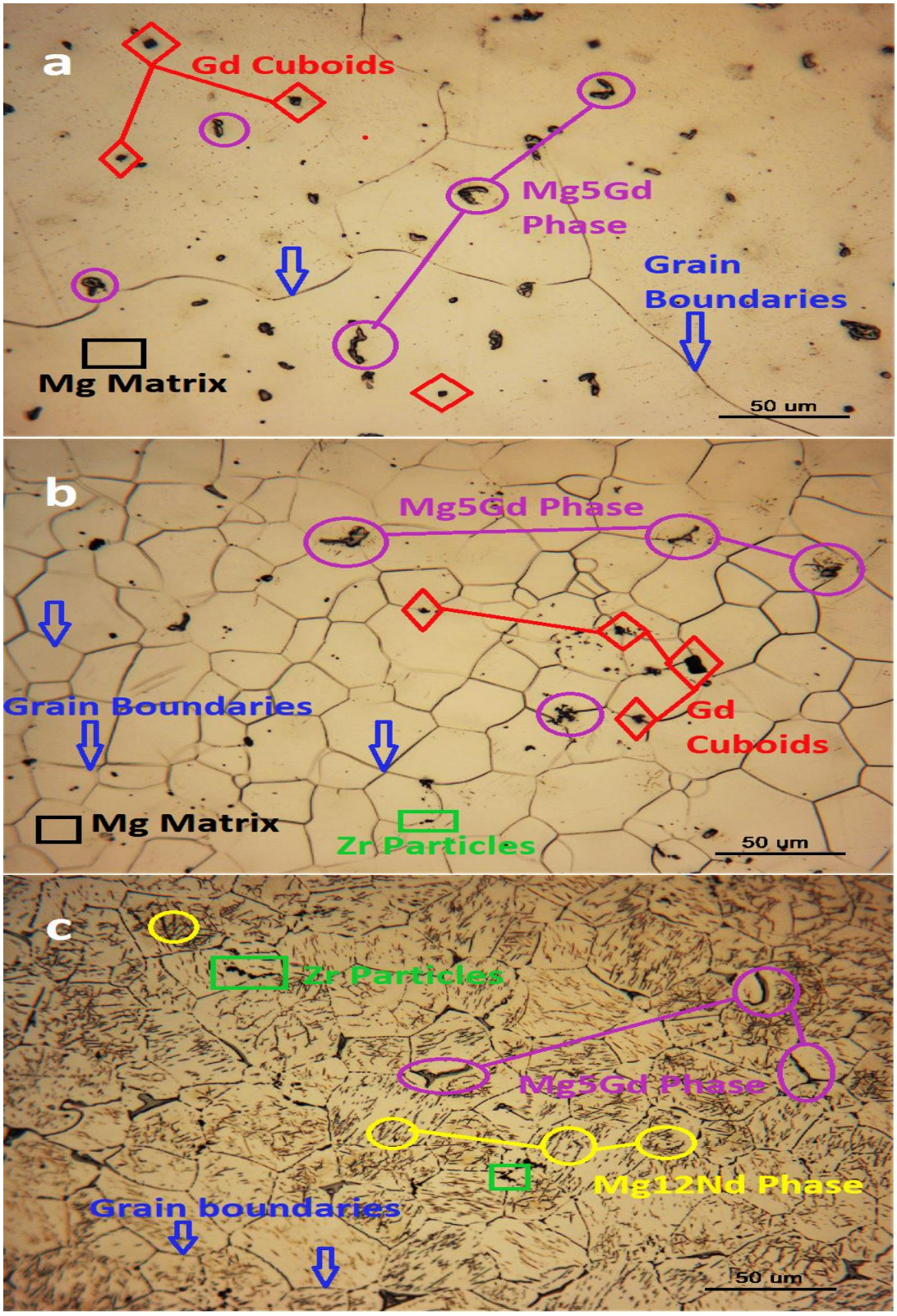

Figure 4. 3 Topographical features of alloy categories a) Mg-10wt%Gd b) Mg-10wt%Gd-0.4wt%Zr c) Mg-5wt%Gd-5wt%Nd-0.4wt%Zr obtained by optical microscope analysis at 400 X.

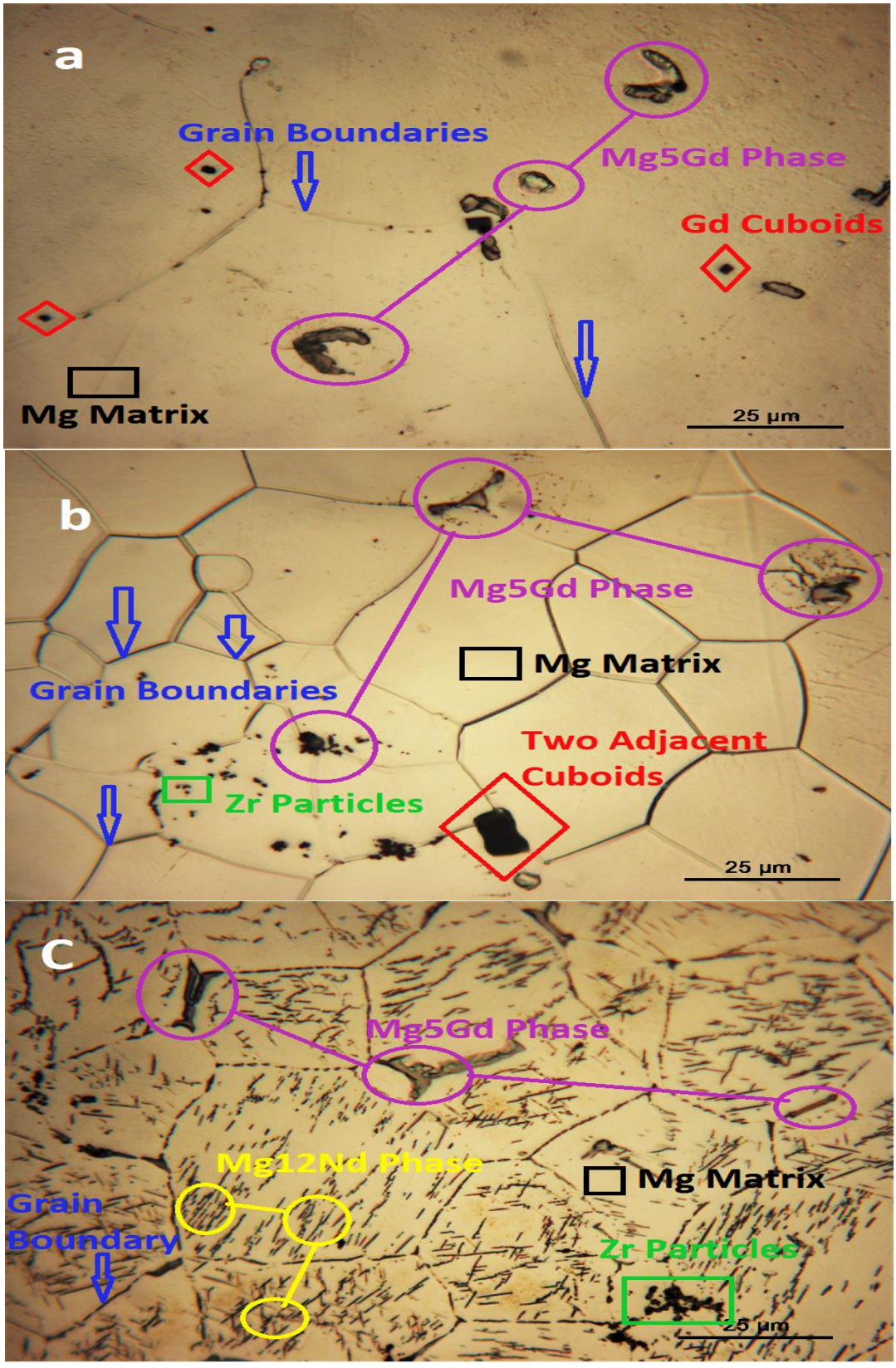

Figure 4. 4 Topographical features of alloy categories a) Mg-10wt%Gd b) Mg-10wt%Gd-0.4wt%Zr c) Mg-5wt%Gd-5wt%Nd-0.4wt%Zr obtained by optical microscope analysis at 1000 X.

In the Mg-10Gd-0.4Zr alloy, the grains are smaller, indicating that grain refinement took place because of adding Zr. Another notable difference in this alloy is that more Mg_5Gd phases are present along the grain boundaries than in Mg matrix. In addition, the grain boundaries look a bit wider. In the Mg 5Gd-5Nd-0.4Zr alloy, $Mg_{12}Nd$ phases are present inside the grains and in the grain boundary. In Mg alloys containing Nd, the needle-shaped phase was Mg12Nd precipitates having a tetragonal structure. It has been extensively reported that the needle-shaped phase in magnesium alloys containing Nd was Mg12Nd precipitates with a tetragonal structure, which was thought to be generated from Nd supersaturated solid and precipitated during slow cooling procedures, such as those used in sand mould casting[157][158]. The $Mg_{12}Nd$ are small needle-shaped phases oriented in all directions, indicating that there is no specific directional orientations for the $Mg_{12}Nd$ intermetallic phases. Again, smaller grains are observed in this alloy. Mg_5Gd phases are also present along the grain boundaries. Figure 4. 3 and Figure 4. 4 show the microstructures at 400 x and 1000 x magnifications. The presence of Gd cuboids were observed in the Mg-10Gd alloy and the Mg-10Gd-0.4Zr alloy. In the Mg-10Gd alloy, the cuboids are present in the grain and grain boundary regions; but in the Mg-10Gd-0.4Zr alloy, the cuboids are present along grain boundaries preferentially. In both cases, the size of the cuboids varies. At higher magnifications and in alloy Mg-10wt%Gd, the flake like Mg_5Gd precipitates present in the grain regions, but in alloy Mg-10wt%Gd-0.4wt, the same phase exhibits a preferential presence along grain boundaries. In addition, Mg matrix that are free of any intermetallic phases were found in microstructures of alloy Mg-10wt%Gd and Mg-10wt%Gd-0.4wt. Also, Zr agglomerations around the grain boundary regions.

4.4 Scanning electron microscopy analysis of the Mg based alloys

The following figures (Figure 4. 5, Figure 4. 6, Figure 4. 7 and Figure 4. 8) show the microstructures of the Mg alloys taken by scanning electron microscopy (SEM). Both secondary electron and back scattered electron images were taken. The back scattered electron images exhibit bright

contrast for the heavier elements; while the secondary electron images are better in capturing the topographical features.

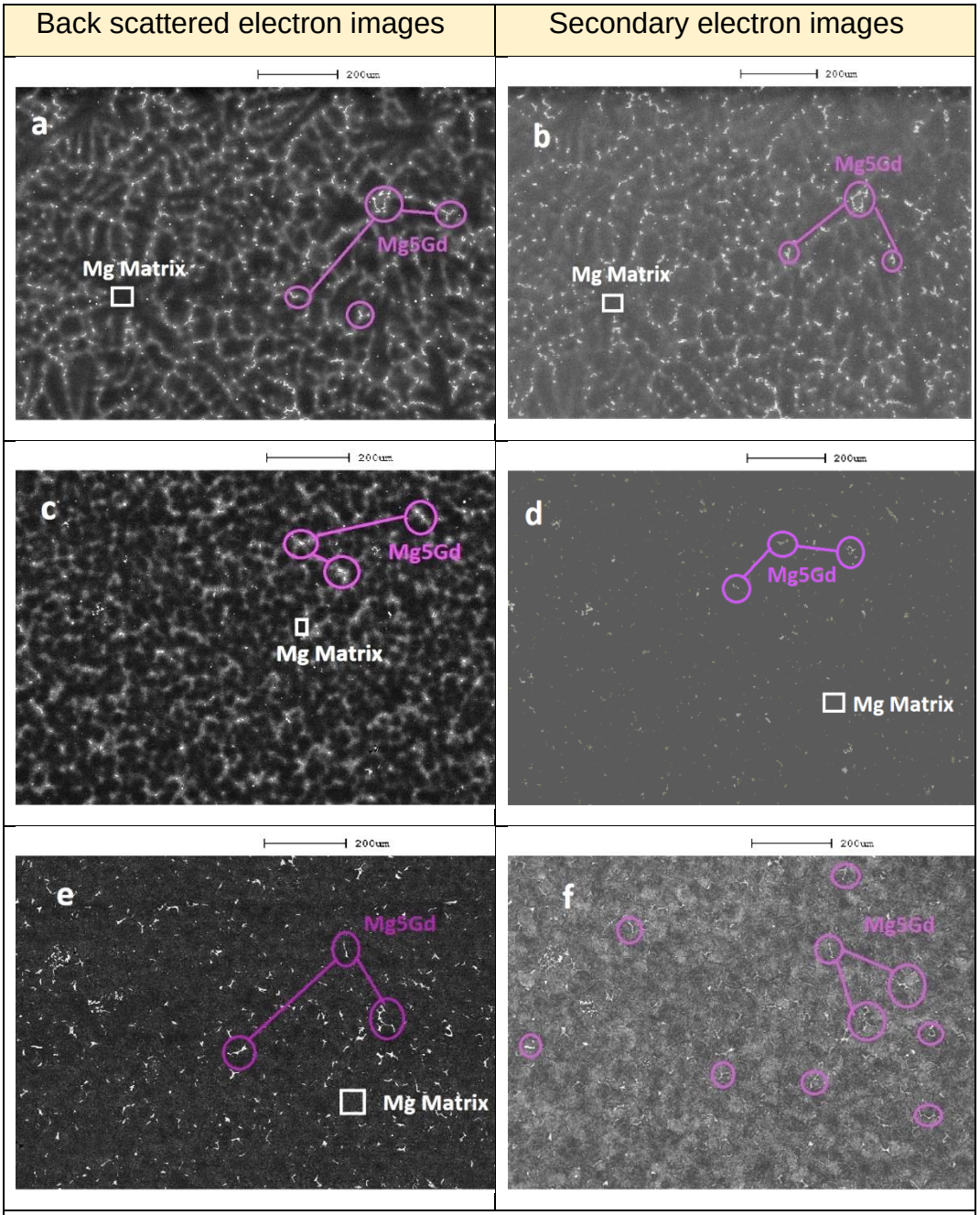

Figure 4. 5. SEM micrographs of the Mg alloys: a) Mg-10wt%Gd, b) Mg-10wt%Gd, c) Mg-10wt%Gd-0.4wt%Zr, d) Mg-10wt%Gd-0.4wt%Zr, e) Mg-5wt%Gd-5wt%Nd-0.4wt%Zr and f) Mg-5wt%Gd-5wt%Nd-0.4wt%Zr at **100X**.

Back scattered electron images	Secondary electron images
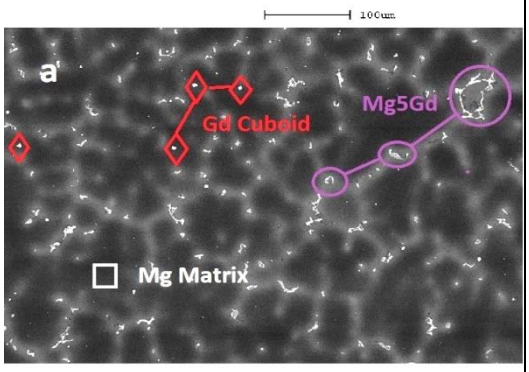	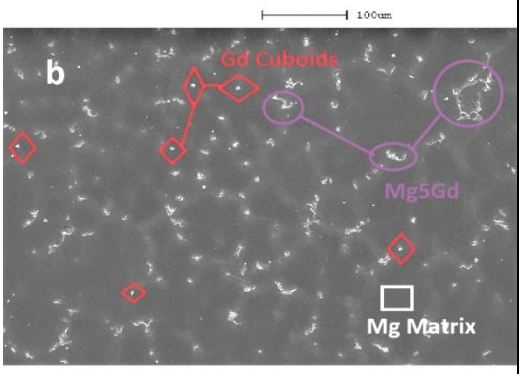
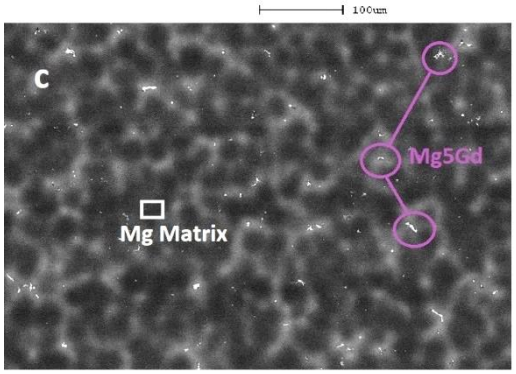	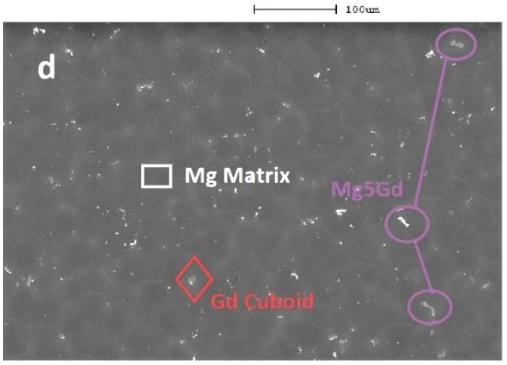
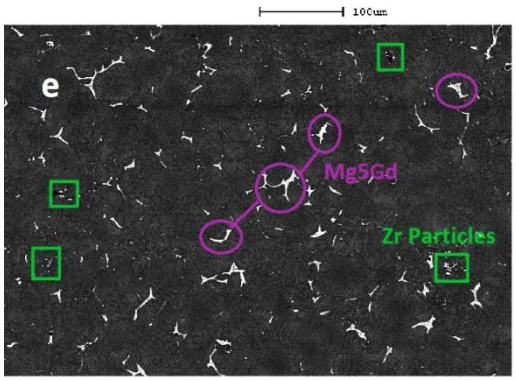	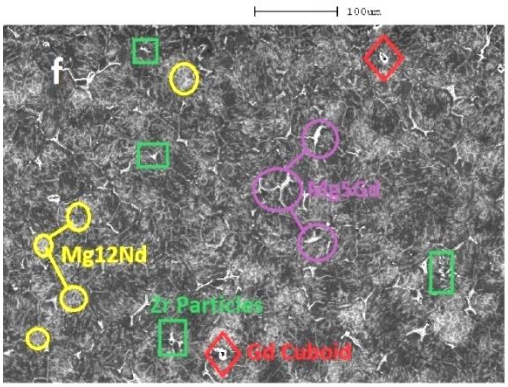

Figure 4. 6 SEM micrographs of the Mg alloys: a) Mg-10wt%Gd, b) Mg-10wt%Gd, c) Mg-10wt%Gd-0.4wt%Zr, d) Mg-10wt%Gd-0.4wt%Zr, e) Mg-5wt%Gd-5wt%Nd-0.4wt%Zr and f) Mg-5wt%Gd-5wt%Nd-0.4wt%Zr at **200X**.

Back scattered electron images	Secondary electron images

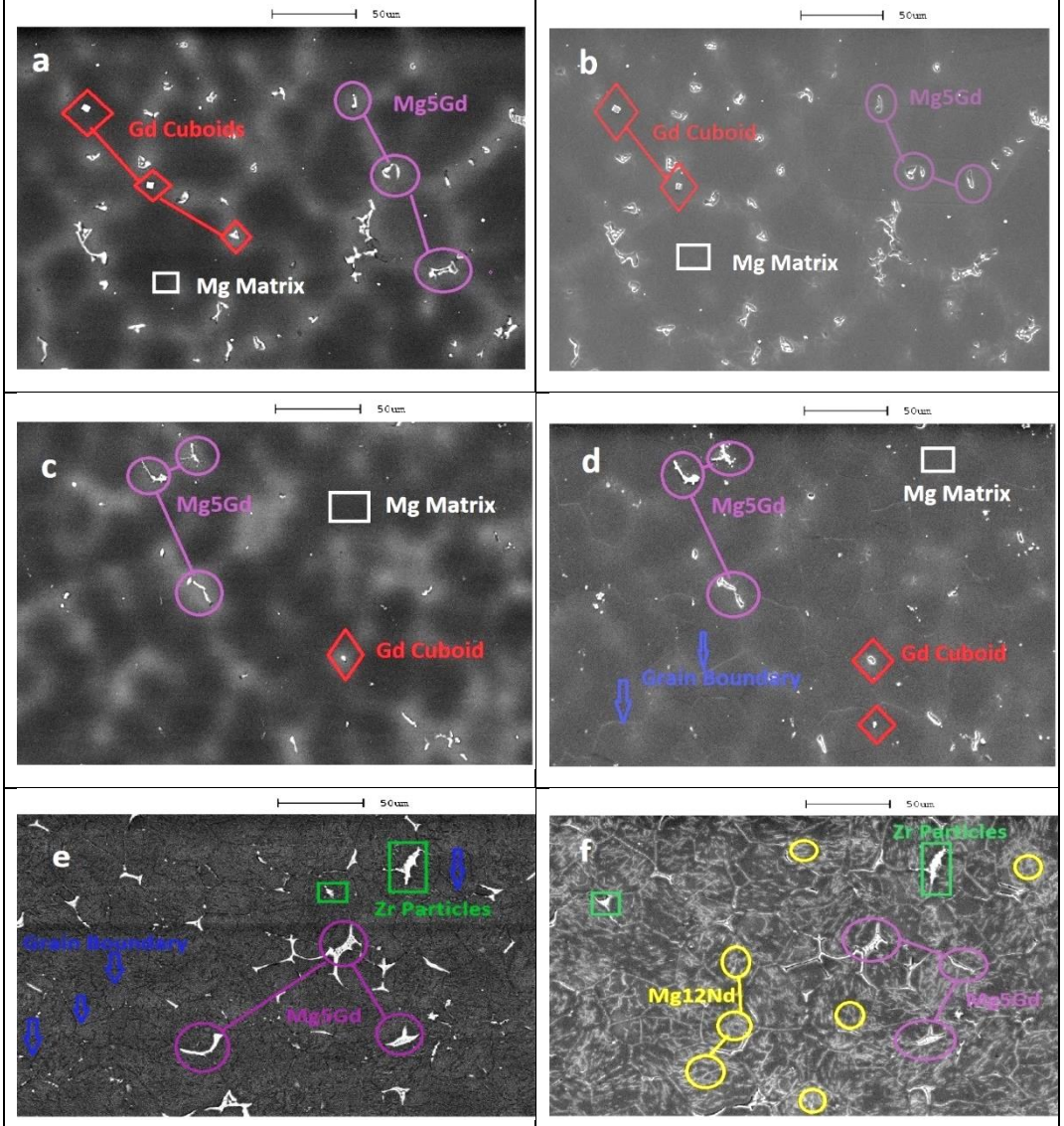

Figure 4. 7 SEM micrographs of the Mg alloys: a) Mg-10wt%Gd, b) Mg-10wt%Gd, c) Mg-10wt%Gd-0.4wt%Zr, d) Mg-10wt%Gd-0.4wt%Zr, e) Mg-5wt%Gd-5wt%Nd-0.4wt%Zr and f) Mg-5wt%Gd-5wt%Nd-0.4wt%Zr at **400X**.

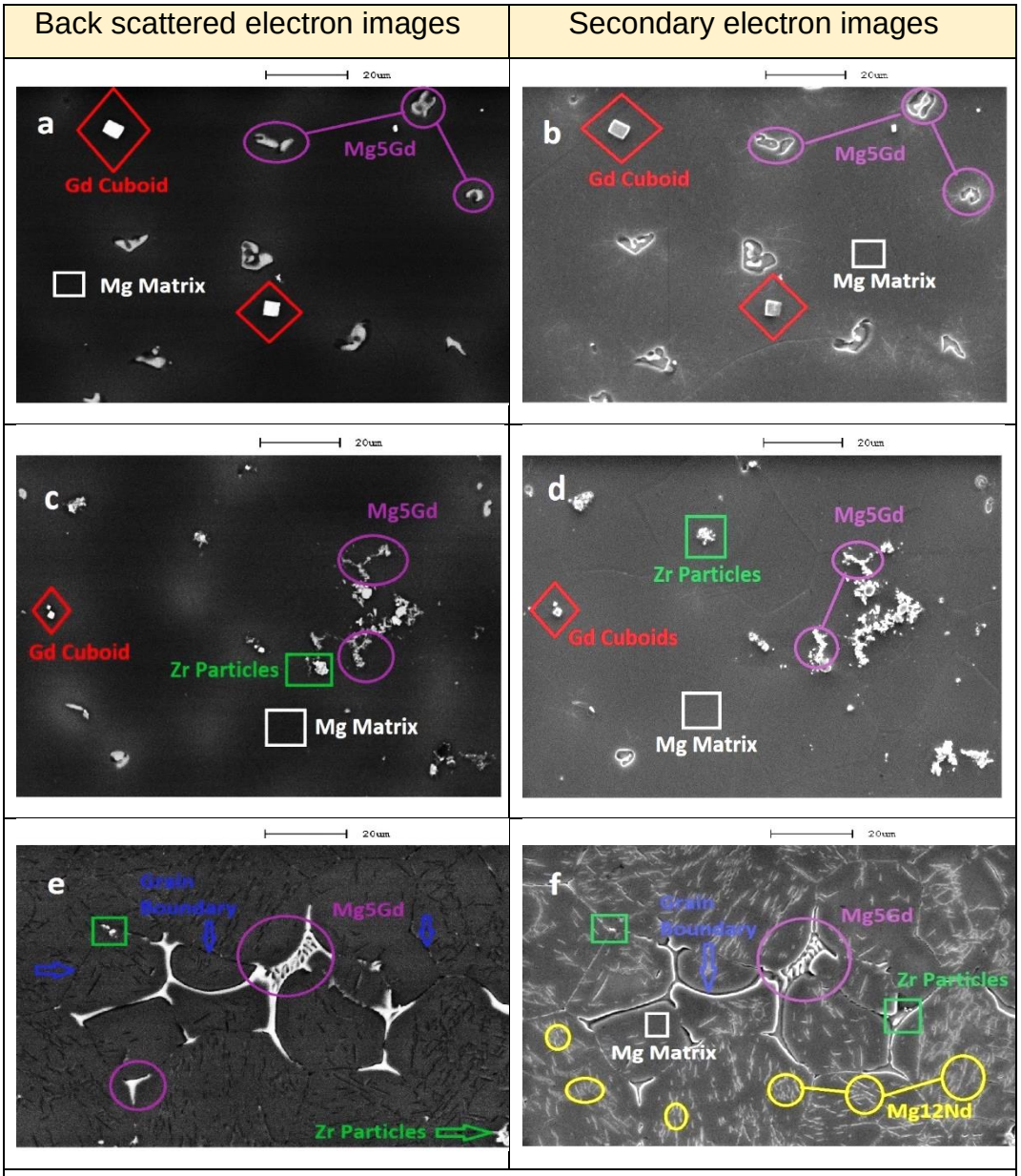

Figure 4. 8 SEM micrographs of the Mg alloys: a) Mg-10wt%Gd, b) Mg-10wt%Gd, c) Mg-10wt%Gd-0.4wt%Zr, d) Mg-10wt%Gd-0.4wt%Zr, e) Mg-5wt%Gd-5wt%Nd-0.4wt%Zr and f) Mg-5wt%Gd-5wt%Nd-0.4wt%Zr at **1000X**.

Figure 4. 6 and Figure 4. 7 shows the microstructures at 100 X and 200 X respectively. The grain boundary regions are clearly revealed by back scattered electron images with Mg_5Gd along the grain boundaries because the Gd atoms is heavier than that of Mg matrix. In the micrographs of alloy Mg-10wt%Gd and Mg-10wt%Gd-0.4wt%Zr the presence of Gd cuboids,

Mg_5Gd flake like structures and Mg matrix are observed. The Mg_5Gd distributed preferentially along the grain boundaries in alloy Mg-10wt%Gd-0.4wt%Zr, compared to that of alloy Mg-10wt%Gd. Micrographs of alloy Mg-5wt%Gd-5wt%Nd-0.4wt%Zr have different microstructural features including the $Mg_{12}Nd$ phase and Zr agglomerations. Figure 4. 7 and Figure 4. 8 illustrate the structures of the alloys at 400 X and 1000 X respectively. At higher magnifications, the Gd cuboids in alloy Mg-10wt%Gd and Mg-10wt%Gd-0.4wt%Zr are clearly observable. Another interesting feature is the size of the Gd cuboids in the alloy Mg-10wt%Gd and Mg-10wt%Gd-0.4wt%Zr. In both cases, the Gd cuboid's size vary. In alloy Mg-10wt%Gd, bigger size cuboids are observed (about 17.5 μm^2) compared to those in alloy Mg-10wt%Gd-0.4wt%Zr (about 6.1 μm^2). In alloy Mg-5wt%Gd-5wt%Nd-0.4wt%Zr, the Gd cuboids are hardly found. This gives the clear evidence of Gd agglomerations slowly transformed into Mg_5Gd precipitations in alloy Mg-10wt%Gd-0.4wt%Zr and Mg-5wt%Gd-5wt%Nd-0.4wt%Zr. Back scattered electron images of Figure 4. 7 and Figure 4. 8 clearly show that the Mg_5Gd flake like structures are present along the grain boundaries in alloy Mg-10wt%Gd-0.4wt. They uniformly distributed in grain and grain boundaries regions in alloy Mg-10wt%Gd-0.4wt%Zr. They uniformly distributed in grain and grain boundaries regions in alloy Mg-10wt%Gd. In addition, the presence of Zr particles as agglomerations in and around the grain boundary regions are clearly exhibited by these microstructures (Figure 4. 7 and Figure 4. 8) at higher magnifications. The secondary electron images at higher magnifications show the presence of $Mg_{12}Nd$ needle like structures in the grain regions.

4.5 Energy Dispersive X-Ray Analysis of the Mg based alloys

Figure 4.9 to Figure 4. 15 show the EDAX spectrum of the alloys 1, 2 and 3. Figure 4. 9a show the EDAX spectrum of bulk analysis of alloy 1 with peaks of Mg and Gd. It proves that the composition of alloy 1 is consisting of Magnesium and Gadolinium. Figure 4. 9b shows the EDAX spectrum of Gd cuboid phase of alloy 1 with peaks of only Gd. This reveals that the cuboids consist of only Gd element. Figure 4. 10 a show the EDAX spectrum of

Magnesium matrix of alloy 1 (Mg-10Gd) with peaks of only Mg. Hence the Magnesium matrix regions free of any precipitates are existing in alloy 1. Figure 4. 10 b shows the EDAX spectrum of Mg_5Gd intermetallic precipitates of alloy 1 with peaks of only Mg and Gd. This proves the presents of Mg_5Gd flake like structures in alloy 1. Small peaks of oxygen represents the oxide scale and carbon represents the very meagre amount of contaminations.

Figure 4. 12 a show the EDAX spectrum of bulk analysis of alloy Mg-10wt%Gd-0.4wt with peaks of Mg, Gd and Zr. Comparatively smaller peak of Zr represents nearly quantity of Zr in alloy 2. Figure 4.12b show the EDAX spectrum of Magnesium matrix of alloy 2 with peaks of Mg. Very small peaks of Gd are observed when compared to that of large Mg peaks. Figure 4. 13a show the EDAX spectrum of Mg_5Gd phase of alloy 2 with peaks of Mg and Gd. Figure 4. 13 b shows the EDAX spectrum of Zr agglomerations of alloy 2 with peaks of Zr only. This proves the presents of Zirconium as agglomerations in and around the grain boundaries.

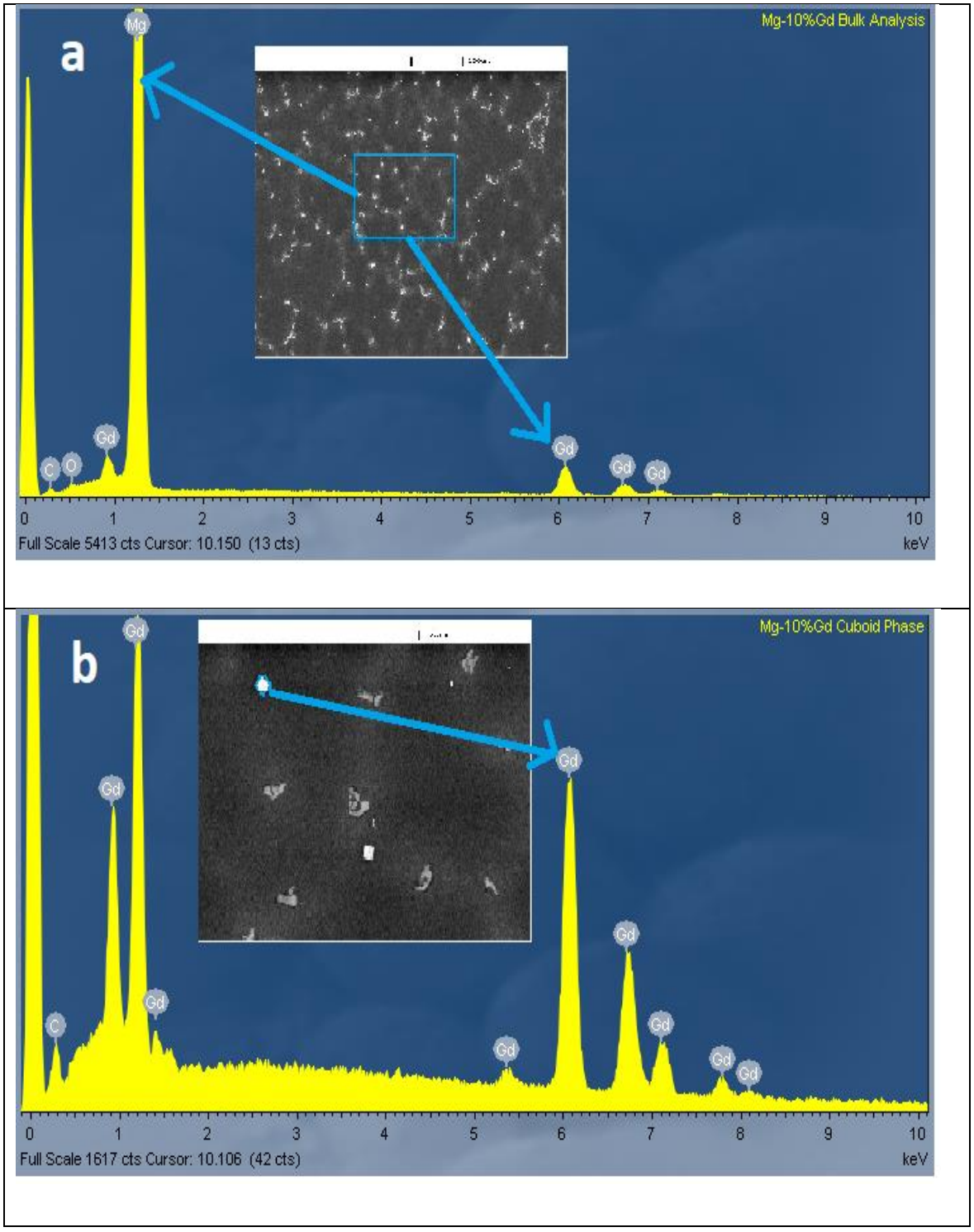

Figure 4. 9 EDAX Spectrum of Mg-10wt%Gd alloy; a) Bulk analysis and b) Gd Cuboid.

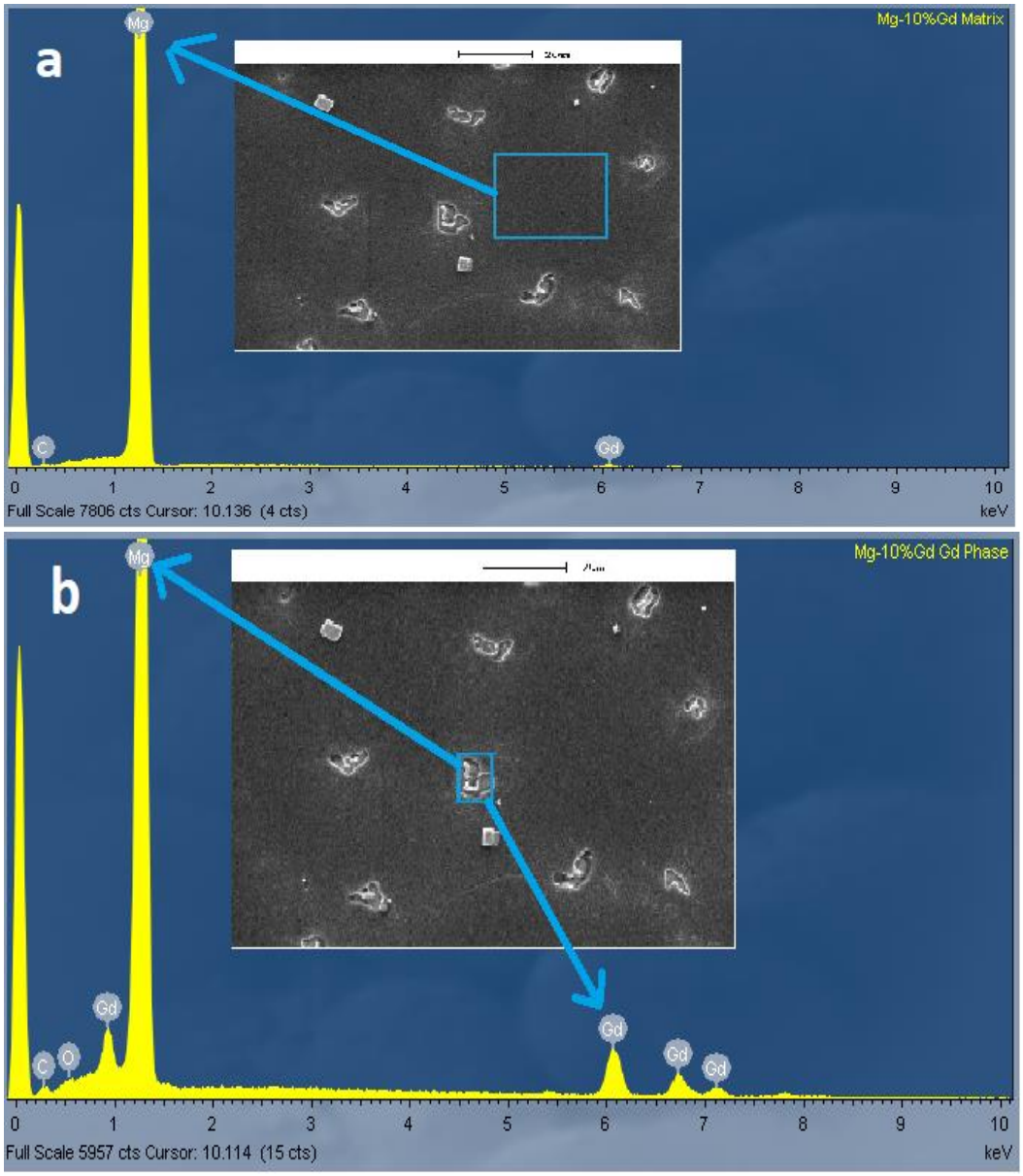

Figure 4. 10 EDAX Spectrum of Mg-10wt%Gd alloy; a) Magnesium Matrix and b) Mg5Gd Phase

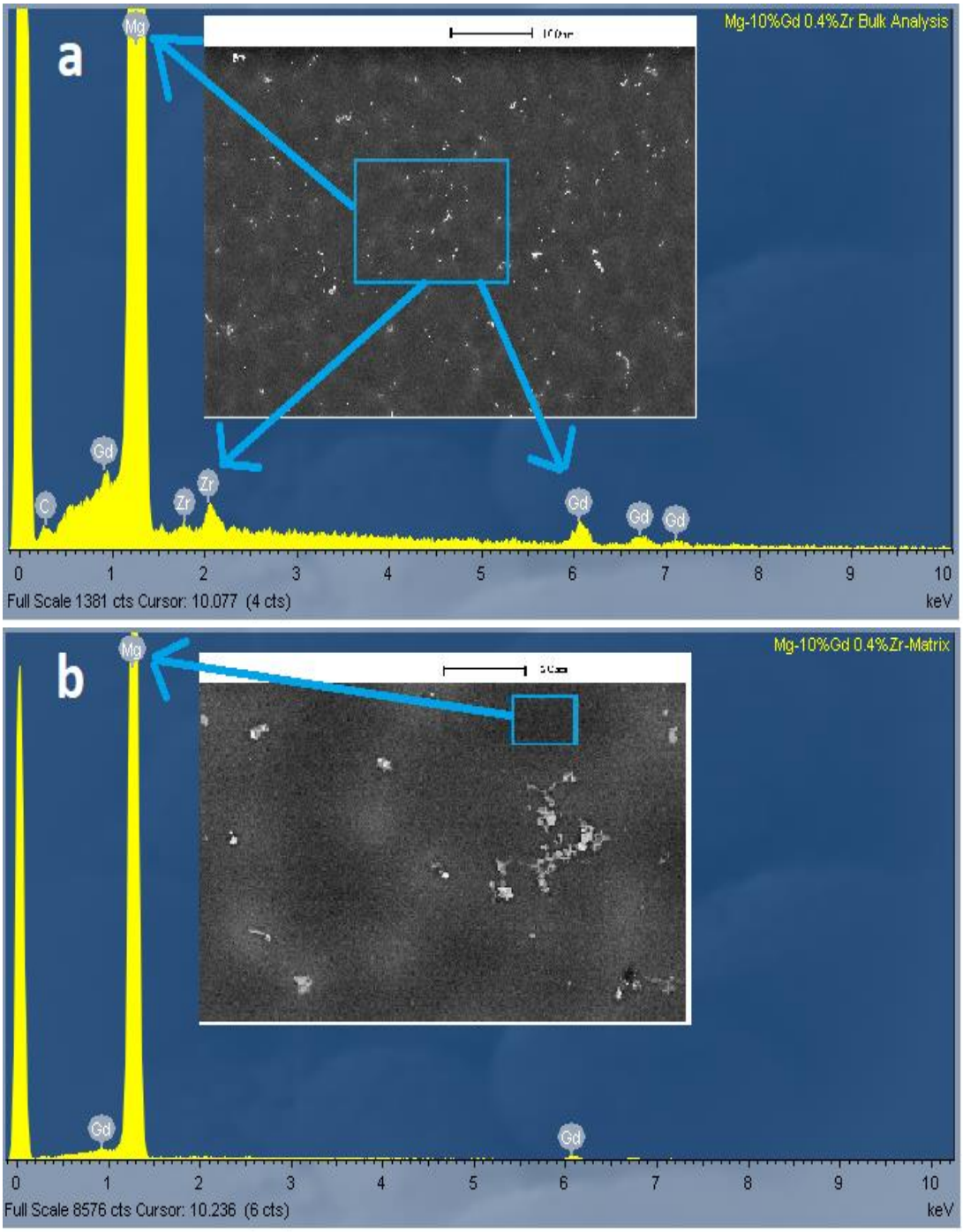

Figure 4. 11 EDAX Spectrum of alloy Mg-10wt%Gd-0.4wt%Zr ; a) Bulk analysis and b) Magnesium matrix

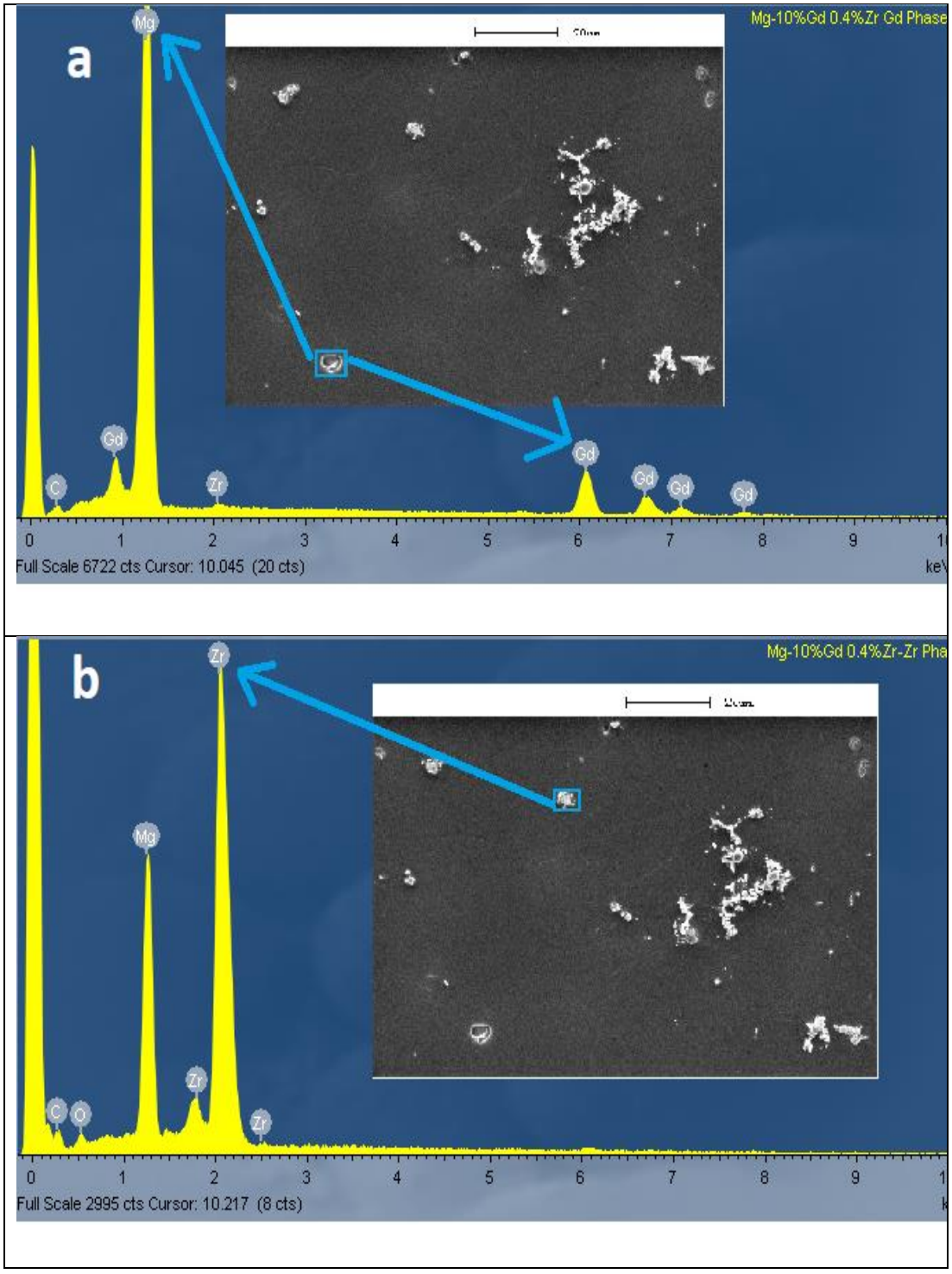

Figure 4. 12 EDAX Spectrum of Mg-10wt%Gd-0.4wt%Zr alloy; a) Mg_5Gd phase and b) Zr agglomerations

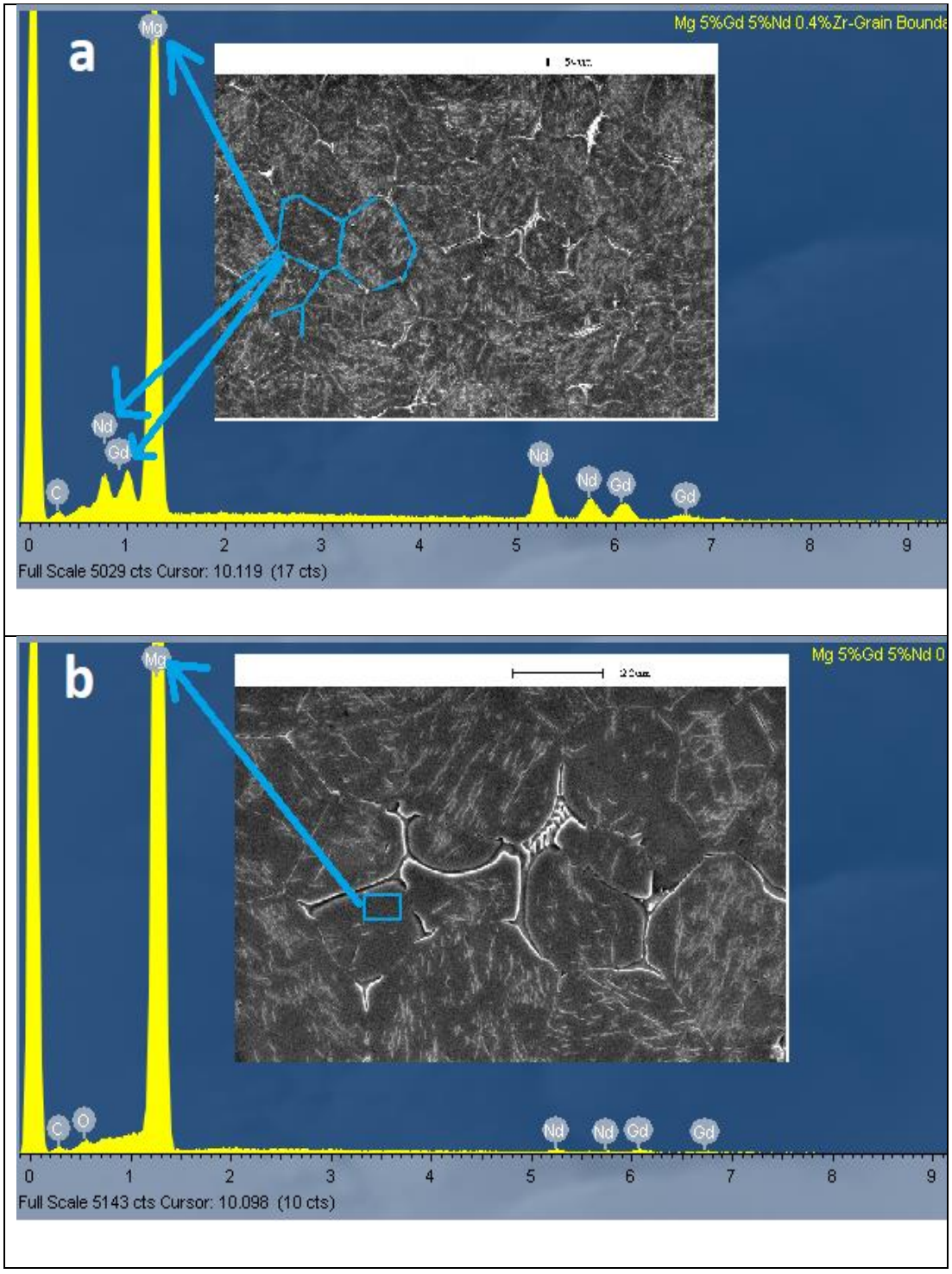

Figure 4. 13 EDAX Spectrum of Mg-5wt%Gd-5wt%Nd-0.4wt%Zr alloy; a) Grain boundary region and b) Mg matrix

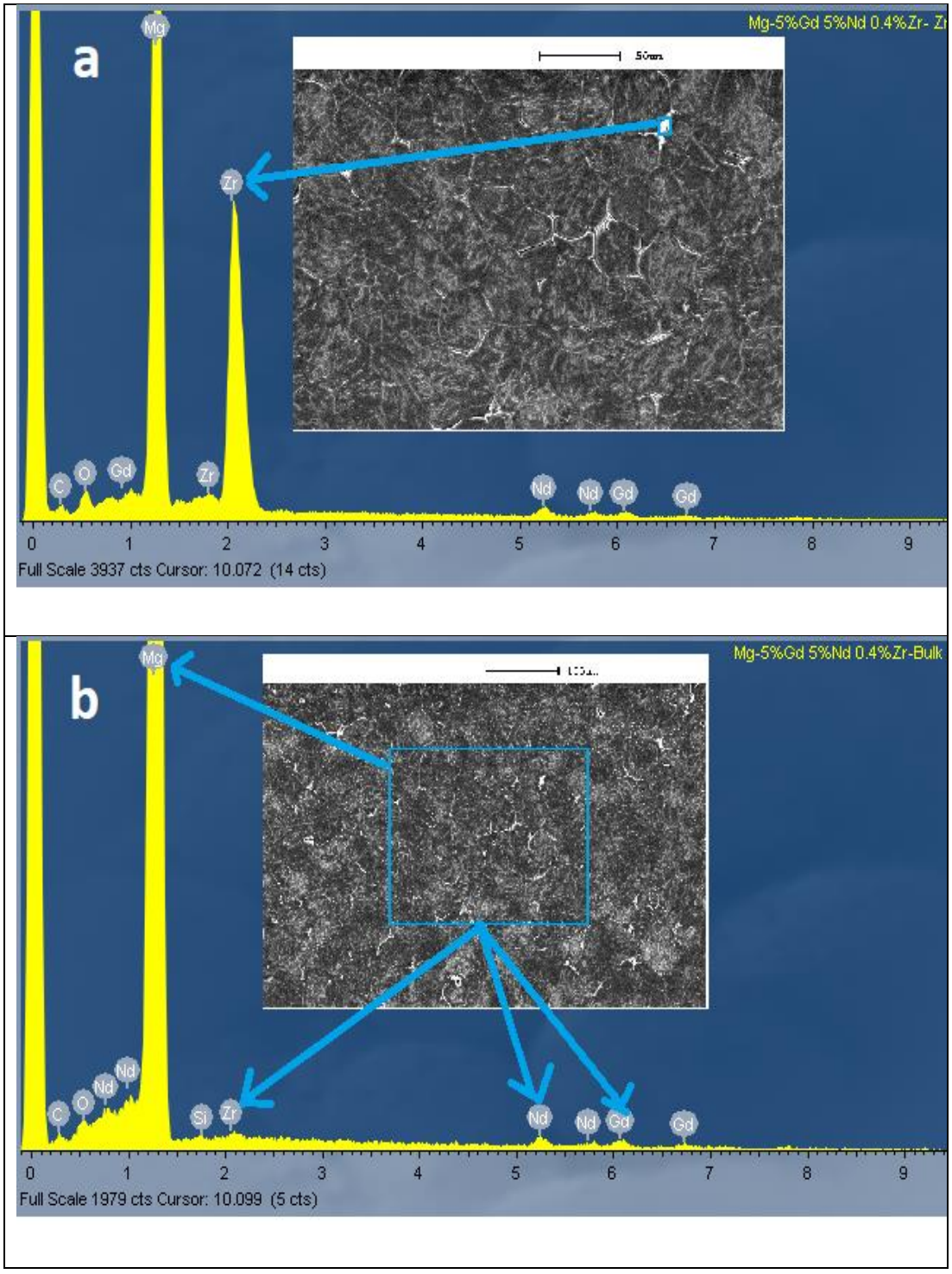

Figure 4. 14 EDAX Spectrum of Mg-5wt%Gd-5wt%Nd-0.4wt%Zr alloy; a) Zr Phase and b) Bulk Analysis

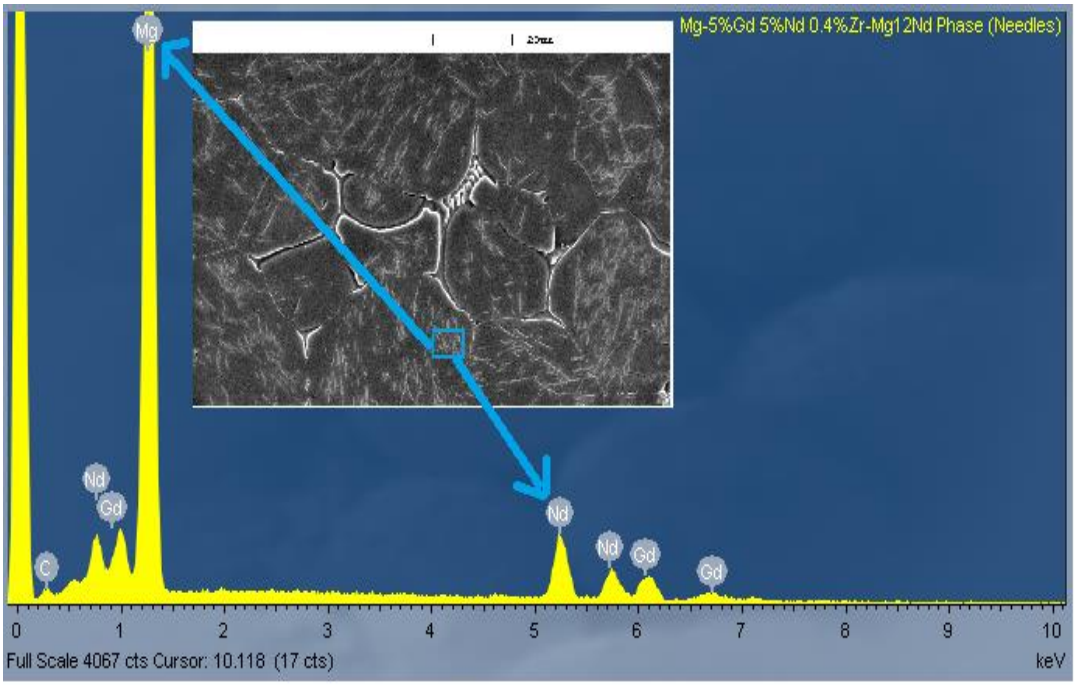

Figure 4. 15 EDAX Spectrum of Mg-5wt%Gd-5wt%Nd-0.4wt%Zr alloy; $Mg_{12}Nd$ Phase

Figure 4. 14a shows the EDAX spectrum of Zirconium agglomerations of alloy Mg-5wt%Gd-5wt%Nd-0.4wt%Zr with peaks of Zirconium and Mg only. This indicates that the presence of Zirconium particles agglomeration in Magnesium matrix.

Figure 4. 14b shows the EDAX spectrum of bulk analysis of alloy Mg-5wt%Gd-5wt%Nd-0.4wt%Zr with peaks of Gd, Mg, Nd and Zr. This proves the alloy Mg-5wt%Gd-5wt%Nd-0.4wt%Zr composition is consisting of Magnesium, Gadolinium, Neodymium and Zirconium. Figure 4. 15 shows the EDAX spectrum of Mg12Nd needle like structure of alloy Mg-5wt%Gd-5wt%Nd-0.4wt%Zr with peaks of Mg and Nd that confirms the presents of Mg12Nd phase in alloy Mg-5wt%Gd-5wt%Nd-0.4wt%Zr.

4.6 Measurement of the hardness of the Mg based alloys

4.6.1 Vickers micro hardness measurements

Micro harness measurements were carried out using Leitz Wetzlar Germany (Model- 8295) Vickers micro hardness tester**.** Specimens of size 2cm x 2cm x 2cm **were** prepared, polished, cleaned and etched before subjecting them to hardness measurements. The procedures of specimen preparations are clearly described in the earlier section of microstructural analysis of the Magnesium based alloy. The governing expression used in Vickers hardness calculations is shown below [159];

$$\text{Vickers micro hardness number (VHN)} = 1.854 \text{ x } \frac{F}{d^2} - - - - - - - (3.1)$$

where F is the load in kgf and d represents the arithmetic mean of the two diagonals, d_1 and d_2 measured in mm.

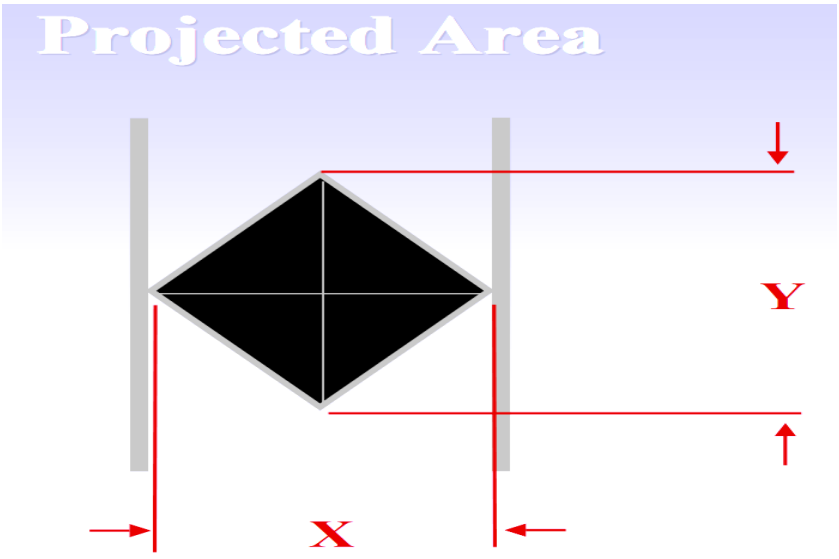

Figure 4. 16 The pictorial representation of diagonal parameters X and Y of the indentation in Vickers hardness measurements.

Table 4. 2 The indentation parameters Vickers hardness measurements of Mg-10wt%Gd

S.No	Diagonal Length X (µm)	Diagonal Length Y (µm)	Mean diagonal Length d (µm)	Hardness Vickers (VHN)
1	51.6	46.6	49.1	76.9
2	47	51	49	77.2
3	51.8	50.15	50.98	91.9
4	54.25	54	54.1	63.3
5	49.5	46.5	48	80.5
6	49.2	48.6	48.9	77.6
7	50.4	50.0	50.2	73.9
8	48.6	49.8	49.2	76.6
9	49.8	48.8	49.3	76.3
10	49.6	48.0	48.8	77.9
11	52.6	47.2	49.9	74.5
12	49.7	49.8	49.75	74.8
Average				**76.7833**

Table 4. 3 The indentation parameters Vickers hardness measurements of Mg-10wt%Gd-0.4wt%Zr alloy

S.No	Diagonal Length X (µm)	Diagonal Length Y (µm)	Mean diagonal Length d (µm)	Hardness Vickers (VHN)
1	48.0	47.8	47.9	80.8
2	50.0	49.9	50.0	74.2
3	51	48	49.5	75.7
4	49	51.7	50.3	73.3
5	53	52.3	52.7	66.8
6	51.8	54.0	52.9	66.3
7	50.5	51.0	50.25	73.3
8	47.6	46.6	47.1	83.6
9	48.6	49.3	48.95	77.2
10	51.6	52.2	51.9	68.6
11	52.1	48.8	50.55	72.7
12	48.0	47.8	47.9	80.8
Average				**74.4416**

Figure 4. 16 shows the X and Y parameters of the indentation in Vickers hardness measurements. Table 4. 2, Table 4.3 and Table 4.4 show the indentation parameters of the Mg based alloys Mg-10wt%Gd, Mg-10wt%Gd-

0.4wt%Zr and Mg-5wt%Gd-5wt%Nd-0.4wt%Zr . A load of 0.1-kilogram force (kgf) is used in all micro hardness tests and a dwell time of 15 seconds is allowed for each test indentation.

Table 4. 4 The indentation parameters Vickers hardness measurements of alloy Mg-5wt%Gd-5wt%Nd-0.4wt%Zr.

S.No	Diagonal Length X (µm)	Diagonal Length Y (µm)	Mean diagonal Length d (µm)	Hardness Vickers (VHN)
1	48.7	47.1	47.9	80.8
2	44.8	45.7	45.3	90.8
3	47.6	45.4	46.5	85
4	47.5	48.5	48.0	80.5
5	48.7	48.6	48.65	78.2
6	47.7	46.8	47.25	82.9
7	46.8	47.2	47.0	83.9
8	47.8	48.3	48.05	80.2
9	44.6	45.2	44.9	92.0
10	47.4	48.2	47.8	81.2
11	47.0	45.7	46.35	86.1
12	48.8	45.8	47.3	82.9
AVERAGE				**83.708**

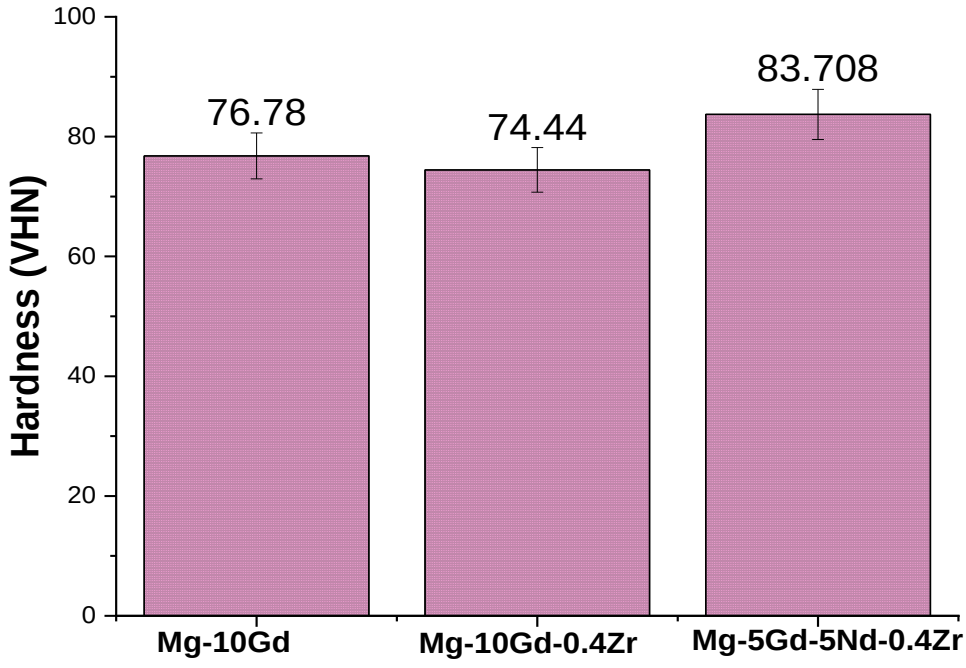

Figure 4. 17: The bar chart of hardness profile of Mg based alloys

It will be very appropriate to carry out nano hardness measurements in order to explore the exact hardness property of each phase regions of the alloys Mg-10wt%Gd, Mg-10wt%Gd-0.4wt%Zr, and Mg-5wt%Gd-5wt%Nd-0.4wt%Zr.

4.6.2 Nano Indentation measurements

In this work, the Nano-indentation experiments are carried out in order to obtain the hardness information for the different phases. The CSM Instruments, Switzerland available at the University of Hull is employed in Nano-indentation experiment.

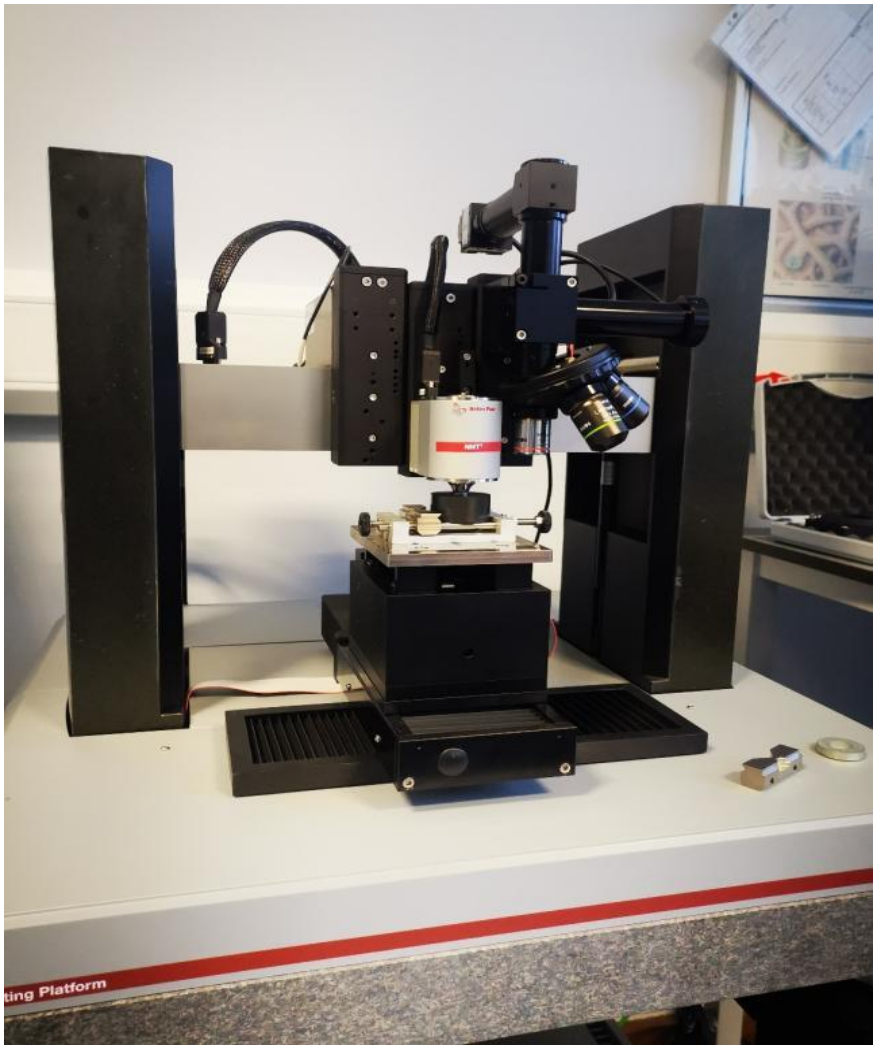

Figure 4. 18: Nano-indentation instrumentation including the indentor, the sample holder and the optical lenses.

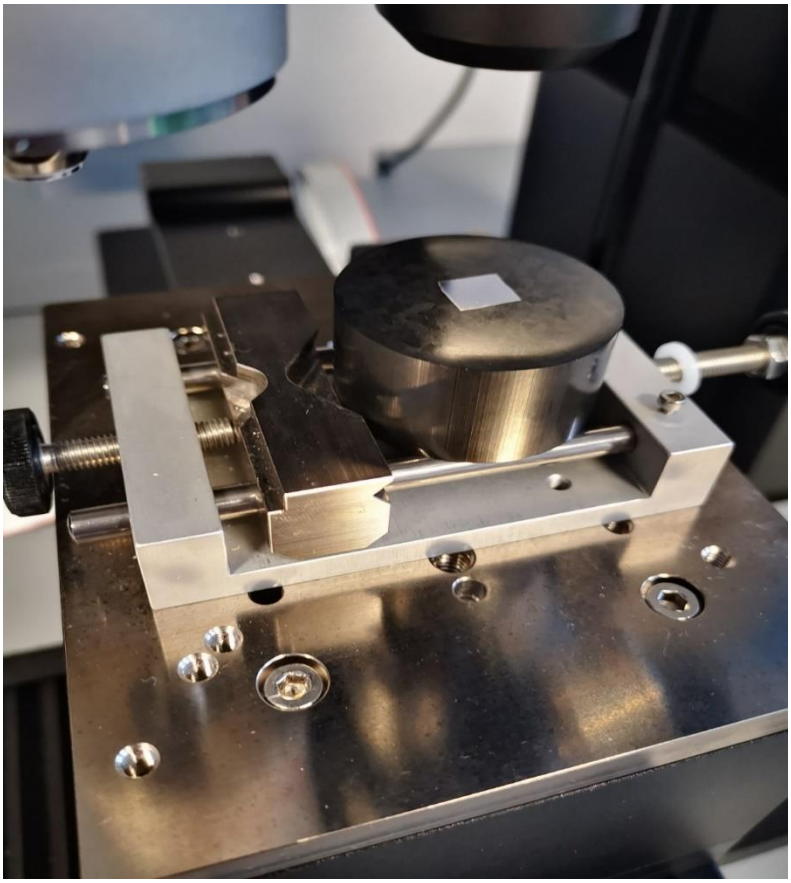

Figure 4. 19**:** Holding the tested samples during the experiments (with the Bakelite).

The specimen to be tested is mounted on conductive Bakelite. An array of indentations was made on each specimen in order to collect sufficient data for the hardness analysis. After the indentation test, the depth of the indentation was viewed using SEM.

The following expressions are representing the equations to calculate the Nano hardness and Young's modulus of the alloy.

$$Nano\ hardness\ (H_{IT}) = \frac{P_{max}}{A_C}$$

$$Youngs\ modulus\ (E) = \frac{\pi}{2}\ x \frac{S}{\sqrt{A_C}}$$

Where A_C is the contact area, calibrated using a silica block, the P_{max} and S is obtained from the nano-indentation graph as illustrated in Figure 4. 20. The

Nano-indentation parameters and specimens that were used in the experiments are presented in the following table (table 4.5)

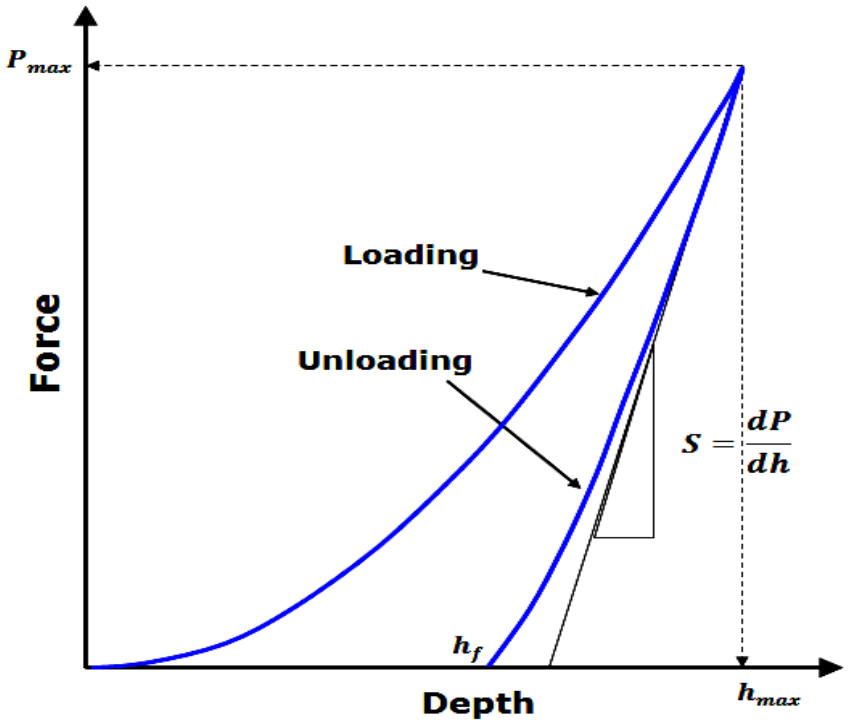

Figure 4. 20: Graph between the load and depth of indentation.

Table 4. 5: Nano-indentation parameters and specimens (alloy Mg-10wt%Gd , alloy Mg-10wt%Gd-0.4wt%Zr and alloy Mg-5wt%Gd-5wt%Nd-0.4wt%Zr).

Sample (1): **Mg-10%Gd** Sample (2): **Mg-10%Gd-0.4%Zr** Sample (3): **Mg-5%Gd-5%Nd-0.4%Zr**	Control Mode	Load
	Maximum Load	100 mN
	Loading Rate	200 mN/min
	Unloading Rate	200 mN/min
	No. of Indentations	30

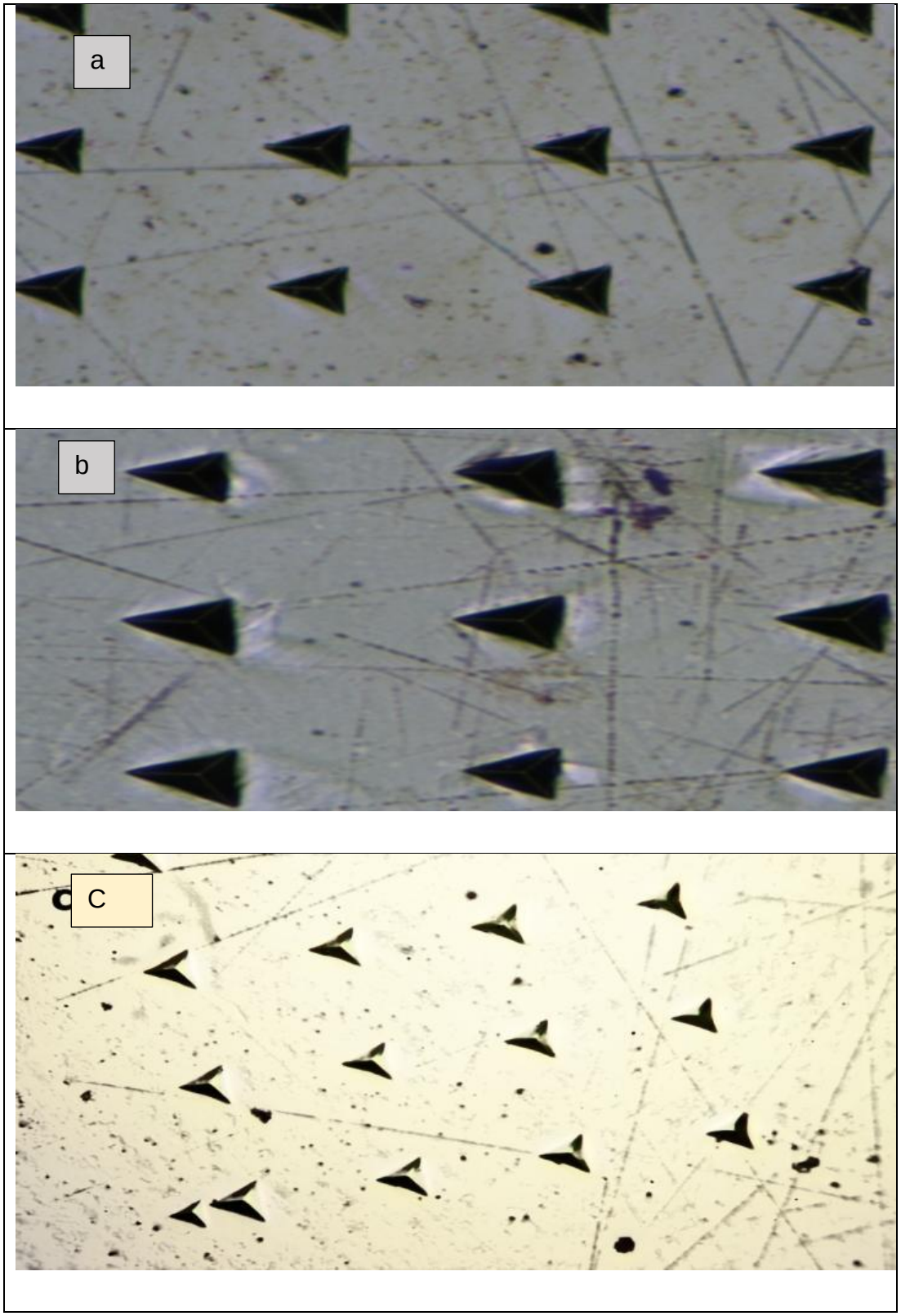

Figure 4. 21**:** The Nano indentations captured on the surface of a) alloy Mg-10wt%Gd, b) alloy Mg-10wt%Gd-0.4wt%Zr, c) alloy Mg-5wt%Gd-5wt%Nd-0.4wt%Zr.

Table 4. 6: The 30 Indentation that were applied to the three specimens (alloys Mg-10wt%Gd, Mg-10wt%Gd-0.4wt%Zr and Mg-5wt%Gd-5wt%Nd-0.4wt%Zr).

Number of indentations	Nano Hardness (Vickers Hardness)		
	Mg-10wt%Gd,	Mg-10wt%Gd-0.4wt%Zr	Mg-5wt%Gd-5wt%Nd-0.4wt%Zr
1	79.616	94.475	118.214
2	94.266	72.073	101.124
3	98.268	88.633	100.277
4	102.458	85.577	95.918
5	96.381	69.218	84.101
6	99.103	76.962	96.348
7	87.772	75.025	88.475
8	107.409	62.724	90.631
9	92.899	88.654	92.56
10	90.283	71.815	105.667
11	77.702	69.428	86.013
12	96.427	81.505	87.386
13	100.302	84.754	96.527
14	76.558	97.464	99.065
15	92.502	74.376	100.767
16	84.032	68.901	99.069
17	82.97	67.12	93.934
18	81.043	85.885	85.264
19	78.972	89.005	87.16
20	86.854	83.476	93.73
21	93.842	72.299	86.267
22	106.038	76.426	94.858
23	88.765	88.425	100.611
24	79.829	76.662	92.552
25		68.837	92.678
26		77.05	94.477
27		56.703	104.44
28		93.219	99.557
29		88.145	102.37
30		85.157	94.369
Average	**90.59546**	**78.99977**	**95.4803**

Further nano-indentation experiments have been carried out for the three alloys (samples A, B and C) in order to make trial to examine a specific phase

such as Mg_5Gd_{12}. The used parameters are the same as the listed in Table 4.5, the only difference here is number of indentations.

Table 4. 7: The recent nano Indentation that were applied to the three specimens (Mg-10wt%Gd, Mg-10wt%Gd-0.4wt%Zr and Mg-5wt%Gd-5wt%Nd-0.4wt%Zr) in order to hit on a specific phases.

Number of indentations	**Nano Hardness (Vickers Hardness)**		
	Mg-10wt%Gd	Mg-10wt%Gd-0.4wt%Zr	Mg-5wt%Gd-5wt%Nd-0.4wt%Zr
1	79.616	52.153	97.646
2	94.266	85.43	67.669
3	98.268	87.356	88.019
4	102.458	71.375	98.864
5	96.381	76.162	81.758
6	99.103	50.854	89.765
7	87.772	91.194	84.334
8	81.043	83.14	88.129
9	92.899	71.052	92.371
10	90.283		100.419
11	77.702		88.234
12	96.427		127.196
Average	**91.3515**	**74.302**	**92.037**

The above table, Table 4. 7 , (the recent Nano-indentation experiments) are in similar behaviour and following the same pattern with the values obtained from the former experiment. The new finding here is that the indentation number 12 of sample 3 was hit on a specific phase (see Figure 4. 22 and Figure 4. 23).

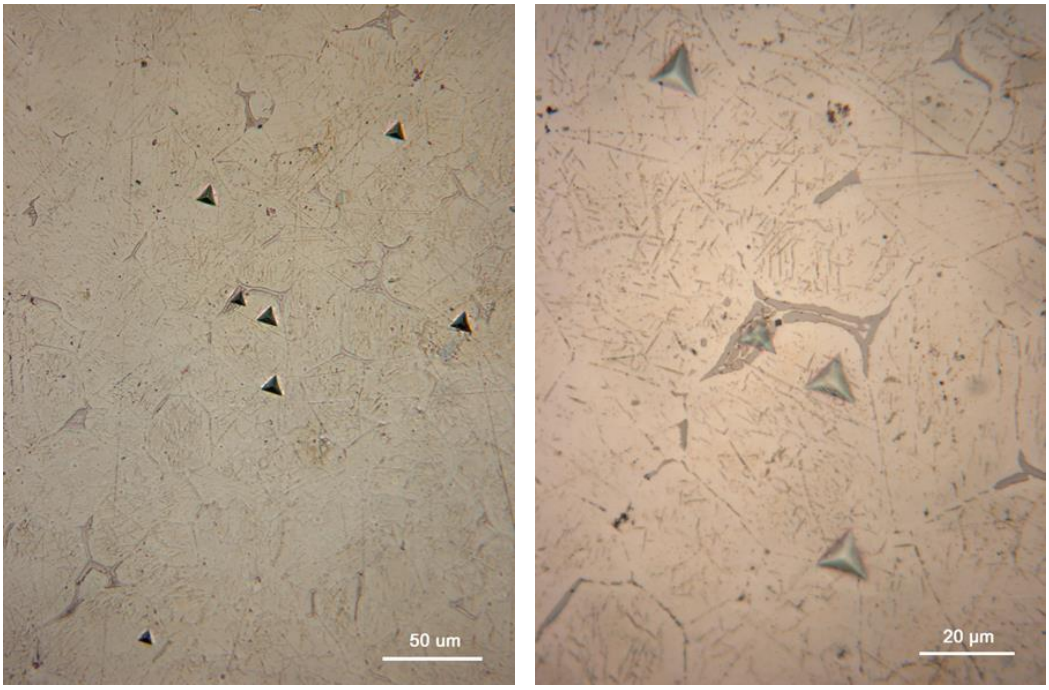

(a) (b)

Figure 4. 22: The optical microscope images of the indentation number 12: a) at 400X magnification and b) at 1000 X magnification.

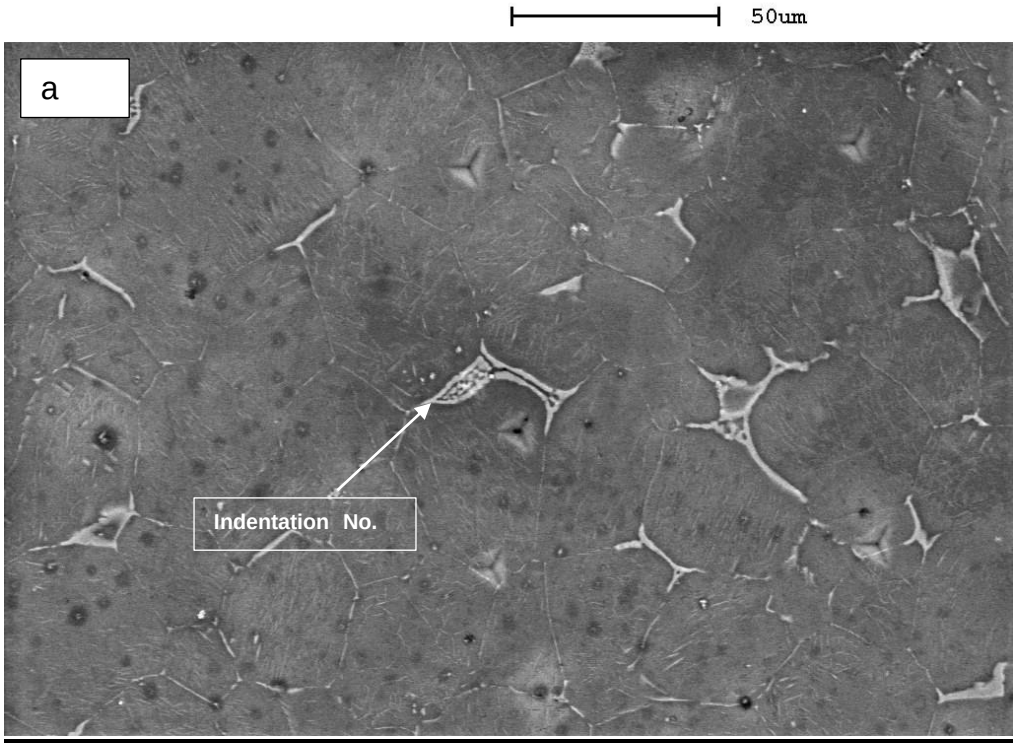

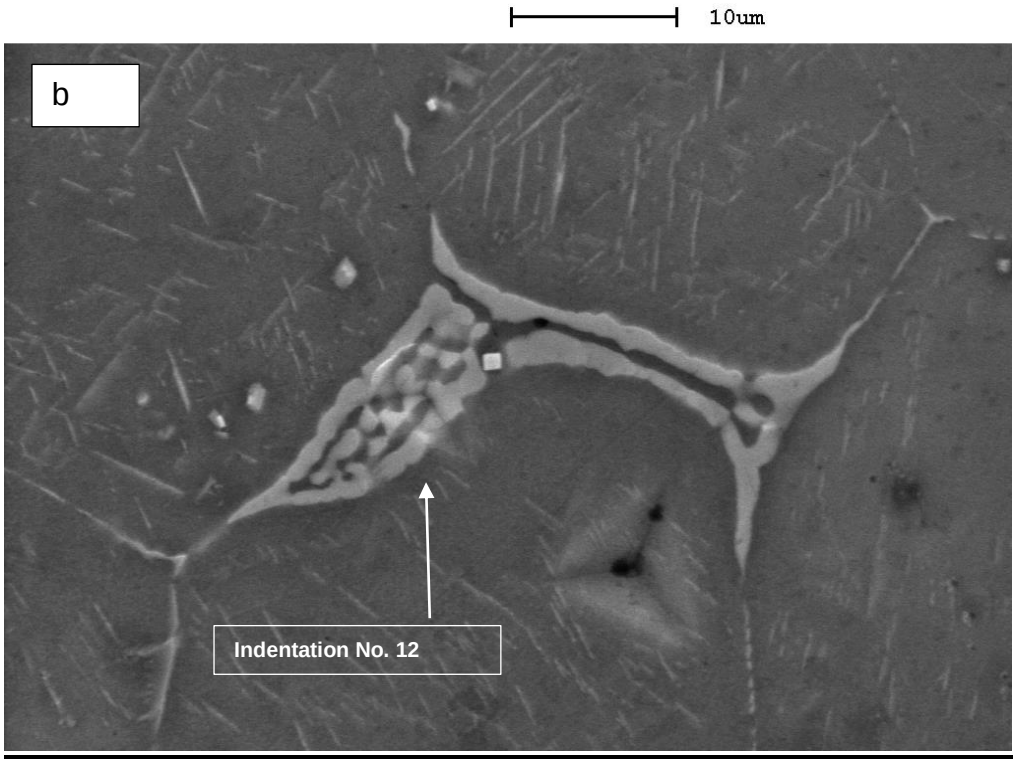

Figure 4. 23: The SEM images of the indentation number 12: a) at 500X magnification and b) at 2000 X magnification.

4.7 Electrochemical corrosion tests

In electrochemical testing, Potentio-dynamic polarisation testing involves scanning the corrosion current variation of the specimen in the specified electrolyte over a range of potential. The range of potential over which the test is carried out depends on the open circuit potential (OCP) measured at the beginning of the experiment. The variation of the current versus the potential is drawn as a curve and it is known as “TAFEL PLOT”.

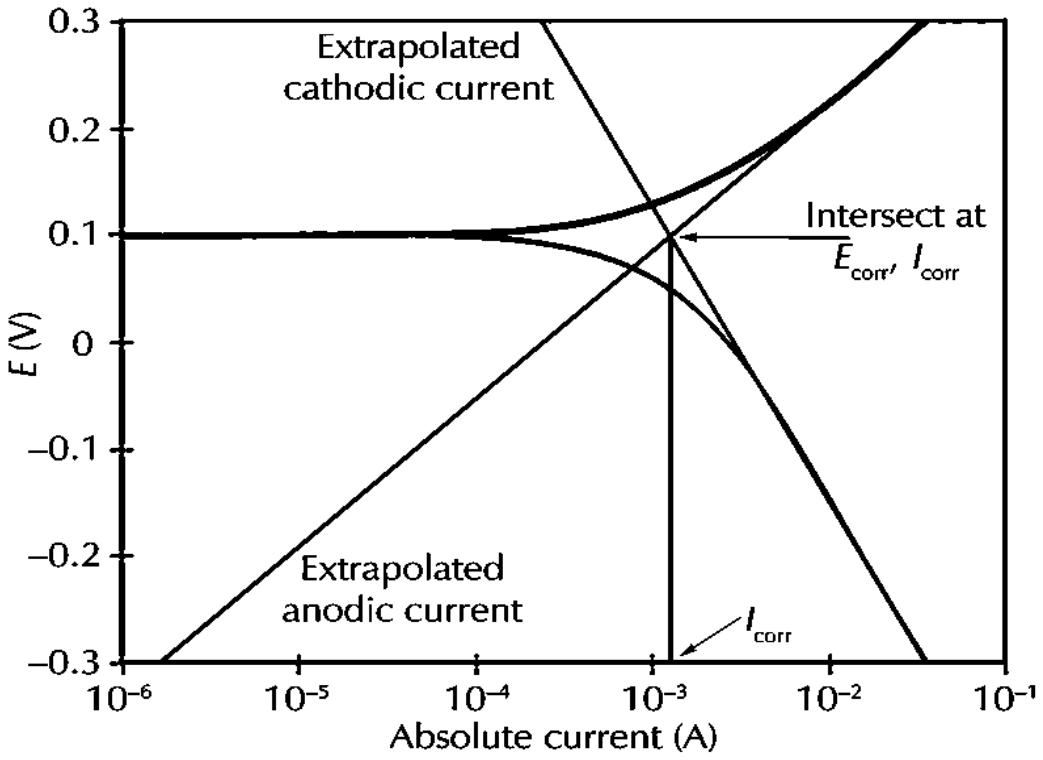

Figure 4. 24**:** TAFEL plot between the measured potential and the current [160].

Figure 4. 24 shows the typical TAFEL PLOT in potentiodynamic polarisation measurement. This consists of cathodic and anodic curves as shown in figure. The extrapolated cathodic current is represented by the slope drawn on the cathodic curve and the extrapolated anodic current is represented by the slope drawn on the anodic curve. The intersection of the both slopes at a point give rise to the corrosion current (I_{corr}). The point on the y axis at which the potential values are common over a current range towards zero current value is known as corrosion potential or zero charge potential (ZCP).

From the TAFEL PLOT the cathodic slope and anodic slopes are measured and substituted in equation 2. Further the corrosion rate of the specimen in the electrolyte is calculated by substituting the corrosion current density in equation 1.

The corrosion rate can be estimated using the following formula [18]

$$CR(mpy) = \frac{0.129x\ I_{CORR}\ xEq.Wt}{D} - - - - - - - - (1)$$

Where, I_{corr} = Corrosion current density in μA/cm^2.

Eq. Wt = Equivalent weight of the corroding specimen in gm.

D = Density of the corroding species in g/cm^3

Dividing the i_{corr} by the specimen area exposed to electrolyte give rise to the corrosion current density I_{corr}.

$$I_{CORR} = \frac{1}{2.3R}\left(\frac{\beta_a\beta_c}{\beta_a+\beta_c}\right) - - - - - - - - - - (2)$$

where R is polarisation resistance (kΩ/cm^2), β_a is anodic slope (Volts/Decade) and β_c is cathodic slope (Volts/Decade). 1 millimetre per year (mmpy) is equal to 39.4 milli inches per year(mpy)

In corrosion measurements of present work, the Magnesium alloy samples of dimensions 2 cm width and 1.5 cm breadth (0.0003 m^2 area) are polished using polishing sheets of SiC grade emery papers and then wet polished using diamond paste of 1 μm size. After the polishing the specimens are subjected to corrosion measurements in 3.5 N NaCl solution and Hank's solution. 600 mL of electrolyte volume is maintained in all electrochemical tests. The potentiodynamic polarisation tests were carried out using corrosion measurement instrument. The method of obtaining the polarization values and R values is the software control of the machine. The time required for the equilibrium curve is three to five minutes. Open circuit potential findings are performed that takes 3 to 5 minutes to achieve equilibrium. The

used software for the experiment is EC-Lab software (version 10.32) and the linear fitting is executed by means of drawing the slopes of anodic and cathodic curves.

Figure 4. 26 shows the three Magnesium alloy specimens just before the test. A three-electrode cell is used to conduct the experiment where the working electrode is the specimen to which the corrosion measurement is carried out, the reference electrode is the calomel electrode and the counter electrode is made of stainless steel. The three-electrode cell is connected to the corrosion-measuring instrument.

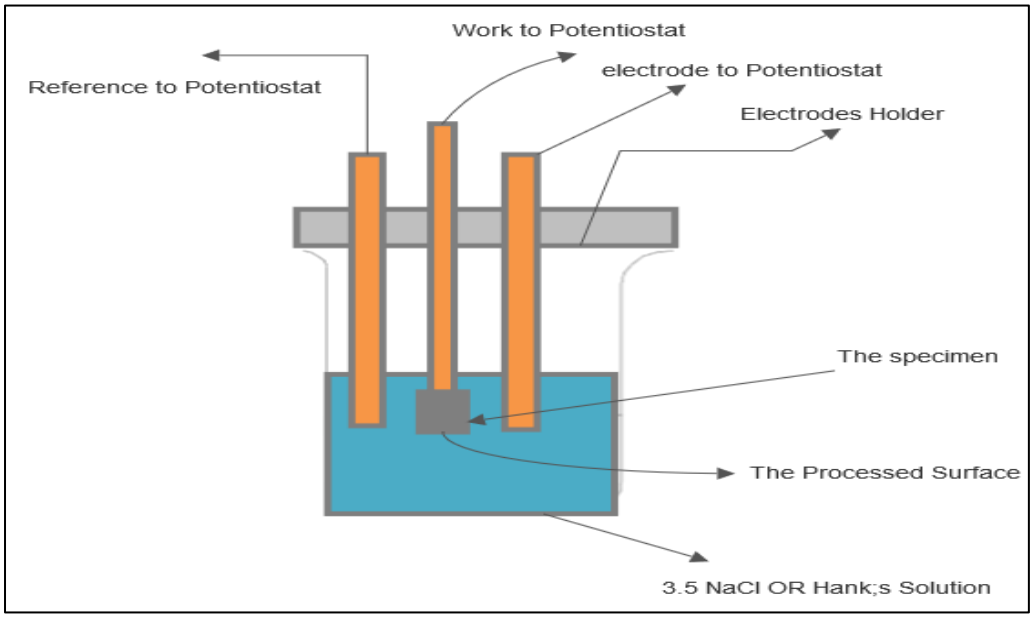

Figure 4. 25: Schematic diagram of electrochemical testing electrode.

Figure 4. 26: Magnesium alloy specimens namely Mg-10wt%Gd, Mg-10wt%Gd-0.4wt%Zr and Mg-5wt%Gd-5wt%Nd-0.4wt%Zr categories before corrosion test.

Table 4. 8: shows the composition of the Hank's solution used in the experimentations.

Number	Constituents	Weight
1	NaCl (mw: 58.44 g/mol)	8 g
2	KCl (mw: 74.55 g/mol)	400 mg
3	$CaCl_2$ (mw: 110.98 g/mol)	140 mg
4	$MgSO_4$-$7H_2O$ (mw: 246.47 g/mol)	100 mg
5	$MgCl_2$-$6H_2O$ (mw: 203.303 g/mol)	100 mg
6	Na_2HPO_4-$2H_2O$ (mw: 177.99 g/mol)	60 mg
7	KH_2PO_4 (mw: 136.086 g/mol)	60 mg
8	D-Glucose (Dextrose) (mw: 180.156 g/mol)	1 g
9	$NaHCO_3$ (mw: 84.01 g/mol)	350 mg

The scanning in polarization of electrochemical test are started from -1800 mV and carried out further up to nearly -1200 mV, after determining the open-circuit corrosion potential for each immersion. The corrosion rates were calculated using the polarization plots registered over the range – 1800 to -1200 to mV. The scan rate in the electrochemical tests were maintained at 0.3 mV/s. In the experiments, the corrosion potentials are referenced to the saturated calomel electrode reference. The corrosion current measurements are carried out in the electrochemical tests.

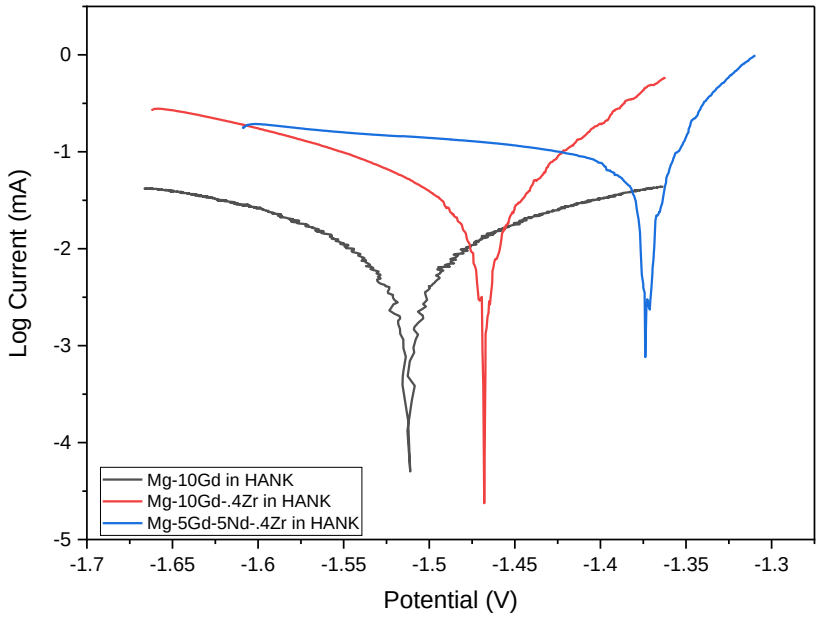

Figure 4. 27: The potentiodynamic polarisation curves of Magnesium alloys in Hank's solution.

Figure 4. 27 show the potentiodynamic polarisation curves of the alloys in Hank's solution. The initial observation shows that the Tafel curve of Alloy Mg-10wt%Gd exists at lower current region when compared to that of other Tafel plots of alloy Mg-10wt%Gd-0.4wt%Zr and Mg-5wt%Gd-5wt%Nd-0.4wt%Zr. This proves that the corrosion current (I_{CORR}) of alloy Mg-10wt%Gd happens to be at lower end when compared to that of the alloy Mg-10wt%Gd-0.4wt%Zr and Mg-5wt%Gd-5wt%Nd-0.4wt%Zr. Similarly, the Tafel plot of alloy Mg-5wt%Gd-5wt%Nd-0.4wt%Zr is at higher current range when compared to that of alloy Mg-10wt%Gd and 10wt%Gd-0.4wt%Zr. This implies that the corrosion current of alloy Mg-5wt%Gd-5wt%Nd-0.4wt%Zr is greater than that of the other groups. The following observation holds good for the magnesium alloys in Hanks solution;

I_{CORR} of alloy Mg-10wt%Gd **<** I_{CORR} of alloy Mg-10wt%Gd-0.4wt%Zr **<** I_{CORR} of alloy Mg-5wt%Gd-5wt%Nd-0.4wt%Zr.

Hence, it can be stated that the alloy Mg-10wt%Gd has lower corrosion rate than that of alloy Mg-10wt%Gd-0.4wt%Zr. The alloy Mg-5wt%Gd-5wt%Nd-0.4wt%Zr has higher corrosion rate in Hank's solution when compared to that of alloy Mg-10wt%Gd and Mg-10wt%Gd-0.4wt%Zr.

4.7.1 Corrosion Rate Calculations

The Tafel plots of the potentiodynamic polarisations analysis give rise to the opportunity to calculate the corrosion rates of the alloy specimens in Hank's solution. This is carried out by drawing the anodic slope and cathodic slope on the Tafel plot of each alloy. A straight line is drawn from the intersection point of the slopes to meet the x axis. The point on x axis where the extrapolated line meets, represents the corrosion current (i_{corr}). The corrosion current density (I_{CORR}) is determined when the corrosion current divided by means of the area of specimen exposed to the electrolyte. Following are the corrosion rate calculation figures of the magnesium alloy groups namely Mg-

10wt%Gd, Mg-10wt%Gd-0.4wt%Zr and Mg-5wt%Gd-5wt%Nd-0.4wt%Zr in Hank's solution (Figure 4. 28, Figure 4.29 and Figure 4.30).

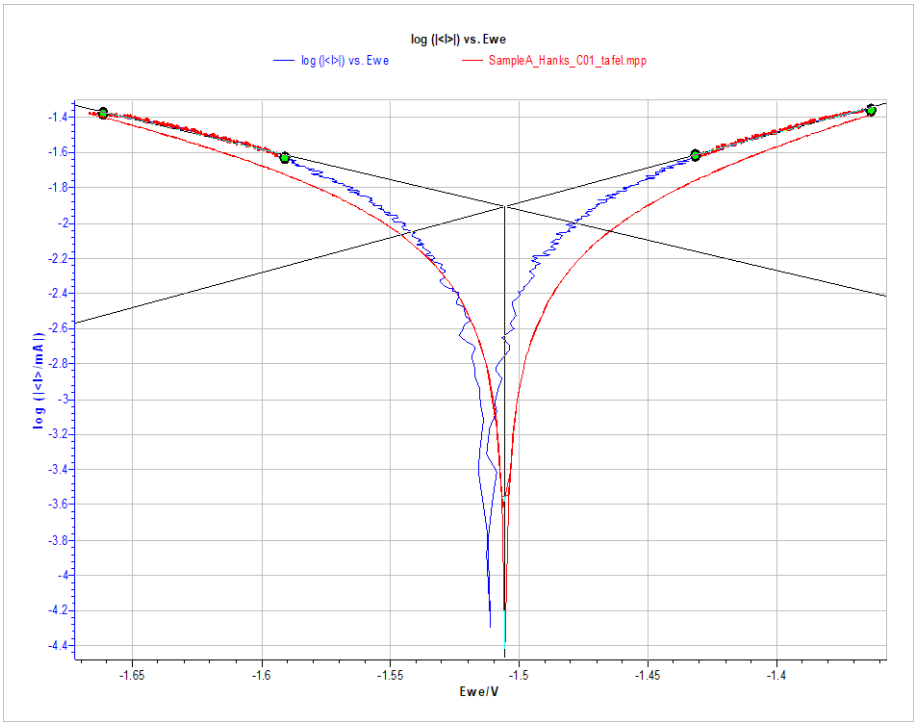

Figure 4. 28: Corrosion rate calculation for the alloy Mg-10wt%Gd in Hank's solution.

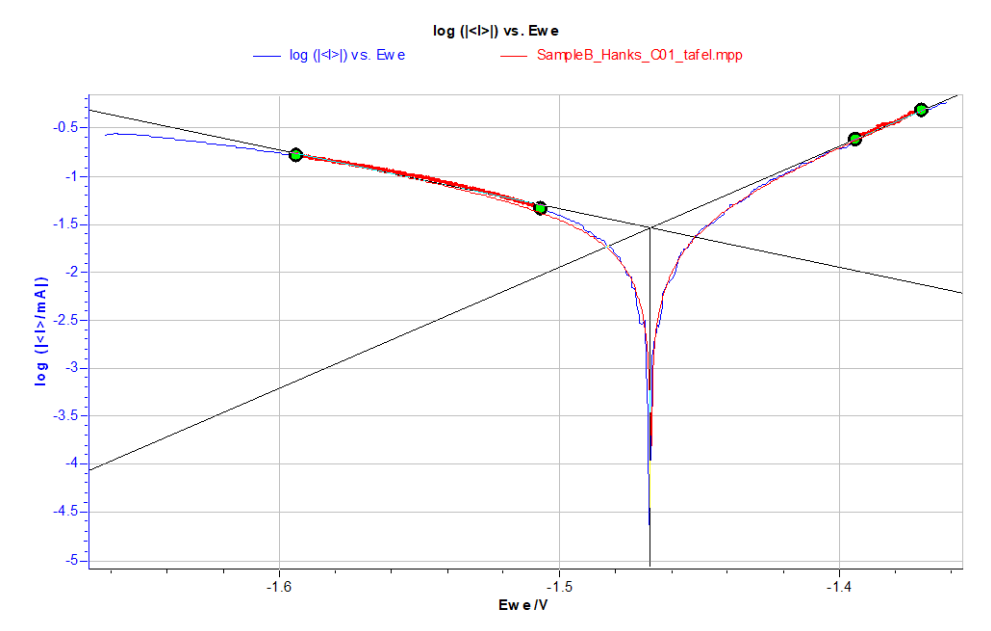

Figure 4. 29: Corrosion rate calculation for the alloy Mg-10wt%Gd-0.4wt%Zr in Hank's solution.

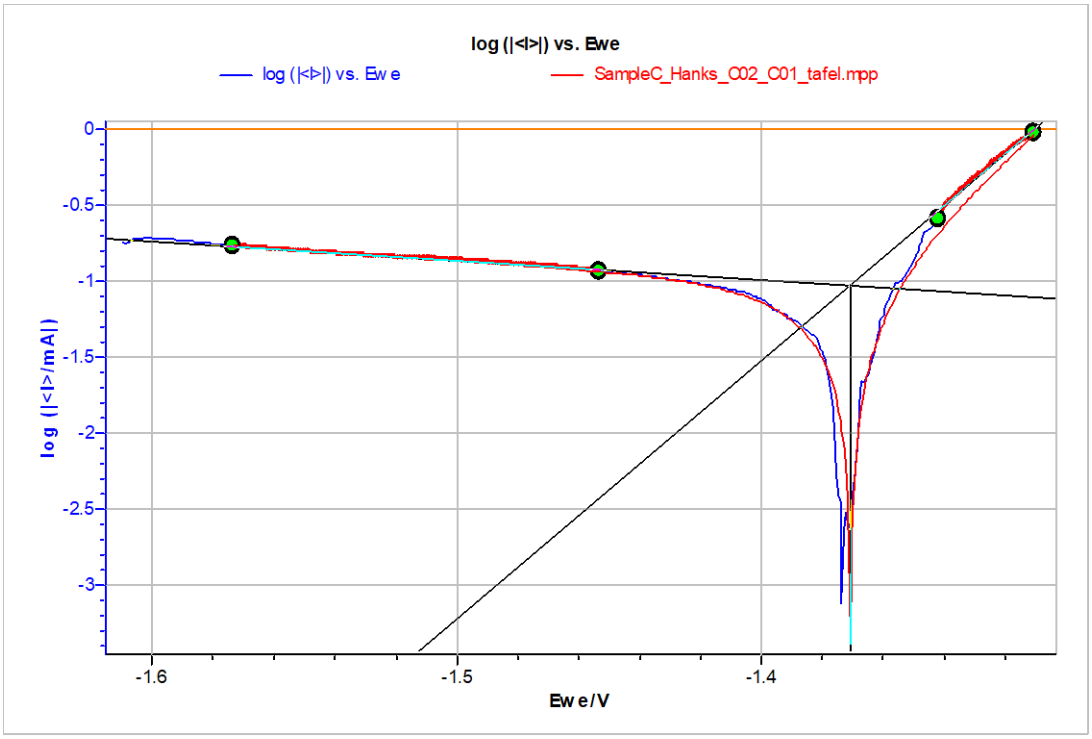

Figure 4. 30: Corrosion rate calculation for the alloy Mg-5wt%Gd-5wt%Nd-0.4wt%Zr in Hank's solution.

Table 4. 9: Corrosion characteristics of the Magnesium alloy groups in Hank's solution

Alloy	**C.R (mmpy)**
Mg-10Gd	0.17661
Mg-10Gd-0.4Zr	0.684213
Mg-5Gd-5Nd-0.4Zr	1.40826

mmpy – millimetre per year

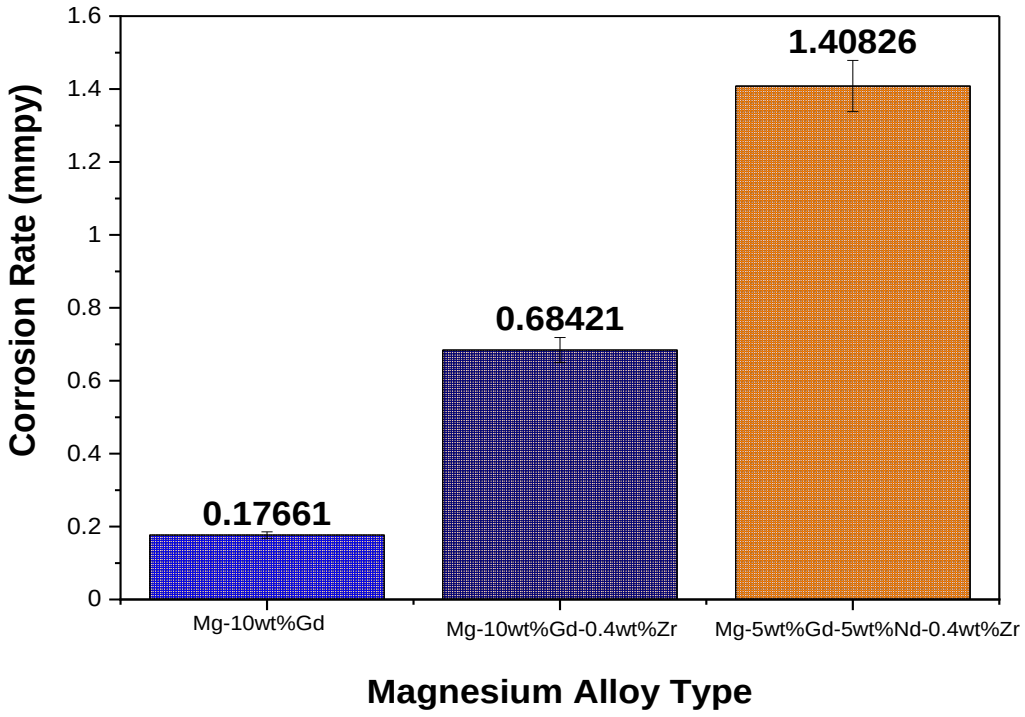

Figure 4. 31 Corrosion rate bar chart for the magnesium alloys in Hank's solution

Table 4. 9 shows the corrosion rates of the magnesium alloys in Hank's solution. The first observation shows that the alloy Mg-10wt%Gd is having lower corrosion rate than alloy Mg-10wt%Gd-0.4wt and Mg-5wt%Gd-5wt%Nd-0.4wt%Zr (Figure 4. 31). The Tafel plot analysis clearly indicates that the corrosion current for alloy is lower than corrosion current of alloy Mg-10wt%Gd-0.4wt. Similarly, the corrosion current of alloy Mg-10wt%Gd-0.4wt is lower than the corrosion current of alloy Mg-5wt%Gd-5wt%Nd-0.4wt%Zr. Hence, this can be directly related to the addition of alloying elements to the Magnesium Gadolinium alloy. Alloy Mg-10wt%Gd contains Magnesium as matrix and Gadolinium as alloying element. Even though the Gadolinium is a rare earth element the intermetallic phases formed by Magnesium and Gadolinium are more noble compare to the matrix. Hence this dissimilarity leads to corrosion of the alloy in Hank's solution [34], [161]. Addition of Nd to the Mg-Gd alloy further leads to grain refinement to the master alloys.

When grain refinement takes place, it leads to improvement in strength of the alloy and it imparts an adverse effect on the corrosion behaviour of the alloy. Generally, grain refinement give rise to quantitative increase in grain boundaries. The grain boundaries are in general, represents the higher energy regions of an alloy matrix. The higher energy region is prone to corrosion in electrolytes when exposed. The grain refinement leads to higher corrosion rate. In addition, the intermetallic precipitates formed in the matrix of the alloy due to addition of Gd and Nd into the Mg matrix are noble by potential than the matrix itself. Hence, this factor can also influence galvanic corrosion of the alloy when exposed to Hank's solution [162], [163].

Addition of Zr further improves the grain refinement to a greater extent leading to much more increase in quantitative nature of the grain boundaries. Hence corrosion rate of alloy Mg-5wt%Gd-5wt%Nd-0.4wt%Zr is more when compared to that of alloy A and B since the combined effect of high level grain refinement and noble nature of intermetallic phases formed by addition of Nd and Zr to the master alloy [164], [165]. Further characterisations like SEM microstructures and EDAX results will explain the corrosion behaviour of the alloys in Hank's solution.

4.7.1.1 Microstructure after electrochemical tests

Figure 4. 32 show the corroded surfaces of magnesium-based alloy groups namely 1, 2 and 3. Fig 10 a, c and e represents the full image of the magnesium alloy specimens 1, 2 and 3 respectively, immersed in Hank's solution for 10 minutes time period. Upon removal, the specimens were dried in air for further investigations.

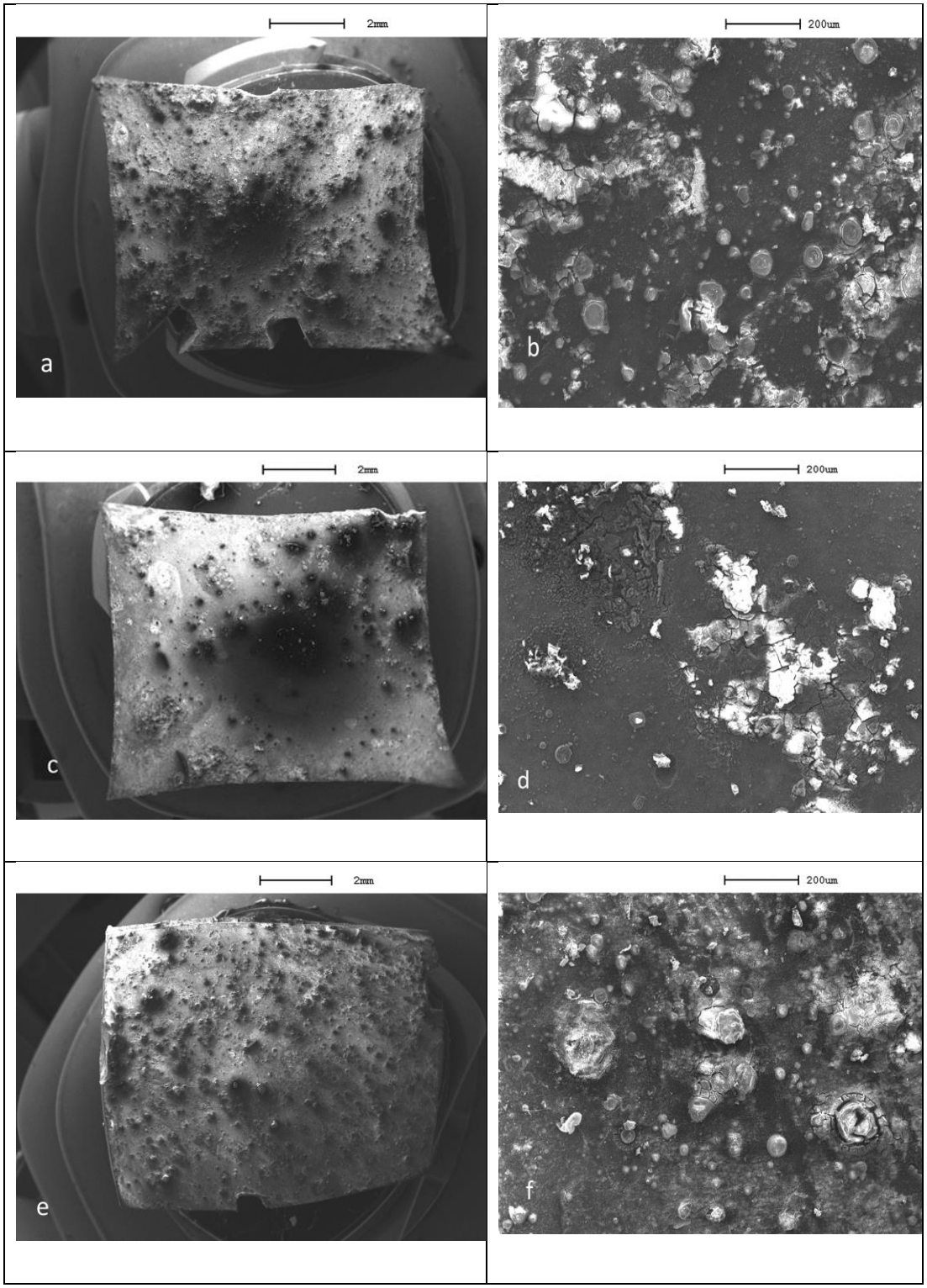

Figure 4. 32: Corroded surfaces after the immersion corrosion test in Hanks solution a) Full specimen of specimen A, b) at higher magnification of specimen A, c) Full specimen of specimen B d) at higher magnification of specimen B, e) Full specimen of specimen C b) at higher magnification of specimen C.

4.7.2 Energy Dispersive X-ray Analysis after the electrochemical Testing

The following figures show the EDAX spectrums of the three samples (sample A, sample B and sample C) after conducting the corrosion behaviour testing (electrochemical).

Figures 4.38, 4.37 and 4.36 show the EDAX spectrum of magnesium alloys A, B and C respectively. All the spectrums show the peaks of oxygen, chlorin, Magnesium, Calcium, Sodium and Potassium revealing that the corrosion has taken place when the alloy A, B and C are immersed in the Hank's solution.

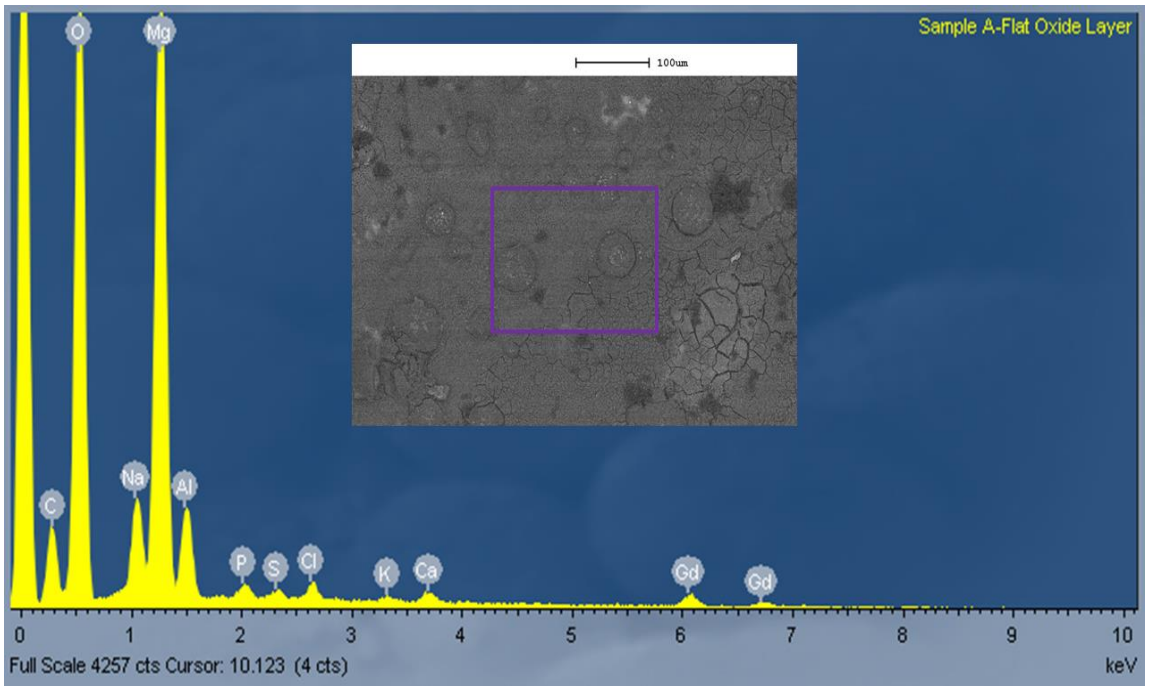

Figure 4. 33: The EDAX spectrum of specimen A after corrosion test in Hank's solution.

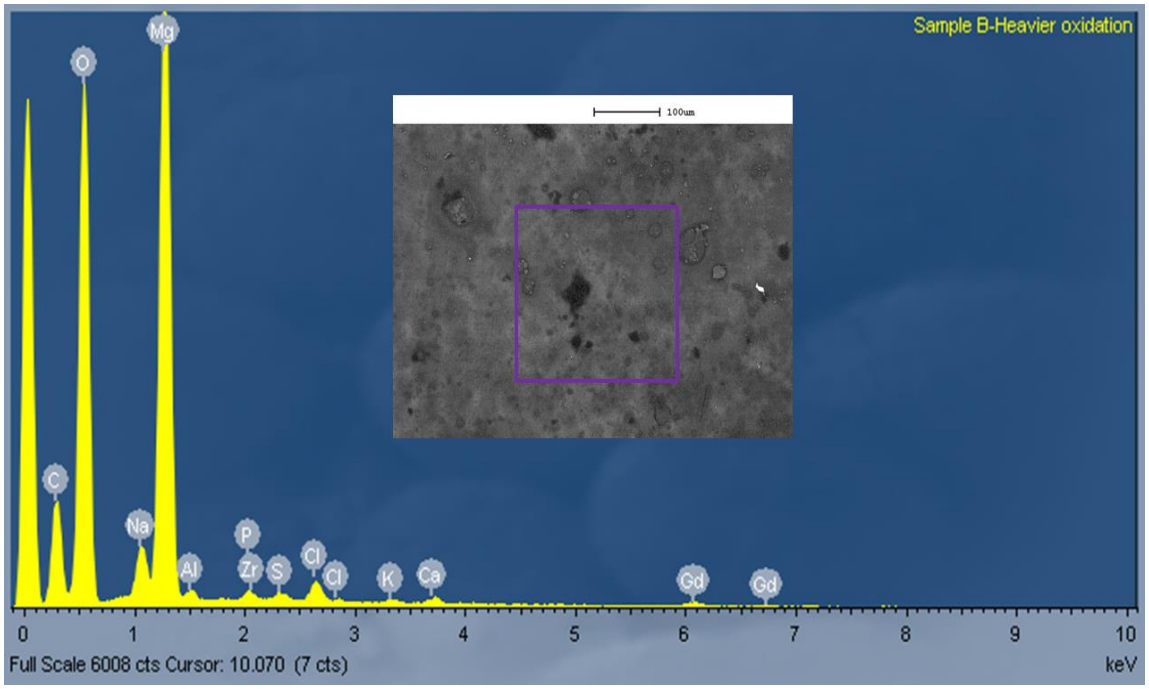

Figure 4. 34: The EDAX spectrum of specimen B after corrosion test in Hank's solution

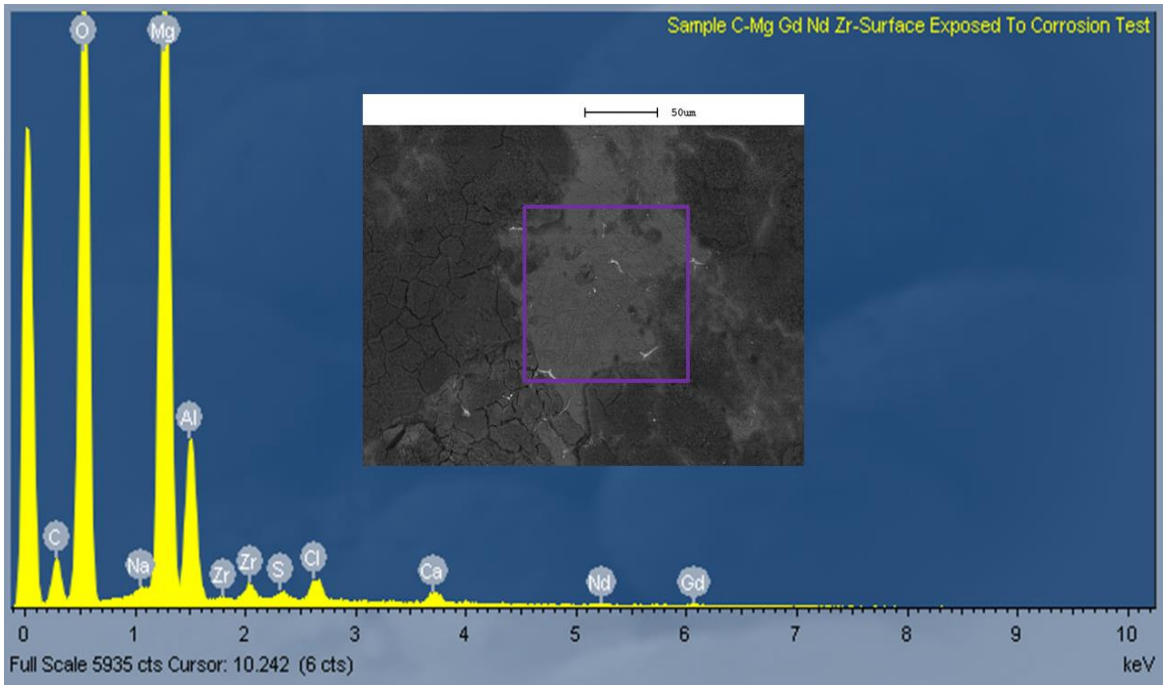

Figure 4. 35: The EDAX spectrum of specimen C after corrosion test in Hank's solution

4.7.3 Summary

Biocompatible grade Magnesium based alloys with alloying elements namely Gadolinium (Gd), Neodymium (Nd) and Zirconium (Zr) are prepared using resistance heating furnace associated with an atmosphere containing both CO2 and SF6. The ratio of CO2 and SF6 gas combinations is maintained as 100:1 respectively. The gas phase Cl6C2 is used for the refining treatment and further the alloy is held at 780 0C for 30 minutes. This leads to melting of the alloy and the molten liquid is poured into pre heated steal die maintained at 740 0C. The prepared alloys groups are named as follows: Category A: Mg-10 wt. % Gd; Category B: Mg-10 wt. % Gd-0.4 wt. % Zr ; Category C: Mg-5 wt. % Gd-5 wt. % Nd-0.4 wt. % Zr.

The initial observation clearly shows the presence of grains and grain boundaries along with the intermetallic precipitates and agglomerations. In the microstructures alloy A, the grains are bigger in size and the intermetallic precipitates namely Mg5Gd are observable uniformly throughout the Magnesium matrix. Intriguing observation of microstructures of Alloy Mg-10wt%Gd-0.4wt reveals the presence of smaller grains. This shows that the grain refinement has taken place to a greater level since the alloy Mg-10wt%Gd-0.4wt has very small grains in comparison with that of alloy A. Another notable difference in alloy Mg-10wt%Gd-0.4wt microstructure is the intermetallic precipitations of Mg5Gd happen to be present more along the grain boundaries than in Magnesium matrix grains. In addition, grain boundaries of thicker nature are observed in alloy Mg-10wt%Gd-0.4wt. The microstructures of alloy Mg-5wt%Gd-5wt%Nd-0.4wt%Zr show that there exists a clear difference in microstructural features in terms of the presence of Mg12Nd phase in the grain regions and as well as in grain boundary regions of the microstructure. The Mg12Nd phase present as small needles oriented in all directions of the grains revealing that there are no specific directional orientations of the needle like structures of Mg12Nd intermetallic phase. The comparative analysis show that in alloy A, the cuboids are present in the grain and grain boundary regions but whereas in alloy Mg-10wt%Gd-0.4wt the cuboids are present along grain boundaries preferentially. These microstructures at higher magnifications prove that in alloy A, the flake like

Mg5Gd precipitates present in the grain regions and where as in alloy Mg-10wt%Gd-0.4wt the same phase exhibit a preferential presence along grain boundaries. The 360 orientations of the Mg12Nd needles are clearly observable in category Mg-5wt%Gd-5wt%Nd-0.4wt%Zr microstructures. At higher magnifications, the presence of Gd cuboids in alloy A and B are clearly observable. In both cases the Gd cuboids are existing in variable sizes. But especially in alloy A, bigger sized cuboids are observed when compared to that of the alloy Mg-10wt%Gd-0.4wt. As one moves on to the alloy Mg-5wt%Gd-5wt%Nd-0.4wt%Zr microstructure, the Gd cuboids are hardly observable. This gives the clear evidence of Gd agglomerations are slowly transforming into Mg5Gd precipitations in alloy Mg-10wt%Gd-0.4wt and Mg-5wt%Gd-5wt%Nd-0.4wt%Zr. The compositional studies by EDAX analysis, reveal that the bulk analysis of alloy A with peaks of Mg and Gd. It proves that the composition of alloy A is consisting of Magnesium and Gadolinium. The EDAX spectrum of Gd cuboid phase of alloy A with peaks of only Gd. This reveals that the cuboids consist of only Gd element. The EDAX spectrum of Magnesium matrix of alloy A with peaks of only Mg. The EDAX spectrum of Mg5Gd intermetallic precipitates of alloy A with peaks of only Mg and Gd. The EDAX spectrum of bulk analysis of alloy Mg-10wt%Gd-0.4wt with peaks of Mg, Gd and Zr. Comparatively smaller peak of Zr represents nearly lower quantity of Zr in alloy Mg-10wt%Gd-0.4wt. The EDAX spectrum of Magnesium matrix of alloy Mg-10wt%Gd-0.4wt with peaks of Mg. Very small peaks of Gd are observed when compared to that of large Mg peaks. The EDAX spectrum of grain boundary region of alloy Mg-5wt%Gd-5wt%Nd-0.4wt%Zr with peaks of Mg, Gd and Nd only. The EDAX spectrum of Zirconium agglomerations of alloy Mg-5wt%Gd-5wt%Nd-0.4wt%Zr with peaks of Zirconium and Mg only. This indicates that the presence of Zirconium particles agglomeration in Magnesium matrix. The EDAX spectrum of Mg12Nd needle like structure of alloy Mg-5wt%Gd-5wt%Nd-0.4wt%Zr with peaks of Mg and Nd. This confirms the presents of Mg12Nd phase in alloy Mg-5wt%Gd-5wt%Nd-0.4wt%Zr.

Further the alloy groups are subjected to hardness measurements. In comparison, alloys A and Mg-10wt%Gd-0.4wt exhibit nearly equivalent resistance to indentation (Hardness) whereas the Vickers hardness value of

alloy Mg-5wt%Gd-5wt%Nd-0.4wt%Zr is greater than that of A and B. This is another supporting result proving the synergic effect of presence of Gd and Nd promoting the precipitation formation due to reduced solid solubility of each element in Magnesium. The higher hardiness value of the alloy Mg-5wt%Gd-5wt%Nd-0.4wt%Zr proves that the precipitation hardening and grain boundary strengthening of the master alloy (Mg – 10 wt.% Gd) when added with 5 wt. % Nd and 0.4 wt.% Zr.

The corrosion mechanism involves metal atoms reacting to Hank's solution containing chlorides, sulphates of Potassium, Magnesium and sodium elements etc. At initial stages, the reactions are confined to few islands expanding in region size and as the time progresses the number and size of islands of corrosion reactions are increasing. This leads to hydrates and hydroxide products on the surface of the exposed alloys for example Cl, K, Na, S and Mg containing hydrates and hydroxides. Upon drying, they transform into oxides and salts layers on the corroded surface of the alloys. Corresponding EDAX analysis show that the surface morphology of the corroded specimen in terms of wide-open oxide scales, stained regions, uniformity and quantitative nature of the settled islands separated by cracks and spallation's clearly indicate that the alloying additions like Nd and Zr to the master alloy leads to increased corrosion activities in Hank's solution.The segregation of Gd cuboids gradually decrease in size as the addition of Nd and Zr are employed to the master alloy A . As the microstructure of the alloys solidified with increasing intensities of magnetic fields were analysed gradually, It can be stated that the synergic effect of Gd and Nd promoting the intermetallic precipitate formation rather than segregation of Gd as cuboids in the Magnesium matrix.

The microstructural features show that the preferential existence of Gd cuboids and Mg_5Gd intermetallic along the grain boundaries. This is very well supported by the EDAX spectrum of grain boundaries of alloy Mg-5wt%Gd-5wt%Nd-0.4wt%Zr showing the peaks of Mg, Gd and Nd. The Higher Gd content in Magnesium alloys, leads to grain refinement as well as solid solution strengthening due to the complete dissolution of Gd in to Magnesium. Addition of Zirconium to the Mg-Gd and Mg-Gd-Nd system,

leads to effective grain refinement by means of pinning the grain boundaries to hinder the further growth of grains. In fact, the presence of Zr particles along the grain boundaries, impede the dislocation motion during the deformation process.

Chapter 5 Discussion of Al-20%Si

In recent years, numerous methodologies including the pulse magnetic field method has been used in grain refinement of Al based alloys. In this research the Al-20%Si alloy was chosen to investigate the effect of pulse magnetic field on the control of the primary Si and the eutectic Si phases. The following section discuss the mechanism of how pulse magnetic field is able to refine the primary Si and the eutectic Si phases.

5.1 The effect of Pulse Magnetic Field on the microstructure of Al – 20%Si

The results of microstructural analysis reveal that the plate like coarser Si phases found in bottom portion of the solidified alloy have undergone several phase changes with respect to the increase in magnetic field intensity. Actually, Si phases are smaller in size and having different shapes like spheroidal and thin plate structures when subjected to pulsed magnetic field intensity. As the discharging voltage increases the Si phases become finer and finer, resulting in uniform distribution throughout the matrix. Similar trend is observed in the case of lamellar structure of Si phases. When there is no magnetic field effect, the lamellar Silicon structures are coarser. Further, when the discharging voltage is increased then the fine nature of the lamellar Si structure increases. Moreover, the grain refinement with respect to application magnetic field is clearly evident. Fig 3.3 to 3.11 represents the SEM micro-structural analysis of the bottom middle and top portions of the pulsed magnetic field assisted solidified Al-20% Silicon alloys. In general, the analysis reveals that the primary Si plate like structures are observed to be coarse and thick in size at zero magnetic field intensity when compared to that of the micro-structures of the alloys solidified at 0.3, 0.7, 0.85, 1 and 1.4 Tesla magnetic field intensity. This is the clear evidence of the virgin Si plate like structures get refined in size and shape as the magnetic field influences the solidification process. This trend is possible in metallic alloys when alternating magnetic field is applied during solidification. In Al-7%Si alloy, grain refinement is achieved by means of magnetic stirring mechanism [166].

The variation in microstructures between the bottom middle, top parts can be correlated to the vertical direction solidification of the alloy due to different cooling rates. A research work carried out in similar domain reports that the differential macro segregation of primary Silicon structures in Aluminium Silicon alloy is possible when the casting is carried out in smaller sized dies or small moulds of thin cross-sections. Differential mass percentage of Silicon are found in wheel casting [167]. Another relevant literature report focused on the joule heating of the molten alloy and discovered that the supplied heat energy has to be uniform throughout the solidifying liquid during the application of magnetic in order to refine the grain size. If there is a variation in heat energy through the liquid, then the re-melting of detached nuclei occurs at higher thermal points [168]. In addition, the magnetic field application, promotes the convectional stirring of the molten liquid enhancing the differential movement of denser medium like primary Silicon embryos to the peripheral regions of the mould especially to the bottom [169].

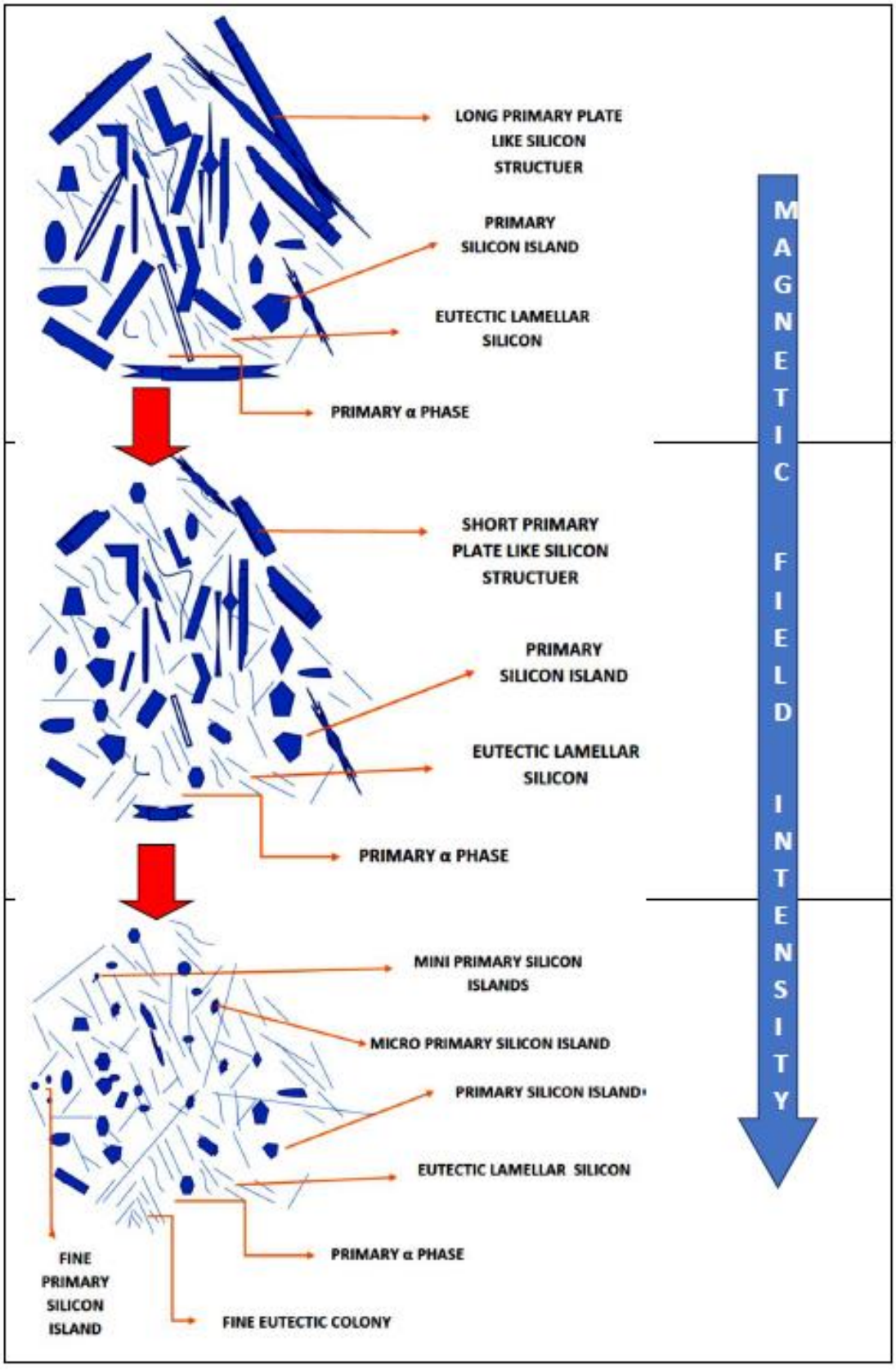

Figure 5. 1**:** represents the pictorial diagram of microstructural transformation of Al-20%Si alloy due to pulsed magnetic field application during solidification.

5.2 The effect of Pulse Magnetic Field on the Primary Si Particles

The primary Si phases are broken into smaller islands of Si at ~1.4 Tesla. The transformation happens by means of restriction of formation of larger size primary Silicon structures during solidification. This in turn vastly improves the distribution of the Si atoms in matrix of Aluminium. The microstructural and EDAX analysis of the alloys clearly reveal that the distribution of Si phases and morphology become more homogenous as the intensity of the magnetic field increased. Fig 3.12 to 3.14 represent the EDAX analysis of the pulsed magnetic field assisted solidified Al- 20% Si alloys. The EDAX spectrum obtained using bulk analysis of the matrix of the alloy show comparatively smaller peak for Si revealing that the Si distribution is less in the matrix for zero magnetic field intensity driven solidification. Whereas the same analysis for the alloys solidified with the exposure to magnetic field intensity show increased peak length for Si revealing that the matrix consisting enhanced Si distribution. Earlier statement relates to the grain refinement occurrence happened to be the cause of achieving uniformity in Si content of the matrix. Hence it can be stated that the EDAX analysis is also supporting the key findings of this work as the grain refinement of primary Si plate-like structure. The uniformity of Si distribution is observed in 6061 Al Si alloy solidification studies carried out under the influence of magnetic field [170].

The larger primary Si phases gradually transform into uniformly distributed Si Islands. 1.4 Tesla resulted in the maximum refinement effect on the primary Si phases. In addition, Figure 5.1 represents the pictorial diagram of morphological changes during pulsed magnetic field assisted solidification showing the gradual changes in microstructures. Hence it can be stated that the pulsed magnetic field application leads to effective grain refinement for the Si phases.

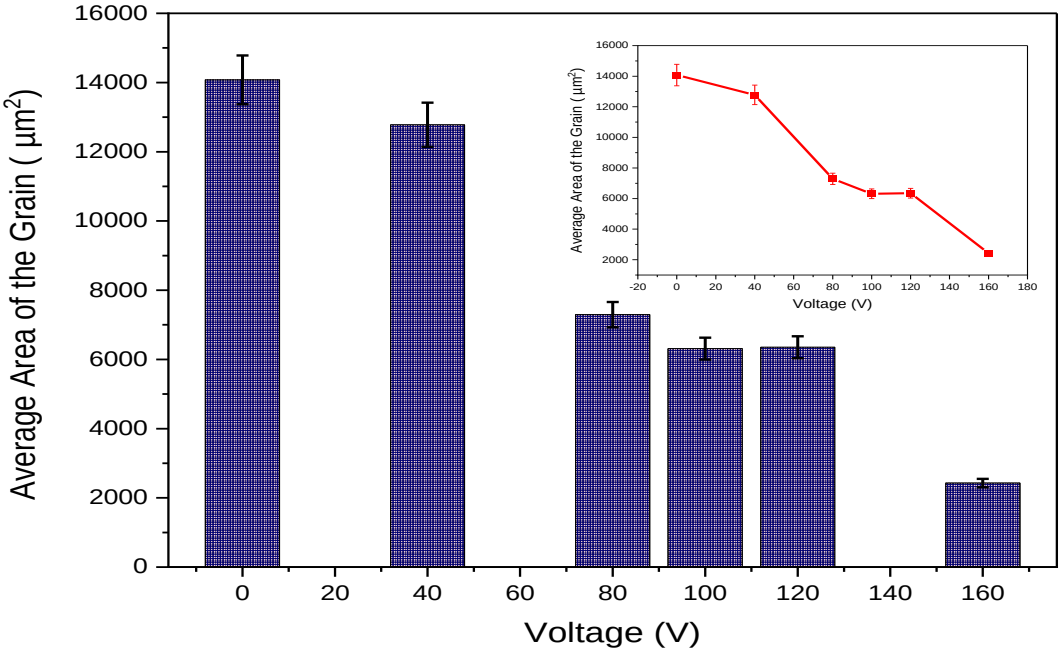

Figure 5. 2**:** The bar chart of variation of Average Grain Area with the voltage.

Figure 5. 2 shows the variation of average area of the grain with respect to the variation in variation in applied magnetic field intensity. In addition, The SEM analysis confirms the presence of primary Aluminium α phase surrounded by the primary Si and the eutectic Si phases. The eutectic regions of the alloys solidified at different discharging voltages are chosen for the elemental analysis. The corresponding peaks observation reveal that the application of the magnetic field leads to the refinement in the eutectic lamellar or acicular Al + Si structure. The Combined analysis of EDAX and SEM micro-structures give clear indication for the grain refinement of the primary Si plate-like structures into a gradual transformation of Al+Si eutectic lamellar structure. The corresponding evidence are observed in Fig 3.3 to 3.11 and Fig. 3.12 to 3.14. In fact, the latter is very clear in terms of the micro structural features registered in this regard. When the grain growth is restricted, possibility of increasing the formation of secondary phase structures is inevitable. The grain growth restriction result of present study is consist with the literature [171][172]. This can be attributed to the reduction in interlamellar spacing within the eutectic phase [148]. The systematic microstructural analysis of the Al-20 %Si alloy solidified with the influence of pulsed electromagnetic fields of varying intensities (aforementioned)

interprets the following microstructural changes with respect to increase magnetic field intensity;

- The massive, longer plate like primary Silicon structures and coarse Silicon islands observed at the zero magnetic field conditions have transformed into shorter plate like primary Silicon precipitates and Silicon islands respectively upon application of magnetic field of discharging voltages from 40 to 100 V. Further increase in magnetic field intensity corresponding to the discharging voltages 120 -160 V, leads to transformations of shorter plate like Silicon structures into primary Silicon islands and the primary Silicon islands into mini, micro, fine Silicon islands (Fig. 3.3 to 3.11). In a related research dealing with Al-30%Si alloy, the Silicon rich layers of the matrix gradually transform into smaller ones as the magnetic field is applied during the solidification [172].
- The restriction of growth of the massive primary Silicon structures enrich the liquid in Silicon content and this leads to formation of virgin eutectic Si+ Al colonies. When there is a quantitative increase in the virgin eutectic Al+ Si colonies, then it is very evident that the lamellar structure also getting refined with the influence of magnetic field of increasing intensity (Corresponding to aforementioned discharging voltages), (Fig.3.25 to 3.26) [169].

5.3 Effect of Magnetic on the Mechanical Properties of Al–20%Si

Vickers harness of the Al-20% Si specimens solidified in the atmosphere of pulsed magnetic field show a clear variation of hardness with respect to the intensity of applied magnetic field. The hardness increases sharply until 0.7 Tesla and a gradual variation is observed until 1.4 Tesla as shown in Figure 5. 3.

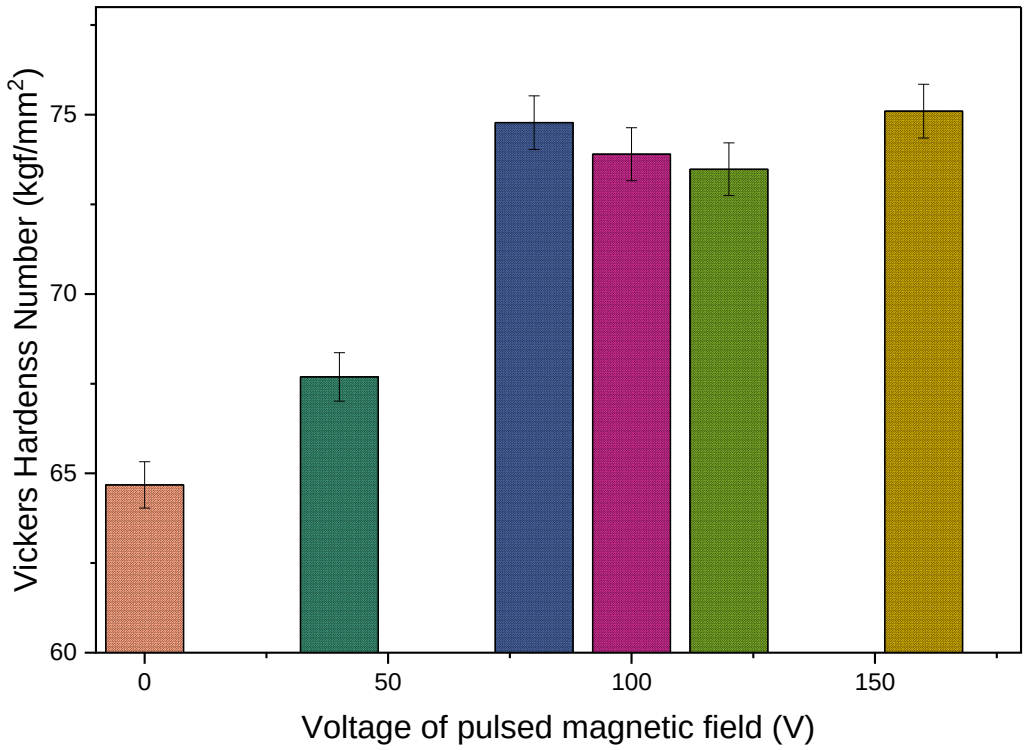

Figure 5. 3**:** The bar chart of hardness number with voltage.

The microstructural correlation with hardness reveals the micro graphical changes taking place with respect to applied pulsed magnetic field. The larger sized primary Silicon plate like structures existing in the microstructures of zero magnetic field- solidified alloy undergo a major transformation into smaller longitudinal thin primary Silicon plates up to 0.7 Tesla. These changes gradually leads to grain refinement and hence increase in mechanical properties due to the strengthening mechanism by grain refinement [173].

When the magnetic field increased up to 1.4 Tesla, leading to the alteration of microstructures resulting in lean-structured primary Silicon layers. By restricting the bigger Silicon structures from forming, the Al-Si eutectic formation is preferred comparatively. This enhanced the distribution of Silicon particles considerably in the matrix of the alloy. As a result, the denser Al-Si dendritic like structure can influence the variation in mechanical characteristics significantly [166]. As per the microstructural morphology of Al-20%Si alloys, primary Silicon plate like structures, primary α phase and

eutectic Al- Si lamellar structures are clearly observable. The result analysis clearly indicates that the primary larger Si plate like structures observed in the magnetic field less solidified alloy are gradually transforming into smaller Si plate like structures, micro Si islands, mini Si islands and fine Si islands. In addition, the macro Al – Si eutectic lamellar phase transforms into micro eutectic Al-Si lamellar phase and finer eutectic Al – Si lamellar structure as the applied magnetic field intensity is increased (Fig.3.6 to Fig. 3.8). The transformation of macro Al-Si eutectic phase into micro phase is reported in Al-Fe-Si alloy [171]. As an overall transformation, the restricted growth of primary Si plate like structures results in finer eutectic Al-Si lamellar phase formations leading to improved uniformity of Si phase distribution in the lattice of Aluminium. Therefore, the micro hardness measurements are focussed and employed on the eutectic Al-Si lamellar phase of the entire category pulsed magnetic field assisted solidified alloys.

Based on results of mechanical testing of Aluminium Silicon alloys, the Vickers hardness value of the solidified alloy increases significantly until the 0.7 Tesla except the gradual fluctuation that was noted at higher power levels (Figure 3. 19). The microstructural correlation with hardness depicts the microstructural changes related to applying pulsed magnetic field. With zero magnetic field-solidified alloys, larger primary Silicon particles plates like structures are observed and they are converted into smaller primary Silicon plates as the application of the magnetic field is employed. The results clearly indicate that the applied pulsed magnetic field intensity effects the grain refinement of Al-20 Si alloy during solidification and in turn resulting in enhancement of its mechanical properties like hardness (Fig.3.34 and Fig. 3.35). In the research work related to the Al-Fe-Si alloy, it is reported that the grain refinement of secondary phases in the matrix of the alloy leads to improvement in mechanical properties [171].

Chapter 6 Discussion of Mg-Gd based alloys

6.1 Design and characterisation of Mg based alloys

In recent years, Mg-Gd based alloys have been developed to have desired mechanical properties and appropriate corrosion behaviour for biomedical applications. The microstructures and properties are tailored by adding appropriate alloying elements like Neodymium, Zirconium. The following sections discuss the composition and microstructure relationship of three Mg alloys with different addition of Nd and Zr.

6.2 Effect of alloying elements on the grain refinement of Mg-Gd master alloy

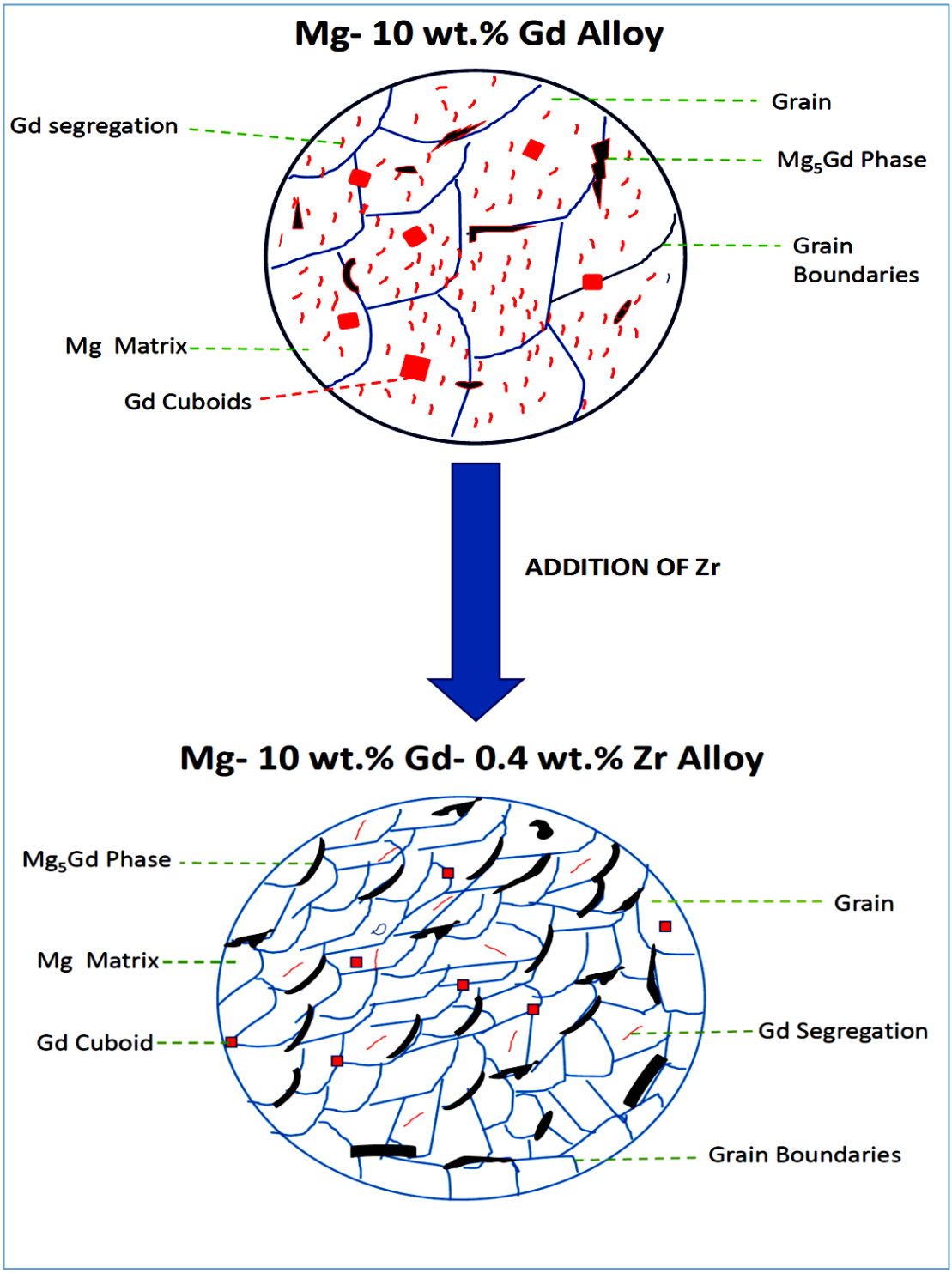

Figure 6.1: The pictorial diagram of microstructural modifications when the Zr is added to master alloy Mg-10 wt. % Gd.

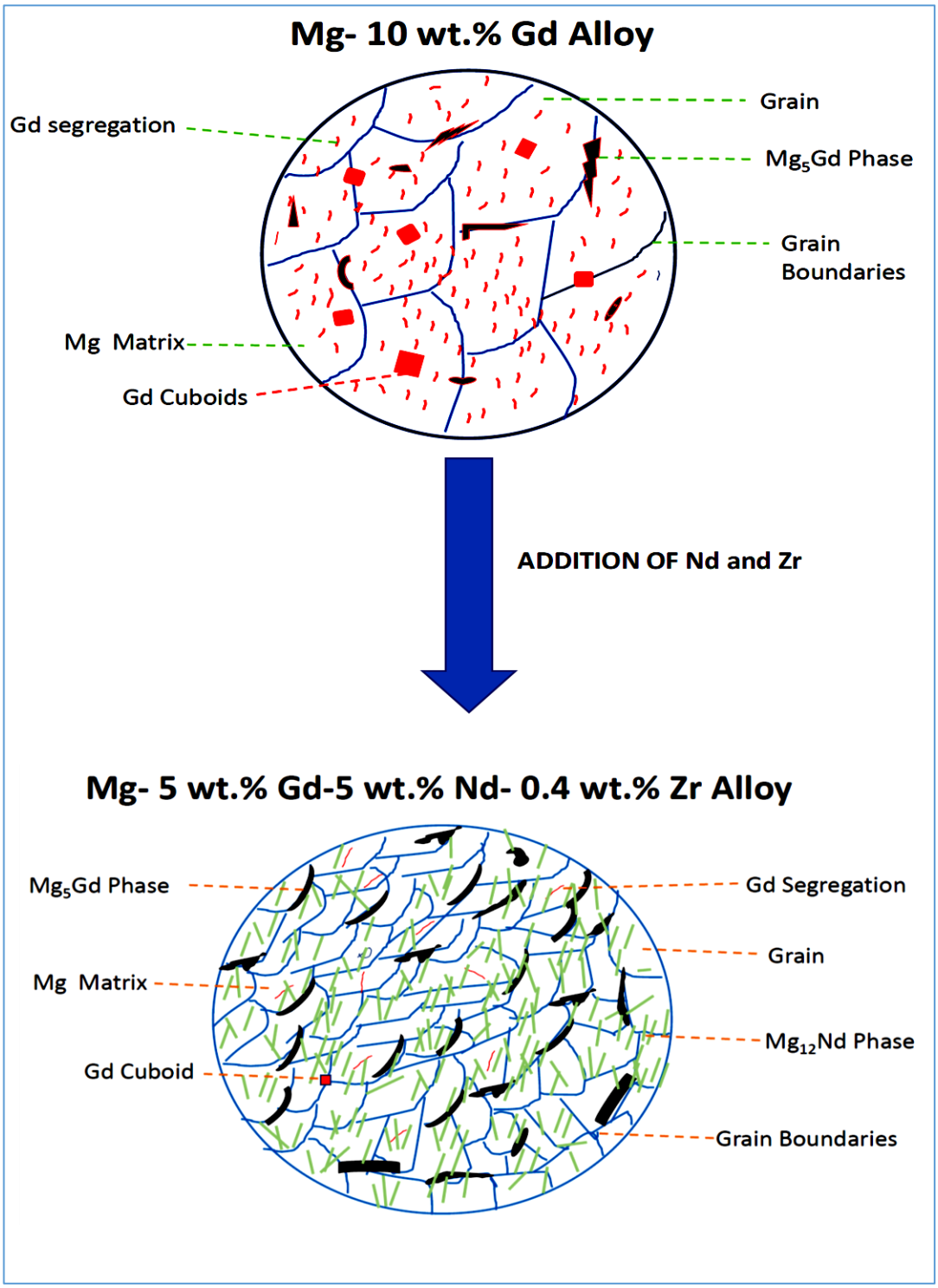

Figure 6.2: The pictorial diagram of microstructural modifications when the Zr and Nd are added to master alloy Mg-10 wt. % Gd.

As per the microstructural and elemental analysis (EDAX) of the developed alloys namely “Mg- 10% Gd - the master alloy” exhibit a microstructure of comparatively bigger grains and quantitatively lesser grain boundary regions. Gadolinium cuboids are very much observable with variable size presence in grains as well as grain boundaries. In the optical microscope pictures (Fig 4.1 to 4.4), it is clearly evident that the variable sized Gd cuboids are present in the matrix. In a research work carried out on Gd containing Mg-Gd-Y-Nd-Zr alloy, it is reported that the dynamic recrystallisation of Gd leads to variation in cuboidal sizes [174]. The segregation of Gd element through the grains are noticed. Mg_5Gd flake like structures are present at the grains and as well as grain boundaries. Magnesium matrix free of any precipitates and segregates are observable. The corresponding scanning electron micro-structural analysis (Fig. 4.5 to 4.8) reveal the non preferential segregation of Gd cuboids both with in grains and at grain boundaries. More over the matrix regions free of the precipitates are also observed. Similar trend is observed in the case of Mg5Gd flake like structures present at both grains as well as grain boundaries. In the similar research domain dealing with Mg-Gd alloy (0.01 and 0.06 At%G), it is revealed that the Gd solute clustering and grain boundary segregation are preferential during sonification [175]. Further Mg-10% Gd - 0.4 % Zr is developed and characterised. Addition of Zirconium leads to grain refinement of the alloy to a greater level. This in turn reduces the size of Gd cuboids. The corresponding inference can be stated as the Zr addition leading to grain refinement, the uniformity in distribution of Gd atoms in the Mg matrix is improved so that the reduced size of Gd observed. In Fig. 4.4 the optical micro-graph of the Mg -10% Gd -0.4 % Zr alloy, noticeable change in grain size is observed when compared to that of the aforementioned master alloy. This trend is observed when analyzing the SEM micro-graphs of the alloys at higher magnifications (Fig.4.8). Fig.4.12 gives the clear evidence for the presence of Mg5Gd precipitates in matrix of the alloys. This is a possible result, similar observations in work concerned to Mg-10Gd is reported recently [165]. Moreover, the preferential presence of Mg_5Gd precipitates at the grain boundaries are noticed and it can be correlated to the increased quantitative nature of the grain boundaries of the matrix with classification as higher energy regions [165], [176].

Addition of 5% of Nd and 0.4 % Zr leads to the development of Mg- 5% Gd – 5% Nd -0.4 % Zr alloy and show the following microstructural modifications. Fig.4.7 and Fig 4.8 show that the addition of Nd to the alloy further enhances the grain refinement. This is observable when the grain sizes are viewed from the micro-structures of the master alloy followed by the Mg-10% Gd - 0.4 % Zr and then the Mg-5% Gd -5% Nd- 0.4 % Zr. Reports suggest that the solid solution strengthening and secondary phase strengthening are possible outcome of increasing Nd/Gd ratio [177]. Grain refinement of the master alloy is further improved by means of the presence of Nd and Gd [178]. Importantly, the precipitations of Mg_5Gd flake like structures is improved quantitatively along with the presence of needle like $Mg_{12}Nd$ structures appearing to be projecting from the grain boundaries to the grain regions [178]. This can be attributed to the synergic effect of the presence of Gd and Nd in the Magnesium matrix. Another interesting observation is the precipitations of Mg_5Gd and $Mg_{12}Nd$ phases not showing any preferred direction of orientations. These phases precipitated in all directions of the matrix revealing that there are no effects of hot working or cold working. The inference can be stated as if the various preparation steps of alloy specimens have not affected its microstructural features, (Fig.4.7 f and Fig 4.8 f). The regions of Magnesium matrix, free of any precipitations and segregations have observed to be gradually decreasing in size when the additions of Zr and Nd to the master alloy. This can be attributed to the grain refining effect of Zr additions and the synergic effect of presence of Gd and Nd promoting the precipitation process rather than segregations in the matrix. These microstructural modifications of the master alloy when added with Nd and Zr are clearly depicted in pictorial diagrams Fig. 6.1 and 6.2.

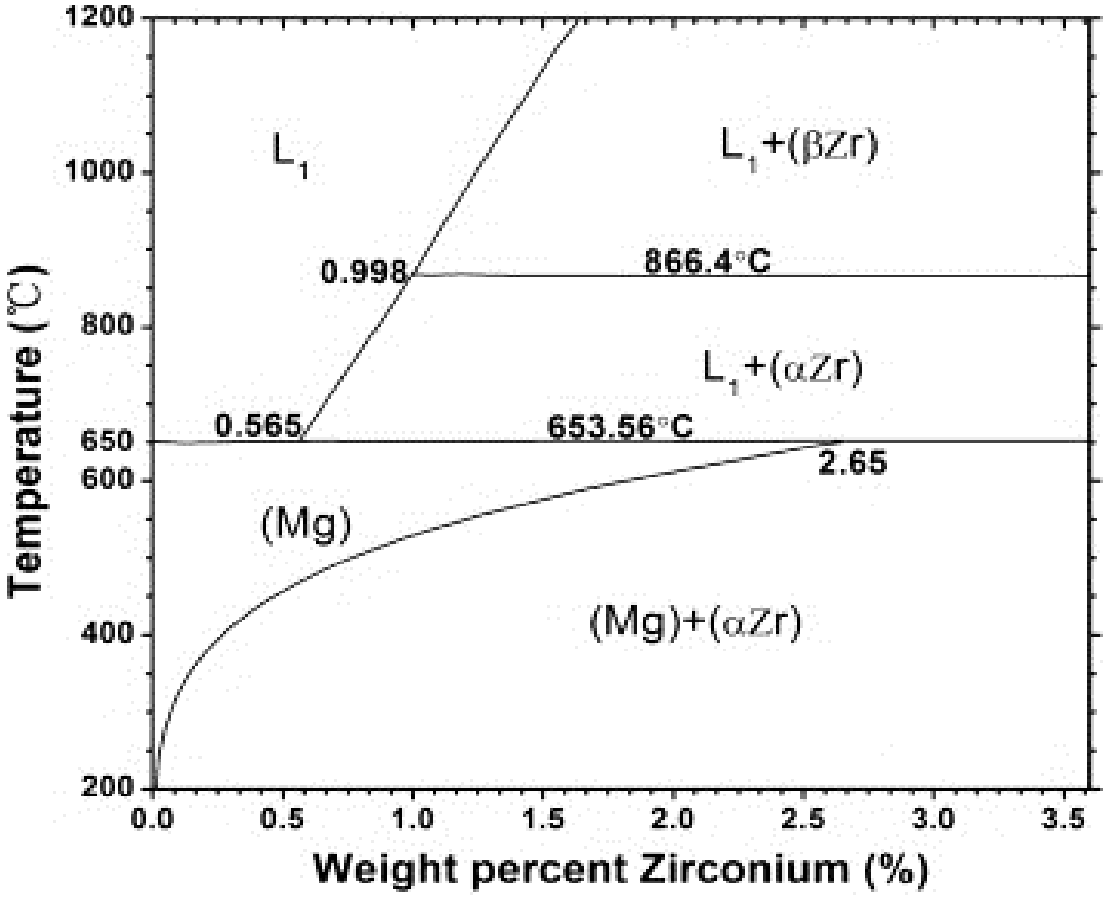

Figure 6.3 Binary phase diagram of Magnesium and Zirconium [176].

Figure 6.3 shows the binary phase diagram of Magnesium and Zirconium. It exhibits that at room temperature, the solid solution of Magnesium + α Zirconium formation takes place. At lower temperature and lower weight percentage of Zirconium, there are no precipitates formations observed. In fact, Zirconium addition to Magnesium alloys leads to formations of intermetallic compounds with alloying elements other than Magnesium, which in turn leads to grain refinement. Fig 4.7clearly depicts the effect of addition of alloying elements like Nd and Zr into master alloy Mg-10wt%Gd leading to grain refinement. As we move from 4.7 a - c - e, the back scattered electron images show there is clear change in grain size. Similar trend is observed with increased clarity when we move from 4.7 b - d - f. These micro-structural features registered are the proving the grain refinement taking place in the magnetic field assisted solidified alloys [165], [177]. The

grain boundary pinning of the intermetallic compounds results in hindering effect on grain growth [179]. In addition, the presence of Zr affects the size and morphology of long period stacking ordered (LPSO) phases in Magnesium based alloys leading to grain refinement [180].

Mg-Gd alloy system is designed due to the fact that the solubility of Gd in Mg is around 23.49 wt.% at a temperature of 548 ^{0}C [181]. But the precipitation strengthening in these alloy systems are possible only when the Gd percentile addition to the alloy is greater than 10 wt% [182]. Hence, a compensating rare earth group alloying element namely Nd is added to Mg-Gd system in order to achieve precipitation strengthening. The solubility of Nd in Mg is around 3.62 wt.% at 552 ^{0}C [183]. The precipitation kinetics of each alloying element is influenced and changed by the presence of other alloying element in the case of Gd and Nd. This leads to enhancement in precipitation strengthening mechanism as a whole in the Mg-Gd-Nd system [184]. It is reported that the solubility of each element in Magnesium is decreased by the presence of other alloying element in the case of Gd and Nd as allying elements. This in turn promotes the precipitations namely Mg_5Gd and $Mg_{12}Nd$ instead of forming a solid solution [155]. Fig.4.9 to 4.15 show the clear proof for the enhancement of precipitations of inter-metallics like Mg5Gd and Mg12 Nd. The EDAX spectrum's show the peaks of concerned alloying elements of the inter-metallics when region specifically analyzed. From the microstructural analysis of these alloys, it is very much evident that the Mg- 5% Gd – 5% Nd -0.4 % Zr alloy contains more of Mg_5Gd flake like precipitates along with the $Mg_{12}Nd$ needle like structures when compared to that of Mg- 10% Gd - 0.4 % Zr alloy, (Fig 4.8 d and f). In another research dealing with Mg-In-Ca alloys, Prismatic precipitates of Mg_5Gd is reported [181]. Hence it can be stated that the presence of Gd and Nd have a “synergic effect” of promoting the formation of the precipitates Mg_5Gd and $Mg_{12}Nd$.This can be corelated to the size variation if Gd cuboids as the analysis of the microstructures of the alloys is carried out. This is clearly observable when one move from 4.8 a to 4.8 c and 4.8 e. Similar trend is observed when one move from 4.8 b to 4.8 d and 4.8 f. The segregation of Gd cuboids gradually decrease in size as the addition of Nd and Zr are

employed to the master alloy. The key observations of master alloy microstructure show bigger sized Gd cuboids and Mg- 10% Gd - 0.4 % Zr alloy show smaller sized cuboids whereas the same is hardly observable in Mg- 5% Gd – 5% Nd -0.4 % Zr alloy microstructure. This is clearly showing that the synergic effect of Gd and Nd promoting the intermetallic precipitate formation rather than segregation of Gd as cuboids in the Magnesium matrix. In Magnesium alloys, the excess percentage of Gadolinium exhibits a segregation behaviour in grains as well as grain boundaries, (Fig 4.7 and 4.8). Preferentially, the segregation happens to be more at grain boundaries being higher energy regions. Small clusters of Gd are observed along grain boundaries. Often these clusters are noticed as cuboids [175], [185]. Microstructural analysis clearly shows the preferential existence of Gd cuboids and Mg_5Gd intermetallic along the grain boundaries. This is very well supported by the corresponding EDAX spectrum of grain boundaries of Mg- 5% Gd – 5% Nd -0.4 % Zr alloy showing the peaks of Mg, Gd and Nd. The Higher Gd content in Magnesium alloys, leads to grain refinement as well as solid solution strengthening due to the complete dissolution of Gd in to Magnesium [186].

Addition of Zirconium to the Mg-Gd and Mg-Gd-Nd system, leads to effective grain refinement by means of pinning the grain boundaries to hinder the further growth of grains. In fact, the presence of Zr particles along the grain boundaries, (Fig 4.7 and Fig 4.8), impede the dislocation motion during the deformation process [165].

6.3 Effect of Neodymium and Zirconium addition to the mechanical properties and corrosion behaviour of Magnesium Gadolinium based alloys.

Figure show the bar chart of the hardness profile of the Magnesium based alloys. In comparison, alloys Mg- 10% Gd and Mg- 10% Gd-0.4%Zr exhibit nearly equivalent resistance to indentation (Hardness) whereas the Vickers hardness value of alloy Mg- 5% Gd-5% Nd- 0.4%Zr is greater than that of aforementioned groups, (Table 4.2 to 4.4). This is another supporting result proving the synergic effect of presence of Gd and Nd promoting the

precipitation formation due to reduced solid solubility of each element in Magnesium. In fact, the area covered by Vickers hardness tester indenter is of micrometre size. This reveals that there is a possibility of each indentation of the tests covering specific phase regions. Hence, the resultant hardness parameter obtained in each test can vary depending on the phase regions encountered the indentation. Due to this fact, variation of hardness values in each alloy is observed. In spite of this fact, the higher hardiness value of the Mg- 5% Gd-5% Nd- 0.4%Zr alloy proves that the precipitation hardening and grain boundary strengthening of the master alloy (Mg – 10 wt.% Gd) when added with 5 wt. % Nd and 0.4 wt. Zr, (Table 4.6 and 4.7).

Hence, it can be stated as the addition of Gd in Magnesium matrix increases the strength of the alloy as a whole. Contributing factors are solid solution strengthening and age hardening leading to enhancement of mechanical properties [187], [188]. In addition, Nd and Zr inclusion to the aforementioned master alloy leads grain refinement to a larger extent so that the grain boundary strengthening come into effect in increasing the strength of the Mg- 10% Gd-0.4%Zr alloy and Mg- 5% Gd-5% Nd- 0.4%Zr alloy when compared to that of the master alloy [189], [190].

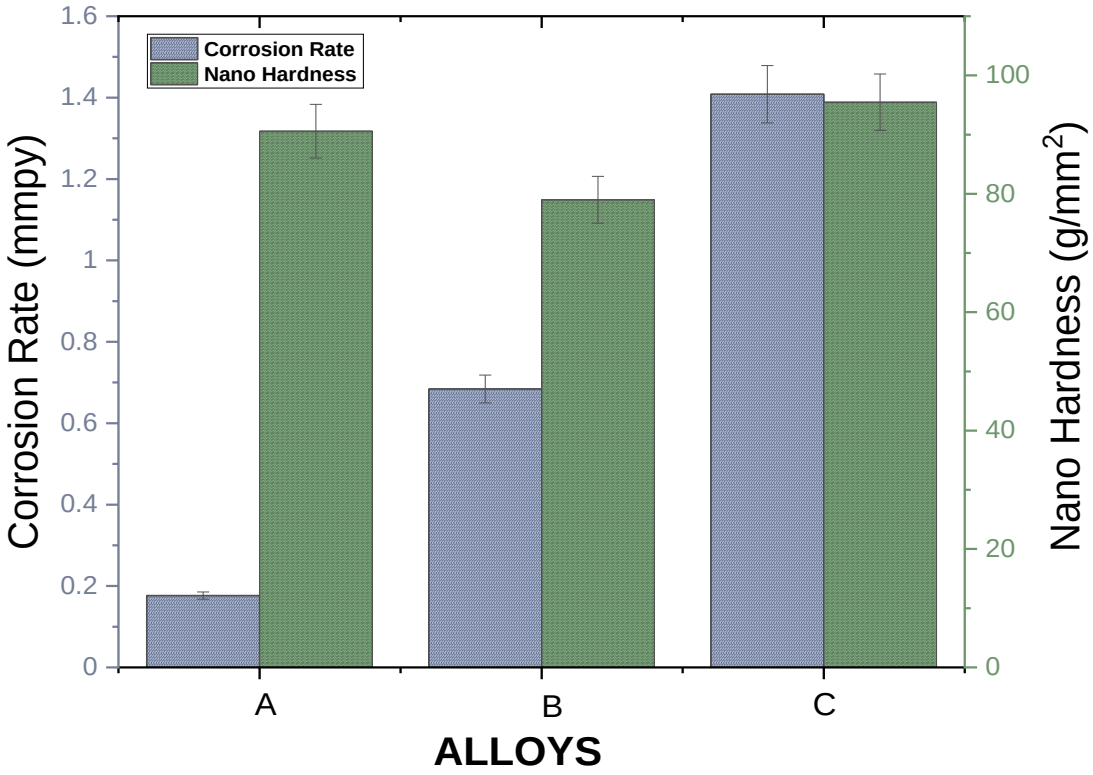

Figure 6.4: The mechanical property and corrosion behaviour correlation chart.

The microstructural observations of these alloys show that the exposed surfaces to Hank's solution get corroded and leading to clearly observed stains over the entire specimen surface (Fig. 4.32). The images of full specimens show that as we do the careful analyse starting from the master alloy, the size of stained regions with spallation's and broken surface layers are increasing. This indicates the corrosion happens to be comparatively at higher scale on the surface of Mg- 5% Gd-5% Nd- 0.4%Zr alloy when compared to that of Mg- 10% Gd-0.4%Zr alloy and Mg- 10% Gd alloy. This explanation holds good when we compare only the corroded surfaces of Mg-10% Gd alloy and Mg- 10% Gd-0.4%Zr alloy, meaning that the Mg- 10% Gd-0.4%Zr alloy exhibiting slightly higher corrosion compared to that of Mg- 10% Gd alloy,(Fig.4.28 to 4.30 and table 4.9). The addition of alloying elements leads to heterogeneity of the alloy matrix which in turn can cause dissimilar metal corrosion in body like liquids [34]. The corrosion mechanism involves metal atoms reacting to Hank's solution containing chlorides, sulphates of

Potassium, Magnesium and sodium elements etc. At initial stages, the reactions are confined to few islands expanding in region size and as the time progresses the number and size of islands of corrosion reactions are increasing. This leads to hydrates and hydroxide products on the surface of the exposed alloys for example Cl, K, Na, S and Mg containing hydrates and hydroxides. Upon drying, they transform into oxides and salts layers on the corroded surface of the alloys [110], [191], [192].

Concerning the EDAX, the surface morphology of the corroded specimen in terms of wide-open oxide scales, stained regions, uniformity and quantitative nature of the settled islands separated by cracks and spallation's clearly indicate that the alloying additions like Nd and Zr to the master alloy leads to increased corrosion activities in Hank's solution (Fig.4.33 to 4.35). Similar trend of results are obtained by other researcher [193]. From Figure , it can be stated that the increase in strength of the magnesium alloy groups by addition of alloying elements leads decrease in corrosion resistance of the alloys.

Chapter 7 Conclusion and Future Work

7.1 Conclusions

The research in my PhD thesis consists of two parts. The first part concerns the microstructure evolution of an Al-20%Si alloy during the solidification inside pulse magnetic fields with different magnetic field flux densities applied. The second part studied systematically the composition and microstructure relationship of three Mg-based alloys.

The key scientific findings for the Al-20%Si alloy work are:

- The research has demonstrated that the pulse magnetic field is a non-contact and effective method for refining the primary silicon particles in the Al-20%Si alloy. With the increasing of the flux density of the magnetic field, the average size of the primary Si particles (for those at the bottom portion of the evaluated specimen) decreased from 14078.7 μm^2 at 0 Tesla to 2427.3 μm^2 at 1.4 Tesla ~6 times smaller after processing by the pulse magnetic field.

- Without magnetic field, the microstructures of the Al-20%Si alloy have long and thick plate like primary Si phases. These plates like Si phases are randomly oriented. In addition, few fine primary Si particles are observed in the alloy matrix. At 40 V discharging voltage (0.3 T), the long plate like primary Si transformed into shorter ones. Moreover, there is a change in the eutectic Al-Si particles. At 80 V discharging voltage (0.7 T), the long and bigger primary Si started to disappear. Only the short primary Si are visible. In addition, the distribution of the short primary Si are more homogenous. The thickness of the primary Si also decreased when compared to that of the same at 40 V. When the discharge voltage is increased to 100V (0.85 T), most of the primary Si became shorter and finer. At a discharging voltage from 120 V to 160 V (1.0 to 1.4 Tesla), the microstructure of the solidified Al-20%Si alloy changed completely. Some of the shorter primary silicon plates have transformed into fine primary silicon islands.

- The increase in discharge voltage leads to the increase in the formation and growth of lamellar Al + Si eutectic colonies, and more uniformed eutectic Al + Si in the matrix.

- At zero magnetic field, the EDAX spectrums of the Al matrix region and bulk region show only peak corresponding to Al surrounded by the primary Si as well as the eutectic phase. Well defined phases of Aluminium and Primary Silicon phase are observable. From 40 V to 160 V, the application of the magnetic field leads to the refinement in the eutectic lamellar or acicular Al + Si structure. These results are clearly evident in analysing concerned EDAX spectrum showing increasing Silicon peaks along with Aluminium peaks. This can be attributed to the reduction in interlamellar spacing with in the eutectic phase revealing the uniformity in Silicon distribution in the matrix and refinement of Si platelets.

- In hardness measurements, from 0 Tesla to 0.7 Tesla, the Vickers hardness increases from 65 to 75 (VHN), and then maintained at this value until 1.4 Tesla. The progressive increase in hardness values of alloy due to magnetic field assisted solidification can be related to the refinement of Primary Si particles in the matrix of Aluminium and transformation of Al + Si phase into finer eutectic lamellar.

The key scientific findings for the Mg alloys experiments are:

- In the microstructures of Mg–10wt.%Gd alloy, the average grain size are bigger (~243216 μm^2) with Mg_5Gd phases uniformly distributed throughout the Mg matrix while the grain size of Mg–10wt.%Gd–0.4 wt.%Zr alloy is smaller (~2270 μm^2) with its Mg_5Gd phases distribute more along the grain boundaries than in Mg matrix.

- The microstructures of Mg–5 wt.% Gd–5 wt.% Nd–0.4 wt.%Zr alloy show a clear difference in microstructural features. The $Mg_{12}Nd$ phases are observed in the grain regions as well as in grain boundary regions. The $Mg_{12}Nd$ phase are registered and micro graphed as small needles oriented

in all directions of the grains. Again, smaller grains are observable in these alloy microstructures along with the Mg_5Gd phase precipitations present along the grain boundaries and Gd cuboids are present as well.

- The analysis of the microstructures shows that in Mg–10 wt.% Gd alloy, the cuboids are present in the grain and grain boundary regions but in alloy Mg–10wt.%Gd–0.4 wt.%Zr the cuboids are present along grain boundaries preferentially. The microstructures at high magnifications prove that in alloy Mg–10wt.%Gd, the flake like Mg_5Gd precipitates present in the grain regions. But in alloy Mg–10wt.%Gd–0.4 wt.%Zr the same phase exhibits a preferentially along grain boundaries. Moreover, Zr segregations were also found in and around the grain boundary regions.

- Another interesting feature is the size of the Gd cuboids in the alloy Mg–10wt.%Gd and alloy Mg–10wt.%Gd–0.4 wt.%Zr. In both cases, the Gd cuboids exist in variable sizes. However, especially in alloy Mg–10wt.%Gd, bigger sized cuboids are observed (~17.5 μm^2) when compared to that of the alloy Mg–10wt.%Gd–0.4 wt.%Zr (about 6.1 μm^2). For alloy Mg–5 wt.% Gd–5 wt.% Nd–0.4 wt.%Zr microstructure, the Gd cuboids are hardly observable. This gives the clear evidence of Gd agglomerations gradually transforming into Mg5Gd precipitations in alloy Mg–5 wt.% Gd–5 wt.% Nd–0.4 wt.%Zr.

- In comparison, alloys Mg–10wt.%Gd and Mg–10wt.%Gd–0.4 wt.%Zr exhibit nearly equivalent resistance to indentation (Hardness) whereas the Vickers hardness value of alloy Mg–5 wt.% Gd–5 wt.% Nd–0.4 wt.%Zr is greater than that of alloys Mg–10wt.%Gd and Mg–10wt.%Gd–0.4 wt.%Zr. This is another supporting result proving the synergic effect of presence of Gd and Nd promoting the precipitation formation due to reduced solid solubility of each element in Magnesium. The higher hardiness value of the alloy Mg–5 wt.% Gd–5 wt.% Nd–0.4 wt.%Zr proves that the precipitation hardening and grain boundary strengthening of the master alloy (Mg – 10 wt.% Gd) when added with 5 wt. % Nd and 0.4 wt.% Zr.

- The corrosion studies of the alloys show that the surface of the alloys get corroded in general and leading to clearly observed stains over the entire specimen surface. The careful analyse of alloys Mg–10wt.%Gd, Mg–10wt.%Gd–0.4 wt.%Zr and Mg–5 wt.% Gd–5 wt.% Nd–0.4 wt.%Zr the size of stained regions with spallation's and broken surface layers are increasing respectively. At initial stages of corrosion, the reactions are confined to few islands and as the time progresses the number and size of islands of corrosion reactions are increasing. This leads to hydrates and hydroxide products on the surface of the exposed alloys for example Cl, K, Na, S and Mg containing hydrates and hydroxides. Upon drying, they transform into oxides and salts layers on the corroded surface of the alloys. The calculated corrosion rates of the alloys reveal that the addition of alloying elements like Gd and Zr to the master alloy Mg–10wt.%Gd influence a minimal reduction in corrosion resistance.

7.2 Future recommended work

Further investigation on the effect of pulsed magnetic field assisted solidification of Al-20%Si alloy on mechanical properties like yield strength, ultimate tensile strength, compression strength and fatigue strength etc will improve the applicability of magnetic field assisted solidified alloy in various industries.

Magnesium based alloys can be tested in terms of toxicity by applying cell viability test. In as-cast material condition, it is recommended for in vitro valid cytotoxicity ratings of degradable materials, to use ten times more removal medium than the ISO standards specified. In addition, magnesium alloys can be tested with primary isolated human osteoblasts or mesenchymal stem cells.

Furthermore, after a systematic study of the magnesium-based alloys, at least one alloy could be chosen to make prototype sample for laboratory test and validation.

References

[1] D. Fainstein-Pedraza and G. F. Bolling, “Superdendritic growth: I. A qualitative analysis,” *Journal of Crystal Growth*, vol. 28, no. 3, pp. 311–318, Jul. 2002,

[2] N. Tenekedjiev and J. E. Gruzleski, “Hypereutectic Aluminium-Silicon Casting Alloys—A Review,” *Taylor & Francis Online*, vol. 3, no. 2, pp. 96–105, Dec. 2016,

[3] F. C. Robles Hernandez, “Improvement in functional characteristics of aluminum-silicon cast components through the utilization of a novel electromagnetic treatment of liquid melts,” Ph.D Dissertation,Dep. Mech. Eng.,University of Windsor., Ontario, 2004.

[4] A. Edrisy, T. Perry, Y. T. Cheng, and A. T. Alpas, “Wear of thermal spray deposited low carbon steel coatings on aluminum alloys,” *Wear*, vol. 251, no. 1–12, pp. 1023–1033, Oct. 2001,

[5] A. Moharrami, A. Razaghian, M. Paidar, M. Šlapáková, O. O. Ojo, and R. Taghiabadi, “Enhancing the mechanical and tribological properties of Mg2Si-rich aluminum alloys by multi-pass friction stir processing,” *Materials Chemistry and Physics*, vol. 250, p. 123066, Aug. 2020,

[6] Y. Xu, Y. Deng, D. Casari, R. H. Mathiesen, X. Liu, and Y. Li, “Revealing the nucleation kinetics of primary Si particles in hypereutectic Al–Si alloys under the influence of P inoculation,” *Journal of Materials Science*, vol. 55, no. 32, pp. 15621–15635, Nov. 2020,

[7] Z. X. Yin, Y. Y. Gong, B. Li, Y. F. Cheng, D. Liang, and Q. J. Zhai, “Refining of pure aluminum cast structure by surface pulsed magneto-oscillation,” *Journal of Materials Processing Technology*, vol. 212, no. 12, pp. 2629–2634, Dec. 2012,

[8] M. P. Staiger, A. M. Pietak, J. Huadmai, and G. Dias, “Magnesium and its alloys as orthopedic biomaterials: A review,” in *Biomaterials*, Mar. 2006, vol. 27, no. 9, pp. 1728–1734.

[9] K. Munir, J. Lin, C. Wen, P. F. A. Wright, and Y. Li, “Mechanical, corrosion, and biocompatibility properties of Mg-Zr-Sr-Sc alloys for biodegradable implant applications,” *Acta Biomaterialia*, vol. 102, pp. 493–507, Jan. 2020,

[10] J. Yan, Y. Sun, F. Xue, S. Xue, and W. Tao, “Microstructure and mechanical properties in cast magnesium-neodymium binary alloys,” *Materials Science and Engineering A*, vol. 476, no. 1–2, pp. 366–371, Mar. 2008,

[11] S. Virtanen, “Biodegradable Mg and Mg alloys: Corrosion and biocompatibility,” *Materials Science and Engineering: B*, vol. 176, no. 20, pp. 1600–1608, Dec. 2011,

[12] N. Hort *et al.*, “Magnesium alloys as implant materials-Principles of property design for Mg-RE alloys,” *Acta Biomaterialia*, vol. 6, no. 5, pp. 1714–1725, May 2010,

[13] J. Bohlen, S. Yi, D. Letzig, and K. U. Kainer, “Effect of rare earth elements on the microstructure and texture development in magnesium-manganese alloys during extrusion,” *Materials Science and Engineering A*, vol. 527, no. 26, pp. 7092–7098, Oct. 2010,

[14] L. H. Campos Becerra, M. A. L. Hernández Rodríguez, H. Esquivel Solís, R. Lesso Arroyo, and A. Torres Castro, “Bio-inspired biomaterial Mg–Zn–Ca: a review of the main mechanical and biological properties of Mg-based alloys,” *Biomedical Physics & Engineering Express*, vol. 6, no. 4, p. 042001, Jun. 2020,

[15] E. G. Bakhoum, “Constant voltage ultracapacitor,” *Journal of Renewable and Sustainable Energy*, vol. 4, no. 3, p. 033116, May 2012,

[16] S. Dan and L. Ning, “The Research on the Quick Discharge Circuit of Shunt Capacitor,” *Journal of Power and Energy Engineering*, vol. 2, pp. 579–585, Apr. 2014,

[17] Z. Yong-Jie, C. Guo-Jun, and T. Chen-Long, “Metallurgical applications of pulsed electromagnetic field,” *Journal of Shanghai Jiaotong University (Science)*, vol. 17, no. 3, pp. 282–285, Jun. 2012,

[18] U. Å. H. Fredriksson, *Materials Processing During Casting | Wiley*. Chichester: John Wiley & Sons Ltd, 2006.

[19] H. Fredriksson and U. Åkerlind, “Structure and Structure Formation in Cast Materials,” in *Materials Processing during Casting*, John Wiley & Sons, Ltd, 2006, pp. 139–182.

[20] D. M. Stefanescu, *Science and Engineering of Casting Solidification*, 3rd ed. Springer, Cham, 2002.

[21] H. Elzanaty, “Effect of composition on the microstructure, tensile and hardness properties of Al-xSi alloys,” *Materials Science & Surface Engineering*, vol. 2, no. 2, pp. 126–129, May 2015,

[22] H. Fredriksson and Ulla Åkerland, *Solidification and Crystallization Processing in Metals and Alloys*. John Wiley & Sons Ltd., Chichester, 2012.

[23] R. Stefanescu, Doru & Ruxanda, “Solidification structure of aluminum alloys,” in *Metallography and Microstructures*, ASM International, 2004, pp. 107–115.

[24] K. M. Jasim and E. S. Dwarakadasa, “Wear in Al-Si alloys under dry sliding conditions,” *Wear*, vol. 119, no. 1, pp. 119–130, Sep. 1987,

[25] Sharma Ashok, “Production and properties of cast Al–Si–Pb composites,” Ph.D Dissertation,Dep. Mech. Eng., University of Rajasthan, Jaipur, India, 1991.

[26] R. Saravanan, S. Nair, and M. Krishnakumar, “Impact of tungsten on the surface of aluminium-silicon alloy on microstructure, hardness and wear rate using GTA,” in *IOP Conference Series*, 2019, pp. 577–012124.

[27] J. Chen, L. Tan, X. Yu, I. P. Etim, M. Ibrahim, and K. Yang, “Mechanical properties of magnesium alloys for medical application: A review,” *Journal of the Mechanical Behavior of Biomedical Materials*, vol. 87. Elsevier Ltd, pp. 68–79, Nov. 01, 2018.

[28] Charles Moosbrugger, *Engineering Properties of Magnesium Alloys*. Novelty, OH: ASM International, 2017.

[29] A. International, *Atlas of stress-strain curves*, 2nd ed. Columbus OH: ASM, 2002.

[30] “Selection and Applications of Magnesium and Magnesium Alloys,” in *Metals Handbook Desk Edition*, ASM International, 2018, pp. 559–570.

[31] F. Witte *et al.*, “IIn vivo corrosion of four magnesium alloys and the associated bone response,” *Biomaterials*, vol. 26, no. 17, pp. 3557–3563, Jun. 2005,

[32] M. H. Hong, T. Hanawa, S. H. Song, B. K. Min, and T. Y. Kwon, “Enhanced biocompatibility of a Ni-Cr alloy prepared by selective laser melting: A preliminary in vitro study,” *Journal of Materials Research and Technology*, vol. 8, no. 1, pp. 1587–1592, Jan. 2019,

[33] P. Yin, N. Feng Li, T. Lei, L. Liu, and C. Ouyang, “Effects of Ca on microstructure, mechanical and corrosion properties and biocompatibility of Mg-Zn-Ca alloys,” *Journal of Materials Science: Materials in Medicine*, vol. 24, pp. 1365–1373, Apr. 2013,

[34] Y. Ding, C. Wen, P. Hodgson, and Y. Li, “Effects of alloying elements on the corrosion behavior and biocompatibility of biodegradable magnesium alloys: A review,” *Journal of Materials Chemistry B*, vol. 2, no. 14, pp. 1912–1933, Apr. 2014,

[35] E. Landi, S. Sprio, M. Sandri, G. Celotti, and A. Tampieri, “Development of Sr and CO3 co-substituted hydroxyapatites for biomedical applications,” *Acta Biomaterialia*, vol. 4, no. 3, pp. 656–663, May 2008,

[36] S. G. Dahl *et al.*, “Incorporation and distribution of strontium in bone,” *Bone*, vol. 28, no. 4, pp. 446–453, Apr. 2001,

[37] D. S. Aydin, • Z Bayindir, and • M O Pekguleryuz, “The effect of strontium (Sr) on the ignition temperature of magnesium (Mg): a look at the pre-ignition stage of Mg-6 wt% Sr,” *Journal of Materials Science*, vol. 48, pp. 8117–8132, Aug. 2013,

[38] M. Alvarez-Lopez *et al.*, “Corrosion behaviour of AZ31 magnesium alloy with different grain sizes in simulated biological fluids,” *Acta Biomaterialia*, vol. 6, no. 5, pp. 1763–1771, May 2010,

[39] M. Guan, Y. Hu, T. Zheng, T. Zhao, and F. Pan, “Composition optimization and mechanical properties of Mg-Al-Sn-Mn alloys by orthogonal design,” *Materials*, vol. 11, no. 8, p. 1424, Aug. 2018,

[40] M. Nagata and B. Lönnerdal, “Role of zinc in cellular zinc trafficking and mineralization in a murine osteoblast-like cell line,” *Journal of Nutritional Biochemistry*, vol. 22, no. 2, pp. 172–178, Feb. 2011,

[41] F. Rosalbino, S. De Negri, G. Scavino, and A. Saccone, “Microstructure and *in vitro* degradation performance of Mg-Zn-Mn alloys for biomedical application,” *Journal of Biomedical Materials Research Part A*, vol. 101A, no. 3, pp. 704–711, Mar. 2013,

[42] H. R. Bakhsheshi-Rad *et al.*, “Mechanical and bio-corrosion properties of quaternary Mg–Ca–Mn–Zn alloys compared with binary Mg–Ca alloys,” *Materials and Design*, vol. 53, pp. 283–292, Jan. 2014,

[43] Q. ; Peng *et al.*, “Influence of inorganic acid pickling on the corrosion resistance of magnesium alloy AZ31 sheet,” *Corrosion Science*, vol. 51, no. 11, pp. 2544–2556, Nov. 2009,

[44] J. Chang, X. Guo, S. He, P. Fu, L. Peng, and W. Ding, “Investigation of the corrosion for Mg-xGd-3Y-0.4Zr (x = 6, 8, 10, 12 wt%) alloys in a peak-aged condition,” *Corrosion Science*, vol. 50, no. 1, pp. 166–177, Jan. 2008,

[45] D. Yu *et al.*, “Improving mechanical properties of ZM61 magnesium alloy by aging before extrusion,” *Journal of Alloys and Compounds*, vol. 690, pp. 553–560, Jan. 2017,

[46] M. Akif Erden *et al.*, “Effect of aging on the microstructure and mechanical properties of magnesium Alloy AZ31,” *Article in Metal Science and Heat Treatment*, vol. 58, pp. 179–184, Jul. 2016,

[47] L. Yan, Z. Zhang, X. Y. N. M. S. of China, and U. 2011, “Influence of aging on microstructure and mechanical properties of AZ80 and ZK60 magnesium alloys,” *Elsevier*, vol. 21, no. 4, pp. 739–744, Apr. 2011,

[48] A. F. Lotfabadi, H. R. Bakhsheshi-Rad, M. H. Idris, E. Hamzah, and M. Kasiri-Asgarani, “The role of solution heat treatment on corrosion and mechanical behaviour of Mg–Zn biodegradable alloys,” *Canadian Metallurgical Quarterly*, vol. 55, no. 1, pp. 53–64, Apr. 2016,

[49] H. Chen, S. B. Kang, H. Yu, J. Cho, H. W. Kim, and G. Min, “Effect of heat treatment on microstructure and mechanical properties of twin roll cast and sequential warm rolled ZK60 alloy sheets,” *Journal of Alloys and Compounds*, vol. 476, no. 1–2, pp. 324–328, May 2009,

[50] X. Zhang, G. Yuan, L. Mao, J. Niu, P. Fu, and W. Ding, “Effects of extrusion and heat treatment on the mechanical properties and biocorrosion behaviors of a Mg-Nd-Zn-Zr alloy,” *Journal of the Mechanical Behavior of Biomedical Materials*, vol. 7, pp. 77–86, Mar. 2012,

[51] Y. Yuan *et al.*, “High mechanical properties of AZ91 mg alloy processed by equal channel angular pressing and rolling,” *Metals*, vol. 9, no. 4, p. 386, Mar. 2019,

[52] M. Pogorielov, E. Husak, A. Solodivnik, and S. Zhdanov, “Magnesium-based biodegradable alloys: Degradation, application, and alloying elements,” *Interventional Medicine and Applied Science*, vol. 9, no. 1. Akademiai Kiado Rt., pp. 27–38, Mar. 01, 2017.

[53] B. D. Ratner, *Biomaterials Science: An Introduction to Materials in Medicine*. Oxford: Elsevier Science, 2012.

[54] M. Ebara *et al.*, *Smart Biomaterials*. Tokyo: Springer Japan, 2014.

[55] F. Witte *et al.*, “Degradable biomaterials based on magnesium corrosion,” *Current Opinion in Solid State and Materials Science*, vol. 12, no. 5–6, pp. 63–72, Oct. 2008,

[56] M. Peuster *et al.*, “A novel approach to temporary stenting : degradable cardiovascular stents produced from corrodible metal — results 6 – 18 months after implantation into New Zealand white rabbits,” vol. 1000, pp. 563–569, Nov. 2001,

[57] E. Zhang, D. Yin, L. Xu, L. Yang, and K. Yang, “Microstructure, mechanical and corrosion properties and biocompatibility of Mg-Zn-Mn alloys for biomedical application,” *Materials Science and Engineering C*, vol. 29, no. 3, pp. 987–993, Apr. 2009,

[58] X. Gu, Y. Zheng, Y. Cheng, S. Zhong, and T. Xi, “In vitro corrosion and biocompatibility of binary magnesium alloys,” *Biomaterials*, vol. 30, no. 4, pp. 484–498, Feb. 2009,

[59] X. Gu, Y. Zheng, S. Zhong, T. Xi, J. Wang, and W. Wang, “Corrosion of, and cellular responses to Mg-Zn-Ca bulk metallic glasses,” *Biomaterials*, vol. 31, no. 6, pp. 1093–1103, Feb. 2010,

[60] X. Liu *et al.*, “Multifunctional MgF2/Polydopamine Coating on Mg Alloy for Vascular Stent Application,” *Journal of Materials Science and Technology*, vol. 31, no. 7, pp. 733–743, Jul. 2015,

[61] S. Zhang *et al.*, “Research on an Mg-Zn alloy as a degradable biomaterial,” *Acta Biomaterialia*, vol. 6, no. 2, pp. 626–640, Feb. 2010,

[62] S. S. Abd El-Rahman, “Neuropathology of aluminum toxicity in rats (glutamate and GABA impairment),” *Pharmacological Research*, vol. 47, no. 3, pp. 189–194, Mar. 2003,

[63] C. H. Ku, D. P. Pioletti, M. Browne, and P. J. Gregson, “Effect of different Ti-6Al-4V surface treatments on osteoblasts behaviour,” *Biomaterials*, vol. 23, no. 6, pp. 1447–1454, Mar. 2002,

[64] Y. Nakamura, Y. Tsumura, Y. Tonogai, T. Shibata, and Y. Ito, “Differences in behavior among the chlorides of seven rare earth elements administered intravenously to rats,” *Fundamental and Applied Toxicology*, vol. 37, no. 2, pp. 106–116, Jun. 1997,

[65] W. Yang, P. Zhang, J. Liu, and Y. Xue, “Effect of long-term intake of Y3+ in drinking water on gene expression in brains of rats,” *Journal of Rare Earths*, vol. 24, no. 3, pp. 369–373, Jun. 2006,

[66] G. Song, “Control of biodegradation of biocompatable magnesium alloys,” *Corrosion Science*, vol. 49, no. 4. Pergamon, pp. 1696–1701, Apr. 01, 2007.

[67] G. Song and S. Song, “A possible biodegradable magnesium implant material,” *Advanced Engineering Materials*, vol. 9, no. 4, pp. 298–302, Apr. 2007,

[68] H. R. Bakhsheshi-Rad *et al.*, “Fabrication of biodegradable Zn-Al-Mg alloy: Mechanical properties, corrosion behavior, cytotoxicity and antibacterial activities,” *Materials Science and Engineering C*, vol. 73, pp. 215–219, 2017,

[69] N. El-Mahallawy, H. Palkowski, A. Klingner, A. Diaa, and M. Shoeib, “Effect of 1.0 wt. % Zn addition on the microstructure, mechanical properties, and bio-corrosion behaviour of micro alloyed Mg-0.24Sn-0.04Mn alloy as biodegradable material,” *Materials Today Communications*, vol. 24, Sep. 2020,

[70] S. Cai, T. Lei, N. Li, and F. Feng, “Effects of Zn on microstructure, mechanical properties and corrosion behavior of Mg-Zn alloys,” *Materials Science and Engineering C*, vol. 32, no. 8, pp. 2570–2577, Dec. 2012,

[71] G. Wu, L. Gong, K. Feng, S. Wu, Y. Zhao, and P. K. Chu, “Rapid degradation of biomedical magnesium induced by zinc ion implantation,” *Materials Letters*, vol. 65, no. 4, pp. 661–663, Feb. 2011,

[72] X. Liu *et al.*, “Effects of alloying elements (Ca and Sr) on microstructure, mechanical property and in vitro corrosion behavior of biodegradable Zn-1.5Mg alloy,” *Journal of Alloys and Compounds*, vol. 664, pp. 444–452, Apr. 2016,

[73] H. Hermawan, H. Alamdari, D. Mantovani, and D. Dubé, “Iron-manganese: New class of metallic degradable biomaterials prepared by powder metallurgy,” *Powder Metallurgy*, vol. 51, no. 1, pp. 38–45, Jul. 2013,

[74] M. Nakai, M. Niinomi, and T. Narushima, *Advances in Metallic Biomaterials Processing and Applications*. London: Springer Berlin Heidelberg, 2015.

[75] N. J. Hallab, C. Vermes, C. Messina, K. A. Roebuck, T. T. Glant, and J. J. Jacobs, “Concentration- and composition-dependent effects of metal ions on human MG-63 osteoblasts,” *Journal of Biomedical Materials Research*, vol. 60, no. 3, pp. 420–433, Jun. 2002,

[76] C. Leyens and M. Peters, *Titanium and Titanium Alloys: Fundamentals and Applications*. Cologne: Wiley, 2006.

[77] S. Song, G. L. Song, W. Shen, and M. Liu, “Corrosion and electrochemical evaluation of coated magnesium alloys,” *The Journal of Science & Engineering*, vol. 68, no. 1, pp. 015005–1–015005–12, Jan. 2012,

[78] F. Zucchi, V. Grassi, A. Frignani, … C. M.-J. of A., and U. 2006, “Electrochemical behaviour of a magnesium alloy containing rare earth elements,” *Journal of Applied Electrochemistry*, vol. 36, pp. 195–204, Oct. 2005,

[79] Z. Li, X. Gu, S. Lou, and Y. Zheng, “The development of binary Mg-Ca

alloys for use as biodegradable materials within bone," *Biomaterials*, vol. 29, no. 10, pp. 1329–1344, Apr. 2008,

[80] N. S. Manam *et al.*, "Study of corrosion in biocompatible metals for implants: A review," *Journal of Alloys and Compounds*, vol. 701. Elsevier Ltd, pp. 698–715, Apr. 15, 2017.

[81] H. Kuwahara, Y. Al-Abdullat, N. Mazaki, S. Tsutsumi, and T. Aizawa, "Precipitation of magnesium apatite on pure magnesium surface during immersing in Hank's solution," *Materials Transactions*, vol. 42, no. 7, pp. 1317–1321, May 2001,

[82] *Magnesium and Its Alloys: Technology and Applications*. Boca Raton: CRC Press, 2019.

[83] L. Tan, X. Yu, P. Wan, K. Y.-J. of M. S. & Technology, and U. 2013, "Biodegradable materials for bone repairs: a review," *Journal of Materials Science and Technology*, vol. 29, no. 6, pp. 503–513, Jun. 2013,

[84] R. H. Doremus, "Bioceramics," *Journal of Materials Science*, vol. 27, no. 2. Kluwer Academic Publishers, pp. 285–297, Jan. 1992.

[85] D. M. Ferrante, G. O. Conti, Z. Rasic-Milutinovic, and D. Jovanovic, *Health Effects of Metals and Related Substances in Drinking Water*. London: IWA Publishing, 2013.

[86] N. Li and Y. Zheng, "Novel Magnesium Alloys Developed for Biomedical Application: A Review," *Journal of Materials Science and Technology*, vol. 29, no. 6, pp. 489–502, Jun. 2013,

[87] M. P. Staiger, A. M. Pietak, J. Huadmai, and G. Dias, "Magnesium and its alloys as orthopedic biomaterials: A review," *Biomaterials*, vol. 27, no. 9, pp. 1728–1734, Mar. 2006,

[88] C. Liu, Y. Xin, G. Tang, and P. K. Chu, "Influence of heat treatment on degradation behavior of bio-degradable die-cast AZ63 magnesium

alloy in simulated body fluid," *Materials Science and Engineering A*, vol. 456, no. 1–2, pp. 350–357, May 2007,

[89] M. O. Wang, J. M. Etheridge, J. A. Thompson, C. E. Vorwald, D. Dean, and J. P. Fisher, "Evaluation of the in vitro cytotoxicity of cross-linked biomaterials," *Biomacromolecules*, vol. 14, no. 5, pp. 1321–1329, May 2013,

[90] N. T. Kirkland, N. Birbilis, M. P. Staiger, N. T. Kirkland, N. Birbilis, and M. P. Staiger, "Assessing the corrosion of biodegradable magnesium implants: A critical review of current methodologies and their limitations," *Elsevier*, vol. 8, no. 3, pp. 925–936, Mar. 2012,

[91] G. Y. Li, J. S. Lian, L. Y. Niu, Z. H. Jiang, and Q. Jiang, "Growth of zinc phosphate coatings on AZ91D magnesium alloy," *Surface and Coatings Technology*, vol. 201, no. 3–4, pp. 1814–1820, Oct. 2006,

[92] E. Ghali, *Corrosion resistance of aluminum and magnesium alloys: understanding, performance, and testing*. Hoboken: Wiley, 2010.

[93] y L.L. Rokhlin, *Magnesium Alloys Containing Rare Earth Metals: Structure and Properties*. London: Taylor & Francis, 2003.

[94] H. Y. Qi, G. X. Huang, H. Bo, G. L. Xu, L. B. Liu, and Z. P. Jin, "Thermodynamic description of the Mg-Nd-Zn ternary system," *Journal of Alloys and Compounds*, vol. 509, no. 7, pp. 3274–3281, Feb. 2011,

[95] G. Xu *et al.*, "Thermodynamic database of multi-component Mg alloys and its application to solidification and heat treatment," *Journal of Magnesium and Alloys*, vol. 4, no. 4, pp. 249–264, Dec. 2016,

[96] D. G. R. William D. Callister, Jr., *Fundamentals of Materials Science and Engineering: An Integrated Approach*, 4th ed. United States: Wiley, 2012.

[97] "Corrosion-resistant alloys in chloride solutions: materials for surgical implants," *Proceedings of the Royal Society of London. Series A.*

Mathematical and Physical Sciences, vol. 294, no. 1439, pp. 486–510, Oct. 1966,

[98] G. L. Makar and J. Kruger, “Corrosion of magnesium,” *International Materials Reviews*, vol. 38, no. 3, pp. 138–153, Jul. 1993,

[99] S. Kim *et al.*, “Synthesis of Si, Mg substituted hydroxyapatites and their sintering behaviors,” *Biomaterials*, vol. 24, no. 8, pp. 1389–1398, Apr. 2003,

[100] C. R. Howlett *et al.*, “The effect of magnesium ion implantation into alumina upon the adhesion of human bone derived cells,” *J. Mater. Sci. Mater. Med.*, vol. 5, pp. 715–722, Sep. 1994,

[101] L. Li, J. Gao, and Y. Wang, “EEEvaluation of cyto-toxicity and corrosion behavior of alkali-heat-treated magnesium in simulated body fluid,” *Surface and Coatings Technology*, vol. 185, no. 1, pp. 92–98, Jul. 2004,

[102] C. A. C. Souza, D. V. Ribeiro, and C. S. Kiminami, “Corrosion resistance of Fe-Cr-based amorphous alloys: An overview,” *Journal of Non-Crystalline Solids*, vol. 442. Elsevier B.V., pp. 56–66, Jun. 15, 2016.

[103] K. Soudki, E. El-Salakawy, and B. Craig, “Behavior of CFRP Strengthened Reinforced Concrete Beams in Corrosive Environment,” *Journal of Composites for Construction*, vol. 11, no. 3, pp. 291–298, Jun. 2007,

[104] W. Zhou, W. P. Weng, and J. X. Hou, “Glass-forming Ability and Corrosion Resistance of Zr-Cu-Al-Co Bulk Metallic Glass,” *Journal of Materials Science and Technology*, vol. 32, no. 4, pp. 349–354, Apr. 2016,

[105] Y. Unigovski, A. Eliezer, E. Abramov, Y. Snir, and E. M. Gutman, “Corrosion fatigue of extruded magnesium alloys,” *Materials Science and Engineering A*, vol. 360, no. 1–2, pp. 132–139, Nov. 2003,

[106] S. Jafari, S. E. Harandi, and R. K. Singh Raman, “A review of stress-corrosion cracking and corrosion fatigue of magnesium alloys for biodegradable implant applications,” *JOM*, vol. 67, no. 5, pp. 1143–1153, May 2015,

[107] C. Smith. M, “Steeling the Show | Science Features | Naked Scientists,” 2012.

[108] R. Ambat, N. N. Aung, and W. Zhou, “Studies on the influence of chloride ion and pH on the corrosion and electrochemical behaviour of AZ91D magnesium alloy,” *Journal of Applied Electrochemistry*, vol. 30, no. 7, pp. 865–874, 2000,

[109] M. P. Staiger, A. M. Pietak, J. Huadmai, and G. Dias, “Magnesium and its alloys as orthopedic biomaterials: A review,” *Biomaterials*, vol. 27, no. 9. pp. 1728–1734, Mar. 2006.

[110] H. Hu, X. Nie, and Y. Ma, “Corrosion and Surface Treatment of Magnesium Alloys,” in *Magnesium Alloys - Properties in Solid and Liquid States*, London: InTech, 2014.

[111] F. Czerwinski, *Magnesium Alloys: Properties in Solid and Liquid States*. London: InTech, 2014.

[112] E. Ghali, *Corrosion Resistance of Aluminum and Magnesium Alloys: Understanding, Performance and Testing*. Hoboken: John Wiley & Sons Inc, 2010.

[113] F. Czerwinski, *Magnesium Alloys: Properties in Solid and Liquid States*. Croatia: IntechOpen, 2014.

[114] K. N. Reichek, K. J. Clark, and J. E. Hillis, “Controlling the salt water corrosion performance of magnesium AZ91 alloy,” Feb. 1985.

[115] S. Jayasathyakawin, M. Ravichandran, N. Baskar, C. A. Chairman, and R. Balasundaram, “Magnesium matrix composite for biomedical applications through powder metallurgy – Review,” *Materials Today:*

Proceedings, vol. 27, no. 2, pp. 736–741, Jun. 2020,

[116] M. Pekguleryuz, K. Kainer, and A. Kaya, *Fundamentals of magnesium alloy metallurgy*. Sawston, Cambridge: Woodhead Publishing Limited, 2013.

[117] O. Khaselev, D. Weiss, and J. Yahalom, “Structure and composition of anodic films formed on binary Mg–Al alloys in KOH–aluminate solutions under continuous sparking,” *Corrosion Science*, vol. 43, no. 7, pp. 1295–1307, Jul. 2001.

[118] C. Wen *et al.*, “Porous bioresorbable magnesium as bone substitute,” *Materials Science Forum*, vol. 419–422, pp. 1001–1006, Mar. 2003,

[119] L. J. Gibson and M. F. Ashby, *Cellular Solids: Structure, Properties and Applications*, 2nd ed. Cambridge: Cambridge University Press, 1999.

[120] J. Banhart, *Manufacture, characterisation and application of cellular metals and metal foams*. Germany: Pergamon, 2001. Accessed: Jul. 26, 2020. [Online]. Available: www.elsevier.com/locate/pmatsci

[121] I. V. Antoniac and D. Laptoiu, “Magnesium aaloys- current orthopedic applications,” *Revista de Ortopedie si Traumatologie a Asociatiei de Ortopedie Româno-Italo-Spaniole*, vol. 4, p. 79, Oct. 2010.

[122] Y. Yamada *et al.*, “Processing of Cellular Magnesium Materials,” *Advanced Engineering Materials*, vol. 2, no. 4, pp. 184–187, Apr. 2000,

[123] * Reifenrath *et al.*, “Subchondral plate reconstruction by fast degrading magnesium scaffolds influence cartilage repair in osteochondral defects,” *ransactions of the 51 st Annual Meeting of the Orthopaedic Research Society (ORS)*, vol. 30, no. S, p. 1347, Feb. 2005.

[124] B. Heublein, R. Rohde, V. Kaese, M. Niemeyer, W. Hartung, and A. Haverich, “Biocorrosion of magnesium alloys: A new principle in cardiovascular implant technology?,” *Heart*, vol. 89, no. 6, pp. 651–656, Jun. 2003,

[125] C. E. Wen, M. Mabuchi, Y. Yamada, K. Shimojima, Y. Chino, and T. Asahina, “Processing of biocompatible porous Ti and Mg,” *Scripta Materialia*, vol. 45, no. 10, pp. 1147–1153, Nov. 2001,

[126] E. M. Bi, Yanming and VanDeMotter, R Renee and Ragab, Ashraf A and Goldberg, Victor M and Anderson, James M and Greenfield, “Titanium particles stimulate bone resorption by inducing differentiation of murine osteoclasts,” *The Journal of Bone and Joint Surgery*, vol. 83, no. 4, p. 501, Apr. 2001.

[127] H. Hu, X. Nie, and Y. Ma, “CCorrosion and Surface Treatment of Magnesium Alloys,” in *Magnesium Alloys - Properties in Solid and Liquid States*, Croatia: IntechOpen, 2014.

[128] T. P. Rüedi and W. M. Murphy, *AO Principles of Fracture Management*. Germany: AO Publishing, 2000.

[129] P. Dearnley and P. A. Dearnley, “A brief review of test methodologies for surface-engineered biomedical implant alloys,” *Surface and Coatings Technology*, vol. 198, no. 1, pp. 483–490, Aug. 2005,

[130] G. Song and A. Atrens, “Understanding Magnesium Corrosion—A Framework for Improved Alloy Performance,” *Advanced Engineering Materials*, vol. 5, no. 12, pp. 837–858, Dec. 2003,

[131] F. Witte, “The history of biodegradable magnesium implants: A review,” *Acta Biomaterialia*, vol. 6, no. 5, pp. 1680–1692, May 2010,

[132] M. R. Smith *et al.*, “Design and assessment of a wrapped cylindrical Ca-P AZ31 Mg alloy for critical-size ulna defect repair,” *Journal of Biomedical Materials Research Part B: Applied Biomaterials*, vol. 100B, no. 1, pp. 206–216, Jan. 2012,

[133] R. Zeng, W. Dietzel, F. Witte, N. Hort, and C. Blawert, “Progress and challenge for magnesium alloys as biomaterials,” *Advanced Engineering Materials*, vol. 10, no. 8, pp. B3–B14, Aug. 2008,

[134] J. E. Gray-Munro, C. Seguin, and M. Strong, “Influence of surface modification on the *in vitro* corrosion rate of magnesium alloy AZ31,” *Journal of Biomedical Materials Research Part A*, vol. 91A, no. 1, pp. 221–230, Oct. 2009,

[135] S. Shadanbaz and G. J. Dias, “Calcium phosphate coatings on magnesium alloys for biomedical applications: A review,” vol. 8, no. 1, pp. 20–30, Jan. 2012,

[136] H. Wang, Y. Estrin, and Z. Zúberová, “Bio-corrosion of a magnesium alloy with different processing histories,” *Materials Letters*, vol. 62, no. 16, pp. 2476–2479, Jun. 2008,

[137] F. Witte *et al.*, “In vivo corrosion and corrosion protection of magnesium alloy LAE442,” *Acta Biomaterialia*, vol. 6, no. 5, pp. 1792–1799, May 2010,

[138] D. Orlov, K. D. Ralston, N. Birbilis, and Y. Estrin, “Enhanced corrosion resistance of Mg alloy ZK60 after processing by integrated extrusion and equal channel angular pressing,” *Acta Materialia*, vol. 59, no. 15, pp. 6176–6186, Sep. 2011,

[139] S. E. Harandi, M. Hasbullah Idris, and H. Jafari, “Effect of forging process on microstructure, mechanical and corrosion properties of biodegradable Mg-1Ca alloy,” *Materials and Design*, vol. 32, no. 5, pp. 2596–2603, May 2011,

[140] G. Song, “Recent Progress in Corrosion and Protection of Magnesium Alloys,” *Advanced Engineering Materials*, vol. 7, no. 7, pp. 563–586, Jul. 2005,

[141] F. Witte *et al.*, “In vitro and in vivo corrosion measurements of magnesium alloys,” *Biomaterials*, vol. 27, no. 7, pp. 1013–1018, Mar. 2006,

[142] A. Yamamoto and S. Hiromoto, “Effect of inorganic salts, amino acids and proteins on the degradation of pure magnesium in vitro,” *Materials*

Science and Engineering C, vol. 29, no. 5, pp. 1559–1568, Jun. 2009,

[143] B. J. Warrell DA, Cox TM, Firth JD, Edward J, *Oxford Textbook of Medicine*. Oxford University Press, 2010.

[144] J. E. Hall, *Guyton and Hall Textbook of Medical Physiology*. United Kingdom: Elsevier Health Sciences, 2015.

[145] J. Walker *et al.*, “Magnesium alloys: Predicting in vivo corrosion with in vitro immersion testing,” *Journal of Biomedical Materials Research Part B: Applied Biomaterials*, vol. 100B, no. 4, pp. 1134–1141, May 2012,

[146] ASTM-G31-72, *Standard Practice for Laboratory Immersion Corrosion Testing of Metals*. United States: ASTM International, 2004.

[147] D. Tan, “In Situ Ultrafast Synchrotron X-RAY Imaging Studies of the Dynamics of Ultrasonic Bubbles in Liquids,” University of Hull, 2015.

[148] T. Liu, Q. Wang, H. W. Zhang, C. S. Lou, K. Nakajima, and J. C. He, “Effects of high magnetic fields on solidification microstructure of Al-Si alloys,” *Journal of Materials Science*, vol. 46, no. 6, pp. 1628–1634, Mar. 2011,

[149] B. Fragoso and H. S. Technology, “Fragoso, Bruno, and Henrique Santos. "Effect of a rotating magnetic field at the microstructure of an A354,” *Journal of Materials Research and Technology*, vol. 2, no. 2, pp. 100–109, Apr. 2013.

[150] J. Abboud, J. M.-S. Reports, and U. 2020, “Developing of nano sized fibrous eutectic silicon in hypereutectic Al–Si alloy by laser remelting,” *Scientific Reports*, vol. 10, no. 1, pp. 1–18, Jul. 2020.

[151] ALLEN and RF, *Standard Test Methods for Determining Average Grain Size*. United States: ASTM International, 2010.

[152] Y. Lu, Y. Huang, F. Feyerabend, R. Willumeit-Römer, K. U. Kainer, and N. Hort, “Microstructure and mechanical properties of Mg-Gd alloys as

biodegradable implant materials," in *TMS 2018 147th Annual Meeting & Exhibition Supplemental Proceedings*, 2018, vol. Part F12, pp. 253–262.

[153] Y. Chen, Z. Xu, C. Smith, and J. Sankar, "Recent advances on the development of magnesium alloys for biodegradable implants," *Acta Biomaterialia*, vol. 10, no. 11. Elsevier Ltd, pp. 4561–4573, Nov. 01, 2014.

[154] L. Yang *et al.*, "Microstructure, mechanical and corrosion properties of Mg-Dy-Gd-Zr alloys for medical applications," *Acta Biomaterialia*, vol. 9, no. 10, pp. 8499–8508, Nov. 2013,

[155] S. Luo, G. Yang, H. Qin, L. Xiao, and W. Jie, "Substitution Effects of Gd with Nd on Microstructures and Mechanical Properties of Mg–10Gd–0.4Zr Alloys," *Advanced Engineering Materials*, vol. 22, no. 7, p. 1901576, Jul. 2020,

[156] N. Liu, Z. Zhang, L. Peng, and W. Ding, "Microstructure evolution and mechanical properties of Mg-Gd-Sm-Zr alloys," *Materials Science and Engineering: A*, vol. 627, pp. 223–229, Mar. 2015,

[157] et al D. Wu, "Effect of heat treatment on the microstructures and mechanical properties of the sand-cast Mg–2.7Nd–0.6Zn–0.5Zr alloy," *Journal of Magnesium and Alloys*, vol. 2, no. 1, pp. 20–26, Mar. 2014.

[158] L. Peng, P. Fu, Z. Li, Y. Wang, and H. Jiang, "High cycle fatigue properties of cast Mg-xNd-0.2Zn-Zr alloys," *Journal of Materials Science*, vol. 49, no. 20, pp. 7105–7115, Jul. 2014,

[159] Метротест, "ASTM E92 Standard test methods for Vickers hardness of metallic materials," 2003.

[160] R. Baboian, *Corrosion Tests and Standards: Application and Interpretation*, 2nd ed. West Conshohocken: ASTM International, 2005.

[161] N. Zidane *et al.*, “Effect of gadolinium content on the corrosion behavior of magnesium alloys in 1 wt.% NaCl solution,” *Portugaliae Electrochimica Acta*, vol. 33, no. 5, pp. 289–304, Apr. 2015,

[162] A. Bahmani, S. Arthanari, and K. S. Shin, “Formulation of corrosion rate of magnesium alloys using microstructural parameters,” *Journal of Magnesium and Alloys*, vol. 8, no. 1. pp. 134–149, Mar. 01, 2020.

[163] X. Zhang, J. Dai, R. Zhang, Z. Ba, and N. Birbilis, “Corrosion behavior of Mg–3Gd–1Zn–0.4Zr alloy with and without stacking faults,” *Journal of Magnesium and Alloys*, vol. 7, no. 2, pp. 240–248, Jun. 2019,

[164] H. Zengin and Y. Turen, “Effect of Y addition on microstructure and corrosion behavior of extruded Mg–Zn–Nd–Zr alloy,” *Journal of Magnesium and Alloys*, vol. 8, no. 3, pp. 640–653, Sep. 2020,

[165] X. Y. Fang, D. Q. Yi, J. F. Nie, X. J. Zhang, B. Wang, and L. R. Xiao, “Effect of Zr, Mn and Sc additions on the grain size of Mg-Gd alloy,” *Journal of Alloys and Compounds*, vol. 470, no. 1–2, pp. 311–316, Feb. 2009,

[166] V. Metan, K. Eigenfeld, D. Räbiger, M. Leonhardt, and S. Eckert, “Grain size control in Al-Si alloys by grain refinement and electromagnetic stirring,” *Journal of Alloys and Compounds*, vol. 487, no. 1–2, pp. 163–172, Nov. 2009,

[167] P. Fan, S. Cockcroft, D. Maijer, L. Yao, C. Reilly, and A. Phillion, “metals Examination and Simulation of Silicon Macrosegregation in A356 Wheel Casting,” *Metals*, vol. 8, no. 7, p. 503, Jul. 2018,

[168] Y. Li, Y. Yang, and X. Ma, “Grain refinement effect of pulsed magnetic field on solidified microstructure of superalloy IN718,” *Journal of Materials Research*, vol. 24, no. 10, pp. 3174–3181, Oct. 2009,

[169] Q. Zou, N. Han, Z. Zhang, J. Jie, F. Xu, and X. An, “metals Enhancing Segregation Behavior of Impurity by Electromagnetic Stirring in the Solidification Process of Al-30Si Alloy,” *Metals*, vol. 10, no. 1, p. 155,

Jan. 2020,

[170] R. Li *et al.*, “Effect of axial magnetic field on TIG welding–brazing of AA6061 aluminum alloy to HSLA350 steel,” *Journal of Materials Research and Technology*, vol. 12, no. 1, pp. 882–893, May 2021.

[171] Y. Han, C. Ban, H. Zhang, H. Nagaumi, Q. Ba, and J. Cui, “Investigations on the solidification behavior of Al-Fe-Si alloy in an alternating magnetic field,” *Materials Transactions*, vol. 47, no. 8, pp. 2092–2098, Aug. 2006,

[172] Q. Zou *et al.*, “Enhancing segregation behavior of impurity by electromagnetic stirring in the solidification process of Al-30Si alloy,” *Metals*, vol. 10, no. 1, Jan. 2020,

[173] Y. Zhang *et al.*, “metals Comparative Study on the Grain Refinement of Al-Si Alloy Solidified under the Impact of Pulsed Electric Current and Travelling Magnetic Field,” *Metals*, vol. 6, no. 7, p. 170, Jul. 2016,

[174] L. Qiuzu, D. Xiaofeng, L. Yanping, and W. Xiaojia, “Analysis on micro-structure and mechanical properties of Mg-Gd-Y-Nd-Zr alloy and its reinforcement mechanism,” *Journal of Alloys and Compounds*, vol. 690, pp. 961–965, Jan. 2017,

[175] J. P. Hadorn, T. T. Sasaki, T. Nakata, T. Ohkubo, S. Kamado, and K. Hono, “Solute clustering and grain boundary segregation in extruded dilute Mg-Gd alloys,” *Scripta Materialia*, vol. 93, pp. 28–31, Dec. 2014,

[176] J. Li, R. Chen, Y. Ma, and W. Ke, “Effect of Zr modification on solidification behavior and mechanical properties of Mg-Y-RE (WE54) alloy,” *Journal of Magnesium and Alloys*, vol. 1, no. 4, pp. 346–351, Dec. 2013,

[177] X. Liu, Q. Le, Z. Zhang, L. Bao, and J. Cui, “Effects of Nd/Gd ratio on the microstructures and mechanical properties of Mg-Gd-Y-Nd-Zr alloys,” *Indian Journal of Engineering & Materials Sciences*, vol. 22, pp. 14–22, 2015.

[178] P. Jiang, C. Blawert, and M. L. Zheludkevich, “corrosion and materials degradation The Corrosion Performance and Mechanical Properties of Mg-Zn Based Alloys-A Review,” *Corrosion and Materials Degradation*, vol. 1, no. 1, pp. 92–158, Apr. 2020,

[179] F. Kabirian and R. Mahmudi, “Effects of Zirconium Additions on the Microstructure of As-Cast and Aged AZ91 Magnesium Alloy,” *Advanced Engineering Materials*, vol. 11, no. 3, pp. 189–193, Mar. 2009,

[180] W. Zhang, Z. Feng, X. Li, and Y. Chen, “Effect of zr content on the distribution characteristic of the 14H and 18R LPSO phases,” *Materials Research*, vol. 23, no. 1, pp. 19–23, Jun. 2020,

[181] J. F. Nie, “Precipitation and hardening in magnesium alloys,” *Metallurgical and Materials Transactions A*, vol. 43, no. 11, pp. 3891–3939, Nov. 2012,

[182] J. F. Nie, X. Gao, and S. M. Zhu, “Enhanced age hardening response and creep resistance of Mg-Gd alloys containing Zn,” *Scripta Materialia*, vol. 53, no. 9, pp. 1049–1053, Nov. 2005,

[183] L. L. Rokhlin, “Regularities of the Mg sides of the Mg-RE (magnesium-rare earth metal) phase diagrams: Comments on evaluations,” *Journal of Phase Equilibria*, vol. 16, no. 6, pp. 504–507, Dec. 1995,

[184] L. L. Rokhlin, T. V. Dobatkina, and N. I. Nikitina, “Constitution and properties of the ternary magnesium alloys containing two rare-earth metals of different subgroups,” in *Materials Science Forum*, 2003, vol. 419–422, no. I, pp. 291–296.

[185] M. Bugnet, A. Kula, M. Niewczas, and G. A. Botton, “Segregation and clustering of solutes at grain boundaries in Mg-rare earth solid solutions,” *Acta Materialia*, vol. 79, pp. 66–73, Oct. 2014,

[186] Y. B. Hu, J. Deng, C. Zhao, F. S. Pan, and J. Peng, “Microstructure and mechanical properties of Mg-Gd-Zr alloys with low gadolinium

contents," *Journal of Materials Science*, vol. 46, no. 17, pp. 5838–5846, Sep. 2011,

[187] Y. Xu, F. Gensch, Z. Ren, K. U. Kainer, and N. Hort, "Effects of Gd solutes on hardness and yield strength of Mg alloys," *Progress in Natural Science: Materials International*, vol. 28, no. 6, pp. 724–730, Dec. 2018,

[188] Y. Zhao *et al.*, "Effect of Gd addition on the age hardening response of Mg–6Zn-1Mn alloy," *Journal of Materials Research and Technology*, vol. 9, no. 4, pp. 8834–8841, Jul. 2020,

[189] D. Qiu and M. X. Zhang, "Strengthening mechanisms and their superposition law in an age-hardenable Mg-10 wt pct y alloy," *Metallurgical and Materials Transactions A*, vol. 43, no. 9, pp. 3314–3324, Sep. 2012,

[190] G. R. Argade, S. K. Panigrahi, and R. S. Mishra, "Effects of grain size on the corrosion resistance of wrought magnesium alloys containing neodymium," *Corrosion Science*, vol. 58, pp. 145–151, May 2012,

[191] F.-Y. Ma, "Corrosive Effects of Chlorides on Metals," in *Pitting Corrosion*, Croatia: IntechOpen, 2012.

[192] N. Eliaz, "materials Corrosion of Metallic Biomaterials: A Review," vol. 12, no. 3, p. 407, Jan. 2019,

[193] C. Schille *et al.*, "Corrosion of experimental magnesium alloys in blood and PBS: A gravimetric and microscopic evaluation," *Materials Science and Engineering B:*, vol. 176, no. 20, pp. 1797–1801, Dec. 2011,

Chapter 8 Appendix

8.1 Appendix A: Comparisons of Silicon particles (tables and graphs)

Table1: Measurement of the primary Si particles and the eutectic Si particles using ImageJ for the samples processed using magnetic field flux density of 0 T (equivalent to 0 voltage input)

100× SEM images were used to measure the primary Si particle areas									
400× SEM images were used to measure the eutectic Si particle areas									
	Measurement position Top			**Measurement position Middle**			**Measurement position Bottom**		
No	**Primary Si (μm^2)**	**Eutectic Si**		**Primary Si (μm^2)**	**Eutectic Si**		**Primary Si (μm^2)**	**Eutectic Si**	
		Length (μm)	**Area (μm^2)**		**Length (μm)**	**Area (μm^2)**		**Length (μm)**	**Area (μm^2)**
1	7382.37	65.553	100.255	2400.794	96.424	197.676	23045	75.087	145.089
2	14786	72.802	94.587	2280.329	60.608	219.197	15853	88.489	201.601
3	10382.65	88.33	122.573	2362.528	39.13	152.154	14617	42.974	74.936
4	15243.76	74.073	103.975	2740.93	44.72	175.889	12786	81.267	109.038
5	13689.06	49.51	116.905	2420.635	109.271	88.919	10453	54.31	235.615
6	23137.76	51.032	215.3	3650.794	75.798	104.063	19858	77.702	115.416
7	24340.99	56.591	75.103	2638.889	107.282	123.902	24873	72.378	145.444
8	13685.03	57.811	50.216	2261.905	105.12	123.193	21104	121.495	255.279
9	14069.59	53.895	69.435	2386.621	70.807	117.082	10377	63.093	67.496
10	12068.94	49.01	171.195	1675.17	63.82	123.813	14668	124.671	142.698
11	13379.29	35.474	148.7	1615.646	65.893	209.809	17322	88.361	108.596
12	9863.25	59.187	79.177	1445.578	83.008	175.712	12164	58.334	48.54
13	8936.058	43.254	86.616	2278.912	97.351	159.682	6401	116.498	57.664
14	11479.85	88.957	128.153	2339.853	111.138	170.93	14780	88.858	66.344
15	12846.88	54.045	130.013	2575.113	73.297	195.285	6917	143.059	75.113
16	15873.2			2206.633			18907		
17	4900.794			3935.658			9431		
18	7821.91			3629.535			13582		
19	5716.37			2957.766			7218		
20	4098.3			3368.764			7218		
Avg	**12185.1**	**59.968**	**112.81**	**2558.603**	**80.24**	**155.82**	**14078.7**	**86.438**	**187.73**

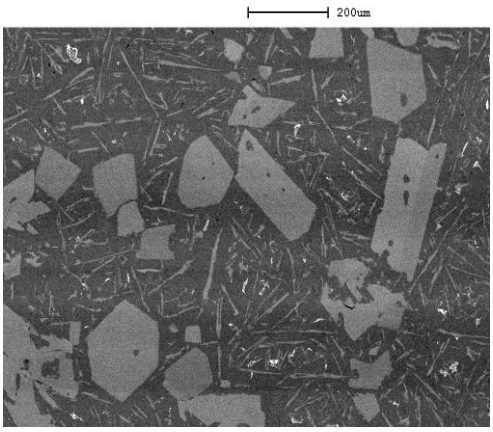

Typical image at the **top** location (100X)

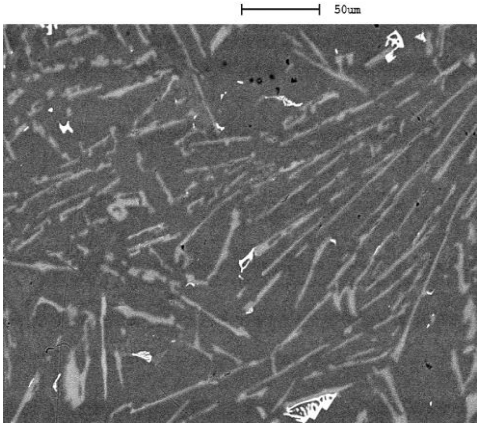

Typical image at the **top** location (400X)

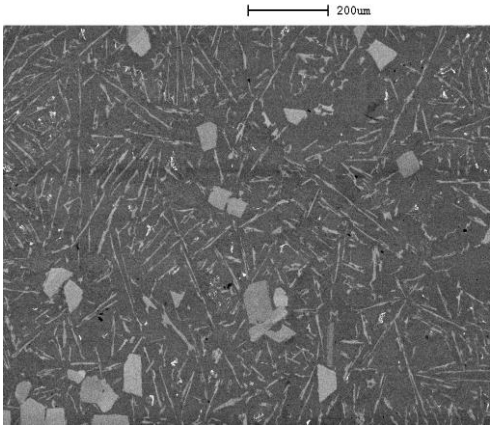

Typical image at the **mid** location (100X)

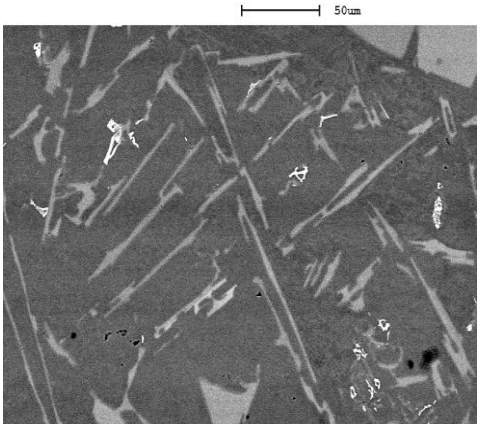

Typical image at the **mid** location (400X)

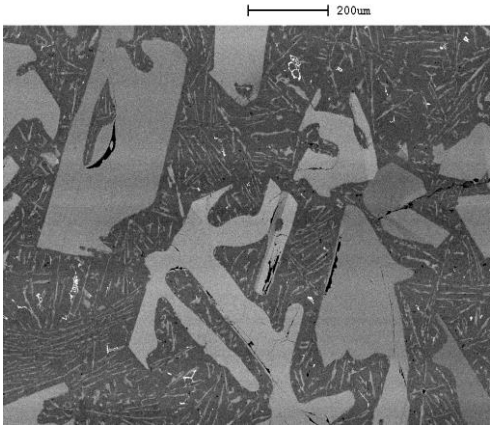

Typical image at the **bottom** location (100X)

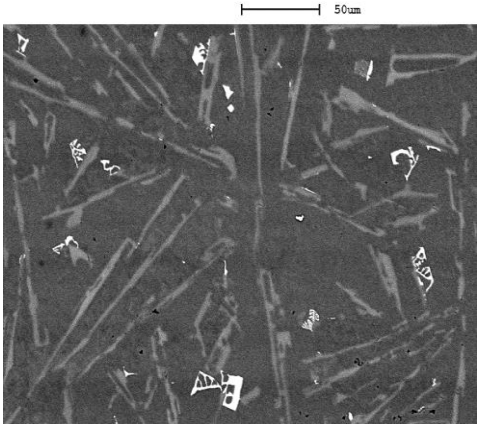

Typical image at the **bottom** location (400X)

Figure 1: SEM images used for measuring the Si particles of the sample processed at 0.3 T (equivalent to 40 voltage input), (a, b, and c) for the primary Si particles. (d, e and f) for the eutectic Al-Si particles.

Table 2: Measurement of the primary Si particles and the eutectic Si particles using ImageJ for the samples processed using magnetic field flux density of 0.3 T (equivalent to 40 voltage input)

100× SEM images were used to measure the primary Si particle areas									
400× SEM images were used to measure the eutectic Si particle areas									
	Measurement position Top			**Measurement position Middle**			**Measurement position Bottom**		
No	**Primary Si (μm^2)**	**Eutectic Si**		**Primary Si (μm^2)**	**Eutectic Si**		**Primary Si (μm^2)**	**Eutectic Si**	
		Length (μ)	**Area (μm^2)**		**Length (μm)**	**Area (μm^2)**		**Length (μm)**	**Area (μm^2)**
1	15006.63	53.21	403.55	2825.487	75.964	101.975	17010.79	65.393	87.619
2	10223.39	129.055	273.037	2816.881	83.698	145.216	12780.24	48.427	125.258
3	6195.991	69.031	293.833	2287.64	90.867	126.484	9684.473	45.571	120.444
4	9467.532	58.25	369.487	2858.475	80.778	246.227	28126.21	47.183	65.386
5	11039.48	78.133	139.835	4233.927	73.631	194.671	7661.223	50.248	86.307
6	3182.617	88.663	165.203	3010.506	76.179	158.783	16087.74	42.374	94.272
7	5190.577	93.493	224.722	3701.818	88.035	97.336	11727.1	50.336	167.186
8	3720.463	84.769	143.51	7524.113	93.195	225.482	12164.41	62.957	137.425
9	3653.053	55.507	382.037	4309.943	72.695	125.521	25585.39	64.354	135.937
10	6287.784	50.356	215.32	2663.416	55.606	138.651	3180.183	47.191	51.556
11	11126.97	58.682	175.36	2832.658	65.646	178.828	11239.97	47.512	114.229
12	4755.997	92.506	309.369	5950.733	77.479	206.663	4987.545	68.517	131.035
13	2898.634	73.671	209.37	4692.89	104.378	292.269	12394.41	60.654	114.054
14	3029.151	81.406	199.375	3891.14	100.881	213.928	25585.39	46.749	130.335
15	2753.774	125.212	315.927	6151.529	87.56	199.923	3180.183	62.516	126.571
16	7914.231			3532.576			10939.97		
17	15812.69			3063.573			4887.545		
18									
19									
20									
Average	**7191.703**	**79.46293**	**254.6623**	**3902.783**	**81.7728**	**176.7971**	**12777.81**	**53.9988**	**112.5076**

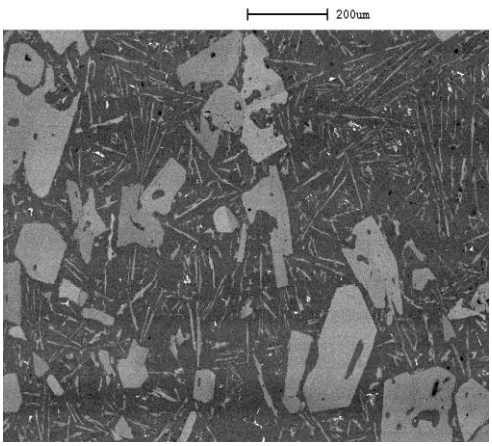

Typical image at the **top** location (100X)

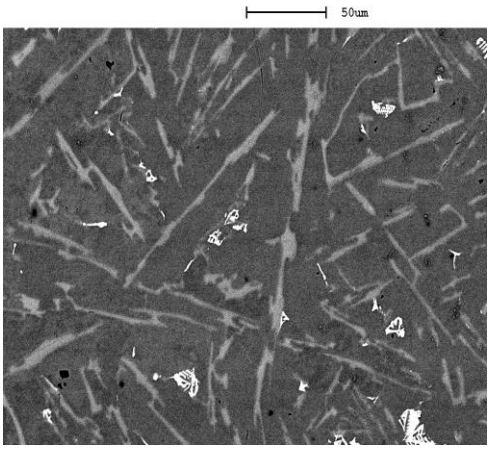

Typical image at the **top** location (400X)

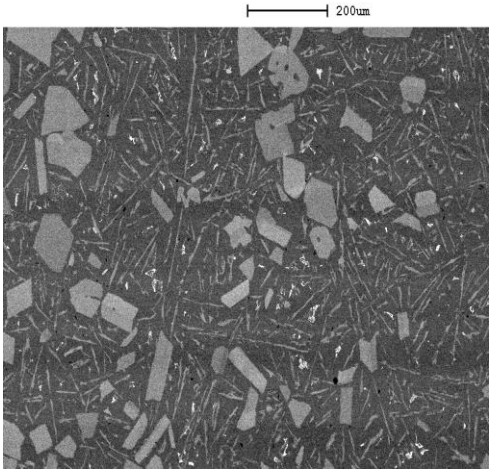

Typical image at the **mid** location (100X)

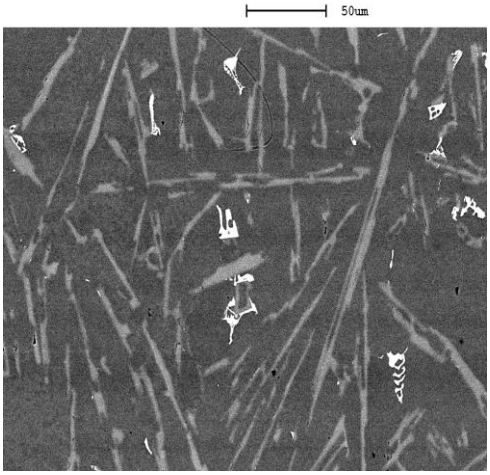

Typical image at the **mid** location (400X)

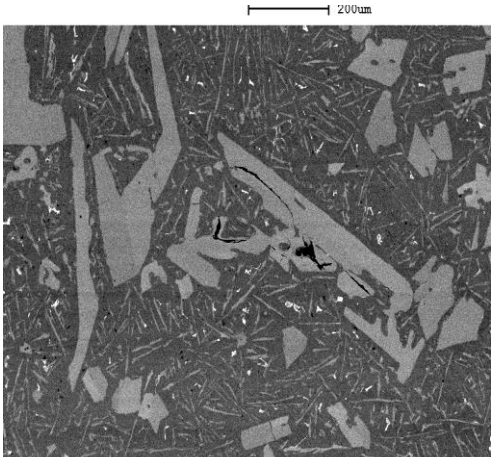

Typical image at the **bottom** location (100X)

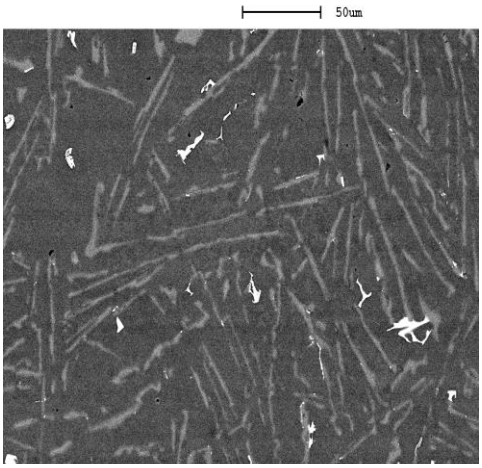

Typical image at the **bottom** location (400X)

Figure 2: SEM images used for measuring the Si particles of the sample processed at 0.3 T (equivalent to 40 voltage input), (a, b, and c) for the primary Si particles. (d, e and f) for the eutectic Al-Si particles.

Table 3: Measurement of the primary Si particles and the eutectic Si particles using ImageJ for the samples processed using magnetic field flux density of 0.7 T (equivalent to 80 voltage input)

100× SEM images were used to measure the primary Si particle areas									
400× SEM images were used to measure the eutectic Si particle areas									
	Measurement position Top			**Measurement position Middle**			**Measurement position Bottom**		
No	**Primary Si (μm^2)**	**Eutectic Si**		**Primary Si (μm^2)**	**Eutectic Si**		**Primary Si (μm^2)**	**Eutectic Si**	
		Length (μm)	**Area (μm^2)**		**Length (μm)**	**Area (μm^2)**		**Length (μm)**	**Length (μm)**
1	3601.063	133.851	236.147	6173.251	89.248	136.232	8921.949	42.838	122.414
2	4868.025	47.673	396.648	3348.804	105.061	111.076	6191.531	105.435	130.74
3	5953.587	207.357	437.128	4546.324	57.959	173.611	6728.757	55.573	224.72
4	2930.735	45.683	410.201	7508.237	153.822	254.482	8396.347	54.931	269.894
5	5527.015	74.499	371.404	8997.697	71.245	311.703	7573.208	119.253	228.086
6	4994.154	122.858	359.889	4842.516	89.626	243.056	8509.098	39.287	255.811
7	4506.643	77.647	92.652	6031.532	98.112	155.098	6914.199	77.222	238.715
8	1831.001	93.951	490.451	1662.356	82.523	230.389	5732.355	87.886	138.003
9	3129.141	60.609	277.866	2144.198	74.05	419.855	7276.225	114.639	218.077
10	3956.776	66.016	258.822	15954.65	85.491	413.744	6027.124	114.931	136.497
11	5439.15	36.819	380.527	13759.43	59.22	310.994	7048.436	94.36	225.429
12	3581.222	71.993	313.652	7005.137	94.821	424.55	8202.878	88.485	347.222
13		51.263	449.706		95.743	232.249		58.158	101.952
14		97.745	515.43		111.578	359.8		41.318	234.552
15		115.09	304.705		66.082	347.222		27.439	136.409
16					88.565	462.284		104.696	182.292
17								114.931	
18									
19									
20									
Average	**4193.209**	**86.87**	**353.0152**	**6831.178**	**88.95**	**286.64**	**7293.51**	**78.9**	**199.42**

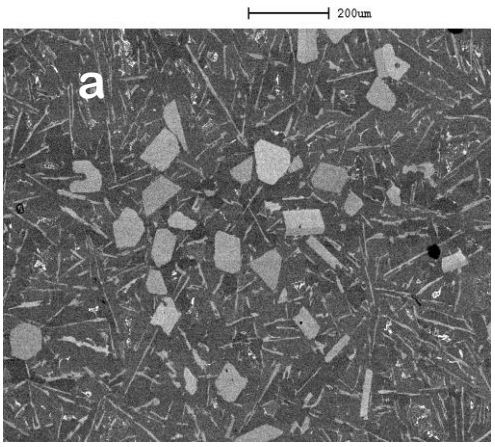

Typical image at the **top** location (100X)

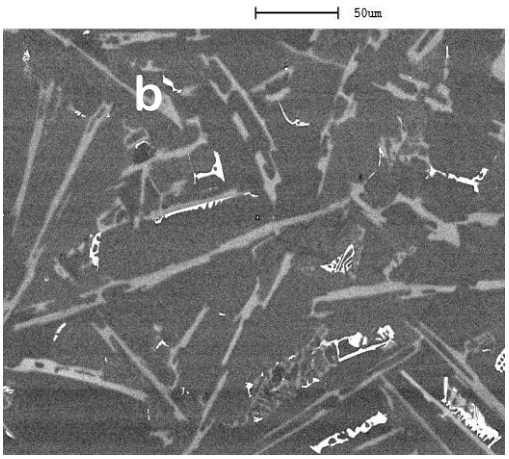

Typical image at the **top** location (400X)

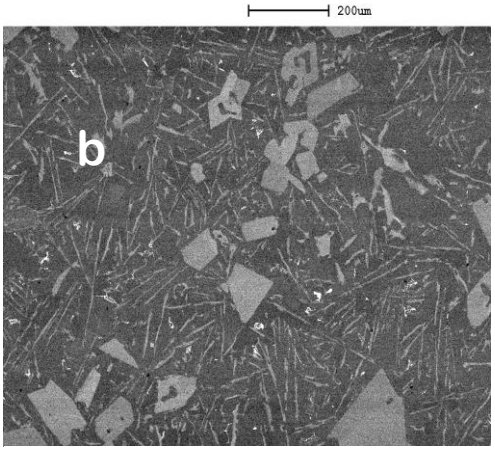

Typical image at the **mid** location (100X)

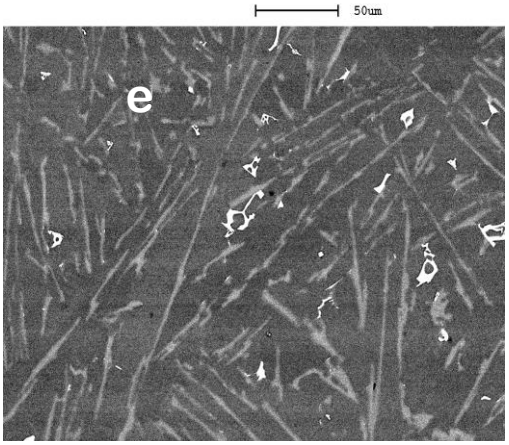

Typical image at the **mid** location (400X)

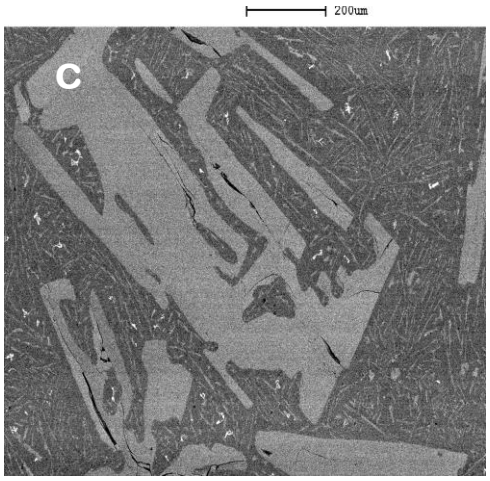

Typical image at the **bottom** location (100X)

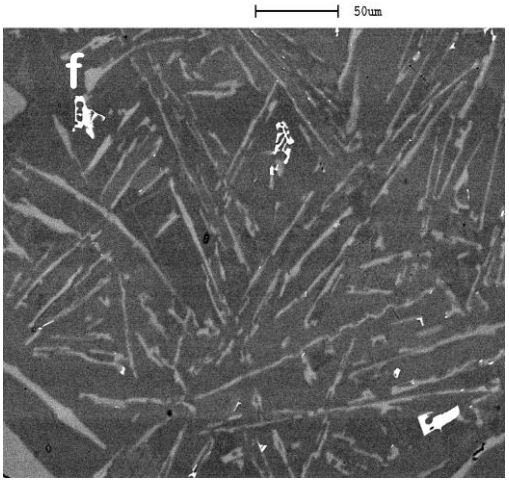

Typical image at the **bottom** location (400X)

Figure 3: SEM images used for measuring the Si particles of the sample processed at 0.7 T (equivalent to 80 voltage input), (a, b, and c) for the primary Si particles. (d, e and f) for the eutectic Al-Si particles.

Table 4: Measurement of the primary Si particles and the eutectic Si particles using ImageJ for the samples processed using magnetic field flux density of 0.85 T (equivalent to 100 voltage input)

100× SEM images were used to measure the primary Si particle areas									
400× SEM images were used to measure the eutectic Si particle areas									
	Measurement position Top			**Measurement position Middle**			**Measurement position Bottom**		
Length (μ)	**Length (μ)**	**Eutectic Si**		**Length (μ)**			**Length (μ)**		
		Length (μm)	**Area ($μm^2$)**		**Length (μm)**	**Area ($μm^2$)**		**Length (μm)**	**Area ($μm^2$)**
1	6354.828	46.04	107.975	3517.074	103.133	144.646	9680.875	64.115	140.129
2	7791.85	75.16	156.25	1981.348	42.418	65.104	7104.899	100.852	140.129
3	7421.708	31.342	82.111	3871.249	41.925	111.43	5705.785	68.28	220.291
4	7385.419	99.276	163.336	4192.038	73.585	139.775	6021.533	20.833	126.134
5	10038.83	74.026	115.15	2187.466	72.441	591.164	5137.282	56.761	26.573
6	10379.94	69.59	64.75	5793.083	24.666	115.239	5947.966	80.922	60.852
7	8439.235	47.876	144.912	4149.944	26.15	264.757	4875.727	59.561	133.397
8	5765.504	63.546	85.92	4203.651	53.417	56.158	6025.464	32.674	92.297
9	6642.232	65.259	105.938	2447.291	32.057	231.629	5925.423	39.399	120.022
10	2804.369	32.993	111.873	3920.601	25.776	326.849	6123.673	33.467	61.295
11	4576.696	45.216	73.696	3913.343	60.578	227.289	6221.917	37.278	36.582
12	2091.665	33.699	142.698	3996.081	52.625	26.927		40.977	84.68
13	14661.97	36.519	147.924	5514.388	45.107	72.456		27.421	171.662
14		59.694	175.383		69.215	244.207		46.544	122.768
15		75.248	211.256		30.603	296.025		67.007	107.798
16		69.671	143.406		22.224	214.445		20.207	120.996
17		43.354	176.003		52.062	415.604		42.96	145.001
18								26.503	
19								16.074	
20								23.101	
21								35.875	
23								29.786	
Average	**7258.019**	**56.97**	**129.9165**	**3822.12**	**48.7**	**208.45**	**6312.441**	**42.17**	**112.39**

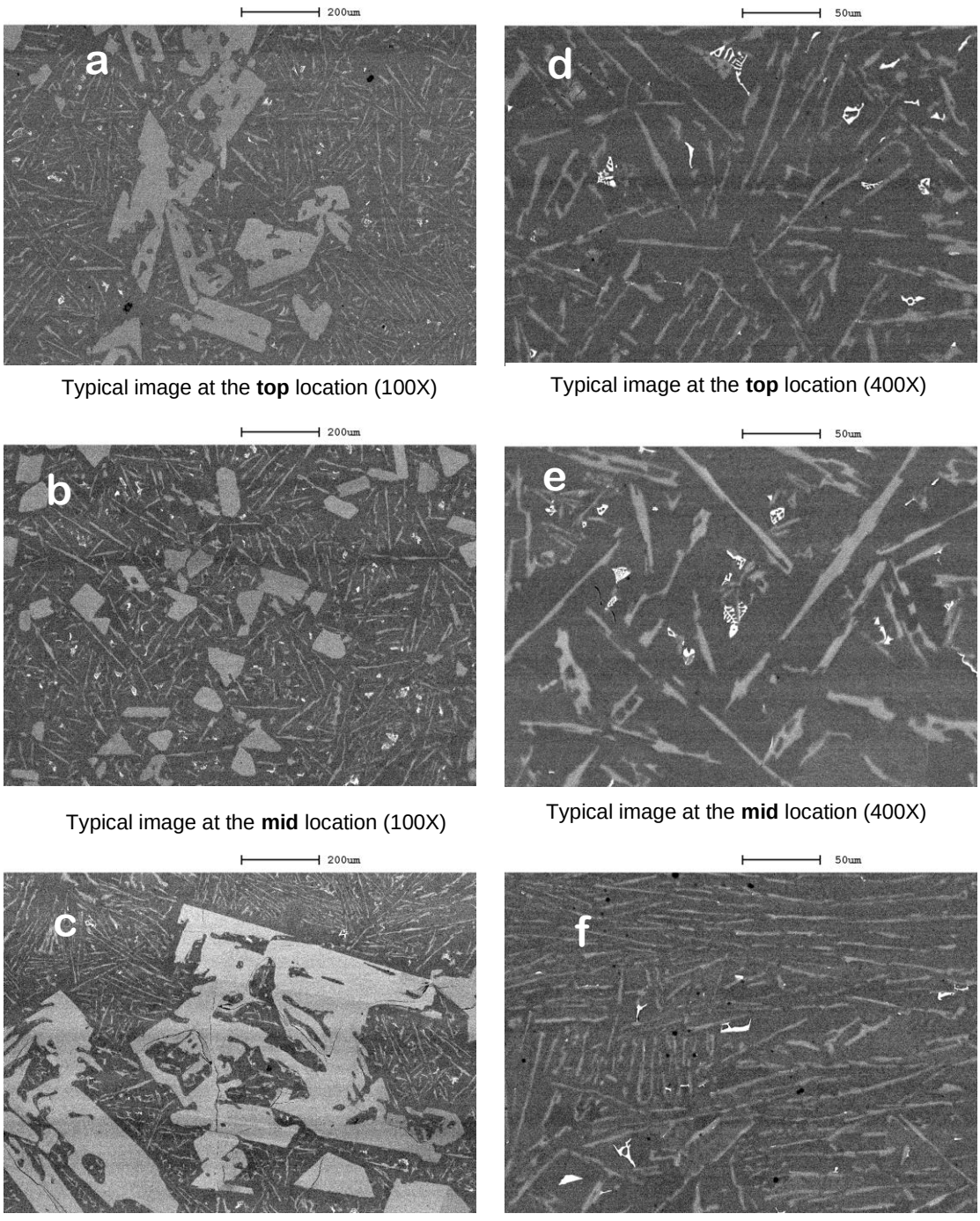

Typical image at the **top** location (100X)

Typical image at the **top** location (400X)

Typical image at the **mid** location (100X)

Typical image at the **mid** location (400X)

Typical image at the **bottom** location (100X)

Typical image at the **bottom** location (400X)

Figure 4: SEM images used for measuring the Si particles of the sample processed at 0.85 T (equivalent to 100 voltage input), (a, b, and c) for the primary Si particles. (d, e and f) for the eutectic Al-Si particles.

Table 5: Measurement of the primary Si particles and the eutectic Si particles using ImageJ for the samples processed using magnetic field flux density of 1.0 T (equivalent to 120 voltage input)

100× SEM images were used to measure the primary Si particle areas									
400× SEM images were used to measure the eutectic Si particle areas									
	Measurement position Top			**Measurement position Middle**			**Measurement position Bottom**		
Length (μ)	**Length (μ)**	**Eutectic Si**		**Length (μ)**	**Eutectic Si**		**Length (μ)**	**Eutectic Si**	
		Length (μm)	**Area (μm^2)**		**Length (μm)**	**Area (μm^2)**		**Length (μm)**	**Area (μm^2)**
1	16694.13	78.179	101.112	7341.873	75.574	297.366	8900.36	34.815	52.797
2	10076.57	55.89	120.832	5086.185	68.781	400.369	5716.856	18.883	196.755
3	1949.414	48.485	43.743	4041.078	36.357	325.69	6408.525	60.554	208.049
4	6009.362	69.357	281.015	1387.669	36.561	702.33	3567.672	22.819	283.166
5	2547.447	58.132	39.53	1707.007	140.718	208.36	7153.335	50.762	82.556
6	1611.206	39.86	82.288	1812.969	10.732	299.36	7644.783	135.576	119.308
7	2659.215	43.716	74.31	6906.412	61.116	511.72	6955.439	36.801	231.266
8	3533.041	36.469	49.122	3377.726	64.115	193.99	2265.43	110.806	98.96
9	18997.71	20.328	80.943	2440.033	122.031	602.36	6174.453	42.851	109.717
10	8919.694	44.979	237.72	4431.542	32.759	97.63	8743.427	33.319	125.134
11		56.054	54.858	4087.528	44.594	103.654		59.332	231.624
12		81.897	56.741	3942.374	37.17	189.27		21.559	130.692
13		52.994	97.616	3643.357	38.083	209.86		34.216	259.502
14		61.464	62.657	2860.979	30.912	211.67		18.263	79.15
15		34.32	139.925	3801.575	31.435	201.28		34.216	61.492
16		36.052	146.199	4221.069	47.937	100.369		28.354	35.407
17		22.952	197.562		33.044	143.81		27.887	36.303
18		28.15				106.87		12.926	110.523
19		21.776							
Average	**7299.78**	**46.9**	**109.77**	**3818.09**	**53.64**	**272.5532**	**6353.03**	**43.55**	**136.24**

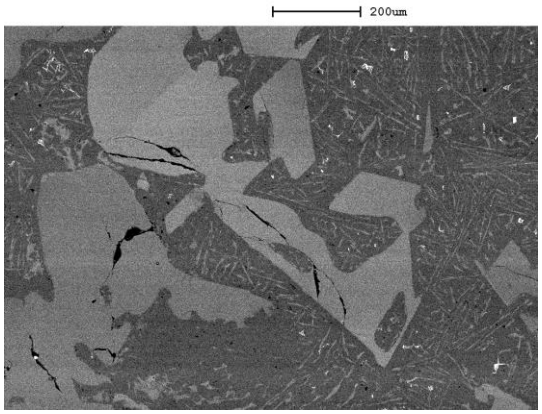

Typical image at the **top** location (100X)

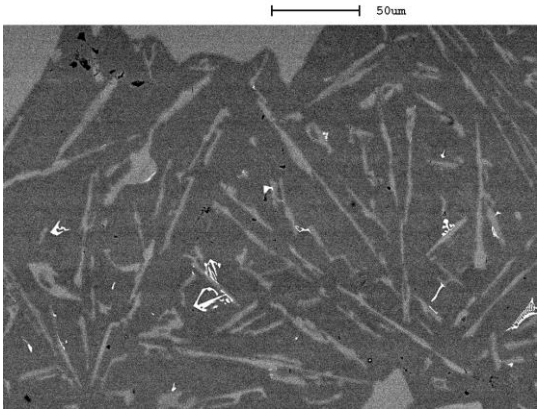

Typical image at the **top** location (400X)

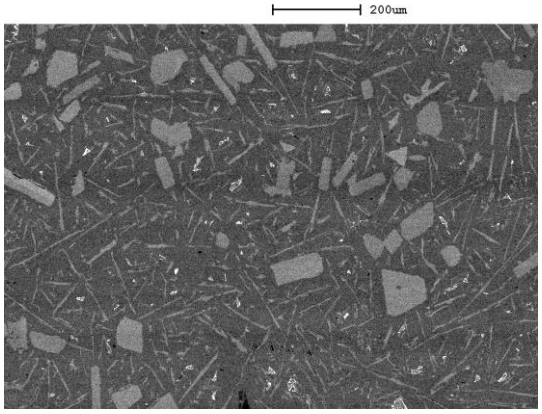

Typical image at the **mid** location (100X)

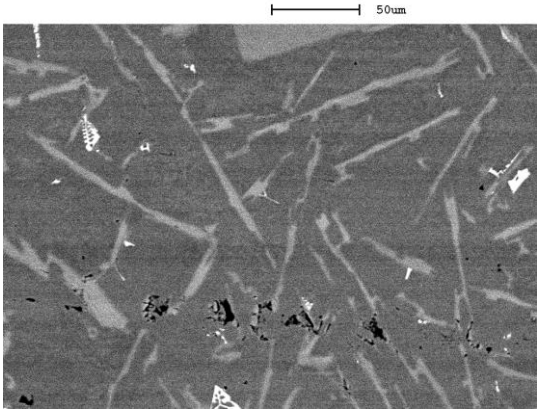

Typical image at the **mid** location (400X)

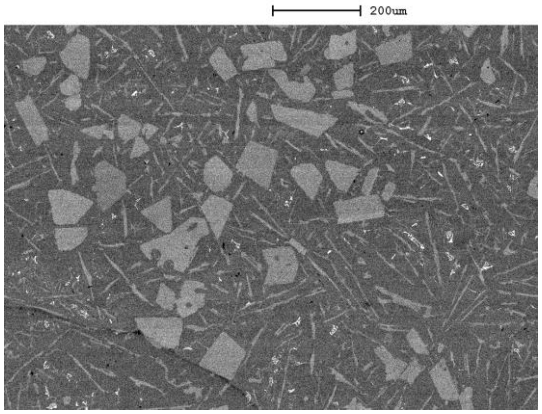

Typical image at the **bottom** location (100X)

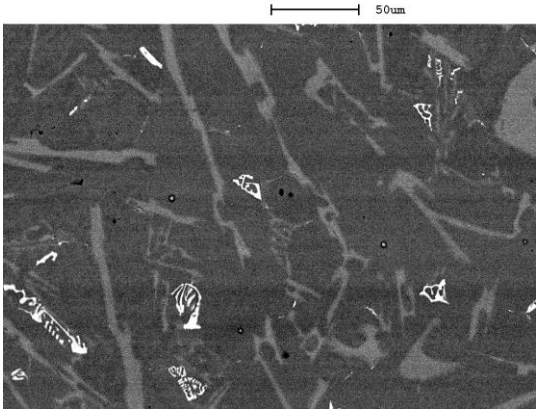

Typical image at the **bottom** location (400X)

Figure 5: SEM images used for measuring the Si particles of the sample processed at 1.0 T (equivalent to 120 voltage input), (a, b, and c) for the primary Si particles. (d, e and f) for the eutectic Al-Si particles.

Table 6: Measurement of the primary Si particles and the eutectic Si particles using ImageJ for the samples processed using magnetic field flux density of 1.4 T (equivalent to 160 voltage input)

100× SEM images were used to measure the primary Si particle areas									
400× SEM images were used to measure the eutectic Si particle areas									
	Measurement position Top			**Measurement position Middle**			**Measurement position Bottom**		
Length (µ)	**Length (µ)**	**Eutectic Si**		**Length (µ)**	**Eutectic Si**		**Length (µ)**	**Eutectic Si**	
		Length (µm)	**Area (µm²)**		**Length (µm)**	**Area (µm²)**		**Length (µm)**	**Area (µm²)**
1	4674.08	63.98	93.803	2766.576	28.484	56.069	1320.232	56.776	56.512
2	4565.072	50.386	70.064	5204.736	34.489	65.193	3169.112	34.475	68.204
3	3456.432	16.501	167.765	5957.696	16.437	169.625	2136.728	17.57	65.193
4	5335.248	79.927	108.507	1890.288	18.155	72.19	3841.683	50.065	44.023
5	2825.392	23.943	79.099	2095.376	26.997	110.013	1709.106	34.893	48.806
6	3495.152	27.376	83.705	5974.896	58.914	60.144	2023.249	27.085	67.85
7	2053.776	134.867	180.52	3978.48	68.379	92.474	1284.251	34.765	51.818
8	3049.12	63.381	63.953	3209.76	70.289	54.298	1972.045	40.625	44.554
9	5204.736	74.667	117.896	2841.168	46.04	75.025	1047.606	21.848	41.1
10	2572.96	83.81	91.677	5756.896	36.485	132.246	1473.291	34.488	30.382
11	3347.44	36.548	148.455	4276.8	60.856	21.081	4893.44	19.8	5.58
12	2703.472	40.024	107.621	2408.032	72.634	162.893	1415.721	45.06	25.156
13	5158.832	43.392	174.674	4410.176	122.354	254.571	1840.576	47.747	52.26
14	2035.136	71.432	55.892	1903.184	26.261	115.062	2241.904	34.103	37.557
15	3363.216	51.84	70.95	3014.704	69.187	295.493	3263.216	19.345	70.419
16	5342.416	20.765	354.131	1824.304	42.644	116.125	2967.063	51.674	37.114
17	1655.072	73.752	217.368	5930.448	57.61	289.027	2872.959	20.791	65.281
18	5643.6	63.941	81.668	4090.352	61.154	67.319	3797.398	37.892	59.524
19	9198.992	36.924	86.274	3899.6	31.616	121.882	1938.832	38.752	25.067
20	2659.024		51.995	2937.248	29.91	193.009	2831.442	32.477	48.363
21	2485.472			3505.2			2932.466		
Avg.	**3848.8**	**55.66**	**120.3**	**3708.377**	**48.94**	**126.187**	**2427.253**	**35.01**	**47.24**

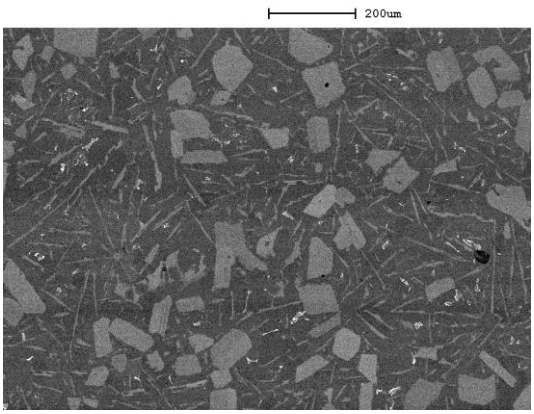

Typical image at the **top** location (100X)

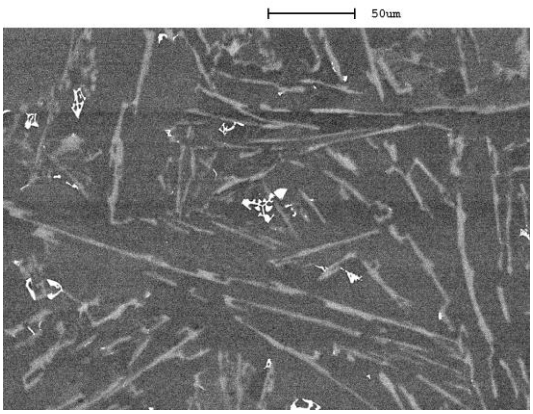

Typical image at the **top** location (400X)

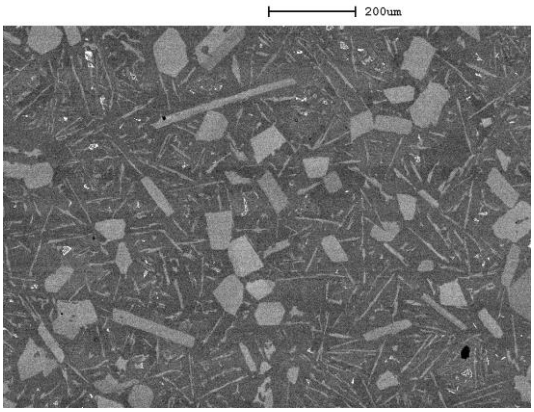

Typical image at the **mid** location (100X)

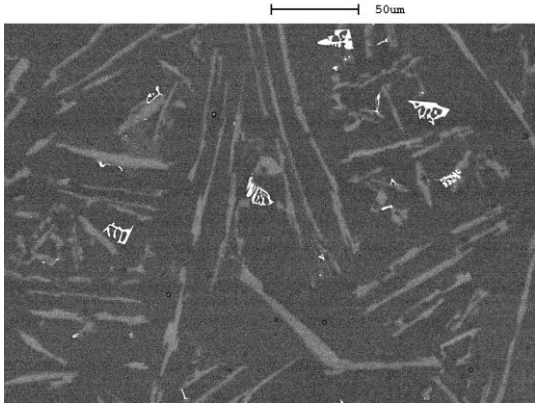

Typical image at the **mid** location (400X)

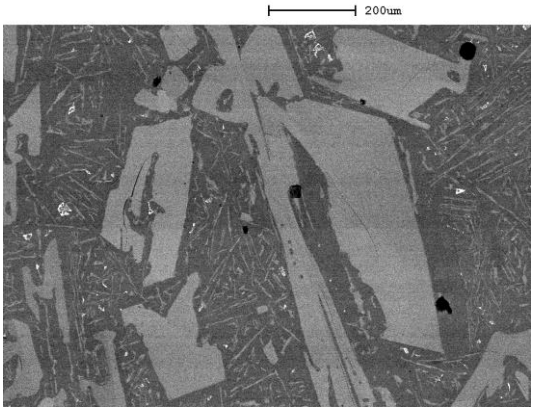

Typical image at the **bottom** location (100X)

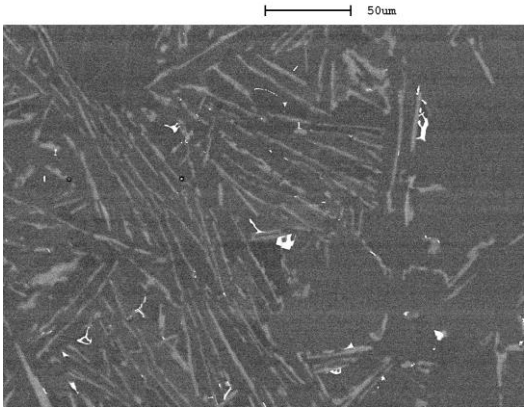

Typical image at the **bottom** location (400X)

Figure 6: SEM images used for measuring the Si particles of the sample processed at 1.4 T (equivalent to 160 voltage input), (a, b, and c) for the primary Si particles. (d, e and f) for the eutectic Al-Si particles.

Table 7: Measurement of the average eutectic Si particles using for all the samples with respect to the position (Top, Middle and Bottom)

The eutectic area and length particles with respect to the position of the samples at the different applied magnetic pulse							
		Top		Mid		Bottom	
Volt	**Tesla**	**Length**	**Area**	**Length**	**Area**	**Length**	**Area**
0	**0**	59.97	112.81	80.24	155.82	86.44	187.73
40	**0.3**	79.46	254.66	81.77	176.8	53.999	112.51
80	**0.7**	86.87	353.02	88.95	286.65	78.9	199.42
100	**0.85**	57	129.92	48.7	208.45	42.71	112.39
120	**1**	46.9	109.77	53.64	272.55	43.55	136.44
160	**1.4**	55.66	120.3	48.94	126.187	35.01	47.24

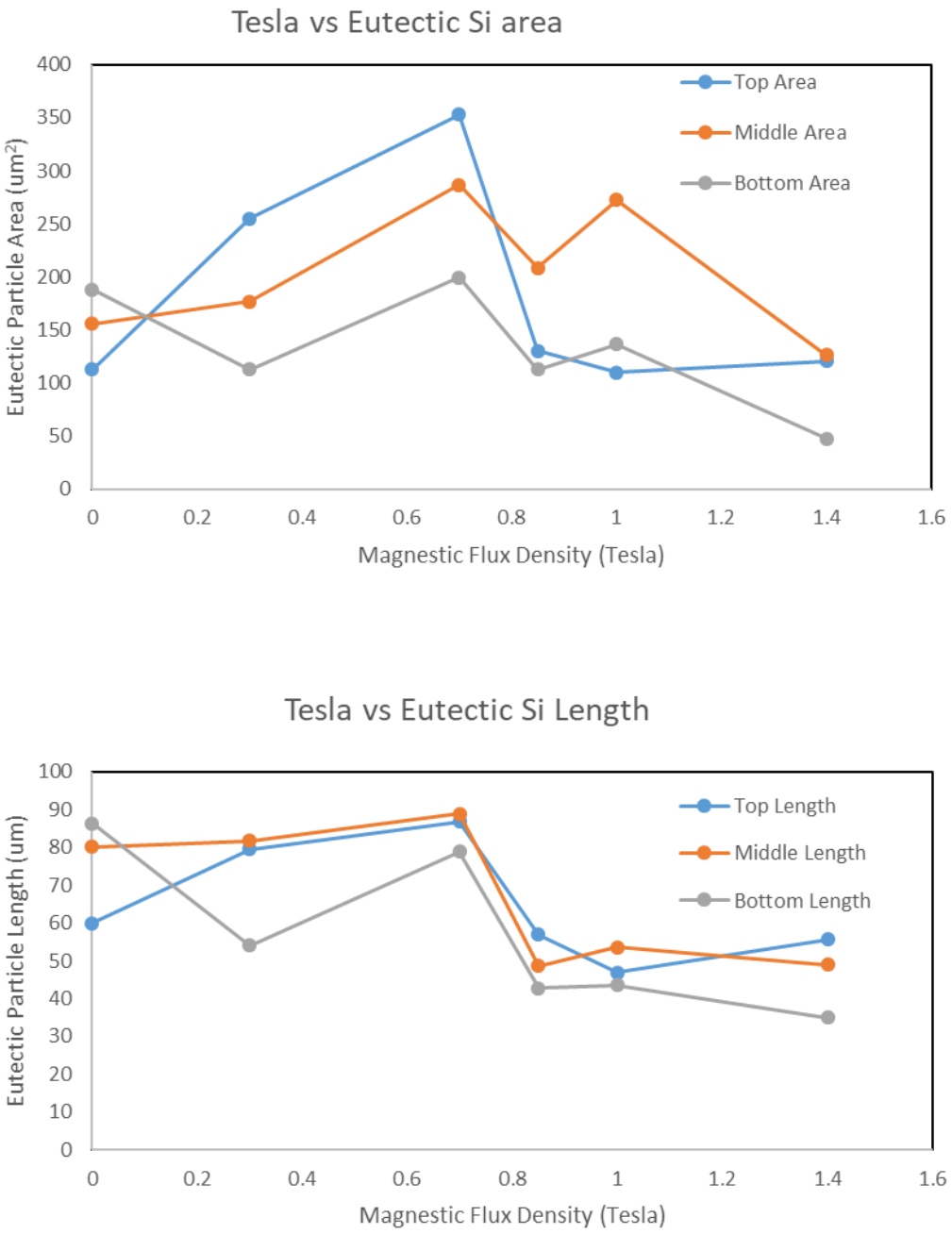

Figure 7: The relationship between the eutectic particles size (Length) and the magnetic flux density.

8.2 Appendix B: Composition of aluminium Silicon Alloys in Chapter 3

Sample 2 (Al-20%Si):

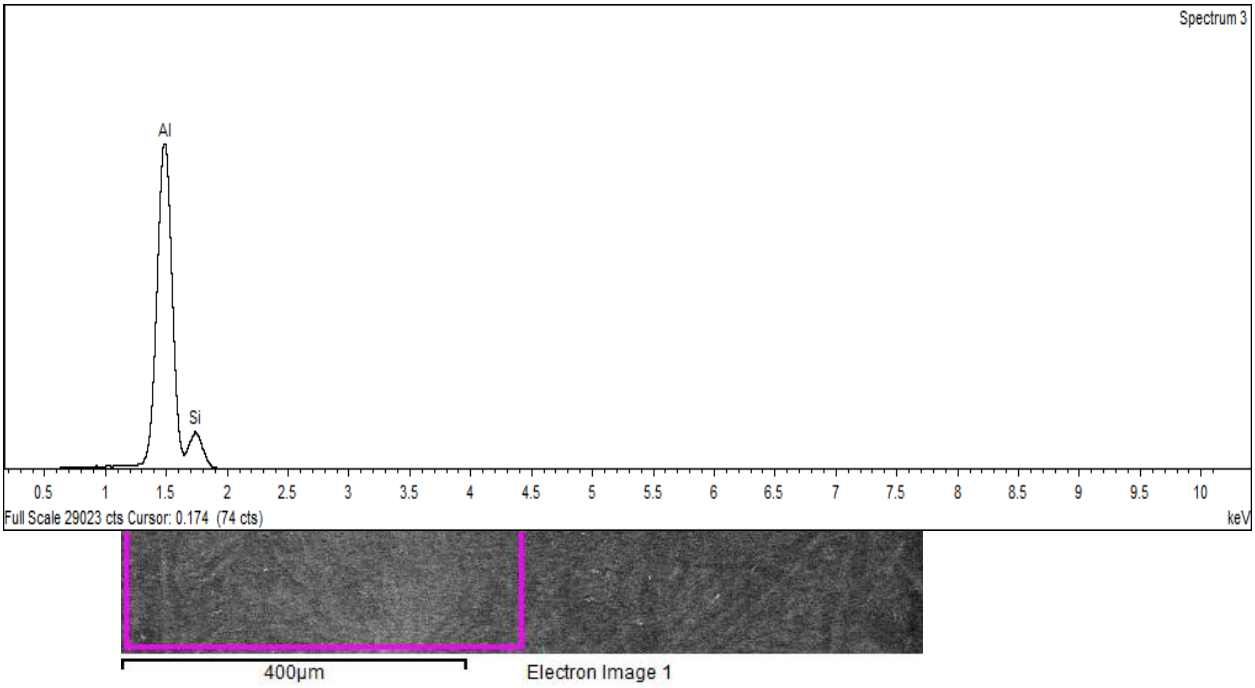

Element	Weight %	Atomic%
C K	9.48	19.04
O K	1.11	1.68
Al K	69.40	62.08
Si K	20.01	17.19
Totals	100.00	

Sample 1 (Al-20%Si):

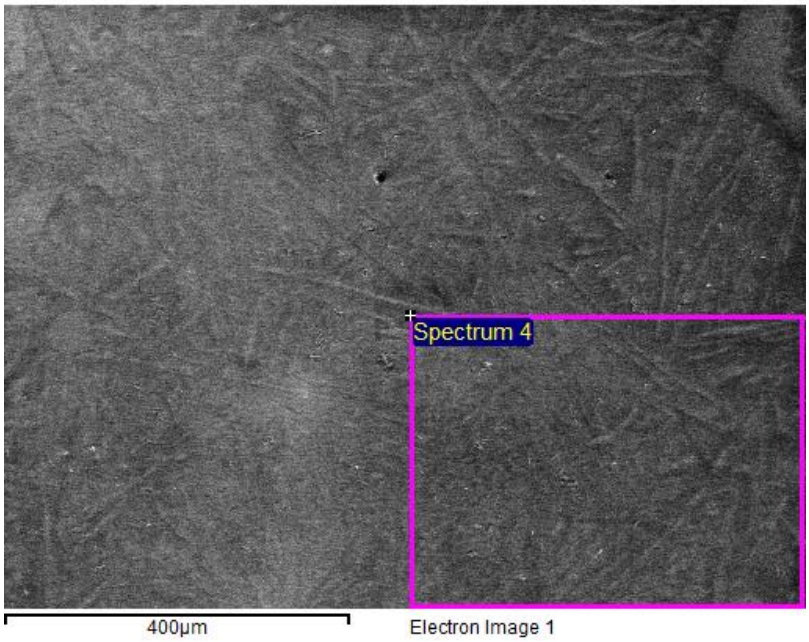

Element	Weight %	Atomic%	
C K	8.44	17.17	
O K	1.07	1.64	
Al K	70.95	64.27	
Si K	19.35	16.84	
Ni K	0.18	0.08	
Totals	100.00		

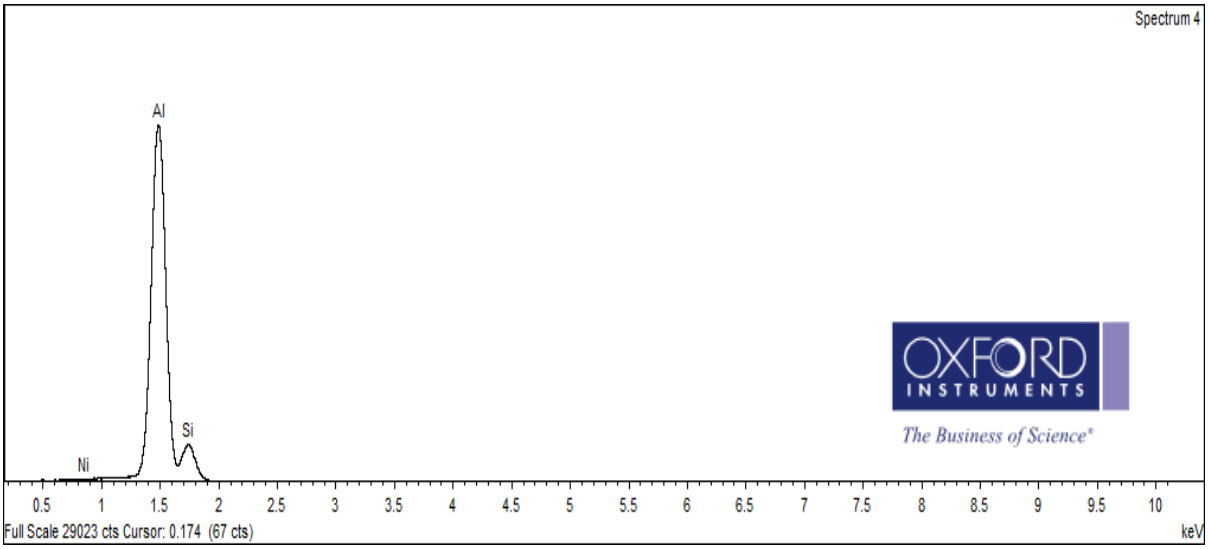

Sample 3 (Al-20%Si):

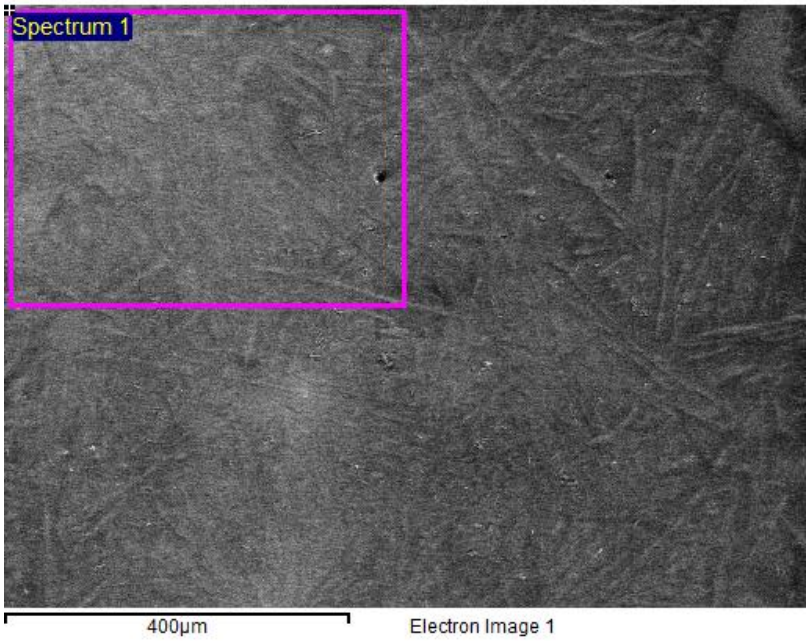

Element	Weight %	Atomic%
C K	8.34	17.02
O K	0.96	1.47
Al K	66.28	60.20
Si K	24.42	21.31
Totals	100.00	

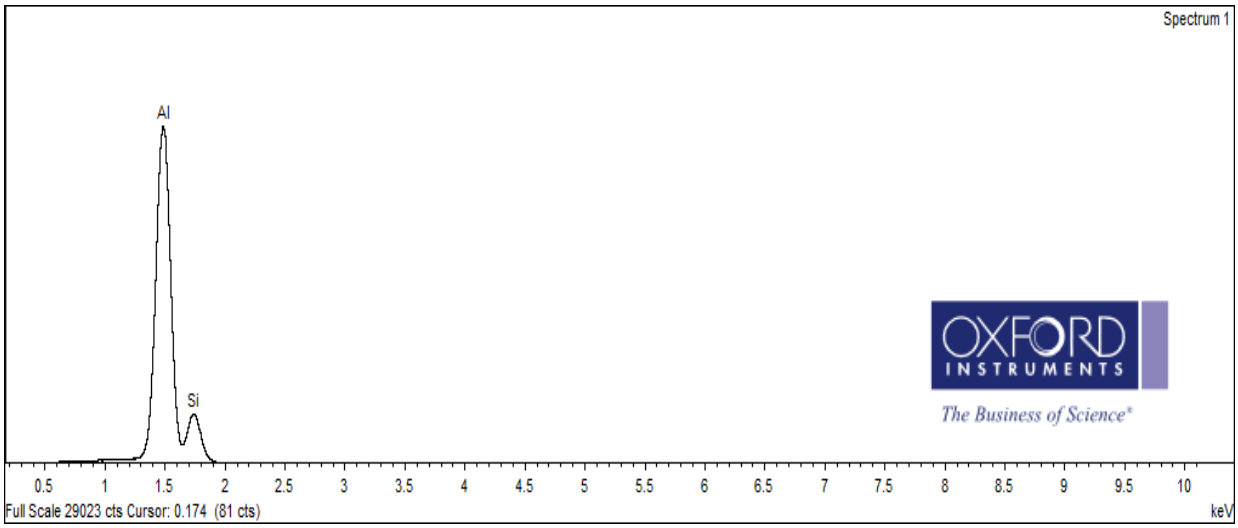
Spectrum 1
Al
Si
OXFORD
INSTRUMENTS
The Business of Science®
0.5 1 1.5 2 2.5 3 3.5 4 4.5 5 5.5 6 6.5 7 7.5 8 8.5 9 9.5 10
Full Scale 29023 cts Cursor: 0.174 (81 cts)
keV